Laser technologies for the development of carbon materials for environmental analytical microsystems

Chiranjeevi Maddi

N°d'ordre NNT :

THESE de DOCTORAT de L'UNIVERSITE DE LYON
opérée au sein de
l'Université Jean Monnet

Ecole Doctorale ED 488
Sciences Ingénierie Santé

Spécialité de doctorat :
Science et Génie des Matériaux

Soutenue publiquement le 5 avril 2016 par :
Chiranjeevi MADDI

Technologies laser pour l'élaboration de matériaux carbonés pour microsystèmes analytiques environnementaux

Devant le jury composé de :

DONNET, Christophe	Professeur, Université Jean Monnet	Président
CHAMPEAUX, Corinne	Professeure, Université de Limoges	Rapporteur
TESSIER, Pierre-Yves	Maître de conférences HDR, Université de Nantes	Rapporteur
CHAIX, Carole	Directrice de Recherche, Université Lyon 1	Examinatrice
SANCHEZ-LOPEZ, Juan-Carlos	Senior Lecturer, CSIC Sevilla, Espagne	Examinateur
LOIR, Anne-Sophie	Maître de conférences, Université Jean Monnet	Examinatrice
BARNIER, Vincent	Ingénieur de Recherche, Ecole des Mines de St-Etienne	Invité
GARRELIE, Florence	Professeure, Université Jean Monnet	Directrice de thèse
WOLSKI, Krzysztof	Professeur, Ecole des Mines de Saint-Etienne	Co-directeur de thèse

Table of content

List of Abbreviations 6

General Introduction 7

References 10

Chapter 1. Carbon based materials for sensors 13

1.1 Introduction 13

1.1.1 Sensors 14

1.1.2 Electrochemical Sensors 16

a. Voltammetry 17

b. Potentiometry 17

c. Conductimetry 18

1.1.3 Electrode materials for heavy metal detection 18

1.1.4 Carbon materials for sensors 19

1.2 Nitrogen doped amorphous carbon materials 22

1.2.1 Nitrogen incorporation in the carbon network 22

1.2.2 Effect of N incorporation on the bonding in CN films 26

1.3 Nitrogen doped amorphous carbon deposition techniques 27

1.3.1 Chemical Vapor Deposition (CVD) 27

1.3.2 Physical Vapor Deposition (PVD) 27

a. Pulsed Laser Deposition (PLD) 28

b. Plasma assisted pulsed laser deposition 31

c. Ultrafast pulsed laser deposition 33

1.4 Objective of the thesis 35

1.5 Conclusions 37

References 38

Chapter 2. Thin film deposition and characterization 55
2.1 Introduction 55
2.2 Thin film deposition method 55
2.2.1 Deposition Chamber 55
2.2.2 Femtosecond laser system 57
2.2.3 Determination of laser fluence 58
2.2.4 Thin film deposition procedure 60
2.2.5 Plasma plume diagnostics experiments 63
2.3 Amorphous carbon nitride (a-C:N) film characterization techniques 64
2.3.1 Multi-wavelength Raman Spectroscopy 65
a. Raman spectra of amorphous carbon 65
b. Raman spectra deconvolution 69
c. Instrumentation of Multi-wavelength Raman spectroscopy 72
2.3.2 X-ray Photoelectron Spectroscopy (XPS) 73
a. Basic Principle 73
b. XPS spectra fitting scheme 74
c. Instrumentation of XPS 75
2.3.3 Electron Energy Loss Spectroscopy (EELS) 76
a. Basic Principle 76
b. Instrumentation of EELS 78
2.3.4 Transmission Electron Microscopy (TEM) 78
a. Basic Principle 78
b. Sample preparation 79
c. Instrumentation of TEM 79
2.3.5 Surface morphology characterization 79
a. Scanning Electron Microscopy (SEM) 79
b. Atomic Force Microscope (AFM) 80
2.3.6 Electrochemical measurement 81

a. Cyclic Voltammetry (CV) technique....81

b. Instrumentation of cyclic voltammetry (CV)....83

C. Differential Pulse Anodic Stripping Voltammetry (DPASV)....83

2.4 Conclusions....85

References....86

Chapter 3. a-C:N thin films: Results and Discussions....89

3.1 Introduction....89

3.2 Film thickness....90

3.3 Surface morphology....90

3.3.1 Scanning Electron Microscopy (SEM)....90

3.3.2 Atomic Force Microscopy (AFM)....92

3.4 Chemical and microstructural analysis of a-C:N films....93

3.4.1 Nitrogen partial pressure effect on the chemical and microstructure of the a-C:N thin films....93

a. X-ray photoelectron spectroscopy....93

b. Electron Energy Loss Spectroscopy (EELS)....98

c. MW-Raman spectroscopy....100

3.4.2 Effect of different DC bias voltage on a-C:N film properties....104

a. X-ray Photoelectron Spectroscopy....104

b. Electron energy loss spectroscopy (EELS)....108

c. High Resolution Transmission Electron Microscopy (HRTEM)....112

d. Raman spectroscopy....113

3.4.3 Plasma assistance deposition effect on a-C:N films....116

a. X- ray Photoelectron Spectroscopy (XPS)....116

b. Electron Energy Loss Spectroscopy (EELS)....121

c. Microstructure characterization of a-C:N films: Multi-wavelength Raman spectroscopy....123

3.5 Conclusions 127
References 129

Chapter 4. Spectroscopic studies of graphite ablation plume under nitrogen gas and plasma assistance 133
4.1 Introduction 133
4.2 Optical characterization of the ablation plumes 134
4.2.1 Identification of the plume components 134
4.2.2 Expansion dynamics of the plume during the deposition 136
4.2.3 Comparison with ex-situ thin film analysis 142
4.3 Plasma dynamics impacts an a-C:N thin films structures 144
4.4 Conclusions 146
References 148

Chapter 5. Amorphous carbon nitride thin film electrodes for electrochemical Sensors 151
5.1 Introduction 151
5.2 Electrochemical properties of a-C:N films 152
5.2.1 Chemicals 152
5.3 Cyclic voltammetry (CV) of a-C:N electrode 153
5.4 Influence of film properties on electrochemical performances of a-CN electrodes 156
5.4.1 Effect of microstructural properties of a-C:N films on electrochemical performances 156
5.4.2 Chemical composition of a-C:N films on electrochemical properties 157
5.5 Detection of heavy metals by an a-C:N (10 at.%) electrode 158
Detection of single Lead ion (Pb^{2+}) 159
5.6 Electrochemical functionalization of a-C:N (10 at.%) electrode 161
5.6.1 In-situ generation of diazonium salt and grafting of 4-ethynylphenyl group 162
5.6.2 Click reaction of ferrocene-azide with 4-ethynylphenyl modified a-C:N electrode 162
5.6.3 Electrochemical characterization of functionalized a-C:N electrode 162
5.7 Conclusions 166
References 168

Chapter 6. N doped graphene: The future material for advanced technology 173

6.1 Introduction 173

6.2 Nitrogen doped graphene 175

6.3 Experimental procedure for N doped graphene synthesis 178

6.4 Results and Discussions 179

6.4.1 Microstructural properties of N doped graphene: Raman spectroscopy 179

a) Graphene 180

b) N doped graphene 182

6.4.2 Surface morphology (SEM and AFM) 186

6.4.3 Chemical composition in N doped graphene: X-ray photoelectron spectroscopy (XPS) 188

6.5 Conclusions 192

References 193

Conclusions and future perspectives 199

List of Figures 205

List of Tables 210

Appendix 211

List of Abbreviations

a-C: Amorphous Carbon

a-C:N: Amorphous Carbon Nitride

AFM: Atomic Force Microscope

BDD: Boron Doped Diamond

BE: Binding Energy

BWF: Breit-Wigner Fano

CPA: Chirped Pulse Amplification

CVD: Chemical Vapour Deposition

CV: Cyclic Volatammetry

CN: Carbon Nitride

DC: Direct Current

DLC: Diamond-Like Carbon

DPASV: Differential Pulse Anodic Stripping Volatammetry

EELS: Electron Energy Loss Spectroscopy

FCVA: Filetred Cathodic Vacuum Arc

FIB: Focused Ion Beam

FWHM: Full Width Half Maximum

GC: Glassy Carbon

HRTEM: High Resolution Transmission Electron Microscopy

IBAD: Ion Beam Assisted Deposition

ICCD: Intensified Charge Coupled Device

NMR: Nuclear Magnetic Resonance

NaCl: Sodium Chloride

PLD: Pulsed Laser Deposition

PVD: Physical Vapour Deposition

SEM: Scanning Electron Microscopy

TEM: Transmission Electron Microscopy

UHV: Ultra High Vacuum

XPS: X-ray Photoelectron Spectroscopy

General Introduction

The carbon is one of the most remarkable elements among all others in periodic table. It has a large number of allotropes. The carbon and carbon-based materials may exhibit exceptional properties such as chemical stability, high hardness, and thermal conductivity. The carbon is the building block of the carbon-based allotropes, such as graphite, diamond, fullerenes, graphene, carbon nanotubes, and amorphous carbon materials [1].

During the two last decades, the carbon has been the key element in the synthesis of thin coatings based on diamond, diamond-like carbon (DLC), various doped and alloyed DLC, carbon nitride and, more recently, graphene. There have also been in particular major developments in the field of disordered carbons. In general, the amorphous carbon (a-C) is a mixture of sp^3, sp^2 and sp^1 hybridization of carbon atoms, with a possible presence of hydrogen, depending on the deposition process. The amorphous carbon with a high fraction of sp^3 bonds is known as diamond like carbon (DLC). The DLC have some extreme properties similar to diamond, such as high mechanical hardness, chemical inertness, optical transparency, biomedical and electrochemical applications and it is a wide band gap semiconductor. It is much cheaper to produce than diamond, and it have wide spread applications [2–7].

In 1989, Cohen and Liu predicted a β-C_3N_4 phase with hardness comparable to diamond. However, the synthesis of super hard carbon nitride is technically very complicated and most of the synthesis led to other interesting types of materials, such as amorphous carbon nitride (a-C:N) material. In the past decades, the nitrogen doped amorphous carbon films have been studied extensively owing to their potential applications [8,9]. The a-C:N thin films are very attractive in electrochemical and bio sensors applications and molecular electronics with enhanced physical and chemical properties [10,11]. Especially, it is a very useful material in the detection of heavy metals and surface functionalization [12]. Now, the aim is to replace the high toxic electrode material like mercury and high temperature deposited Boron Doped Diamond (BDD) electrodes by amorphous carbon nitride (a-C:N) thin films material.

The production of high N content and more ordered graphitic-like structures are thus interesting to use in environmental analytical microsystems for electrochemical and biosensor devices.

To achieve this goal, various techniques have been used for the preparation of carbon nitride films under a wide range of deposition parameters [8]. Among these techniques, pulsed laser deposition (PLD) technique has a lot of advantages. Especially, the pulsed laser deposited carbon based coatings showed promising applications in electrochemical detection of heavy metals and bio-medical applications[13–15]. Until now, most of the work dealt with nanosecond PLD. Recently, the deposition of carbon materials by femtosecond pulsed laser deposition (fs-PLD) has attracted a lot of interest. The carbon films deposited by femtosecond PLD showed good electrochemical performances and high sp^2 content [16–18]. The femtosecond PLD grown amorphous carbon nitride films may be attractive in the analytical microsystems for electrochemical and bio sensors devices integrated in microfluidic channels for quick detection of hazardous pollutants, heavy metals and bio pathogens at low concentration in lab-on-chip devices and grating surfaces by organic compounds to increase the sensitivity of electrode for detection of bio molecules.

The present PhD has been carried in the context of a research program financed by "Université de Lyon" within the PALSE (Programme Avenir Lyon Saint-Etienne). The project, entitled "POLCARB", has been performed through a scientific collaboration between Laboratoire Hubert Curien (Université Jean Monnet and CNRS), Institute des Sciences Analytiques (CNRS and Université Claude Bernard Lyon 1), and Laboratoire Georges Friedel (Ecole Nationale Supérieure des Mines de Saint-Etienne and CNRS). The POLCARB overall aim was to build a new kind of microsystem determining toxic metals, emerging pollutants and pathogens in combined sewer overflow and river water. POLCARB wanted to respond to a strong societal demand in public health and environmental safety.
The present PhD is a contribution to the POLCARB program. It focus on the synthesis and characterization of carbon nitride films, and in a less extend, to nitrogen doped graphene.

This manuscript is organized in six chapters outlined below.

Chapter 1: In the first chapter, we discuss about the sensors, their characteristics and their potential use in the detection of hazardous heavy metals, about carbon-based materials such as

amorphous carbon and N doped amorphous carbon coatings and their deposition techniques. In the last section, we discuss about the pulsed laser deposition technique and the possibility to deposit a-C:N films by ultrashort pulsed laser deposition.

Chapter 2: we describe the detailed experimental procedure of thin film deposition by conventional and DC bias assistance femtosecond pulsed laser deposition, and detailed experimental procedure of plasma plume studies by using optical emission spectroscopy and spectrally 2D imagining techniques. In the last section, we discuss about the potential use of the wide variety of surface characterization techniques, their principle and instrumentation along with their operation conditions.

Chapter 3: We present the results obtained by different characterization techniques and discuss on the morphological, chemical and microstructural characteristics of CN films deposited by unbiased and DC biased femtosecond PLD.

Chapter 4: We present the *in situ* plasma plume results obtained during femtosecond PLD, by optical emission spectroscopy and by spectrally resolved 2D imaging techniques, along with the properties of the thin films used in plasma study and we discuss on the those ablation plume results.

Chapter 5: The electrochemical properties of selected a-C:N films are studied by Cyclic Voltammetry (CV) and Differential Pulse Anodic Stripping Voltammetry (DPASV). We perform heavy metal (Pb) detection by DPASV technique for a selective a-C:N electrode and functionalization of surface by organic molecules for a future selective detection of chemical and biological molecules.

Chapter 6: As a future prospective, we present the direct synthesis of N doped graphene from amorphous carbon nitride (a-C:N) thin films deposited by femtosecond pulsed laser deposition (fs-PLD) and perform the characterization by Multi-wavelength Raman spectroscopy, X-ray photoelectron spectroscopy for the chemical composition, and microstructural properties. In the last section, we discuss and propose suitable potential future applications.

References

(1) Donnet, C.; Erdemir, A. *Tribology of Diamond-like Carbon Films: Fundamentals and Applications*; Springer Science & Business Media, 2007.

(2) Voevodin, A. A.; Phelps, A. W.; Zabinski, J. S.; Donley, M. S. Friction Induced Phase Transformation of Pulsed Laser Deposited Diamond-like Carbon. *Diam. Relat. Mater.* **1996**, *5*, 1264–1269.

(3) Hauert, R. A Review of Modified DLC Coatings for Biological Applications. *Diam. Relat. Mater.* **2003**, *12*, 583–589.

(4) Dearnaley, G.; Arps, J. H. Biomedical Applications of Diamond-like Carbon (DLC) Coatings: A Review. *Surf. Coat. Technol.* **2005**, *200*, 2518–2524.

(5) Roy, R. K.; Lee, K.-R. Biomedical Applications of Diamond-like Carbon Coatings: A Review. *J. Biomed. Mater. Res. B Appl. Biomater.* **2007**, *83*, 72–84.

(6) Robertson, J. Properties of Diamond-like Carbon. *Surf. Coat. Technol.* **1992**, *50*, 185–203.

(7) Robertson, J. Diamond-like Amorphous Carbon. *Mater. Sci. Eng. R Rep.* **2002**, *37*, 129–281.

(8) Muhl, S.; Méndez, J. M. A Review of the Preparation of Carbon Nitride Films. *Diam. Relat. Mater.* **1999**, *8*, 1809–1830.

(9) Rodil, S. E.; Muhl, S. Bonding in Amorphous Carbon Nitride. *Diam. Relat. Mater.* **2004**, *13*, 1521–1531.

(10) Kikuchi, Y.; Chang, X.; Sakakibara, Y.; Inoue, K. Y.; Matsue, T.; Nozawa, T.; Samukawa, S. Amorphous Carbon Nitride Thin Films for Electrochemical Electrode: Effect of Molecular Structure and Substrate Materials. *Carbon* **2015**, *93*, 207–216.

(11) Medeiros, R. A.; Matos, R.; Benchikh, A.; Saidani, B.; Debiemme-Chouvy, C.; Deslouis, C.; Rocha-Filho, R. C.; Fatibello-Filho, O. Amorphous Carbon Nitride as an Alternative Electrode Material in Electroanalysis: Simultaneous Determination of Dopamine and Ascorbic Acid. *Anal. Chim. Acta* **2013**, *797*, 30–39.

(12) Jribi, S.; Cordoba de Torresi, S. I.; Augusto, T.; Cachet, H.; Debiemme-Chouvy, C.; Deslouis, C.; Pailleret, A. Determination of Surface Amine Groups on Amorphous Carbon Nitride Thin Films Using a One Step Covalent Grafting of a Redox Probe. *Electrochimica Acta* **2014**, *136*, 473–482.

(13) Maalouf, R.; Chebib, H.; Saikali, Y.; Vittori, O.; Sigaud, M.; Garrelie, F.; Donnet, C.; Jaffrezic-Renault, N. Characterization of Different Diamond-like Carbon Electrodes for Biosensor Design. *Talanta* **2007**, *72*, 310–314.

(14) Sbartai, A.; Namour, P.; Barbier, F.; Krejci, J.; Kucerova, R.; Krejci, T.; Nedela, V.; Sobota, J.; Jaffrezic-Renault, N. Electrochemical Performances of Diamond like Carbon Films for Pb(II) Detection in Tap Water Using Differential Pulse Anodic Stripping Voltammetry Technique. *Sens. Lett.* **2013**, *11*, 1524–1529.

(15) Loir, A.-S. Elaboration de couches minces de carbone par ablation laser femtoseconde pour application aux biomatériaux implantables. phdthesis, Université Jean Monnet - Saint-Etienne, 2004.

(16) Sbartai, A.; Namour, P.; Errachid, A.; Krejči, J.; Šejnohová, R.; Renaud, L.; Hamlaoui, M. L.; Loir, A.-S.; Garrelie, F.; Donnet, C.; *et al.* Electrochemical Boron-Doped

Diamond Film Microcells Micromachined with Femtosecond Laser: Application to the Determination of Water Framework Directive Metals. *Anal. Chem.* **2012**, *84*, 4805–4811.

(17) Khadro, B.; Sikora, A.; Loir, A.-S.; Errachid, A.; Garrelie, F.; Donnet, C.; Jaffrezic-Renault, N. Electrochemical Performances of B Doped and Undoped Diamond-like Carbon (DLC) Films Deposited by Femtosecond Pulsed Laser Ablation for Heavy Metal Detection Using Square Wave Anodic Stripping Voltammetric (SWASV) Technique. *Sens. Actuators B Chem.* **2011**, *155*, 120–125.

(18) Sikora, A.; Garrelie, F.; Donnet, C.; Loir, A. S.; Fontaine, J.; Sanchez-Lopez, J. C.; Rojas, T. C. Structure of Diamondlike Carbon Films Deposited by Femtosecond and Nanosecond Pulsed Laser Ablation. *J. Appl. Phys.* **2010**, *108*, 113516.

Chapter 1. Carbon based materials for sensors

1.1 Introduction

With the explosive growth of the world population and the rapid development of industrialization, the amount of toxic chemicals released into the environment has grown enormously due to the frequent human activities. These chemicals in air, water and soil have unknown toxicity and may cause health problems. The environmental pollution has become one of the most acute problems and has naturally captured the world's attentions. The analysis of environmental contaminants is a key step in understanding and managing the risks to human health and environment. Therefore, there is an urgent need to develop fast and reliable environmental monitoring methods. The increasing amount of potentially harmful pollutants in environment calls for the development of fast and cost-effective analytical techniques. Although highly sensitive and selective, conventional chromatography and spectroscopy analytical methods exist but they are time-consuming and laborious when a large number of samples have to be screened. Besides, they require expensive equipment, skilled operators and complicated pretreatment steps. The need of disposable tools for environmental monitoring encourages the development of simple, rapid, continuous, cost-effective and field-portable screening methods for analysis of environmental contaminants. Toxic metals including "heavy metals" are individual metal ions and metal compounds that negatively affect people's health. Some toxic and semi metallic elements are included in this group. In very small amounts, some of these metals are necessary to support life. However, in large amounts they may build up in biological systems and become a significant health hazard. Because of their persistence in nature, heavy metals are major contributors to the pollution of the biosphere and pose important environmental risks. The power industries, agricultural and waste disposal activities are among the leading generators of heavy metals such as lead, arsenic, and mercury. The ability to detect and monitor these metals is crucial for our well-being. The heavy metals like copper, cobalt, iron, manganese, and zinc are required in lower quantity for living organisms but lead to health problems in a high concentration, and the metals like arsenic, cadmium, chromium, lead and mercury are hazardous compounds even in lower concentration range [[1]]. Therefore, there is an urgent need to develop

an environmental friendly detection method to detect the heavy metals, pollutants and bio pathogens. With this aim, we tried to develop stable, non-toxic, high performance and cost effective electrodes in analytical methods to detect heavy metals, pollutants and bio pathogens at low concentrations in lab on chip devices.

This chapter will give detailed information about the carbon based materials and their importance when used as electrochemical sensors. We will emphasis on the N doped carbon based materials, especially on N doped amorphous carbon and N doped graphene materials with emerging applications. We will also discuss different possible deposition techniques for a successful synthesis of amorphous carbon nitride thin films. We will give a brief discussion about the deposition technique used in this work and will present a sound literature review on amorphous carbon nitride deposition by pulsed laser techniques. The last part of this chapter will give an overview on pulsed laser deposition of amorphous carbon (a-C) and amorphous carbon nitride (a-C:N) thin films by ultra-short pulsed laser deposition and also will cover the possible potential use of plasma assistance during pulsed laser deposition.

1.1.1 Sensors

The research and technology development in the field of sensors has clearly increased in the last decade due to the necessity of solving different current problems in our society [2,3]. Sensors are devices, that register a physical, chemical or biological change and convert that into a measurable quantity [4,5]. Sensors are composed of an active sensing material with a signal transducer. The role of these two important components in sensors is to transmit the signal without any amplification from a selective compound or from a change in a reaction. The sensors produce any one of these as output signals *i.e.*, electrical, thermal or optical signals, which could be converted into digital signals for further processing. Sensors can be broadly classified into two main categories such as chemical sensors and biosensors [6,7]. A chemical sensor is a self-contained analytical device that can provide information about the chemical composition of its environment. The biosensors can be defined in terms of sensing aspects, where these sensors can sense biochemical compounds such as biological proteins, nucleotides and even tissues [8–10]. Within these sensors, the active sensing material on the electrode act as a catalyst and catalyze the reaction of the biochemical and chemical compounds to obtain the output signals [11,12]. The

combination of these two different ways of classifications has given rise to a new type of sensors, called electrochemical biosensors, where the electrochemical methods are applied for the construction and working of a biosensors [13–16]. A schematic representation of a biosensor is reported on Figure 1.1 [3]. There has been a strong demand to produce highly selective, sensitive, responsive and cost effective electrochemical sensors. The selection and the development of the active material are still a challenge. The active sensing materials may be of any kind that act as a catalyst for sensing, particularly an analyte or a set of analytes. The major areas of applications are in environmental monitoring, medical and health diagnosis, industrial safety, surveillance, automotive industry and security for military applications.

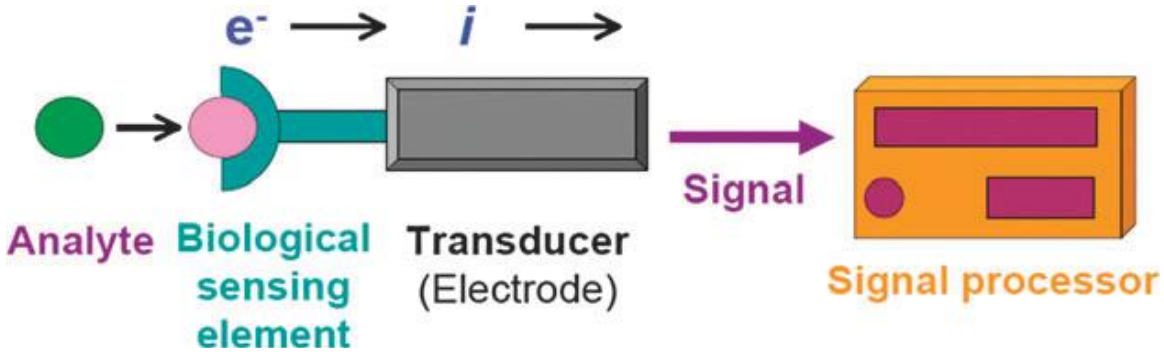

Figure 1. 1 Schematic of a biosensor with electrochemical transducer [3].

Among all, electrochemical sensors possess advantages over the others because their electrodes can sense materials present within the host material and without damaging the system [17]. The recent development in materials research has paved the way for a large number of new materials and devices of desirable properties, which have useful functions for numerous electrochemical sensor and biosensor applications. In recent years, the increased concerns about the toxic effects of chemicals in the environment have led to the necessity for monitoring pollutant levels at various points in industrial processes and recycling processes, in effluent and wastewater, and at industrial, agricultural, and urban sites. Additionally, continuous monitoring of environmental pollution in the field requires portable fast-response sensors that should be robust, sensitive and with long lifetime. Our goal is to design carbon based electrode materials for environmental analytical microsystems for electrochemical sensors.

1.1.2 Electrochemical Sensors

Electrochemical sensors represent an important subclass of chemical sensors in which an electrode is used as the transduction element, and are highly qualified for meeting the size, cost, and power requirements of on-site environmental monitoring [18–20].

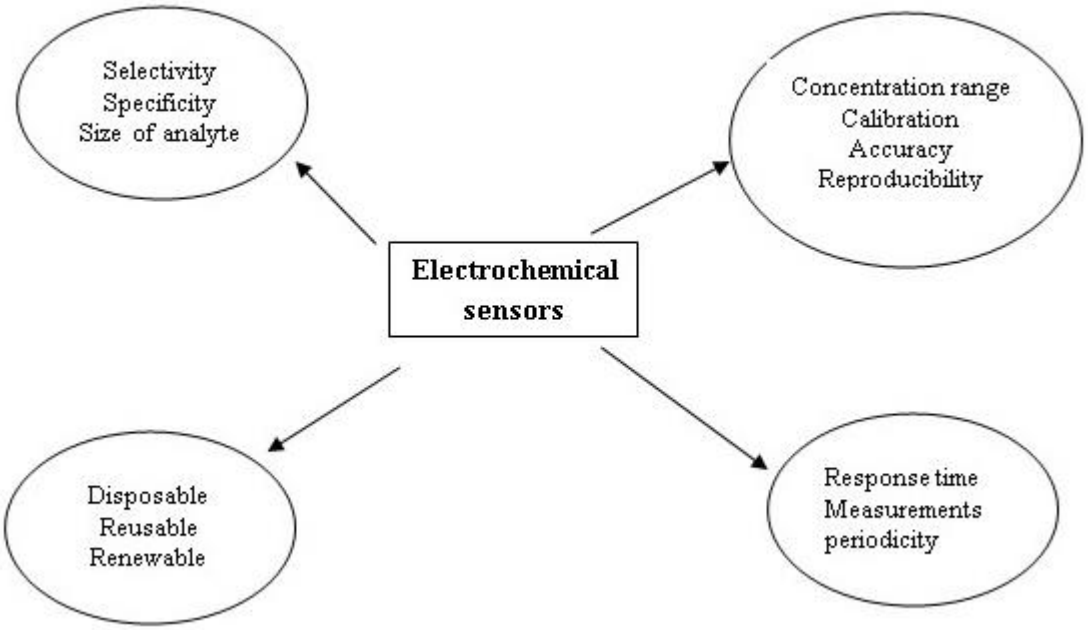

Figure 1. 2 Important aspects for choosing electrochemical sensors for environmental monitoring.

A chemical sensor can be defined as a device that provides continuous information about its environment. Ideally, a chemical sensor provides a certain type of response, which is directly related to the quantity of a specific chemical species. The electrochemical sensors consist of a transducer, which transforms the response into a detectable signal on modern instrumentation, and a chemically selective layer, which isolates the response of the analyte from its immediate environment. They can be classified according to their properties to be determined as: electrical, optical, mass or thermal sensors and they are designed to detect and respond to an analyte in the gaseous, liquid or solid state. Compared to optical, mass and thermal sensors, electrochemical sensors are especially attractive because of their remarkable detectability, experimental simplicity and low cost. The electrochemical sensors have a leading position among the presently available sensors and they have reached the commercial stage. The Figure 1.2 presents the important

aspects to consider to choose electrochemical sensor. The electrochemical sensing systems include a high sensitivity and selectivity, a wide linear range, a minimal space, low power requirements and a low cost instrumentation. Electrochemical sensing devices have given a lot of importance in a wide range of applications in recent years in clinical, industrial, environmental and agricultural fields. The electroanalytical sensors are concerned with the interplay between electricity and chemistry, namely the measurements of electrical quantities, such as current, potential or charge and their relationship to chemical parameters. The electrochemical devices have been used for several decades for field monitoring of a variety of water quality parameters [5], these have led to a wide range of environmental applications including the measurement of trace metals in natural water [10,21–25]. The development of biosensors are used for the detection of organic pollutants in ground water [26,27], environmental protection and clean energy conversion [28,29]. The stability of natural water samples during long term storage is questionable, as they are subject to various biological, chemical and physical effects [30–33]. Most of the electrochemical devices used for environmental monitoring, fall within three categories described below and ultimately depend on the specific analyte, nature of the sample matrix and the sensitivity and selectivity requirements [34].

a. Voltammetry

The uses of an applied potential between reference and working electrodes are causing the oxidation or reduction of an electroactive species. The applied potential thus serves as the driving force for the electron-transfer reactions. The resulting current is a direct measure of the rate of the electron transfer reaction and is proportional to the target analyte concentration.

b. Potentiometry

In potentiometric sensors (primarily ion-selective electrodes), the analytical information is obtained by converting an ion recognition event into a potential signal. A local equilibrium is established across the recognition membrane, leading to a change in the membrane potential. The analytical information is obtained from the potential difference between the ion selective electrode and a reference electrode. Potentials are a function of an activity of species but not on a concentration.

c. Conductimetry

Conceptually it is the simplest electroanalytical techniques but inherently non-specific. The concentration of the charge is obtained through measurement of solution resistance.

Above aforementioned analytical techniques, the voltammetry technique is widely used due to its sensitivity, inexpensive instrumentation and advance development in all areas of voltammetry. The common characteristic of all the voltammetry techniques is that they involve the application of potential (E) to an electrode and the monitoring of the resulting current (i) flowing through the electrochemical cell.

The analytical advantages of the various voltammetric techniques include an excellent sensitivity with a very large useful linear concentration range for both organic and inorganic species, a large number of useful solvents and electrolytes, a wide range of temperatures, rapid analysis times, the ability to determine kinetic parameters, a well-defined theory, simultaneous determination of several analytes [35–37].

1.1.3 Electrode materials for heavy metal detection

A lot of research and development are going on to find environmental friendly electrodes for electrochemical sensors for the detection of heavy metals and bio pathogens. In the past, two basic electrode systems were used in electrochemical analysis as electrode materials, such as mercury film electrode and hanging mercury drop electrode. The mercury electrode was gained wide acceptance in the development of stripping voltammetry. In most of the cases, a Glassy Carbon (GC) electrode or a carbon fiber one are used to support the mercury film. The best results were obtained with the mercury electrodes [38,39]. However, because of the toxicity, the future regulations and occupational health considerations may severely restrict the use of mercury as an electrode material, and the disposal problems and cost are the major drawbacks of the mercury electrode. New alternative electrode materials with a similar performance are highly desired, particularly for meeting the growing demands for on-site environmental monitoring the trace metals and decentralized clinical testing of toxic metals. The gold and iridium electrodes have been used as possible alternative to the mercury electrode [40–43]. While offering useful signals for several metals, the overall performance of these non-mercury electrodes has not

approached the mercury electrode, due to a low cathodic potential limit, multiple peaks, or large background contributions [44]. The pre-concentration modified electrodes, based on surface-confined ligands or ion exchangers have been proposed, but their overall sensitivity and reproducibility has not been satisfactory for routine measurements of trace metals [45]. Despite these intensive efforts, an alternative electrode to the mercury has not emerged. Thus, it is important to move toward different materials and non-mercury sensor materials. Successes have been registered, particularly with regard to carbon materials. Carbon and carbon-based electrodes have been proposed as suitable electrodes for the heavy metals detection and the surface functionalization for bioorganic compound attachment to increase further the sensitivity of the electrodes in electrochemical sensors [46–51].

1.1.4 Carbon materials for sensors

Carbon based materials are extremely attractive as electrodes in electrochemical sensors for the analysis of heavy metals, as they have extreme properties such as acceptable biocompatibility, high hardness, chemical and electrochemical stability and good electrical conductivity. Carbon is very versatile and can be crystallized in various forms extending from Diamond to Graphite. Carbon remains one of the most attractive and well-studied materials systems in the scientific community due to its amazing variety and versatility in combination with low cost, availability and wide variety of applications. There have also been major developments in the field of disordered carbons. In general, an amorphous carbon (a-C) can have any mixture of sp^3, sp^2 and sp^1 sites, with the possible presence of hydrogen bonds. Their physical properties depend on the ratio of graphite-like sp^2 and the diamond-like sp^3 bonds. Aisenberg and Chabot reported the properties of a-C thin films prepared by ion beam deposition (IBD) with properties closer to diamond than graphite [52]. The expression “diamond-like carbon” (DLC) was created. The DLC can have some extreme properties similar to diamond, such as high mechanical hardness, chemical inertness, and optical transparency and is a wide bandgap semiconductor. The DLC films have a wide spread of applications as protective coatings in areas such as optical windows, magnetic storage disks, car parts, biomedical coatings and as micro-electromechanical devices (MEMS) [53]. The term DLC includes many sub forms of amorphous carbon materials. Among them graphitic carbon or glassy carbon, polymer-like carbon, and tetrahedral amorphous carbon

(ta-C) can be found. The terminology of DLC materials is based on the amount of hydrogen in the carbon matrix as well as the mixture of sp^3- and sp^2 hybridized carbon. The C bond in a sp^2 configuration may always be present to a certain extent in this material class, but the content of C bond in sp^3 manner is limited and a maximum amount of 90 % was found in ta-C. In the case of the carbon thin films without nitrogen, the ternary phase diagram describes the carbon compositions shown in Figure 1.3,

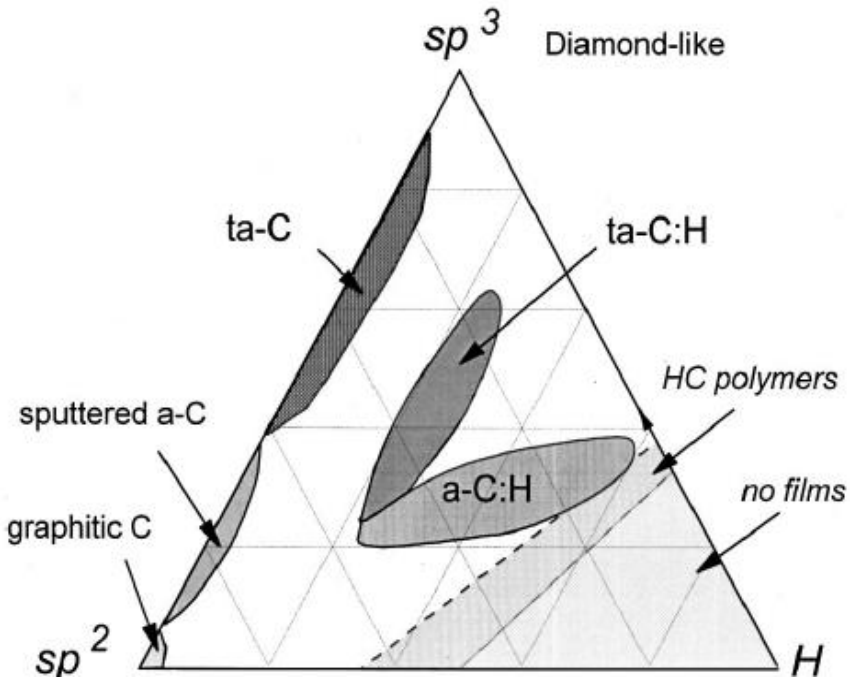

Figure 1. 3 Ternary phase diagram of different amorphous carbon types [54].

According to the ratio of sp^2/sp^3 bonds, the films can show various properties. While the significant sp^3 hybridized carbon coatings were showing high hardness, chemical inertness, optical transparency and a wide bandgap, the more graphitic films are softer but also chemically inert, highly transparent and biocompatible. Moreover, these graphitic films have a variable band such as semiconductors. The graphitic carbon films find some applications in the electrochemical and the biochemical sensors [55], and the protection of medical implants in aggressive environments [56].

Among the carbon based electrodes, Glassy Carbon (GC) has been one of the most widely used electrode materials in electroanalytical applications due to its smooth and robust nature, easy fabrication and wide working potential window. Its eletroanalytical performances frequently

suffer from high reproducible background contributions and from gradual loss of surface activity. There is a growing need for the reliable measurements of biological important compounds for clinical screening and trace metals for environmental monitoring. The need has stimulated attempts to develop alternative, disposable carbon based electrodes being able to allow mass production of electrically conductive electrodes of remarkable properties [57,58]. The diamond conductivity comes from the damage generated sp^2 (graphitic) contents in case of ion-implanted diamond or the boron doped in case of CVD diamond films [59]. The latter films have shown a large electrochemical window, a low background current for aqueous systems and a remarkable stability comparable with the chemical resistance of pure carbon diamond. However, there are some practical problems for synthesis of such material. The high film procession temperature, 100-800^{o}C of substrate temperature for CVD diamond film deposition [60], and 1100^{o}C for pyrolyzing process [61], limited their applications of diamond films. Unlike these carbon materials, the DLC films can be deposited at room temperature without specific surface treatment or metal catalyst. Therefore, they can easily be fabricated into micro-devices with conventional semiconductor technology in mass production. The electrical conductivity of DLC is tuned by adjusting the elaboration process or by doping. These characteristics have led to recent efforts in studying the electrochemistry of intrinsic DLC, BDD and doped DLC with a goal to replace high temperature deposited boron doped CVD diamond as electrode materials. The performance of DLC and doped DLC, compare favorably well with those of BDD materials in terms of high chemical inertness, wide potential window and low background current and their process are easier and cheaper (e.g. low temperature without catalyst) [62–70]. This latter feature makes them good candidates for electrochemical and many other promising applications, *e.g,* sensing humidity [71,72] and water concentration in oil [73], detection of heavy metals by stripping voltammetry [53,74–76], coating electrochemical quartz crystal micro balance (EQCM) [70], tip electrode for scanning electrochemical microscopy (SECM) [77], protection layer against corrosion [74] and optical transparent electrode [78]. Besides these applications, the high bio fouling resistance, low polarization, and large anodic potential limits of the materials recently generates interest in applying them in bio sensing, water treatment and electrochemical energy engineering [53]. Up to now, a lot of work has been done based on amorphous carbon materials. As doping a-C films alter the bandgap and changing the material to n-type from being p-type, a large variety of carbonaceous materials are largely unexplored in environmental analytical

microsystems. The performance of DLC, especially nitrogen-doped a-C is favorably well comparable to those BDD materials with a high chemical inertness, a wide potential window, a low background current and their easier and cheaper process [79–90]. Therefore, our interest is to study and develop doped a-C films for analytical microsystems to replace the high toxic mercury and high temperature deposited BDD electrodes in the near future.

1.2 Nitrogen doped amorphous carbon materials

Doping is the most feasible method to control the conducting properties in the conventional semiconductor community. The B and N atoms are the natural candidates for doping of carbon-based materials such as amorphous carbon and graphene, because of their similar atomic size as the size of C and of their hole acceptor and electron donor characters for substitutional B- and N-doping, respectively. The doping of a-C by boron is giving p-type dopant while nitrogen doping is giving n-type semiconductor [68]. Nitrogen doped amorphous carbon possess many unique electrochemical properties compare to other dopants.

1.2.1 Nitrogen incorporation in the carbon network

Among possible chemical choices for carbon modification, nitrogen doping has long been a natural and widely studied option. Nitrogen-containing carbon structures have attracted great attention in the past because of their abundance, accessibility, and low health risk.

Nitrogen is the natural choice for efficient and beneficial modification of carbon films due to three specific reasons. Firstly, N is one neighbor away from C on the periodic table and by replacing one C with N in the carbon network the total number of electrons in the system can be tailor. Secondly, N has an atomic radius similar to that of C, thereby preventing significant lattice mismatch. Thirdly, N-doping can induce n-type electronic modification to the carbon structure, in analogy to typical semiconducting materials, which enables the potential use of these C–N structures in multiple important applications.

The idea about preparation of super hard materials began in 1989 when Cohen and Liu predicted a phase β-C_3N_4 with a hardness comparable to diamond [91] and caused a sharp increase of interest in this material. However, the synthesis of super hard carbon nitride is technically very

complicated and most of them resulted in amorphous carbon nitride phase successfully prepared [92,93]. Currently, boron carbides, boron carbon nitrides and other composites have been used as super hard coatings. The amorphous carbon nitride (a-C:N) have also given a lot of interest in research due to their extraordinary properties such as biocompatibility, chemical inertness and variable bandgap, and to its most noticeable application as a protection of computer hard discs [94]. In the past years, the trend shifted to the use of more sp^2 graphitic structured films and their use in electrochemical and chemical applications [72,95]. They can also be used as a protection material in aggressive environments (e.g. as a protection of medical implants) [96–98]. This modification allows for the beneficial properties of the carbon by fine-tuning the final electrical, morphological, and chemical properties of the functionalized carbon network.

Carbon nitride films are classified according to the ratio of the sp^2/sp^3 hybridization with the content of nitrogen and hydrogen having a high impact on the films properties. In the work of A. C. Ferrari and J. Robertson [99] two ternary phase diagrams of amorphous carbon nitride (a-C:N) film with and without hydrogen were presented. The diagram is shown in the Figure 1.4.

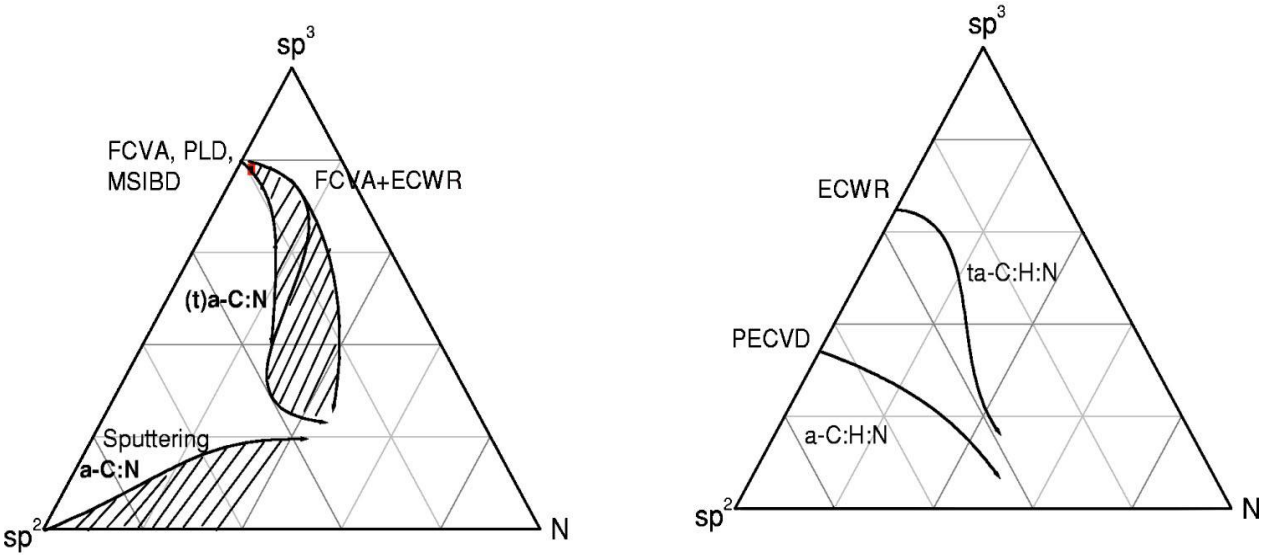

Figure 1. 4 Ternary phase diagram of amorphous carbon nitride (a-C:N) alloys, without hydrogen (left) and with hydrogen (right) showing sp^3, sp^2 and N content [99].

In the Figure 1.4, there are phase diagrams of (hydrogenated) carbon nitride films. The area where the films are soft, amorphous and hard tetrahedral amorphous composition is present together with the preparation techniques. According to the diagram, the carbon nitride coatings

can be divided into two main groups, more sp^2 bonded a-C:N films and more sp^3 bonded ta-C:N films. The kind of film depends on the deposition technique used for preparation.

The properties of carbon nitride films strongly depend on the bonding between carbon and nitrogen atoms. The atomic arrangement in carbon nitride films was demonstrated by the contrast between graphite and diamond. The bonding configurations have four neighbors, as in diamond sp^3 bonding, and nitrogen has three neighbors, as in graphite sp^2 bonding with a lone pair as in Figure 1.5a. However, the bonding in carbon nitride systems is rather difficult because both carbon and nitrogen can exist in three hybridization sp^3, sp^2 and sp^1. Therefore, at least nine different bonding configurations are possible, as shown in Figure 1.5b, taken from S. E. Rodil *et al*.[100]. The existence of different bonding types shown in Figure 1.5b, (a) N_3^0 atom with three σ bonds leads to two remaining electrons in a lone pair, in its simple trivalent configuration. (b) N_4^- uses four electrons in σ bonds with the remaining unpaired electron available for doping, in a fourfold coordinated substitutional site. (c) N_4^+—C_3^- pair forms a trivalent carbon site and the unpaired electron transfers to the carbon to give a positive N^+/C^-. The remaining configurations are corresponding to π bonding: The nitrogen can substitute for carbon in a benzene ring, (d) pyridine type, and (e) doped pyridine-like. (f) The pyrrole type is the nitrogen bonded to three neighbors in a five-fold ring, three electrons are in bonds and the two others are used to complete the aromatic ring. The other variants of π bonding are, with nitrogen two-fold coordinated. (g) A double bond unit has two electrons in σ bonds and one in π bond, leaving a non-bonding pair. (h) A double bond unit uses three electrons in σ bonds, one in π bond and the fifth in an antibonding π* state, available for doping. (i) The last configuration is the triple bond with an isolated lone pair, as in cyanide. However, the most difficult task is the identification of bonding in the carbon nitride films.

The characterization of pure amorphous carbon films induces complications and a big challenge for the characterization of carbon nitride films, but the characteristics of CN films must nevertheless be accessible.

(a)

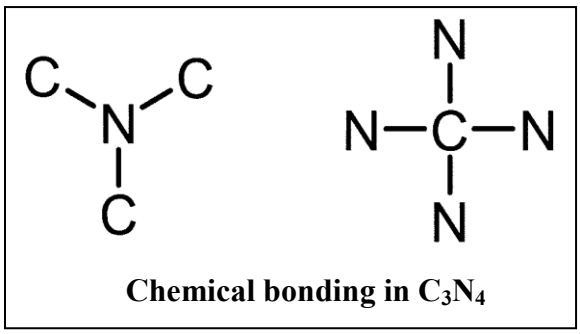

Chemical bonding in C_3N_4

(b)

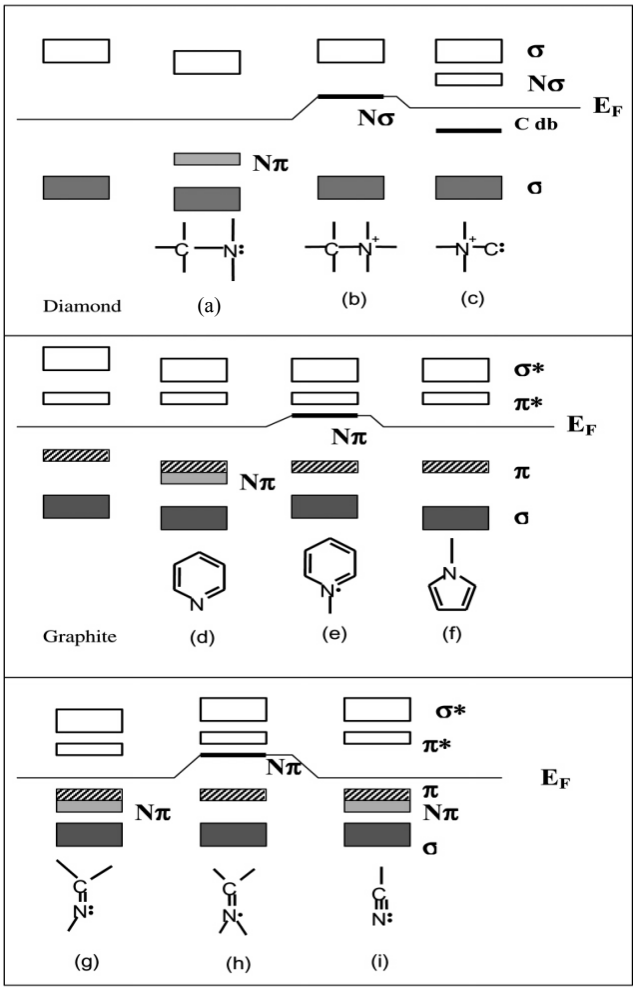

Figure 1. 5 (a) The chemical bonding in C_3N_4 phase, (b) Different CN_x bonding configurations, paired bonds are depicted as lines, unpaired electrons are represented by one dot and paired electrons in non-bonding lone pair as two dots [100].

1.2.2 Effect of N incorporation on the bonding in CN films

As we clearly mentioned in the above section, the doping of nitrogen leads to the formation of a different bonding, and the determination of bonding configuration is complicated due to the amorphous nature of the films. Up to now, a lot of research was done on the carbon nitride films. However, some problems are encountered in the precise characterization of carbon nitride films. There is a little disagreement about the interpretation of the spectra obtained for the carbon nitride films for any of the common tools used to study chemical bonding. The most direct measurement of chemical bonding is ^{13}C NMR [101]. The Nuclear Magnetic Resonance (NMR) has been used only in the few occasions in which enough material could be needed and the results suggest that high nitrogen content films are preferentially sp^2 bonded [102–107]. The Electron Energy Loss Spectroscopy (EELS) and Near-Edge X-ray Absorbance Spectroscopy (NEXAFS) suggest a decrease in the Csp^3 bonding induced by the increase in the nitrogen content, *i. e*, at high N at.% the CN films are preferentially π bonded [100,108–113]. From EELS and NEXAFS it is also clear that as the nitrogen content in films increases, the CC sp^3 bonds are rapidly substituted by CN sp^2 or sp^1 bonds, therefore there is a clear indication that at high N content all the carbon nitride films should be π bonded. The X-ray Photoelectron Spectroscopy (XPS) technique can also be used to quantify the doping content and the bonding structure in films but there is still no completely acceptable identification scheme for all the carbon and nitrogen peaks observed [114–125]. Both the XPS nitrogen and carbon peaks were simulated normally by the sum of various individual peaks related to different atomic bonding configurations. Similarly, the interpretation of Raman spectra in carbon nitride films suggested the formation of single bonded CN phases and difficulties associated with the interpretation of the different spectra [99,126]. Therefore, it is necessary to characterize amorphous carbon nitride films with careful attention by using many techniques before claiming any conclusions. In this work, we focused on CN bonding regimes present in a-C:N films by different complimentary characterization techniques such as Multi-wavelength Raman spectroscopy, X-ray photoelectron spectroscopy (XPS) and Electron energy loss spectroscopy (EELS). These techniques allow us to draw common arguments of amorphous carbon nitride in between microstructure and chemical structure. The microstructure and chemical bonding depend on the deposition techniques used.

1.3 Nitrogen doped amorphous carbon deposition techniques

Carbon based materials have been prepared by numerous deposition techniques [72,95–97,127]. The thin films properties depend on deposition techniques, which are vacuum based thin films deposition techniques. They are broadly categorized as Physical Vapor Deposition (PVD) and Chemical Vapor Deposition (CVD) techniques. The synthesis of β-C_3N_4 was not successful up to date, although other interesting materials were synthesized, such as sp^2 rich amorphous carbon nitride (a-C:N) films. A large number of techniques were applied to deposit amorphous carbon nitride (a-C:N) films so far, although there are few reports in deposition of crystalline β-C_3N_4 films, most of the films are amorphous in nature. The aim of these techniques was to achieve energetic species of carbon and nitrogen. Some of the techniques are direct, *i.e*, produced energetic carbon and nitrogen species and then combined them to produce a a-C:N films.

1.3.1 Chemical Vapor Deposition (CVD)

The CVD technique is widely used for the preparation of carbon nitride films. The CVD method is used mainly for one or more elements belonging to the films, so that these elements generate chemical reactions on the surface of the substrate and generate the film. The CVD methods include electron cyclotron resonance [128–130], hot filament assisted [131], and microwave plasma chemical vapor deposition [132]. The preparation of films is more likely to generate C-H and N-H bonds under the CVD conditions, and most of CN films are amorphous. When the CVD methods are used to prepare the CN films, the choice of substrate material is crucial. The a-C:N films grow by chemical vapor deposition technique at elevated temperatures (T>1000^{o}C) and by using toxic gases. However, high temperatures deposited a-C:N films are not suitable in environmental friendly electrochemical applications. Therefore, the CVD techniques are unsuitable for our coatings for electrodes in electrochemical applications, tuning the interest of PVD grown carbon nitride electrodes.

1.3.2 Physical Vapor Deposition (PVD)

The physical vapor deposition comprises several techniques, such as pulsed laser deposition (PLD) [122,133–136], magnetron sputtering (RFMS and DCMS) [137–142], ion beam assisted

deposition (IBAD) [143], filtered cathodic arc deposition [144]. The PVD technique usually employs significantly lower growth temperatures, ranging from room temperature (RT) to T<900°C.

A. Fernandez *et al.*[138] obtained the carbon nitride films by reactive magnetron sputtering in pure N_2 discharge. Their studies found that N/C ratio reached to 0.5, and that found the formation of polymer like CN amorphous phase, which contains the C≡N, C=N and C-N bonds. In the same year, S. Logothetidis *et al.*[137] reported the nitrogenated amorphous carbon films prepared by reactive r. f. magnetron sputtering from a graphite target in a nitrogen containing plasma on Si substrate. They obtained a different degree of N concentration up to 4.4 % achieved. The films were shown composed of two phases, a C_3N_4 like phase of sp^3 bonded crystallites and an amorphous phase of sp^2 bonded CN one. Subsequently, a large number of researchers also obtained the CN films by similar method [139–141].

Before Niu *et al.*[134], most of the carbon nitride films deposition dealt with sputtering techniques. The successful demonstration of high N content carbon nitride films deposition by pulsed laser technique have grown a huge interest in the scientific community and also a lot of potential applications were demonstrated by using PLD grown carbon nitride films.

Niu *et al.*[134] obtained the CN_x films on silicon substrate by using pulsed laser evaporation of C target, auxiliary deposition nitrogen. Their studies found that N content reached 40 at.% in films and C and N atoms combined with nonpolar covalent bond. Subsequently, Sharma *et al.*[145] and Zhang *et al.*[146] also obtained CN_x films by a similar method. Mihailescu *et al.*[147] produced a hard carbon nitride films with carbon nitrogen single bond, double bond and triple bond by using ammonia instead of N_2 pressure.

Among the above mentioned techniques, the PLD is a promising way to deposit carbon nitride films with enhanced physical, chemical and electrochemical properties because it can be easily carried out even on non-conductive substrates and at low substrate temperatures during the film growth.

a. Pulsed Laser Deposition (PLD)

Pulsed laser deposition (PLD) is a versatile thin film deposition technique. The pulsed laser ablation principle is illustrated schematically in the Figure 1.6. A solid material is irradiated with an intense laser beam and a small amount of material on the surface is vaporized and ejected from

the sample. The ejected matter is a collection of atoms, molecules, ions and electrons, from which the exact ratio and kinetic energy depend on the laser parameters (intensity, wavelength, pulse width). If the vapor comes in contact with another surface then it may re-condense on the surface. Repeated pulses of laser and subsequently repeated vapor plumes build up material on the substrate surface, which grow the thin film [148].

The growth and quality of the resulting film generally depends on a number of fundamental parameters, including the choice of substrate, the substrate temperature, T_S, and the absolute and relative kinetic energies and/or arrival rates of the various constituents within the plume. The latter may be affected by the choice of excitation wavelength, laser pulse duration, energy and intensity, and the presence of any background gas [149].

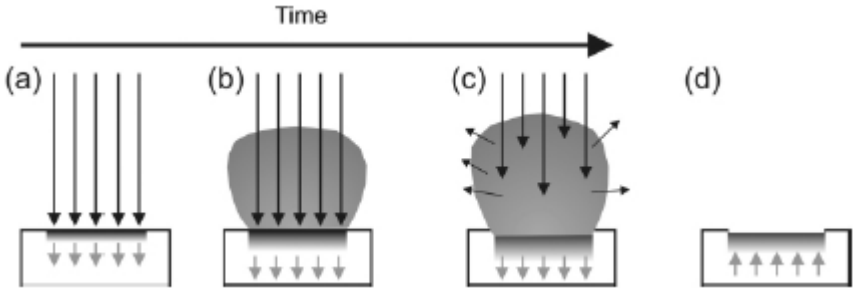

Figure 1. 6 Schematic diagram of laser ablation process., (a) Initial absorption of laser radiation, melting and vaporization begin, (b) Melt front propagates into the solid, vaporization continues and laser plume interactions start to become important, (c) Absorption of incident laser radiation by the plume, and plasma formation, (d) Melt front recedes leading to eventual re-solidification [150].

The PLD process can be divided into the following steps:

- Laser radiation interaction with the target materials
- Dynamic of the ablation materials
- Decomposition of the ablation materials onto the substrate
- Nucleation and growth of a thin film on the substrate surface

Each step is dependent on experimental parameters such as laser wavelength, laser fluence and pulse width, background gas type and pressure, substrate type and temperature and deposition geometry.

The PLD technique was first demonstrated several years after the invention of the ruby laser. At first, Smith and Turner (1965), used a ruby laser to deposit thin films, which marked the very

beginning of the development of pulsed laser deposition technique [151]. Dijkkamp *et al*. (1987) demonstrated the deposition of a high temperature super conductivity material $YBa_2Cu_3O_7$ [152], from that PLD became an attractive thin film deposition technique. Since the work of Dijkkamp *et al*, PLD technique has been employed to fabricate crystalline thin films, ceramic oxides, nitride films, metallic multilayers and various super lattices [148,153–158].

Recently, a lot of attention was given to synthesize carbon-based materials, such as amorphous carbon [159], amorphous carbon nitride [134,160,161] and graphene [162,163]. The thin films grown by PLD have shown promising applications in the field of biosensors. Especially, the films grown by PLD have attracted much attention as electrode materials in electrochemical biosensors for the detection of heavy metals, pollutants and bio pathogens [164–167]. The advantages of using PLD technique is that the many experimental parameters can be changed, which has a strong influence on films properties; laser fluence, wavelength, pulse duration, repetition rate, target to substrate distance, substrate temperature and background pressure are the parameters that influence the film growth process [168]. The PLD deposited films have less contamination than the sputtered deposited films. In complex multicomponent material deposition with conventional evaporation methods, the various species come from different sources to produce a right mixture in the deposited film, the rate of arrival of each species must be monitored and controlled, which becomes difficult when large background pressures are used during deposition. The PLD deposited multicomponent films does not require such monitoring because the composition of the film replicates the composition of the target. Also, in most of the ion beam based techniques the pressure of the background gas in the chamber puts limitations on the operating parameters. For example, in the electron beam evaporation technique, the background gas pressure cannot exceeds 10^{-4} mbar. In addition, different molecules require different background pressures for forming the required phase. With PLD, the background gas pressure does not affect the passage or absorption of the laser beam and the same system can be used to fabricate thin films composed of many materials, by simply changing the background gas pressure. The thin films deposited by PLD have a higher purity than by the other processes.

The carbon nitride films grown by PLD technique can be classified two categories: conventional PLD and plasma assisted PLD (reactive PLD) techniques. The reactive PLD uses an additional energetic source to bombard the film surface during the deposition of the film.

b. Plasma assisted pulsed laser deposition

Pulsed laser deposition (PLD) is a well-established technique for the synthesize of carbon based materials and amorphous materials, such as, Diamond Like Carbon (DLC) [169–172] and more recently graphene [163,173–177]. The pulsed laser deposition technique has been used in two ways to attempt the fabrication of carbon nitride materials: ablation of graphite target using nanosecond lasers such as excimer, and Nd:YAG and CO_2 lasers [160,178–190] in nitrogen or ammonia atmosphere, both with and without ion bombardment of the substrate. In the ablation case, without using any additional nitrogen bombardment or a secondary discharge to generate nitrogen ions, it is difficult to get high levels of nitrogen. The deposition of carbon nitride material has been proven to be particularly challenging because of the difficulty of incorporating nitrogen in the growing amorphous carbon matrix. To achieve high N content and different film properties, an extensive research can be found on the effect of the different process parameters, such as laser fluence [186,188,191,192], nitrogen partial pressure [135,136,193] and substrate temperature [194–198], but in many cases, the nitrogen content is reported between 30 to 40 at.% [91,122,123,160,178–190,199–205].

Muhl *et al.*, [206] reviewed all the deposition methods of carbon nitride films and pointed out that to overcome this limitation, atomic or ionic sources should be used to bombard the film surfaces during the deposition process to achieve higher N content in carbon nitride films.

Several groups chose ion or plasma assisted PLD in attempt to increase the nitrogen incorporation in amorphous carbon thin film material. The Table 1.1 presents an overview of the different PLD deposition of carbon nitride films. A more formal article by Niu *et al.* [134] described Nd:YAG laser ablation of graphite with intense low energy atomic nitrogen beam incident on the substrate. The N/C ratio was directly proportional to the atomic nitrogen flux, the maximum value, 0.82, was independent of substrate temperature up to 600^{o}C and the deposition was thermally stable up to 800^{o}C. The C and N atoms were combined with non-polar covalent bond. Subsequently, some other researchers also successfully obtained the carbon nitride films with variable N content and variable chemical bonding by using different kind of plasma sources, such as RF [122,123,134,189,200,207], DC [195,208–210], surface wave discharge [135,190,196,211], kaufman type ion source [212], RF radical beam source [197,213,214], ion beam bombardment [180,215] and

ECR plasma [216–218] with PLD process. The bombardment of atomic or ionic nitrogen on the film surface affects not only the film composition and structure, but also the properties of CN films.

Until now, most of the work dealt with a radio frequency plasma and ion beam energy assisted PLD to deposit the carbon nitride films. Song *et al*. [219] found that the concentration of oxygen atoms in $YBa_2Cu_3O_{7-x}$ superconducting films deposited by pulsed laser deposition could be enhanced significantly by a DC discharge. Recently, Y. H. Cheng *et al*. [195,208–210], reported the successful deposition of CN films by Direct Current (DC) bias assisted PLD technique, which generated a lot of interest for growing amorphous carbon nitride films by DC bias assistance pulsed laser deposition with high N content and different chemical and structural properties. The DC glow discharge is also an effective way to enhance the ionization of the gas molecules. Compared with RF and ion beam source, the direct current glow discharge is simpler and easier to operate. The DC bias assistance PLD technique also has a variety of deposition parameters, that affest the CN films properties: DC bias voltages, the variation of nitrogen partial pressure, the substrate temperature, and laser parameters [195,208–210]. However, most of the work deals with nanosecond DC bias assistance pulsed laser ablation.

The ultrashort-pulsed laser deposition technique have been showing a promising way to deposit a wide variety of thin films. It has especially risen a great interest in depositing carbon-based materials by femtosecond pulsed laser deposition technique [220–223].

Laser source	Plasma source	Highest N %	Bonding information
Nd:YAG [134]	Flux of atomic nitrogen	45 %	Diffraction pattern, Un-polarized covalent bonds
Excimer [122,123]	RF	>30 %	Obtained mixture of sp^2 and sp^3
CO_2 [224]	Nitrogen after glow	43 %	Showed higher CN sp^3 than the CN sp^2
Excimer [225,226]	RF	47 %	Increase of N-sp^2
Excimer [135,190,196,211]	Post discharge	19 %	Increase of sp^2C bonded to N
Excimer [195,208–210]	DC	38 %	Increase of sp^2 C bonded to N

Table 1. 1 Literature review presentation of different PLD deposited CN films presenting the highest N content.

c. Ultrafast pulsed laser deposition

Laser technologies began to move into the sub picosecond time regime in the early seventies [227–229]. In the following years sub picosecond and femtosecond laser pulses were primarily applied for the study of a broad variety of ultrafast processes in different scientific fields, such as plasma physics and fusion research, atomic molecular and optical physics, femtosecond chemistry, astrophysics, high energy physics, materials science, biology and medicine [230,231].

The femtosecond lasers have opened a wide range of exciting new possibilities in the microfabrication of metals [232], polymers [233,234], semiconductors [235], ultra-hard materials, and transparent materials and tissues [236,237]. They can be used in automotive, pharmaceutical, defense, aerospace, and medicine industries, as well as for process and automation, information, telecommunication, measurement and microscopy, environmental, bio technology, micromachining and sensors [238,239].

The approximate time scales in nanosecond and femtosecond energy absorption and laser ablation process are given in the Figure 1.7. The most important advantage of femtosecond laser is that the pulse duration is shorter than the characteristic relaxation times, such as the electron to ion energy transfer time, electron heat conduction time and hydrodynamic or expansion time. They all occur in very short time scales, on the order of several picoseconds after the laser absorption. These offers a reduced thermal damage and heat affected zone in the target due to the negligible heat conduction and hydrodynamic motion during the laser pulse duration [240].

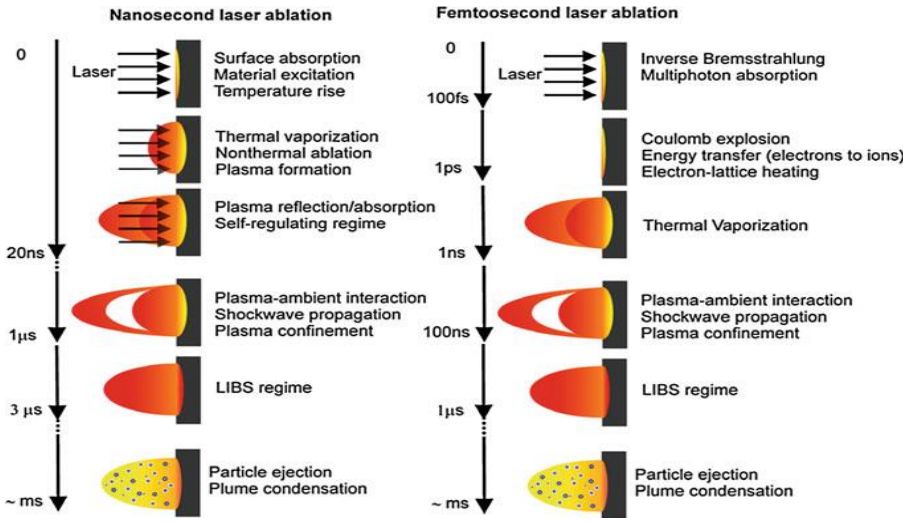

Figure 1. 7 The energy absorption and laser ablation process in nanosecond and femtosecond at approximate time scales along with various process [240].

The ultrashort pulses have given a lot of interest and applications in precise machining, laser induced spectroscopy or biological characterization [241]. The synthesis and/or the transfer of a large class of materials like diamond like carbon (DLC) [220,242,243], oxides [244], nitrides [161,245,246], carbides [247] and metals [248] are demonstrated by fs-PLD. Recent studies have shown the ability to deposit amorphous carbon [220,242,243,249] and doped amorphous carbon materials [133,161,245,246,250] by femtosecond pulsed laser ablation. The structure of the films depends on the type of PLD techniques used. Recently, Sikora *et al*.[249] reported that pure a-C films deposited by femtosecond pulsed laser deposition showed high sp^2 content around 60-70% and the a-C films deposited by nanosecond PLD showed a Csp^2 content in the 15-25% range. The nitrogen doped amorphous carbon films deposited by fs-PLD [251] is an interesting field of study. The ablation with ultrashort pulses offers different process conditions in contrast to ns-PLD. The nitrogen-doped a-C films grown by fs-PLD have advantages to grow more sp^2 graphitic like structures, which will increase the conductivity of films; hence, it performs good electrode materials in electrochemical applications.

Femtosecond (fs)-PLD is an emerging thin film deposition technique, offering a new set of opportunities for materials deposition. The energy transfer from the electron to the lattice is the result of electron phonon interactions. The lattice melts in a few picoseconds after the laser irradiation, leading to material ablation. These processes occur in a short time scales (~ps), the heat loaded to the surrounding material is minimized. Hence the craters formed by fs laser ablation are cleaner and their edges are well defined, and ultrafast lasers are capable to increase the target ablation compared to ns pulse lasers [240,252]. These advantages have motivated the use of femtosecond lasers for a wide range of applications in high precision materials for micro-machining [253]. For PLD, this high intensity laser regime can be a promising alternative to the more conventional well-established nanosecond regime. The reduced thermal conduction to the bulk may lead to a reduction on the production of molten droplets as it is commonly observed with nanosecond laser deposited films. One of the drawbacks of using nanosecond PLD is that there is a comparatively larger heat affected zone, which can rise the generation of molten droplets. A few reports on short pulse duration laser deposition have shown that a reduction in particulates was possible [244,254–256]. Although, many theoretical and experimental studies suggest that in some conditions, ultra-short pulsed laser ablation can lead to mechanical fragmentation [257] or cluster emission [258] and generation of sub-micron size particulates

[254,259,260]. The extreme conditions of temperature and pressure in the area irradiated by ultrashort pulses can lead to different properties of the ablated species with consequences for the deposited films. Only a few number of research has been carried on the deposition of amorphous carbon nitride films by using femtosecond pulsed laser deposition (conventional PLD), without using any energetic ion source.

Z. Geretorsky, *et al.,* [245,246], have deposited a-C:N films onto Si substrate by using hybrid dye/excimer laser with a pulse duration 500 fs, pulse energy 10 mJ and wavelength 248 nm. The N content achieved less than 10 %.

McCann *et al.*[251] have deposited a-C:N films onto Si substrate by using a Ti: Sapphire femtosecond laser with a pulse duration of 60 fs. The effects of both the nitrogen partial pressure and the laser fluence were examined on the carbon nitride materials. The N content achieved by this conventional femtosecond PLD reached 17 at.%, which is high compared to the nanosecond PLD under N_2 atmospheric pressure. XPS analysis of films revealed that as the nitrogen content increases, the CN sites increases at the expense of CC bonded carbon sites. The N content achieved with classic fs-PLD is very low. There is a possibility to increase the nitrogen percentage in films with reactive fs-PLD. Due to the limitations in N content by classical fs-PLD, a lot of interest was risen to try to deposit a-C:N films with plasma assistance fs-PLD technique.

As we stated in the section 3.2, a possible way to incorporate high N content in films is the use of energetic ion sources, either by RF, ion beam and DC assistance. In particularly, direct current bias assistance fs-PLD has not yet been reported. Our interest is to develop good a-C:N electrodes by conventional fs-PLD and DC bias assistance fs-PLD in electrochemical applications.

1.4 Objective of the thesis

The objective of this thesis is to open a new laser technology path allowing the carbon based coating of microelectrodes in electrochemical sensors. The DLC coatings were already used for the detection of heavy metals or pollutants in water [164]. Doped carbon materials have been giving a great interest for a wide variety of applications [261,262], especially doped amorphous carbon films which show better electrode performances in heavy metals detection [164,165]. The nitrogen doping is an effective way to tailor the properties of carbon-based materials and tune

the materials for various applications of interest. Recently, nitrogen doped amorphous carbon materials have risen interest in environmental and energy applications [263–265]. Our interest is to grow nitrogen doped amorphous carbon and graphene by femtosecond pulsed laser deposition for electrochemical applications. The aimed sensor materials should have the properties of high chemical inertness, wide potential window and low background current, and their process is to be easier, cheaper, and low temperature deposition. The emergency is to deposit high N-content sp^2 graphitic like structured amorphous carbon nitride films by fs-PLD and to get a good electrode in electrochemical sensors. Thus, we can detect heavy metals and pollutants and the functionalization electrode surface by biomolecules will increase the sensitivity of electrode for a future use in biosensor applications.

In the first step, the synthesis and comparison of pure amorphous carbon and nitrogen doped amorphous carbon films will be deposited by conventional femtosecond pulsed laser deposition and reactive fs-PLD, and we will develop the DC bias assistance fs-PLD. An optimization of the nitrogen incorporation is envisaged by combining classic pulsed laser deposition technique with nitrogen plasma assistance (reactive PLD).

In the second step, we will study the films properties such as surface morphology, chemical and microstructural properties by a wide variety of characterization techniques. Scanning Electron Microscopy (SEM) and Atomic Force Microscopy (AFM) will be used to study surface morphology, X-ray photoelectron spectroscopy (XPS) and Electron Energy Loss Spectroscopy (EELS) will be used to study chemical properties, Multi-wavelength Raman spectroscopy will be used to study microstructural properties of films. From these techniques, we will be able to select good a-C:N films for electrochemical measurements. The electrochemical properties will be studied by using Cyclic Voltammetry (CV) technique. Based on CV performance we will choose the best electrode for the detection of heavy metals and surface functionalization. The detection of heavy metals will be performed by Differential Pulse Anodic Stripping Voltammetry (DPASV) technique.

The electrochemical properties of a-C:N films will be studied regarding the applications in the electrochemical detection of heavy metals or pollutants in water, and functionalization of

surface by organic molecules for detection of chemical and/or biological molecules in future.

We will study the ablation plumes produced from the graphite targets by ultrashort laser ablation in vacuum, nitrogen atmosphere and DC bias nitrogen plasma. The plumes properties will be analyzed via ultrafast optical emission spectroscopy technique and spectrally resolved ultrafast 2D imaging, in order to address a better understanding of C-N bonding formation and high N content incorporation into the films produced by DC bias assisted femtosecond PLD.

For the future prospective, the last section is dedicated to the most popular carbon based material: N doped graphene. We will propose a new synthesis method to produce the N doped graphene. The approach we proposed in this PhD is an opening up new synthesis method to N doped graphene with great prospectives.

1.5 Conclusions

This chapter introduced different types of sensors and presented their working principles and possible potential applications, especially in heavy metal detection. We discussed also the importance of carbon-based materials as electrochemical sensors. In the second part, we introduced the large family of carbon nitride materials. We gave an overview of different deposition techniques for the successful deposition of amorphous carbon nitride thin films. In the last part, we emphasized on the deposition technique of a-C:N films used in this thesis. We presented the pulsed laser deposition technique, its principles and its potential advantages in thin film deposition. We discussed the ultrashort laser and its advantages of using it with PLD for thin film deposition. We presented the pulsed laser deposition of amorphous carbon (a-C) and amorphous carbon nitride (a-C:N) thin films by ultra-short lasers and we explained the possible potential use of femtosecond plasma assistance pulsed laser deposition.

References

(1) Gumpu, M. B.; Sethuraman, S.; Krishnan, U. M.; Rayappan, J. B. B. A Review on Detection of Heavy Metal Ions in Water – An Electrochemical Approach. *Sens. Actuators B Chem.* **2015**, *213*, 515–533.

(2) Eggins, B. R. *Chemical Sensors and Biosensors*; John Wiley & Sons, 2008.

(3) Ronkainen, N. J.; Halsall, H. B.; Heineman, W. R. Electrochemical Biosensors. *Chem. Soc. Rev.* **2010**, *39*, 1747–1763.

(4) Grieshaber, D.; MacKenzie, R.; Vörös, J.; Reimhult, E. Electrochemical Biosensors - Sensor Principles and Architectures. *Sensors* **2008**, *8*, 1400–1458.

(5) Hanrahan, G.; Patil, D. G.; Wang, J. Electrochemical Sensors for Environmental Monitoring: Design, Development and Applications. *J. Environ. Monit.* **2004**, *6*, 657–664.

(6) Yogeswaran, U.; Chen, S.-M. A Review on the Electrochemical Sensors and Biosensors Composed of Nanowires as Sensing Material. *Sensors* **2008**, *8*, 290–313.

(7) Wang, J. *Analytical Electrochemistry*; John Wiley & Sons, 2006.

(8) Wilson, G. S.; Gifford, R. Biosensors for Real-Time in Vivo Measurements. *Biosens. Bioelectron.* **2005**, *20*, 2388–2403.

(9) Chen, S.-M.; Chzo, W.-Y. Simultaneous Voltammetric Detection of Dopamine and Ascorbic Acid Using Didodecyldimethylammonium Bromide (DDAB) Film-Modified Electrodes. *J. Electroanal. Chem.* **2006**, *587*, 226–234.

(10) Tercier, M.-L.; Buffle, J. Antifouling Membrane-Covered Voltammetric Microsensor for in Situ Measurements in Natural Waters. *Anal. Chem.* **1996**, *68*, 3670–3678.

(11) Vasantha, V. S.; Chen, S.-M. Electrocatalysis and Simultaneous Detection of Dopamine and Ascorbic Acid Using poly(3,4-Ethylenedioxy)thiophene Film Modified Electrodes. *J. Electroanal. Chem.* **2006**, *592*, 77–87.

(12) Simoyi, M. F.; Falkenstein, E.; Van Dyke, K.; Blemings, K. P.; Klandorf, H. Allantoin, the Oxidation Product of Uric Acid Is Present in Chicken and Turkey Plasma. *Comp. Biochem. Physiol. B Biochem. Mol. Biol.* **2003**, *135*, 325–335.

(13) Balasubramanian, K.; Burghard, M. Biosensors Based on Carbon Nanotubes. *Anal. Bioanal. Chem.* **2006**, *385*, 452–468.

(14) Zhang, S.; Wang, N.; Niu, Y.; Sun, C. Immobilization of Glucose Oxidase on Gold Nanoparticles Modified Au Electrode for the Construction of Biosensor. *Sens. Actuators B Chem.* **2005**, *109*, 367–374.

(15) Wang, J. Carbon-Nanotube Based Electrochemical Biosensors: A Review. *Electroanalysis* **2005**, *17*, 7–14.

(16) Clark, L. C.; Lyons, C. Electrode Systems for Continuous Monitoring in Cardiovascular Surgery. *Ann. N. Y. Acad. Sci.* **1962**, *102*, 29–45.

(17) Chaubey, A.; Malhotra, B. D. Mediated Biosensors. *Biosens. Bioelectron.* **2002**, *17*, 441–456.

(18) Wang, J. *Analytical Electrochemistry*; John Wiley & Sons, 2006.

(19) Taillefert, M.; Luther, G. W.; Nuzzio, D. B. The Application of Electrochemical Tools for In Situ Measurements in Aquatic Systems. *Electroanalysis* **2000**, *12*, 401–412.

(20) Bakker, E.; Telting-Diaz, M. Electrochemical Sensors. *Anal. Chem.* **2002**, *74*, 2781–2800.

(21) G. E. Batley. Electroanalytical Techniques for the Determination of Heavy Metals in Seawater. *Mar. Chem.* **1983**, *12*, 107–117.
(22) Tercier, M.-L.; Buffle, J. In Situ Voltammetric Measurements in Natural Waters: Future Prospects and Challenges. *Electroanalysis* **1993**, *5*, 187–200.
(23) Tercier-Waeber, M.-L.; Confalonieri, F.; Riccardi, G.; Sina, A.; Graziottin, F.; Buffle, J. Multi Physical-Chemical Profiler for Real-Time Automated in Situ Monitoring of Specific Fractions of Trace Metals and Master Variables. *J. Phys. IV - Proc.* **2003**, *107*, 4.
(24) Wang, J.; Larson, D.; Foster, N.; Armalis, S.; Lu, J.; Rongrong, X.; Olsen, K.; Zirino, A. Remote Electrochemical Sensor for Trace Metal Contaminants. *Anal. Chem.* **1995**, *67*, 1481–1485.
(25) Wang, J. In Situ Electrochemical Monitoring: From Remote Sensors to Submersible Microlaboratories. *Lab. Robot. Autom.* **2000**, *12*, 178–182.
(26) Wang, J.; Chen, Q. Remote Electrochemical Biosensor for Field Monitoring of Phenolic Compounds. *Anal. Chim. Acta* **1995**, *312*, 39–44.
(27) Budnikov, G. K.; Evtyugin, G. A.; Rizaeva, E. P.; Ivanov, A. N.; Latypova, V. Z. Comparative assessment of electrochemical biosensors for determining inhibitors-environmental pollutants. *J Anal Chem* **1999**, *54*, 864–871.
(28) Walsh, F. C. Electrochemical Technology for Environmental Treatment and Clean Energy Conversion. *Pure Appl. Chem.* **2009**, *73*, 1819–1837.
(29) Janssen, L. J. J.; Koene, L. The Role of Electrochemistry and Electrochemical Technology in Environmental Protection. *Chem. Eng. J.* **2002**, *85*, 137–146.
(30) Héninger, I.; Potin-Gautier, M.; Gregori, I. de; Pinochet, H. Storage of Aqueous Solutions of Selenium for Speciation at Trace Level. *Fresenius J. Anal. Chem.* **1997**, *357*, 600–610.
(31) Aminot, A.; Kérouel, R. Assessment of Heat Treatment for Nutrient Preservation in Seawater Samples. *Anal. Chim. Acta* **1997**, *351*, 299–309.
(32) Gardolinski, P. C. F. C.; Hanrahan, G.; Achterberg, E. P.; Gledhill, M.; Tappin, A. D.; House, W. A.; Worsfold, P. J. Comparison of Sample Storage Protocols for the Determination of Nutrients in Natural Waters. *Water Res.* **2001**, *35*, 3670–3678.
(33) Polya, D. A.; Lythgoe, P. R.; Abou-Shakra, F.; Gault, A. G.; Brydie, J. R.; Webster, J. G.; Brown, K. L.; Nimfopoulos, M. K.; Michailidis, K. M. IC-ICP-MS and IC-ICP-HEX-MS Determination of Arsenic Speciation in Surface and Groundwaters: Preservation and Analytical Issues. *Mineral. Mag.* **2003**, *67*, 247–261.
(34) Brett, C. M. A. Electrochemical Sensors for Environmental Monitoring. Strategy and Examples. *Pure Appl. Chem.* **2001**, *73*.
(35) Allen J. Bard. *Electroanalytical Chemistry: A Series of Advances:*; CRC Press, 1990.
(36) Braĭnina, K. Z.; Braĭnina, K. Z.; Neyman, E. *Electroanalytical Stripping Methods*; John Wiley & Sons, 1993.
(37) Zoski, C. G. *Handbook of Electrochemistry*; Elsevier, 2007.
(38) Economou, A.; Fielden, P. R. Mercury Film Electrodes: Developments, Trends and Potentialities for Electroanalysis. *Analyst* **2003**, *128*, 205–213.
(39) Florence, T. M. Anodic Stripping Voltammetry with a Glassy Carbon Electrode Mercury-Plated in Situ. *J. Electroanal. Chem. Interfacial Electrochem.* **1970**, *27*, 273–281.
(40) Kumar Jena, B.; Retna Raj, C. Gold Nanoelectrode Ensembles for the Simultaneous Electrochemical Detection of Ultratrace Arsenic, Mercury, and Copper. *Anal. Chem.* **2008**, *80*, 4836–4844.

(41) Wang, J.; Tian, B. Mercury-Free Disposable Lead Sensors Based on Potentiometric Stripping Analysis of Gold-Coated Screen-Printed Electrodes. *Anal. Chem.* **1993**, *65*, 1529–1532.
(42) Nolan, M. A.; Kounaves, S. P. Microfabricated Array of Iridium Microdisks as a Substrate for Direct Determination of Cu2+ or Hg2+ Using Square-Wave Anodic Stripping Voltammetry. *Anal. Chem.* **1999**, *71*, 3567–3573.
(43) Noh, M. F. M.; Tothill, I. E. Development and Characterisation of Disposable Gold Electrodes, and Their Use for lead(II) Analysis. *Anal. Bioanal. Chem.* **2006**, *386*, 2095–2106.
(44) Economou, A. Bismuth-Film Electrodes: Recent Developments and Potentialities for Electroanalysis. *TrAC Trends Anal. Chem.* **2005**, *24*, 334–340.
(45) Arrigan, D. W. M. Tutorial Review. Voltammetric Determination of Trace Metals and Organics after Accumulation at Modified Electrodes. *Analyst* **1994**, *119*, 1953–1966.
(46) Pleskov, Y. V.; Krotova, M. D.; Elkin, V. V.; Ekimov, E. A. Electrochemical Behaviour of Boron-Doped Diamond Compacts – a New Electrode Material. *Electrochimica Acta*.
(47) Sbartai, A.; Namour, P.; Errachid, A.; Krejči, J.; Šejnohová, R.; Renaud, L.; Larbi Hamlaoui, M.; Loir, A.-S.; Garrelie, F.; Donnet, C.; *et al.* Electrochemical Boron-Doped Diamond Film Microcells Micromachined with Femtosecond Laser: Application to the Determination of Water Framework Directive Metals. *Anal. Chem.* **2012**, *84*, 4805–4811.
(48) McCreery, R. L. Advanced Carbon Electrode Materials for Molecular Electrochemistry. *Chem. Rev.* **2008**, *108*, 2646–2687.
(49) McGaw, E. A.; Swain, G. M. A Comparison of Boron-Doped Diamond Thin-Film and Hg-Coated Glassy Carbon Electrodes for Anodic Stripping Voltammetric Determination of Heavy Metal Ions in Aqueous Media. *Anal. Chim. Acta* **2006**, *575*, 180–189.
(50) Wang, J.; Lu, J.; Hocevar, S. B.; Farias, P. A. M.; Ogorevc, B. Bismuth-Coated Carbon Electrodes for Anodic Stripping Voltammetry. *Anal. Chem.* **2000**, *72*, 3218–3222.
(51) Xu, J.; Granger, M. C.; Chen, Q.; Strojek, J. W.; Lister, T. E.; Swain, G. M. Peer Reviewed: Boron-Doped Diamond Thin-Film Electrodes. *Anal. Chem.* **1997**, *69*, 591A – 597A.
(52) Aisenberg, S.; Chabot, R. Ion-Beam Deposition of Thin Films of Diamondlike Carbon. *J. Appl. Phys.* **1971**, *42*, 2953–2958.
(53) Zeng, A.; Neto, V. F.; Gracio, J. J.; Fan, Q. H. Diamond-like Carbon (DLC) Films as Electrochemical Electrodes. *Diam. Relat. Mater.* **2014**, *43*, 12–22.
(54) Robertson, J. Diamond-like Amorphous Carbon. *Mater. Sci. Eng. R Rep.* **2002**, *37*, 129–281.
(55) Qureshi, A.; Kang, W. P.; Davidson, J. L.; Gurbuz, Y. Review on Carbon-Derived, Solid-State, Micro and Nano Sensors for Electrochemical Sensing Applications. *Diam. Relat. Mater.* **2009**, *18*, 1401–1420.
(56) Thorwarth, G.; Falub, C. V.; Müller, U.; Weisse, B.; Voisard, C.; Tobler, M.; Hauert, R. Tribological Behavior of DLC-Coated Articulating Joint Implants. *Acta Biomater.* **2010**, *6*, 2335–2341.
(57) Swain, G. M.; Ramesham, R. The Electrochemical Activity of Boron-Doped Polycrystalline Diamond Thin Film Electrodes. *Anal. Chem.* **1993**, *65*, 345–351.
(58) Miller, B.; Kalish, R.; Feldman, L. C.; Katz, A.; Moriya, N.; Short, K.; White, A. E. Patterned Electrical Conductance and Electrode Formation in Ion-Implanted Diamond Films. *J. Electrochem. Soc.* **1994**, *141*, L41–L43.

(59) Strojek, J. W.; Granger, M. C.; Swain, G. M.; Dallas, T.; Holtz, M. W. Enhanced Signal-to-Background Ratios in Voltammetric Measurements Made at Diamond Thin-Film Electrochemical Interfaces. *Anal. Chem.* **1996**, *68*, 2031–2037.
(60) Xu, J.; Granger, M. C.; Chen, Q.; Strojek, J. W.; Lister, T. E.; Swain, G. M. Peer Reviewed: Boron-Doped Diamond Thin-Film Electrodes. *Anal. Chem.* **1997**, *69*, 591A – 597A.
(61) Brett, C. M. A.; Angnes, L.; Liess, H.-D. Carbon Film Resistors as Electrodes: Voltammetric Properties and Application in Electroanalysis. *Electroanalysis* **2001**, *13*, 765–769.
(62) Grill, A. Diamond-like Carbon: State of the Art. *Diam. Relat. Mater.* **1999**, *8*, 428–434.
(63) Hauert, R. A Review of Modified DLC Coatings for Biological Applications. *Diam. Relat. Mater.* **2003**, *12*, 583–589.
(64) Maalouf, R.; Chebib, H.; Saikali, Y.; Vittori, O.; Sigaud, M.; Garrelie, F.; Donnet, C.; Jaffrezic-Renault, N. Characterization of Different Diamond-like Carbon Electrodes for Biosensor Design. *Talanta* **2007**, *72*, 310–314.
(65) Garrelie, F.; Loir, A. S.; Donnet, C.; Rogemond, F.; Le Harzic, R.; Belin, M.; Audouard, E.; Laporte, P. Femtosecond Pulsed Laser Deposition of Diamond-like Carbon Thin Films for Tribological Applications. *Surf. Coat. Technol.* **2003**, *163–164*, 306–312.
(66) Donnet, C.; Grill, A. Friction Control of Diamond-like Carbon Coatings. *Surf. Coat. Technol.* **1997**, *94–95*, 456–462.
(67) Sikora, A.; Garrelie, F.; Donnet, C.; Loir, A. S.; Fontaine, J.; Sanchez-Lopez, J. C.; Rojas, T. C. Structure of Diamondlike Carbon Films Deposited by Femtosecond and Nanosecond Pulsed Laser Ablation. *J. Appl. Phys.* **2010**, *108*, 113516.
(68) Zeng, A.; Neto, V. F.; Gracio, J. J.; Fan, Q. H. Diamond-like Carbon (DLC) Films as Electrochemical Electrodes. *Diam. Relat. Mater.* **2014**, *43*, 12–22.
(69) Loir, A. S.; Garrelie, F.; Donnet, C.; Rogemond, F.; Subtil, J. L.; Forest, B.; Belin, M.; Laporte, P. Towards the Deposition of Tetrahedral Diamond-like Carbon Films on Hip Joints by Femtosecond Pulsed Laser Ablation. *Surf. Coat. Technol.* **2004**, *188–189*, 728–734.
(70) Moon, J.-M.; Park, S.; Lee, Y.-K.; Sook Bang, G.; Hong, Y.-K.; Park, C.; Cheol Jeon, I. Diamond-like Carbon Electrodes in Electrochemical Microgravimetry. *J. Electroanal. Chem.* **1999**, *464*, 230–237.
(71) Lee, J. G.; Lee, S. P. Humidity Sensing Properties of CNx Film by RF Magnetron Sputtering System. *Sens. Actuators B Chem.* **2005**, *108*, 450–454.
(72) Lee, J. G.; Lee, S. P. Impedance Characteristics of Carbon Nitride Films for Humidity Sensors. *Sens. Actuators B Chem.* **2006**, *117*, 437–441.
(73) Noh, G.-H.; Bordeanu, A.; Lee, J.; Pyun, J.-C. Development of a Diamond-like Carbon (DLC) Electrode for Brake Fluid Monitoring. *Curr. Appl. Phys.* **2009**, *9*, e243–e245.
(74) Khun, N. W.; Liu, E. Effect of Substrate Temperature on Corrosion Performance of Nitrogen Doped Amorphous Carbon Thin Films in NaCl Solution. *Thin Solid Films* **2009**, *517*, 4762–4766.
(75) Khun, N. W.; Liu, E. Linear Sweep Anodic Stripping Voltammetry of Heavy Metals from Nitrogen Doped Tetrahedral Amorphous Carbon Thin Films. *Electrochimica Acta* **2009**, *54*, 2890–2898.
(76) Liu, L. X.; Liu, E. Nitrogenated Diamond-like Carbon Films for Metal Tracing. *Surf. Coat. Technol.* **2005**, *198*, 189–193.

(77) Tamiasso-Martinhon, P.; Cachet, H.; Deslouis, C.; Vivier, V. Amorphous Carbon Nitride a-CNx Microelectrode: Fabrication and Characterization. *Electrochem. Commun.* **2010**, *12*, 1074–1076.
(78) Menegazzo, N.; Kahn, M.; Berghauser, R.; Waldhauser, W.; Mizaikoff, B. Nitrogen-Doped Diamond-like Carbon as Optically Transparent Electrode for Infrared Attenuated Total Reflection Spectroelectrochemistry. *The Analyst* **2011**, *136*, 1831–1839.
(79) Zeng, A.; Liu, E.; Tan, S. N.; Zhang, S.; Gao, J. Cyclic Voltammetry Studies of Sputtered Nitrogen Doped Diamond-Like Carbon Film Electrodes. *Electroanalysis* **2002**, *14*, 1110–1115.
(80) Zeng, A.; Liu, E.; Tan, S. N.; Zhang, S.; Gao, J. Stripping Voltammetric Analysis of Heavy Metals at Nitrogen Doped Diamond-Like Carbon Film Electrodes. *Electroanalysis* **2002**, *14*, 1294–1298.
(81) Yang, X.; Haubold, L.; DeVivo, G.; Swain, G. M. Electroanalytical Performance of Nitrogen-Containing Tetrahedral Amorphous Carbon Thin-Film Electrodes. *Anal. Chem.* **2012**, *84*, 6240–6248.
(82) Tanaka, Y.; Furuta, M.; Kuriyama, K.; Kuwabara, R.; Katsuki, Y.; Kondo, T.; Fujishima, A.; Honda, K. Electrochemical Properties of N-Doped Hydrogenated Amorphous Carbon Films Fabricated by Plasma-Enhanced Chemical Vapor Deposition Methods. *Electrochimica Acta* **2011**, *56*, 1172–1181.
(83) Zeng, A.; Bilek, M. M. M.; McKenzie, D. R.; Lay, P. A.; La Fontaine, A.; Keast, V. J. Correlation between Film Structures and Potential Limits for Hydrogen and Oxygen Evolutions at a-C:N Film Electrochemical Electrodes. *Carbon* **2008**, *46*, 663–670.
(84) Cachet, H.; Deslouis, C.; Chouiki, M.; Saidani, B.; Conway, N. M. J.; Godet, C. Electrochemistry of Nitrogen-Incorporated Hydrogenated Amorphous Carbon Films. *J. Electrochem. Soc.* **2002**, *149*, E233–E241.
(85) Lagrini, A.; Deslouis, C.; Cachet, H.; Benlahsen, M.; Charvet, S. Elaboration and Electrochemical Characterization of Nitrogenated Amorphous Carbon Films. *Electrochem. Commun.* **2004**, *6*, 245–248.
(86) Cachet, H.; Debiemme-Chouvy, C.; Deslouis, C.; Lagrini, A.; Vivier, V. Correlation between Electrochemical Reactivity and Surface Chemistry of Amorphous Carbon Nitride Films. *Surf. Interface Anal.* **2006**, *38*, 719–722.
(87) Yoo, K.; Miller, B.; Kalish, R.; Shi, X. Electrodes of Nitrogen-Incorporated Tetrahedral Amorphous Carbon A Novel Thin-Film Electrocatalytic Material with Diamond-like Stability. *Electrochem. Solid-State Lett.* **1999**, *2*, 233–235.
(88) Maddi, C.; Donnet, C.; Loir, A.-S.; Tite, T.; Barnier, V.; Rojas, T. C.; Sanchez-Lopez, J. C.; Wolski, K.; Garrelie, F. High N-Content a-C:N Films Elaborated by Femtosecond PLD with Plasma Assistance. *Appl. Surf. Sci.* **2015**, *332*, 346–353.
(89) Ghamouss, F.; Tessier, P.-Y.; Djouadi, A.; Besland, M.-P.; Boujtita, M. Screen-Printed Carbon Electrode Modified on Its Surface with Amorphous Carbon Nitride Thin Film: Electrochemical and Morphological Study. *Electrochimica Acta* **2007**, *52*, 5053–5061.
(90) Tessier, P. Y.; Pichon, L.; Villechaise, P.; Linez, P.; Angleraud, B.; Mubumbila, N.; Fouquet, V.; Straboni, A.; Milhet, X.; Hildebrand, H. F. Carbon Nitride Thin Films as Protective Coatings for Biomaterials: Synthesis, Mechanical and Biocompatibility Characterizations. *Diam. Relat. Mater.* **2003**, *12*, 1066–1069.
(91) Liu, A. Y.; Cohen, M. L. Prediction of New Low Compressibility Solids. *Science* **1989**, *245*, 841–842.

(92) Matsumoto, S.; Xie, E.-Q.; Izumi, F. On the Validity of the Formation of Crystalline Carbon Nitrides, C3N4. *Diam. Relat. Mater.* **1999**, *8*, 1175–1182.
(93) Uddin, M. N.; Yang, Y. S. Formation of Nano-Crystalline C3N4 Thin Films on Stainless Steel from Hexamethylenetetramine and Urea Using Simple Sol–gel Method. *Thin Solid Films* **2013**, *548*, 27–33.
(94) Neuhaeuser, M.; Hilgers, H.; Joeris, P.; White, R.; Windeln, J. Raman Spectroscopy Measurements of DC-Magnetron Sputtered Carbon Nitride (a-C:N) Thin Films for Magnetic Hard Disk Coatings. *Diam. Relat. Mater.* **2000**, *9*, 1500–1505.
(95) Lagrini, A.; Charvet, S.; Benlahsen, M.; Cachet, H.; Deslouis, C. On the Relation between Microstructure and Electrochemical Reactivity of Sputtered Amorphous Carbon Nitride Electrodes. *Diam. Relat. Mater.* **2007**, *16*, 1378–1382.
(96) Marton, M.; Kovalčík, D.; Vojs, M.; Zdravecká, E.; Varga, M.; Michalíková, L.; Veselý, M.; Redhammer, R.; Písečný, P. Electrochemical Corrosion Behavior of Amorphous Carbon Nitride Thin Films. *Vacuum* **2012**, *86*, 696–698.
(97) Marton, M.; Zdravecká, E.; Vojs, M.; Ižák, T.; Veselý, M.; Redhammer, R.; Varga, M.; Šatka, A. Study of Adhesion of Carbon Nitride Thin Films on Medical Alloy Substrates. *Vacuum* **2009**, *84*, 65–67.
(98) Marton, D.; Boyd, K. J.; Rabalais, J. W. Synthesis of Carbon Nitride. *Int. J. Mod. Phys. B* **1995**, *09*, 3527–3558.
(99) Ferrari, A. C.; Rodil, S. E.; Robertson, J. Interpretation of Infrared and Raman Spectra of Amorphous Carbon Nitrides. *Phys. Rev. B* **2003**, *67*, 155306.
(100) Rodil, S. E.; Muhl, S. Bonding in Amorphous Carbon Nitride. *Diam. Relat. Mater.* **2004**, *13*, 1521–1531.
(101) Carduner, K. R.; Rokosz, M. J.; Tamor, M. A.; Vassell, W. C. Solid State NMR Study of Carbon Bonding in Amorphous Hydrogenated Carbon Films. *Appl. Magn. Reson.* **1991**, *2*, 647–653.
(102) Lukins, P. B.; MKenzie, D. R.; Vassallo, A. M.; Hanna, J. V. 13C NMR and FTIR Study of Thermal Annealing of Amorphous Hydrogenated Carbon. *Carbon* **1993**, *31*, 569–575.
(103) Braddock-Wilking, J.; Lin, S.-H.; Feldman, B. J. 13C NMR Spectroscopy of Amorphous Hydrogenated Carbon — Further Evidence of Inhomogeneity. *Solid State Commun.* **2001**, *119*, 19–21.
(104) Sánchez-López, J. C.; Donnet, C.; Lefèbvre, F.; Fernández-Ramos, C.; Fernández, A. Bonding Structure in Amorphous Carbon Nitride: A Spectroscopic and Nuclear Magnetic Resonance Study. *J. Appl. Phys.* **2001**, *90*, 675–681.
(105) Maniwa, Y.; Sato, M.; Kume, K.; Kozlov, M. E.; Tokumoto, M. Comparative NMR Study of New Carbon Forms. *Carbon* **1996**, *34*, 1287–1291.
(106) Pan, H.; Pruski, M.; Gerstein, B. C.; Li, F.; Lannin, J. S. Local Coordination of Carbon Atoms in Amorphous Carbon. *Phys. Rev. B* **1991**, *44*, 6741–6745.
(107) Xu, J.; Watanabe, S.; Hayashi, H.; Kawaguchi, M.; Kato, T. Structural Characterization of Ion-Vapor Deposited Hydrogenated Amorphous Carbon Coatings by Solid State 13C Nuclear Magnetic Resonance. *J. Appl. Phys.* **2014**, *115*, 014303.
(108) Waidmann, S.; Knupfer, M.; Fink, J.; Kleinsorge, B.; Robertson, J. Electronic Structure Studies of Undoped and Nitrogen-Doped Tetrahedral Amorphous Carbon Using High-Resolution Electron Energy-Loss Spectroscopy. *J. Appl. Phys.* **2001**, *89*, 3783–3792.

(109) Hu, J.; Yang, P.; Lieber, C. M. Nitrogen-Driven ${\mathrm{sp}}^{3}$ to ${\mathrm{sp}}^{2}$ Transformation in Carbon Nitride Materials. *Phys. Rev. B* **1998**, *57*, R3185–R3188.
(110) Silva, S. R. P.; Robertson, J.; Amaratunga, G. a. J.; Rafferty, B.; Brown, L. M.; Schwan, J.; Franceschini, D. F.; Mariotto, G. Nitrogen Modification of Hydrogenated Amorphous Carbon Films. *J. Appl. Phys.* **1997**, *81*, 2626–2634.
(111) Rodil, S. E.; Ferrari, A. C.; Robertson, J.; Muhl, S. Infrared Spectra of Carbon Nitride Films. *Thin Solid Films* **2002**, *420–421*, 122–131.
(112) Jiménez, I.; Tong, W. M.; Shuh, D. K.; Holloway, B. C.; Kelly, M. A.; Pianetta, P.; Terminello, L. J.; Himpsel, F. J. Bonding Modifications in Carbon Nitride Films Induced by Thermal Annealing: An X-Ray Absorption near Edge Study. *Appl. Phys. Lett.* **1999**, *74*, 2620–2622.
(113) Ray, S. C.; Pao, C. W.; Chiou, J. W.; Tsai, H. M.; Jan, J. C.; Pong, W. F.; McCann, R.; Roy, S. S.; Papakonstantinou, P.; McLaughlin, J. A. Electronic Properties of a-CNx Thin Films: An X-Ray-Absorption and Photoemission Spectroscopy Study. *J. Appl. Phys.* **2005**, *98*, 033708.
(114) Ech-chamikh, E.; Essafti, A.; Ijdiyaou, Y.; Azizan, M. XPS Study of Amorphous Carbon Nitride (a-C:N) Thin Films Deposited by Reactive RF Sputtering. *Sol. Energy Mater. Sol. Cells* **2006**, *90*, 1420–1423.
(115) Jansen, R. J. J.; van Bekkum, H. XPS of Nitrogen-Containing Functional Groups on Activated Carbon. *Carbon* **1995**, *33*, 1021–1027.
(116) Zheng, W. T.; Xing, K. Z.; Hellgren, N.; Lögdlund, M.; Johansson, Å.; Gelivs, U.; Salaneck, W. R.; Sundgren, J.-E. Nitrogen 1s Electron Binding Energy Assignment in Carbon Nitride Thin Films with Different Structures. *J. Electron Spectrosc. Relat. Phenom.* **1997**, *87*, 45–49.
(117) Gammon, W. J.; Kraft, O.; Reilly, A. C.; Holloway, B. C. Experimental Comparison of N(1s) X-Ray Photoelectron Spectroscopy Binding Energies of Hard and Elastic Amorphous Carbon Nitride Films with Reference Organic Compounds. *Carbon* **2003**, *41*, 1917–1923.
(118) Pels, J. R.; Kapteijn, F.; Moulijn, J. A.; Zhu, Q.; Thomas, K. M. Evolution of Nitrogen Functionalities in Carbonaceous Materials during Pyrolysis. *Carbon* **1995**, *33*, 1641–1653.
(119) Titantah, J. T.; Lamoen, D. Carbon and Nitrogen 1s Energy Levels in Amorphous Carbon Nitride Systems: XPS Interpretation Using First-Principles. *Diam. Relat. Mater.* **2007**, *16*, 581–588.
(120) Chowdhury, A. K. M. S.; Cameron, D. C.; Hashmi, M. S. J. Bonding Structure in Carbon Nitride Films: Variation with Nitrogen Content and Annealing Temperature. *Surf. Coat. Technol.* **1999**, *112*, 133–139.
(121) Ronning, C.; Feldermann, H.; Merk, R.; Hofsäss, H.; Reinke, P.; Thiele, J.-U. Carbon Nitride Deposited Using Energetic Species: A Review on XPS Studies. *Phys. Rev. B* **1998**, *58*, 2207–2215.
(122) Cappelli, E.; Orlando, S.; Trucchi, D. M.; Bellucci, A.; Valentini, V.; Mezzi, A.; Kaciulis, S. Carbon Nitride Films by RF Plasma Assisted PLD: Spectroscopic and Electronic Analysis. *Appl. Surf. Sci.* **2011**, *257*, 5175–5180.
(123) Cappelli, E.; Trucchi, D. M.; Kaciulis, S.; Orlando, S.; Zanza, A.; Mezzi, A. Effect of Deposition Temperature on Chemical Composition and Electronic Properties of

Amorphous Carbon Nitride (a-CNx) Thin Films Grown by Plasma Assisted Pulsed Laser Deposition. *Thin Solid Films* **2011**, *519*, 4059–4063.
(124) Wang, P.; Takeno, T.; Fontaine, J.; Aono, M.; Adachi, K.; Miki, H.; Takagi, T. Effects of Substrate Bias Voltage and Target Sputtering Power on the Structural and Tribological Properties of Carbon Nitride Coatings. *Mater. Chem. Phys.* **2014**, *145*, 434–440.
(125) Wang, P.; Takeno, T.; Adachi, K.; Miki, H.; Takagi, T. Preparation and Tribological Characterization of Amorphous Carbon Nitride Coatings in a RF PECVD–DC PVD Hybrid Coating Process. *Appl. Surf. Sci.* **2012**, *258*, 6576–6582.
(126) Y. H. Cheng; B. K. Tay; S. P. Lau; X. Shi; X. L. Qiao; J. G. Chen; Y. P. Wu; C. S. Xie. Raman Spectroscopy of Carbon Nitride Films Deposited Using the Filtered Cathodic Vacuum-Arc Technique Combined with a Radio-Frequency Nitrogen-Ion Beam. *Appl. Phys. A* **2001**, *73*, 341–345.
(127) Lagrini, A.; Charvet, S.; Benlahsen, M.; Debiemme-Chouvy, C.; Deslouis, C.; Cachet, H. Microstructure and Electronic Investigations of Carbon Nitride Films Deposited by RF Magnetron Sputtering. *Thin Solid Films* **2005**, *482*, 41–44.
(128) Liu, X. W.; Tseng, C. H.; Lin, J. H.; Chao, L. T.; Shih, H. C. Optical Properties of Amorphous Carbon Nitride Synthesized on Si by ECR-CVD. *Surf. Coat. Technol.* **2001**, *135*, 184–187.
(129) Liu, X. W.; Lin, J. H.; Tseng, C. H.; Shih, H. C. Optical and Structural Properties of the Amorphous Carbon Nitride by ECR-Plasma. *Mater. Chem. Phys.* **2001**, *72*, 258–263.
(130) Sung, S. L.; Tseng, C. H.; Chiang, F. K.; Guo, X. J.; Liu, X. W.; Shih, H. C. A Novel Approach to the Formation of Amorphous Carbon Nitride Film on Silicon by ECR-CVD. *Thin Solid Films* **1999**, *340*, 169–174.
(131) Kundoo, S.; Chattopadhyay, K. K.; Banerjee, A. N.; Nandy, S. K. Synthesis and Optical Characterization of Amorphous Carbon Nitride Thin Films by Hot Filament Assisted RF Plasma CVD. *Vacuum* **2003**, *69*, 495–500.
(132) Hayashi, Y.; Yu, G.; Rahman, M. M.; Krishna, K. M.; Soga, T.; Jimbo, T.; Umeno, M. Spectroscopic Properties of Nitrogen Doped Hydrogenated Amorphous Carbon Films Grown by Radio Frequency Plasma-Enhanced Chemical Vapor Deposition. *J. Appl. Phys.* **2001**, *89*, 7924–7931.
(133) Szörényi, T.; Fogarassy, E.; Fuchs, C.; Hommet, J.; Normand, F. L. Chemical Analysis of a-CNx Thin Films Synthesized by Nanosecond and Femtosecond Pulsed Laser Deposition. *Appl. Phys. A* **1999**, *69*, S941–S944.
(134) Niu, C.; Lu, Y. Z.; Lieber, C. M. Experimental Realization of the Covalent Solid Carbon Nitride. *Science* **1993**, *261*, 334–337.
(135) Tabbal, M.; Mérel, P.; Chaker, M. Effect of Process Parameters on the Mechanical Properties of Carbon Nitride Thin Films Synthesized by Plasma Assisted Pulsed Laser Deposition. *Appl. Phys. A* **2004**, *79*, 1365–1367.
(136) Voevodin, A. A.; Jones, J. G.; Zabinski, J. S.; Czigány, Z.; Hultman, L. Growth and Structure of Fullerene-like CNx Thin Films Produced by Pulsed Laser Ablation of Graphite in Nitrogen. *J. Appl. Phys.* **2002**, *92*, 4980–4988.
(137) Logothetidis, S.; Lefakis, H.; Gioti, M. Carbon Nitride Thin Films Prepared by Reactive R.f. Magnetron Sputtering. *Carbon* **1998**, *36*, 757–760.
(138) Fernández, A.; Sánchez-López, J. C.; Lassaletta, G. Characterisation of Carbon Nitride Thin Films Prepared by Reactive Magnetron Sputtering. *Carbon* **1998**, *36*, 761–764.

(139) Mubumbila, N.; Tessier, P.-Y.; Angleraud, B.; Turban, G. Effect of Nitrogen Incorporation in CNx Thin Films Deposited by RF Magnetron Sputtering. *Surf. Coat. Technol.* **2002**, *151-152*, 175–179.
(140) Broitman, E.; Hellgren, N.; Järrendahl, K.; Johansson, M. P.; Olafsson, S.; Radnóczi, G.; Sundgren, J.-E.; Hultman, L. Electrical and Optical Properties of CNx($0 \leqslant x \leqslant 0.25$) Films Deposited by Reactive Magnetron Sputtering. *J. Appl. Phys.* **2001**, *89*, 1184–1190.
(141) Derradji, N. E.; Mahdjoubi, M. L.; Belkhir, H.; Mumumbila, N.; Angleraud, B.; Tessier, P. Y. Nitrogen Effect on the Electrical Properties of CNx Thin Films Deposited by Reactive Magnetron Sputtering. *Thin Solid Films* **2005**, *482*, 258–263.
(142) Zheng, W. T.; Broitman, E.; Hellgren, N.; Xing, K. Z.; Ivanov, I.; Sjöström, H.; Hultman, L.; Sundgren, J.-E. Reactive Magnetron Sputtering of CNx Thin Films at Different Substrate Bias. *Thin Solid Films* **1997**, *308–309*, 223–227.
(143) Song, H. W.; Cui, F. Z.; He, X. M.; Li, W. Z.; Li, H. D. Carbon Nitride Films Synthesized by NH 3 -Ion-Beam-Assisted Deposition. *J. Phys. Condens. Matter* **1994**, *6*, 6125.
(144) Tucker, M. D.; Czigány, Z.; Broitman, E.; Näslund, L.-Å.; Hultman, L.; Rosen, J. Filtered Pulsed Cathodic Arc Deposition of Fullerene-like Carbon and Carbon Nitride Films. *J. Appl. Phys.* **2014**, *115*, 144312.
(145) Sharma, A. K.; Ayyub, P.; Multani, M. S.; Adhi, K. P.; Ogale, S. B.; Sunderaraman, M.; Upadhyay, D. D.; Banerjee, S. Synthesis of Crystalline Carbon Nitride Thin Films by Laser Processing at a Liquid–solid Interface. *Appl. Phys. Lett.* **1996**, *69*, 3489–3491.
(146) Zhang, Z. J.; Fan, S.; Huang, J.; Lieber, C. M. Diamondlike Properties in a Single Phase Carbon Nitride Solid. *Appl. Phys. Lett.* **1996**, *68*, 2639–2641.
(147) Mihailescu, I. N.; Gyorgy, E.; Alexandrescu, R.; Luches, A.; Perrone, A.; Ghica, C.; Werckmann, J.; Cojocaru, I.; Chumash, V. Optical Studies of Carbon Nitride Thin Films Deposited by Reactive Pulsed Laser Ablation of a Graphite Target in Low Pressure Ammonia. *Thin Solid Films* **1998**, *323*, 72–78.
(148) Chrisey, D. B.; Hubler, G. K. *Pulsed Laser Deposition of Thin Films*; Wiley, 1994.
(149) Willmott, P. R.; Huber, J. R. Pulsed Laser Vaporization and Deposition. *Rev. Mod. Phys.* **2000**, *72*, 315–328.
(150) Ashfold, M. N. R.; Claeyssens, F.; Fuge, G. M.; Henley, S. J. Pulsed Laser Ablation and Deposition of Thin Films. *Chem. Soc. Rev.* **2004**, *33*, 23–31.
(151) Smith, H. M.; Turner, A. F. Vacuum Deposited Thin Films Using a Ruby Laser. *Appl. Opt.* **1965**, *4*, 147.
(152) Dijkkamp, D.; Venkatesan, T.; Wu, X. D.; Shaheen, S. A.; Jisrawi, N.; Min-Lee, Y. H.; McLean, W. L.; Croft, M. Preparation of Y-Ba-Cu Oxide Superconductor Thin Films Using Pulsed Laser Evaporation from High Tc Bulk Material. *Appl. Phys. Lett.* **1987**, *51*, 619–621.
(153) Fogarassy, E.; Fuchs, C.; Slaoui, A.; Stoquert, J. P. SiO2 Thin-film Deposition by Excimer Laser Ablation from SiO Target in Oxygen Atmosphere. *Appl. Phys. Lett.* **1990**, *57*, 664–666.
(154) Balooch, M.; Tench, R. J.; Siekhaus, W. J.; Allen, M. J.; Connor, A. L.; Olander, D. R. Deposition of SiC Films by Pulsed Excimer Laser Ablation. *Appl. Phys. Lett.* **1990**, *57*, 1540–1542.

(155) Krebs, H. U.; Störmer, M.; Fähler, S.; Bremert, O.; Hamp, M.; Pundt, A.; Teichler, H.; Blum, W.; Metzger, T. H. Structural Properties of Laser Deposited Metallic Alloys and Multilayers. *Appl. Surf. Sci.* **1997**, *109–110*, 563–569.
(156) Krebs, H.-U.; Bremert, O.; Luo, Y.; Fähler, S.; Störmer, M. Structure of Laser-Deposited Metallic Alloys and Multilayers. *Thin Solid Films* **1996**, *275*, 18–21.
(157) Biunno, N.; Narayan, J.; Hofmeister, S. K.; Srivatsa, A. R.; Singh, R. K. Low-temperature Processing of Titanium Nitride Films by Laser Physical Vapor Deposition. *Appl. Phys. Lett.* **1989**, *54*, 1519–1521.
(158) Hansen, S. G.; Robitaille, T. E. Formation of Polymer Films by Pulsed Laser Evaporation. *Appl. Phys. Lett.* **1988**, *52*, 81–83.
(159) Siegal, M. P.; Martinez-Miranda, L. J.; DiNardo, N. J.; Tallant, D. R.; Barbour, J. C.; Newcomer Provencio, P. Characterization of Amorphous Carbon Films Grown by Pulsed Laser Deposition. In *Proc. SPIE 3343. High-power Laser Ablation, 885*; 1998; Vol. 3343, pp. 885–894.
(160) J. Bulíř; M. Jelínek; V. Vorlíček; J. Zemek; V. Peřina. Study of Nitrogen Pressure Effect on the Laser-Deposited Amorphous Carbon Films. *Thin Solid Films* **1997**, *292*, 318–323.
(161) Zhang, Z.; VanRompay, P. A.; Nees, J. A.; Clarke, R.; Pan, X.; Pronko, P. P. Nitride Film Deposition by Femtosecond and Nanosecond Laser Ablation in Low-Pressure Nitrogen Discharge Gas. *Appl. Surf. Sci.* **2000**, *154–155*, 165–171.
(162) Wang, K. Laser Based Fabrication of Graphene. In *Advances in Graphene Science*; Aliofkhazraei, M., Ed.; InTech, 2013.
(163) Wang, K.; Tai, G.; Wong, K. H.; Lau, S. P.; Guo, W. Ni Induced Few-Layer Graphene Growth at Low Temperature by Pulsed Laser Deposition. *AIP Adv.* **2011**, *1*, 022141.
(164) Khadro, B.; Sikora, A.; Loir, A.-S.; Errachid, A.; Garrelie, F.; Donnet, C.; Jaffrezic-Renault, N. Electrochemical Performances of B Doped and Undoped Diamond-like Carbon (DLC) Films Deposited by Femtosecond Pulsed Laser Ablation for Heavy Metal Detection Using Square Wave Anodic Stripping Voltammetric (SWASV) Technique. *Sens. Actuators B Chem.* **2011**, *155*, 120–125.
(165) Sbartai, A.; Namour, P.; Errachid, A.; Krejči, J.; Šejnohová, R.; Renaud, L.; Hamlaoui, M. L.; Loir, A.-S.; Garrelie, F.; Donnet, C.; *et al.* Electrochemical Boron-Doped Diamond Film Microcells Micromachined with Femtosecond Laser: Application to the Determination of Water Framework Directive Metals. *Anal. Chem.* **2012**, *84*, 4805–4811.
(166) Maalouf, R.; Chebib, H.; Saikali, Y.; Vittori, O.; Sigaud, M.; Garrelie, F.; Donnet, C.; Jaffrezic-Renault, N. Characterization of Different Diamond-like Carbon Electrodes for Biosensor Design. *Talanta* **2007**, *72*, 310–314.
(167) Fortgang, P.; Tite, T.; Barnier, V.; Zehani, N.; Maddi, C.; Lagarde, F.; Loir, A.-S.; Jaffrezic-Renault, N.; Donnet, C.; Garrelie, F.; *et al.* Robust Electrografting on Self-Organized 3D Graphene Electrodes. *ACS Appl. Mater. Interfaces* **2016**, *8*, 1424–1433.
(168) Eason, R. *Pulsed Laser Deposition of Thin Films: Applications-Led Growth of Functional Materials*; John Wiley & Sons, 2007.
(169) Voevodin, A. A.; Donley, M. S. Preparation of Amorphous Diamond-like Carbon by Pulsed Laser Deposition: A Critical Review. *Surf. Coat. Technol.* **1996**, *82*, 199–213.
(170) Cho, H.; Kim, S.; Ki, H. Pulsed Laser Deposition of Functionally Gradient Diamond-like Carbon (DLC) Films Using a 355 Nm Picosecond Laser. *Acta Mater.* **2012**, *60*, 6237–6246.

(171) Voevodin, A. A.; Phelps, A. W.; Zabinski, J. S.; Donley, M. S. Friction Induced Phase Transformation of Pulsed Laser Deposited Diamond-like Carbon. *Diam. Relat. Mater.* **1996**, *5*, 1264–1269.
(172) Thema, F. T.; Beukes, P.; Ngom, B. D.; Manikandan, E.; Maaza, M. Free Standing Diamond-like Carbon Thin Films by PLD for Laser Based Electrons/protons Acceleration. *J. Alloys Compd.* **2015**, *648*, 326–331.
(173) Dhar, S.; Barman, A. R.; Ni, G. X.; Wang, X.; Xu, X. F.; Zheng, Y.; Tripathy, S.; Ariando; Rusydi, A.; Loh, K. P.; *et al.* A New Route to Graphene Layers by Selective Laser Ablation. *AIP Adv.* **2011**, *1*, 022109.
(174) Tite, T.; Donnet, C.; Loir, A.-S.; Reynaud, S.; Michalon, J.-Y.; Vocanson, F.; Garrelie, F. Graphene-Based Textured Surface by Pulsed Laser Deposition as a Robust Platform for Surface Enhanced Raman Scattering Applications. *Appl. Phys. Lett.* **2014**, *104*, 041912.
(175) Wang, K. Laser Based Fabrication of Graphene. In *Advances in Graphene Science*; Aliofkhazraei, M., Ed.; InTech, 2013.
(176) Hemani, G. K.; Vandenberghe, W. G.; Brennan, B.; Chabal, Y. J.; Walker, A. V.; Wallace, R. M.; Quevedo-Lopez, M.; Fischetti, M. V. Interfacial Graphene Growth in the Ni/SiO2 System Using Pulsed Laser Deposition. *Appl. Phys. Lett.* **2013**, *103*, 134102.
(177) Koh, A. T. T.; Foong, Y. M.; Chua, D. H. C. Cooling Rate and Energy Dependence of Pulsed Laser Fabricated Graphene on Nickel at Reduced Temperature. *Appl. Phys. Lett.* **2010**, *97*, 114102.
(178) González, P.; Soto, R.; Parada, E. G.; Redondas, X.; Chiussi, S.; Serra, J.; Pou, J.; León, B.; Pérez-Amor, M. Carbon Nitride Films Prepared by Excimer Laser Ablation. *Appl. Surf. Sci.* **1997**, *109–110*, 380–383.
(179) Zhao, X.-A.; Ong, C. W.; Tsang, Y. C.; Wong, Y. W.; Chan, P. W.; Choy, C. L. Reactive Pulsed Laser Deposition of CNx Films. *Appl. Phys. Lett.* **1995**, *66*, 2652–2654.
(180) Zhong-Min Ren; Yong-Feng Lu; Zhi-Feng He. Carbon Nitride Materials Synthesized by Ion-Assisted Pulsed Laser Deposition. *Focus. 2nd Int. Symp. Laser Precis. Microfabr. LPM2001*.
(181) Narayan, J.; Reddy, J.; Biunno, N.; Kanetkar, S. M.; Tiwari, P.; Parikh, N. Ion-Assisted Laser Processing of CNx Films. *Mater. Sci. Eng. B* **1994**, *26*, 49–53.
(182) Polo, M. C.; Aguiar, R.; Serra, P.; Clèries, L.; Varela, M.; Esteve, J. Carbon Nitride Thin Films Obtained by Laser Ablation of Graphite in a Nitrogen Plasma. *Appl. Surf. Sci.* **1996**, *96–98*, 870–873.
(183) Zhang, Z. J.; Huang, J.; Fan, S.; Lieber, C. M. Phases and Physical Properties of Carbon Nitride Thin Films Prepared by Pulsed Laser Deposition. *Mater. Sci. Eng. A* **1996**, *209*, 5–9.
(184) Ren, Z.-M.; Wang, P.-N.; Du, Y.-C.; Ying, Z.-F.; Li, F.-M. Optical Studies on the Deposition of Carbon Nitride Films by Laser Ablation. *Appl. Phys. A* **1997**, *65*, 407–409.
(185) Saito, K.; Koga, Y. Characterization of Carbon Films Produced by Laser Ablation of Graphite in Helium and Nitrogen Gas Atmosphere. *Nucl. Instrum. Methods Phys. Res. Sect. B Beam Interact. Mater. At.* **1997**, *121*, 400–403.
(186) Acquaviva, S.; D'Anna, E.; De Giorgi, M. L.; Fernández, M.; Leggieri, G.; Luches, A.; Zocco, A.; Majni, G. Carbon Nitride Films Deposited by Very High-Fluence XeCl Excimer-Laser Reactive Ablation. *Appl. Surf. Sci.* **2000**, *154–155*, 369–375.

(187) E D'Anna; M. L De Giorgi; A Luches; M Martino; A Perrone; A Zocco. Study of C-N Binding States in Carbon Nitride Films Deposited by Reactive XeCl Laser Ablation. *Thin Solid Films* **1999**, *347*, 72–77.
(188) Le Normand, F.; Hommet, J.; Szörényi, T.; Fuchs, C.; Fogarassy, E. XPS Study of Pulsed Laser Deposited CNx Films. *Phys. Rev. B* **2001**, *64*, 235416.
(189) Itoh, M.; Suda, Y.; Bratescu, M. A.; Sakai, Y.; Suzuki, K. Amorphous Carbon Nitride Film Preparation by Plasma-Assisted Pulsed Laser Deposition Method. *Appl. Phys. A* **2004**, *79*, 1575–1578.
(190) Tabbal, M.; Christidis, T.; Isber, S.; El Khakani, M. A.; Mérel, P.; Chaker, M. Graphitic Nanoclustering in Pulsed Laser Deposited Diamond-like-Carbon and Carbon Nitride Thin Films. *Thin Solid Films* **2004**, *453–454*, 234–238.
(191) Zhao, J. P.; Chen, Z. Y.; Yano, T.; Ooie, T.; Yoneda, M.; Sakakibara, J. Structural and Bonding Properties of Carbon Nitride Films Synthesized by Low Energy Nitrogen-Ion-Beam-Assisted Pulsed Laser Deposition with Different Laser Fluences. *J. Appl. Phys.* **2001**, *89*, 1634–1640.
(192) De Giorgi, M. L.; Leggieri, G.; Luches, A.; Martino, M.; Perrone, A.; Zocco, A.; Barucca, G.; Majni, G.; Gyorgy, E.; Mihailescu, I. N.; *et al.* Carbon Nitride Films Deposited by Reactive Laser Ablation. *Appl. Surf. Sci.* **1998**, *127–129*, 481–485.
(193) Szörényi, T.; Antoni, F.; Fogarassy, E.; Bertóti, I. Dependence of Nitrogen Content and Deposition Rate on Nitrogen Pressure and Laser Parameters in ArF Excimer Laser Deposition of Carbon Nitride Films. *Appl. Surf. Sci.* **2000**, *168*, 248–250.
(194) Fuge, G. M.; Rennick, C. J.; Pearce, S. R. J.; May, P. W.; Ashfold, M. N. R. Structural Characterisation of CNx Thin Films Deposited by Pulsed Laser Ablation. *Diam. Relat. Mater.* **2003**, *12*, 1049–1054.
(195) Cheng, Y. H.; Qiao, X. L.; Chen, J. G.; Wu, Y. P.; Xie, C. S.; Wang, Y. Q.; Xu, D. S.; Mo, S. B.; Sun, Y. B. Dependence of the Composition and Bonding Structure of Carbon Nitride Films Deposited by Direct Current Plasma Assisted Pulsed Laser Ablation on the Deposition Temperature. *Diam. Relat. Mater.* **2002**, *11*, 1511–1517.
(196) Tabbal, M.; Mérel, P.; Moisa, S.; Chaker, M.; Ricard, A.; Moisan, M. X-ray Photoelectron Spectroscopy of Carbon Nitride Films Deposited by Graphite Laser Ablation in a Nitrogen Postdischarge. *Appl. Phys. Lett.* **1996**, *69*, 1698–1700.
(197) Aoi, Y.; Ono, K.; Sakurada, K.; Kamijo, E.; Sasaki, M.; Sakayama, K. Effects of Heat Treatment on Structure of Amorphous CNx Thin Films by Pulsed Laser Deposition. *Thin Solid Films* **2001**, *389*, 62–67.
(198) Fogarassy, E.; Szorényi, T.; Antoni, F.; Pirio, G.; Olivier, J.; Legagneux, P.; Boher, P. Field Emission Properties of a-CNx Films Prepared by Pulsed Laser Deposition. *Appl. Phys. A* **2003**, *76*, 15–19.
(199) Yap, Y. K.; Kida, S.; Aoyama, T.; Mori, Y.; Sasaki, T. Influence of Negative Dc Bias Voltage on Structural Transformation of Carbon Nitride at 600 °C. *Appl. Phys. Lett.* **1998**, *73*, 915–917.
(200) Yap, Y. K.; Mori, Y.; Kida, S.; Aoyama, T.; Sasaki, T. Carbon Nitride Thin Films Synthesized at High Temperature by Using RF-Plasma PLD. *J. Cryst. Growth* **1999**, *198–199, Part 2*, 1028–1031.
(201) Kokai, F.; Yamamoto, K.; Koga, Y.; Fujiwara, S.; Heimann, R. B. Characterization of Ablation Plumes and Carbon Nitride Films Produced by Reactive Pulsed Laser Deposition in the Presence of a Magnetic Field. *Appl. Phys. A* **1998**, *66*, 403–406.

(202) Suda, Y.; Nakazono, T.; Ebihara, K.; Baba, K.; Aoqui, S. Pulsed Laser Deposition of Carbon Nitride Thin Films from Graphite Targets. *Carbon* **1998**, *36*, 771–774.
(203) Franco, L. M.; Pérez, J. A.; Riascos, H. Chemical Analysis of Thin Films Produced by Pulsed Laser Ablation. *Microelectron. J.* **2008**, *39*, 1363–1365.
(204) Ong, C. W.; Zhao, X.-A.; Tsang, Y. C.; Choy, C. L.; Chan, P. W. Structural Studies of Reactive Pulsed Laser-Deposited CNx Films by X-Ray Photoelectron Spectroscopy and Infrared Absorption. *J. Mater. Sci.* **1997**, *32*, 2347–2352.
(205) Riascos, H.; Neidhardt, J.; Radnóczi, G. Z.; Emmerlich, J.; Zambrano, G.; Hultman, L.; Prieto, P. Structure and Properties of Pulsed-Laser Deposited Carbon Nitride Thin Films. *Thin Solid Films* **2006**, *497*, 1–6.
(206) Muhl, S.; Méndez, J. M. A Review of the Preparation of Carbon Nitride Films. *Diam. Relat. Mater.* **1999**, *8*, 1809–1830.
(207) Thärigen, T.; Lippold, G.; Riede, V.; Lorenz, M.; Koivusaari, K. J.; Lorenz, D.; Mosch, S.; Grau, P.; Hesse, R.; Streubel, P.; *et al.* Hard Amorphous CSixNy Thin Films Deposited by RF Nitrogen Plasma Assisted Pulsed Laser Ablation of Mixed graphite/Si3N4-Targets. *Thin Solid Films* **1999**, *348*, 103–113.
(208) Cheng, Y. H.; Qiao, X. L.; Chen, J. G.; Wu, Y. P.; Xie, C. S.; Wang, Y. Q.; Xu, D. S.; Mo, S. B.; Sun, Y. B. Effect of Laser Fluences on the Structure of Carbon Nitride Films Deposited by Direct Current Plasma Assisted Pulsed Laser Ablation. *Surf. Coat. Technol.* **2002**, *160*, 269–276.
(209) Cheng, Y. H.; Sun, Z. H.; Tay, B. K.; Lau, S. P.; Qiao, X. L.; Chen, J. G.; Wu, Y. P.; Xie, C. S.; Wang, Y. Q.; Xu, D. S.; *et al.* Influence of Deposition Pressure on the Composition and Structure of Carbon Nitride Films Deposited by Direct Current Plasma Assisted Pulsed Laser Ablation. *Appl. Surf. Sci.* **2001**, *182*, 32–39.
(210) Cheng, Y. H.; Qiao, X. L.; Chen, J. G.; Wu, Y. P.; Xie, C. S.; Muo, S. B.; Sun, Y. B.; Tay, B. K. Synthesis of Carbon Nitride Films by Direct Current Plasma Assisted Pulsed Laser Deposition. *Appl. Phys. A* **2002**, *74*, 225–231.
(211) Tabbal, M.; Mérel, P.; Moisa, S.; Chaker, M.; Gat, E.; Ricard, A.; Moisan, M.; Gujrathi, S. XPS and FTIR Analysis of Nitrogen Incorporation in CNx Thin Films. *Surf. Coat. Technol.* **1998**, *98*, 1092–1096.
(212) Feng, L. Y.; Min, R. Z.; Qiao, N. H.; Feng, H. Z.; Chan, D. S. H.; Seng, L. T.; Yin, C. S.; Gamani, K.; Geng, C.; Kun, L. Carbon Nitride Thin Films Deposited by Nitrogen-Ion-Assisted KRF Excimer Ablation of Graphite. *Appl. Surf. Sci.* **1999**, *138–139*, 494–498.
(213) Aoi, Y.; Ono, K.; Kamijo, E. Preparation of Amorphous CNx Thin Films by Pulsed Laser Deposition Using a Radio Frequency Radical Beam Source. *J. Appl. Phys.* **1999**, *86*, 2318–2322.
(214) Aoi, Y.; Sakurada, K.; Kamijo, E. Pulsed Laser Deposition of Amorphous Carbon Nitride Thin Films and Their Electrical Properties. *Appl. Phys. A* **2004**, *79*, 1533–1536.
(215) Ren, Z.-M.; Du, Y.-C.; Qiu, Y.; Wu, J.-D.; Ying, Z.-F.; Xiong, X.-X.; Li, F.-M. Carbon Nitride Films Synthesized by Combined Ion-Beam and Laser-Ablation Processing. *Phys. Rev. B* **1995**, *51*, 5274–5277.
(216) Ling, H.; Wu, J. D.; Sun, J.; Shi, W.; Ying, Z. F.; Xu, N.; Pan, W. J.; Ding, X. M.; Zhou, Z. Y. Influences of Substrate Bias on the Composition and Structure of Carbon Nitride Thin Films Prepared by ECR-Plasma Assisted Pulsed Laser Deposition. *Diam. Relat. Mater.* **2002**, *11*, 1584–1591.

(217) Dong, Z. B.; Lu, Y. F.; Gao, K.; Shi, L. Q.; Sun, J.; Xu, N.; Wu, J. D. Thermal Stability of Carbon Nitride Thin Films Prepared by Electron Cyclotron Resonance Plasma Assisted Pulsed Laser Deposition. *Thin Solid Films* **2008**, *516*, 8594–8598.
(218) Shen, X. K.; Sun, J.; Xu, N.; Ying, Z. F.; Shi, L. Q.; Wu, A. M.; Gong, Z. S.; Wu, J. D. Spectroscopic Study on Pulsed Laser Ablation of Graphite Target in ECR Nitrogen Plasma for Carbon Nitride Film Deposition. *Diam. Relat. Mater.* **2006**, *15*, 1350–1356.
(219) Song, H. W.; Cui, F. Z.; He, X. M.; Li, W. Z.; Li, H. D. Carbon Nitride Films Synthesized by NH 3 -Ion-Beam-Assisted Deposition. *J. Phys. Condens. Matter* **1994**, *6*, 6125.
(220) Qian, F.; Craciun, V.; Singh, R. K.; Dutta, S. D.; Pronko, P. P. High Intensity Femtosecond Laser Deposition of Diamond-like Carbon Thin Films. *J. Appl. Phys.* **1999**, *86*, 2281.
(221) Jegenyes, N.; Toth, Z.; Hopp, B.; Klebniczki, J.; Bor, Z.; Fotakis, C. Femtosecond Pulsed Laser Deposition of Diamond-like Carbon Films: The Effect of Double Laser Pulses. *Appl. Surf. Sci.* **2006**, *252*, 4667–4671.
(222) Garrelie, F.; Loir, A. S.; Donnet, C.; Rogemond, F.; Le Harzic, R.; Belin, M.; Audouard, E.; Laporte, P. Femtosecond Pulsed Laser Deposition of Diamond-like Carbon Thin Films for Tribological Applications. *Surf. Coat. Technol.* **2003**, *163–164*, 306–312.
(223) Benchikh, N.; Garrelie, F.; Wolski, K.; Donnet, C.; Fillit, R. Y.; Rogemond, F.; Subtil, J. L.; Rouzaud, J. N.; Laval, J. Y. Nanocomposite Tantalum–carbon-Based Films Deposited by Femtosecond Pulsed Laser Ablation. *Thin Solid Films* **2006**, *494*, 98–104.
(224) Jama, C.; Dessaux, O.; Goudmand, P.; Soro, J.-M.; Rats, D.; von Stebut, J. Structural and Micro-Mechanical Studies of CNx Films Deposited on Silicon Substrates in a Remote Nitrogen Plasma. *Surf. Coat. Technol.* **1999**, *116–119*, 59–64.
(225) Jelínek, M.; Zemek, J.; Trchová, M.; Vorlíček, V.; Lančok, J.; Tomov, R.; Šimečková, M. CNx Films Created by Combined Laser Deposition and R.f. Discharge: XPS, FTIR and Raman Analysis. *Thin Solid Films* **2000**, *366*, 69–76.
(226) Jelínek, M.; Kulisch, W.; Delplancke-Ogletree, M. P.; Lancok, J.; Jastrabík, L.; Chvostová, D.; Popov, C.; Bulír, J. Mechanical and Optical Properties of CNx Films with High N/C Ratio. *Appl. Phys. A* **2001**, *73*, 167–170.
(227) Penzkofer, A.; Linde, D. von der; Laubereau, A.; Kaiser, W. Generation of Single Picosecond and Subpicosecond Light Pulses. *Appl. Phys. Lett.* **1972**, *20*, 351–354.
(228) Penzkofer, A. Passive Q-Switching and Mode-Locking for the Generation of Nanosecond to Femtosecond Pulses. *Appl. Phys. B* **1988**, *46*, 43–60.
(229) Penzkofer, A.; Von Der Linde, D.; Laubereau, A. The Intensity of Short Light Pulses Determined with Saturable Absorbers. *Opt. Commun.* **1972**, *4*, 377–379.
(230) S. L. Shapiro. *Ultrashort Light Pulses: Picosecond Techniques and Applications*; Springer Science & Business Media, 2013.
(231) Kaiser, W. Ultrashort Laser Pulses and Applications. **1988**.
(232) Preuss, S.; Demchuk, A.; Stuke, M. Sub-Picosecond UV Laser Ablation of Metals. *Appl. Phys. A* **1995**, *61*, 33–37.
(233) Küper, S.; Stuke, M. UV-Excimer-Laser Ablation of Polymethylmethacrylate at 248 Nm: Characterization of Incubation Sites with Fourier Transform IR- and UV-Spectroscopy. *Appl. Phys. A* **1989**, *49*, 211–215.
(234) Baudach, S.; Bonse, J.; Kautek, W. Ablation Experiments on Polyimide with Femtosecond Laser Pulses. *Appl. Phys. A* **1999**, *69*, S395–S398.

(235) Simon, P.; Ihlemann, J. Machining of Submicron Structures on Metals and Semiconductors by Ultrashort UV-Laser Pulses. *Appl. Phys. A* **1996**, *63*, 505–508.
(236) Chen, K.; Nielsen, M.; Yang, G. R.; Rymaszewski, E. J.; Lu, T.-M. Study of Amorphous Ta2O5 Thin Films by DC Magnetron Reactive Sputtering. *J. Electron. Mater.* **1997**, *26*, 397–401.
(237) Loesel, F. H.; Fischer, J. P.; Götz, M. H.; Horvath, C.; Juhasz, T.; Noack, F.; Suhm, N.; Bille, J. F. Non-Thermal Ablation of Neural Tissue with Femtosecond Laser Pulses. *Appl. Phys. B* **1998**, *66*, 121–128.
(238) Y. F Lu; Y Zhang; Y. H Wan; W. D Song. Laser Cleaning of Silicon Surface with Deposition of Different Liquid Films. *Appl. Surf. Sci.* **1999**, *138–139*, 140–144.
(239) Bao, M.; Wang, W. Future of Microelectromechanical Systems (MEMS). *Sens. Actuators Phys.* **1996**, *56*, 135–141.
(240) Harilal, S. S.; Freeman, J. R.; Diwakar, P. K.; Hassanein, A. Femtosecond Laser Ablation: Fundamentals and Applications. In *Laser-Induced Breakdown Spectroscopy*; Musazzi, S.; Perini, U., Eds.; Springer Series in Optical Sciences; Springer Berlin Heidelberg, 2014; pp. 143–166.
(241) *Femtosecond Technology for Technical and Medical Applications*; Dausinger, F.; Lubatschowski, H.; Lichtner, F., Eds.; Topics in Applied Physics; Springer Berlin Heidelberg: Berlin, Heidelberg, 2004; Vol. 96.
(242) Garrelie, F.; Loir, A. S.; Donnet, C.; Rogemond, F.; Le Harzic, R.; Belin, M.; Audouard, E.; Laporte, P. Femtosecond Pulsed Laser Deposition of Diamond-like Carbon Thin Films for Tribological Applications. *Surf. Coat. Technol.* **2003**, *163–164*, 306–312.
(243) Banks, P. S.; Dinh, L.; Stuart, B. C.; Feit, M. D.; Komashko, A. M.; Rubenchik, A. M.; Perry, M. D.; McLean, W. Short-Pulse Laser Deposition of Diamond-like Carbon Thin Films. *Appl. Phys. A* **1999**, *69*, S347–S353.
(244) Dominguez, J. E.; Pan, X. Q.; Fu, L.; Rompay, P. A. V.; Zhang, Z.; Nees, J. A.; Pronko, P. P. Epitaxial SnO2 Thin Films Grown on (1̄012) Sapphire by Femtosecond Pulsed Laser Deposition. *J. Appl. Phys.* **2002**, *91*, 1060–1065.
(245) Geretovszky, Z.; Kántor, Z.; Bertóti, I.; Szörényi, T. Pulsed Laser Deposition of Carbon Nitride Films by a Sub-Ps Laser. *Appl. Phys. A* **2000**, *70*, 9–11.
(246) Geretovszky, Z.; Kántor, Z.; Szörényi, T. Structure and Composition of Carbon-Nitride Films Grown by Sub-Ps PLD. *Appl. Surf. Sci.* **2003**, *208–209*, 547–552.
(247) Ghica, C.; Ristoscu, C.; Socol, G.; Brodoceanu, D.; Nistor, L. C.; Mihailescu, I. N.; Klini, A.; Fotakis, C. Growth and Characterization of β-SiC Films Obtained by Fs Laser Ablation. *Appl. Surf. Sci.* **2006**, *252*, 4672–4677.
(248) Klini, A.; Loukakos, P. A.; Gray, D.; Manousaki, A.; Fotakis, C. Laser Induced Forward Transfer of Metals by Temporally Shaped Femtosecond Laser Pulses. *Opt. Express* **2008**, *16*, 11300.
(249) Sikora, A.; Garrelie, F.; Donnet, C.; Loir, A. S.; Fontaine, J.; Sanchez-Lopez, J. C.; Rojas, T. C. Structure of Diamondlike Carbon Films Deposited by Femtosecond and Nanosecond Pulsed Laser Ablation. *J. Appl. Phys.* **2010**, *108*, 113516.
(250) Rode, A. V.; Luther-Davies, B.; Gamaly, E. G. Ultrafast Ablation with High-Pulse-Rate Lasers. Part II: Experiments on Laser Deposition of Amorphous Carbon Films. *J. Appl. Phys.* **1999**, *85*, 4222–4230.

(251) McCann, R.; Roy, S. S.; Papakonstantinou, P.; McLaughlin, J. A.; Ray, S. C. Spectroscopic Analysis of a-C and a-CNx Films Prepared by Ultrafast High Repetition Rate Pulsed Laser Deposition. *J. Appl. Phys.* **2005**, *97*, 073522.
(252) Chichkov, B. N.; Momma, C.; Nolte, S.; Alvensleben, F. von; Tünnermann, A. Femtosecond, Picosecond and Nanosecond Laser Ablation of Solids. *Appl. Phys. A* **1996**, *63*, 109–115.
(253) Rizvi, N. H. Femtosecond Laser Micromachining: Current Status and Applications. *Riken Rev.* **2003**, 107–112.
(254) Guillermin, M.; Colombier, J. P.; Valette, S.; Audouard, E.; Garrelie, F.; Stoian, R. Optical Emission and Nanoparticle Generation in Al Plasmas Using Ultrashort Laser Pulses Temporally Optimized by Real-Time Spectroscopic Feedback. *Phys. Rev. B* **2010**, *82*, 035430.
(255) Rode, A. V.; Luther-Davies, B.; Gamaly, E. G. Ultrafast Ablation with High-Pulse-Rate Lasers. Part II: Experiments on Laser Deposition of Amorphous Carbon Films. *J. Appl. Phys.* **1999**, *85*, 4222–4230.
(256) Angleraud, B.; Garrelie, F.; Tétard, F.; Catherinot, A. Study of Particles Ejected after Pulsed Laser Ablation of a Graphite Target. *Appl. Surf. Sci.* **1999**, *138–139*, 507–511.
(257) Perez, D.; Lewis, L. J. Ablation of Solids under Femtosecond Laser Pulses. *Phys. Rev. Lett.* **2002**, *89*, 255504.
(258) Zhigilei, L. V. Dynamics of the Plume Formation and Parameters of the Ejected Clusters in Short-Pulse Laser Ablation. *Appl. Phys. A* **2003**, *76*, 339–350.
(259) Amoruso, S.; Bruzzese, R.; Spinelli, N.; Velotta, R.; Vitiello, M.; Wang, X.; Ausanio, G.; Iannotti, V.; Lanotte, L. Generation of Silicon Nanoparticles via Femtosecond Laser Ablation in Vacuum. *Appl. Phys. Lett.* **2004**, *84*, 4502–4504.
(260) Garrelie, F.; Benchikh, N.; Donnet, C.; Fillit, R.-Y.; Rouzaud, J.-N.; Laval, J.-Y.; Pailleret, A. One-Step Deposition of Diamond-like Carbon Films Containing Self-Assembled Metallic Nanoparticles, by Femtosecond Pulsed Laser Ablation. *Appl. Phys. - Mater. Sci. Process.* **2008**, *90*, 211–217.
(261) Wood, K. N.; O'Hayre, R.; Pylypenko, S. Recent Progress on Nitrogen/carbon Structures Designed for Use in Energy and Sustainability Applications. *Energy Environ. Sci.* **2014**, *7*, 1212–1249.
(262) Choi, C. H.; Park, S. H.; Woo, S. I. Binary and Ternary Doping of Nitrogen, Boron, and Phosphorus into Carbon for Enhancing Electrochemical Oxygen Reduction Activity. *ACS Nano* **2012**, *6*, 7084–7091.
(263) Kikuchi, Y.; Chang, X.; Sakakibara, Y.; Inoue, K. Y.; Matsue, T.; Nozawa, T.; Samukawa, S. Amorphous Carbon Nitride Thin Films for Electrochemical Electrode: Effect of Molecular Structure and Substrate Materials. *Carbon* **2015**, *93*, 207–216.
(264) Jribi, S.; Cordoba de Torresi, S. I.; Augusto, T.; Cachet, H.; Debiemme-Chouvy, C.; Deslouis, C.; Pailleret, A. Determination of Surface Amine Groups on Amorphous Carbon Nitride Thin Films Using a One Step Covalent Grafting of a Redox Probe. *Electrochimica Acta* **2014**, *136*, 473–482.
(265) Zeng, A.; Neto, V. F.; Gracio, J. J.; Fan, Q. H. Diamond-like Carbon (DLC) Films as Electrochemical Electrodes. *Diam. Relat. Mater.* **2014**, *43*, 12–22.

Chapter 2. Thin film deposition and characterization

2.1 Introduction

In this chapter, we first give the details of the femtosecond laser system, the deposition procedure of amorphous carbon (a-C) and amorphous carbon nitride (a-C:N) thin films by using femtosecond pulsed laser deposition techniques. We describe the two deposition techniques : conventional fs-PLD and plasma assisted fs-PLD, along with their deposition parameters. In the second part, we describe the ablation of graphite target under nitrogen pressure and the nitrogen plasma effect on the film structure by optical spectroscopy techniques. We used two techniques, the Optical Emission Spectroscopy (OES) technique and the spectrally resolved 2D imaging technique, to study the ablation plume characteristics in order to understand the thin film formation and the high N content deposition. In the third section, we describe the different characterization techniques, which are used to characterize the a-C and a-C:N thin films to study the morphological, physical, chemical and electrochemical properties. We used a wide range of techniques to characterize the films: Scanning Electron Microscope (SEM) and Atomic Force Microscope (AFM) for morphological, Multi-wavelength Raman spectroscopy for microstructure, X-ray photoelectron spectroscopy (XPS) and Electron Energy Loss Spectroscopy (EELS) for chemical composition and chemical bonding, and Cyclic Voltammetry (CV) and Differential Pulse Anodic Stripping Voltammetry (DPASV) for electrochemical properties. The characterization methods are used not only on questions to be answered, but also to study the nature of films and substrate.

2.2 Thin film deposition method

2.2.1 Deposition Chamber

The thin films depositions were carried out in MECA 2000 stainless steel chamber. The vacuum chamber is shown in the Figure 2.1.

The vacuum chamber is connected with two pumps. The first pump is for primary vacuum (10^{-3} mbar) achieved by the use of Varian Triscroll vacuum pump. Once the primary vacuum is reached, the second pump is used to achieve high vacuum 10^{-7} mbar. The chamber is provided with a quartz window of 5 mm thickness and positioned at 45^{o} relates to the target. The window allows the transmission of the laser beam incident on the outer face with an energy loss estimated on the both sides approximately at 10 %. The chamber has two manipulators, which are positioned at 90° to each other. The first manipulator is for substrate and has substrate holder, with a four-degrees of freedom (3 directions in space and a 360° rotation), which allows to change the substrate at specific position. The second one is the target holder, it has two degrees of freedom, one allows to vary the target to substrate distance, and the other allows to rotate the motor to 360° and the motor allows us to work with different targets. The target holder has eight rotatory targets that can change the choice of different target position during the deposition. The distance between the target and the substrate can varied by rotating the substrate and target holders. The nitrogen pressure (of purity 99.9995%) is allowed by a micro valve, which is controlled by Alicat Scientific mass flow controller. The flow rate of N_2 pressure is constant at 20 SCCM of flow for all the experiments.

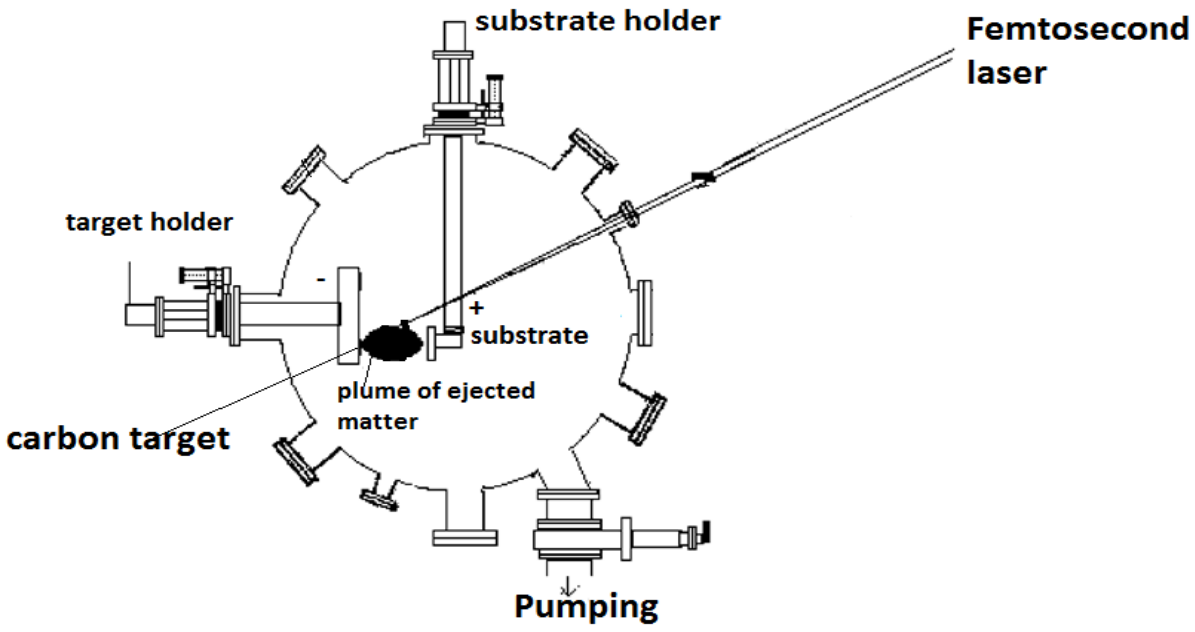

Figure 2. 1 Schematic view of the film deposition vacuum chamber in fs-PLD.

2.2.2 Femtosecond laser system

In this work, we used the Ti:Sapphire laser (Coherent Legend Elite) system for the deposition of thin films. The system has a 60 fs fundamental pulse duration at the central wavelength of 800 nm and a repetition rate of 1 kHz and a laser energy of 1 mJ was employed for the deposition of a-C, a-C:N and N doped graphene films. The Legend consists of two basic parts, oscillator and amplifier. The Figure 2.2 shows the schematic of laser system. The oscillator produces the femtosecond laser pulses of low energy, which is amplified by amplifier with principle of chirped pulse amplification (CPA). The oscillator is pumped by optically pumped semiconductor laser, operated at ~5 W power and 532 nm wavelength. The mode-locked oscillator produces ~0.5 W output power at a repetition rate of 80 MHz. The output pulses have a bandwidth of 85 nm and a wavelength of 800 nm. The ultrashort pulses are developed in the cavity by a passive mode locking technique.

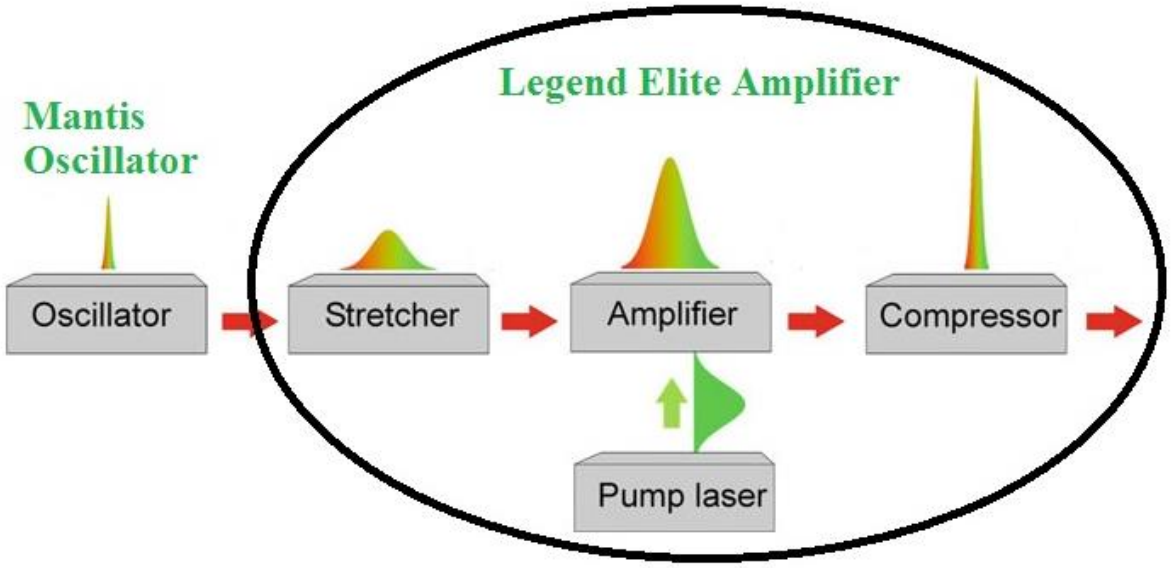

Figure 2. 2 Schematic of chirped pulse amplification (CPA) of femtosecond laser system.

The amplifier consists of three parts: the stretcher, the amplifier and the compressor. At first, the pulse duration is stretched up to 150 fs by the stretcher, then the amplifier amplifies the stretched laser pulse to 3 W at 1 kHz repetition rate, and finally, the compressor compresses the laser pulse back to fs pulse duration. The output power of laser is 2.5 W, short pulse duration 60 fs,

repetition rate 1 kHz and bandwidth of 36 nm. The laser pulse duration and bandwidth was measured by using the FROG and auto correlator systems.

The laser beam was guided through series of mirrors and a diaphragm. At the end, the beam was magnified to obtain a high fluence, which effects on the beam diameter and so reduces focal point. A focal lens was mounted on the micrometer displacement and the laser beam was focused on the target. The energy of laser beam was measured with a power meter Gentec solo 2 after crossing beam convergence. The energy of the beam at the target was calculated taking account of the transmission of the window. The laser beam entered the chamber with an angle of 45° onto the target. The plume was generated and ejected perpendicularly to the target and preferentially towards the substrate.

2.2.3 Determination of laser fluence

The laser fluence is denoted by F, which is defined as the ratio of energy per pulse (E) in joule and Σ is the surface of the laser spot in cm^2.

$$F = \frac{E}{\Sigma} \tag{1}$$

We measured the laser fluence according to the procedure proposed by Liu [1]. To measure the spot size, we used the Gaussian beam. In Eq 1, the E is the energy by impulsion in J, and Σ is the surface of the beam in cm^2. This definition is based on the characteristics of a laser impulsion. In the same way, we can describe those two sizes of macroscopic factors (parameters) associated to the laser source. Then, we write:

$$F = \frac{P}{k\Sigma} \tag{2}$$

where, P is the average power in W and k is the repetition of the laser in Hz.

Then, we used the Gaussian beam to measure the spot size. In that case, the limits of the beam are defined as $1/e^2$ of the sizes evaluated in its center. In practice, the fluence and the laser intensity are evaluated through the measure of the average power when the laser in a continuous mode. The precise knowledge of the interaction surface requires a more elaborated approach.

The control of the spot size was obtained by the precise position of the focal lens of the laser beam that permits to fix the distance target to lens, D. At first, it is necessary to select a spot size approximatively. For this, first series of laser impacts were realized in a static mode by making the lens position vary and the surface of the corresponding crater ablation was measured. We fixed the distance D = 13 mm for the position of the lens associated to the crater showing the smallest surface. Then we could report on a graph the value of the surface ablated according to the lens position and the distance D (showed in Figure 2.3) and selected approximatively the size of the interaction zone. Nevertheless, to evaluate correctly the fluence, the measure of the surface of an ablated zone is not adapted because this value changes according to the beam energy and the nature of the irradiated material. We need to know the surface Σ of the laser beam.

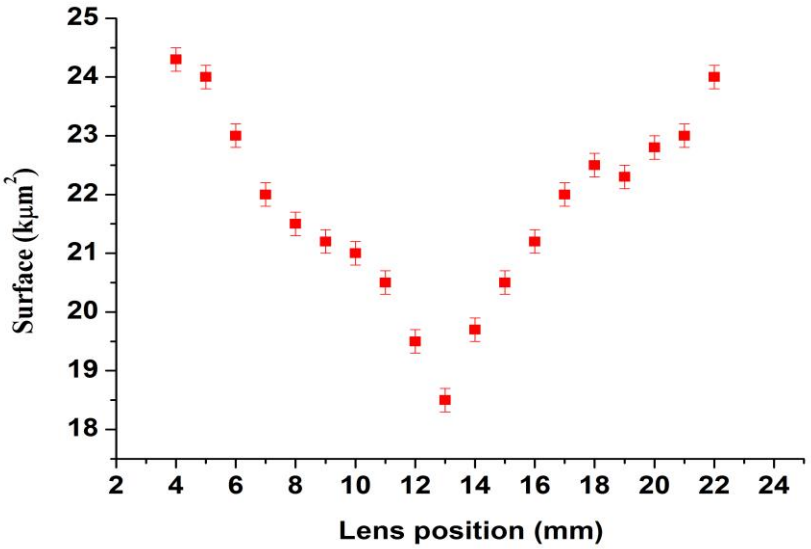

Figure 2. 3 Size of the laser spot on graphite target according to the position of the focusing lens.

This size is accessible by the analyze of a new series of impacts realized by changing the beam energy. Indeed, the fluence is not constant but depends on the distance r from the center of the beam and is written in the Gaussian approximation.

$$F(r) = F_{crete} e^{-2\frac{\pi r^2}{\pi \omega^2}} \quad (3)$$

where, F_{crete} is the fluence in the center of the beam and ω is the beam ray.

The material is ablated if the fluence exceeds its threshold fluence $F_{th(crete)}$ which means $F \geq F_{th(crete)}$. Therefore, we can define the ablated surface Σ_{th} as well as its ray r_{th} and write as,

$$\Sigma_{th} = \frac{\Sigma}{2}[lnF_{crete} - lnF_{th(crete)}] \quad (4)$$

The peak value of a Gaussian size is double of its average value. Then Eq 1, we have,

$$\Sigma_{th} = \frac{\Sigma}{2}[lnF - lnF_{th}] \quad (5)$$

where, E_{th} is the energy by minimum impulsion for ablating the material and $F_{th}=E_{th}/\Sigma$, the average threshold fluence.

Therefore, we have a linear relation between the ablated surface and the logarithm of the energy. The surface of the beam is double of the right slope. The surface was calculated and estimated at 10,500 μm^2. We obtained also the energy and the threshold fluence by extrapolation for a null ablated surface.

Contrary to the evaluation of the irradiated surface by a simple measure of the ablated surface in a particular energetic conditions, this method permit to obtain an independent value of the energy of impulsions. The laser fluence was calculated by the above procedure is 5 J/cm^2. This fluence will be used for all the experiments.

2.2.4 Thin film deposition procedure

Amorphous carbon (a-C) and amorphous carbon nitride (a-C:N) thin films have been prepared by femtosecond pulsed laser deposition (fs-PLD) with and without the assistance of Direct Current (DC) discharge plasma. The substrates were cleaned during 3 minutes under ultrasonic bath in acetone, ethanol, and then dried with nitrogen. The depositions of films were performed at room temperature by ablating a graphite target onto silicon (Si), Si_3N_4 and NaCl substrates. A femtosecond laser system working at 800 nm wavelength, with pulse duration of 60 fs and a repetition rate of 1 kHz was used. The laser beam was focused at an angle of 45° onto a high purity graphite target (99.9995% purity). The substrates were mounted on sample holder at a

distance of 36 mm from the target. High purity (99.9995%) N_2 gas was used as the reactant gas. A DC source (Advanced energy) Pinnacle Plus +5 kW was used to generate plasma of nitrogen into the chamber. The negative electrode of the DC power supply is connected to the sample holder to increase the incoming ion energy and the positive electrode is grounded. The snapshot of nitrogen plasma under DC bias was shown in the Figure 2.4. The scheme of the two experimental configurations is shown in the Figure 2.5. The deposition has been carried out with and without the DC power supply in order to study the effect of plasma assistance on the composition and the properties of growing films, especially in terms of nitrogen content and carbon hybridization. Before the deposition, the chamber was pumped until a base pressure of 10^{-4} Pa. A mass flow controller regulates the static pressure of N_2 flux between 0-50 Pa pressure and DC discharge voltages between 0–350 V were used to deposit the films. For all the deposition conditions, the laser fluence is kept constant at 5 J/cm^2. All the deposited films along with their deposition rates and with deposition conditions DC bias and N_2 pressures are listed in the Table 2.1.

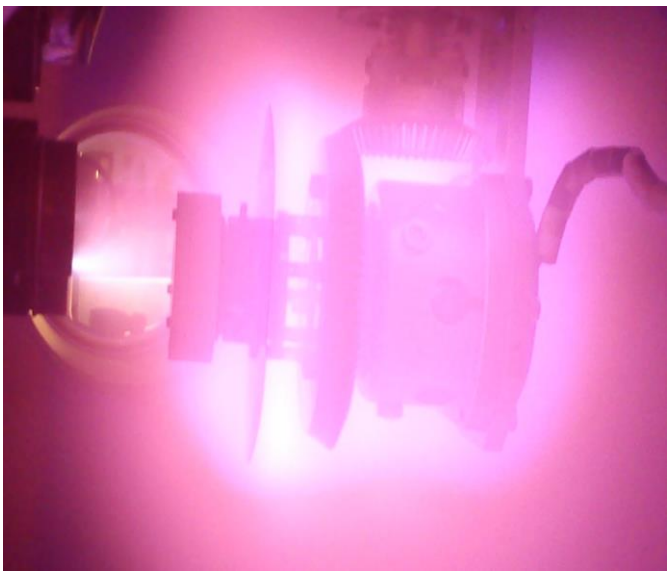

Figure 2. 4 Snapshot of nitrogen plasma under DC bias.

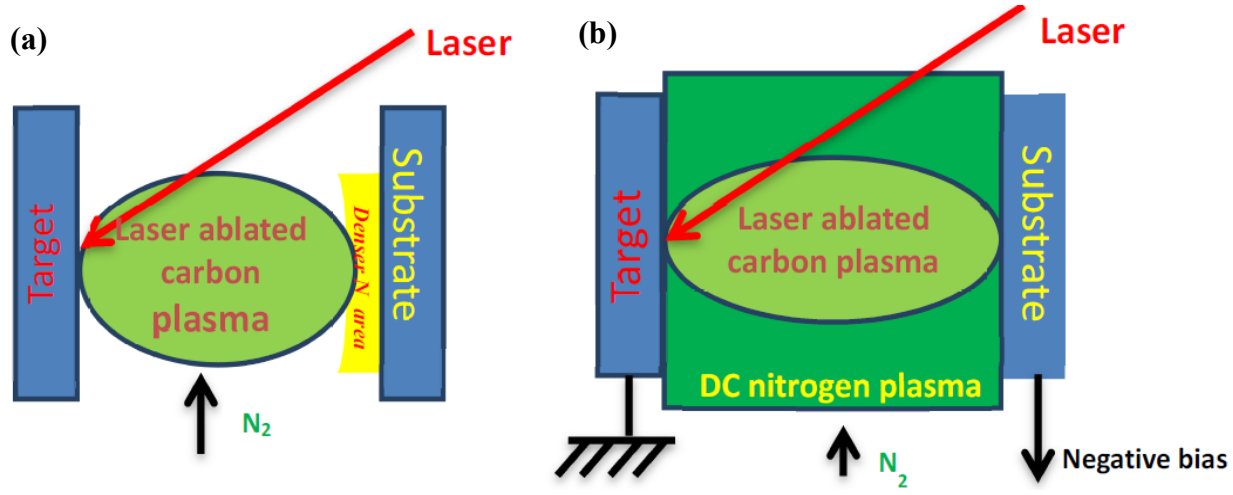

Figure 2. 5 Schematic view of the deposition configuration, a) Without bias assistance, b) with bias assistance.

DC Bias / Deposition rate (nm/min) / $P(N_2)$ Pa	*0 V*	*150 V*	*200 V*	*250 V*	*300 V*	*350 V*
0 (pure a-C)	✔/ 10	-	-	-	-	-
0.5 Pa	✔/ 9	-	-	-	-	-
1 Pa	✔/ 7	✔/ 10	-	✔/ 12	-	✔/ 10
2.5 Pa	-	-	-	✔	-	-
5 Pa	✔/ 5	✔/ 10	✔/ 10	✔/ 8	✔/7	✔/ 5
7.5 Pa	-	-	-	✔	-	-
10 Pa	✔/ 2.5	✔/ 0.25	-	✔/ 5	-	✔/ 0.25
30 Pa	✔/ 1.8	-	-	-	-	-
50 Pa	✔/ 1	-	-	-	-	-

Table 2. 1 The deposited films along with their deposition rate, and with the different experimental parameters of DC bias and N_2 pressure values.

The deposition rate varies largely as a function of the N_2 pressure or not and with plasma. The deposition rates of different conditions are stated in Table 2.1, indeed the deposition rate varies from vacuum deposited films (a-C) to N_2 pressure deposited films (a-C:N). Since the deposition rate decreases under N_2 pressure, it is reasonable to argue that ablated carbon species are decelerated due to increase of collisions with ambient N_2 molecules, some of them being unable to reach the substrate, leading to a decrease of the deposition rate with N_2 pressure increase. In case of biased a-C:N films, the deposition rate is greatly increased compared to deposited film without any bias. Genrally, plasma generates high electric field near the region of substrate surface leading to higher velocities of ionic carbon species as well as better incorporation of nitrogen species in the laser induced carbon palsma compared to snowplow effect of the residual N_2 pressure during expansion of the laser carbon plume. The deposition rate is thus increasing with biased a-C:N films.

2.2.5 Plasma plume diagnostics experiments

The deposition of a-C and a-C:N films has been presented above in the experimental section. To understand the process of CN bonding during the ablation plume generation, the expansion and the deposition on the substrate, as well as the plume interaction with the ambient gas, two ICCD based technique were used to record the optical emission of the ablation plume. The first one was Optical Emission Spectroscopy (OES): the emission from the first 7 mm of the plume along the ejection axis was collected in an UV-Visible optical fiber through a 35 mm focal lens. The signal from the fiber was sent into a Princeton Acton SP2150 spectrometer coupled with a Princeton PIMAX-3 Intensified Charge-Coupled Device (ICCD) camera, giving it a spectral resolution under 0.25 nm, with a temporal resolution of 10 ns (The PIMAX3 UV-Visible (250-900 nm) are the CCD resolution 1024x256 pixels and spot size 26.6x6.7 mm^2). In parallel, the plume was studied by direct ICCD imaging using a Hamamatsu Orca 12 ER with a UV-Visible (250-900 nm) objective. Optical band pass filters with a 10 nm bandwidth were set in front of the camera to select a spectral range of emission from selected species from the plume, specifically CN and C_2. In both cases, the use of ICCD allowed a precise record of the temporal evolution of both the plume dynamics and plume composition, with a resolution better than 10 ns in both cases. All delays given in the following sections are counted from the laser pulse interaction with the target.

The scheme of the fs-PLD setup with DC-plasma assistance and the two optical ICCD *in situ* characterization setup is represented the Figure 2.6.

The below setup was used to precisely observe the different plume species evolution and dynamics, and in particular the apparition of CN molecules and their behavior compared to the rest of the plume. In order to understand the arising of different N contents in nitrogenated amorphous carbon thin films, as well as the reasons for higher N content incorporation with plasma assistance, we study the plasma characterizations by the below set-up.

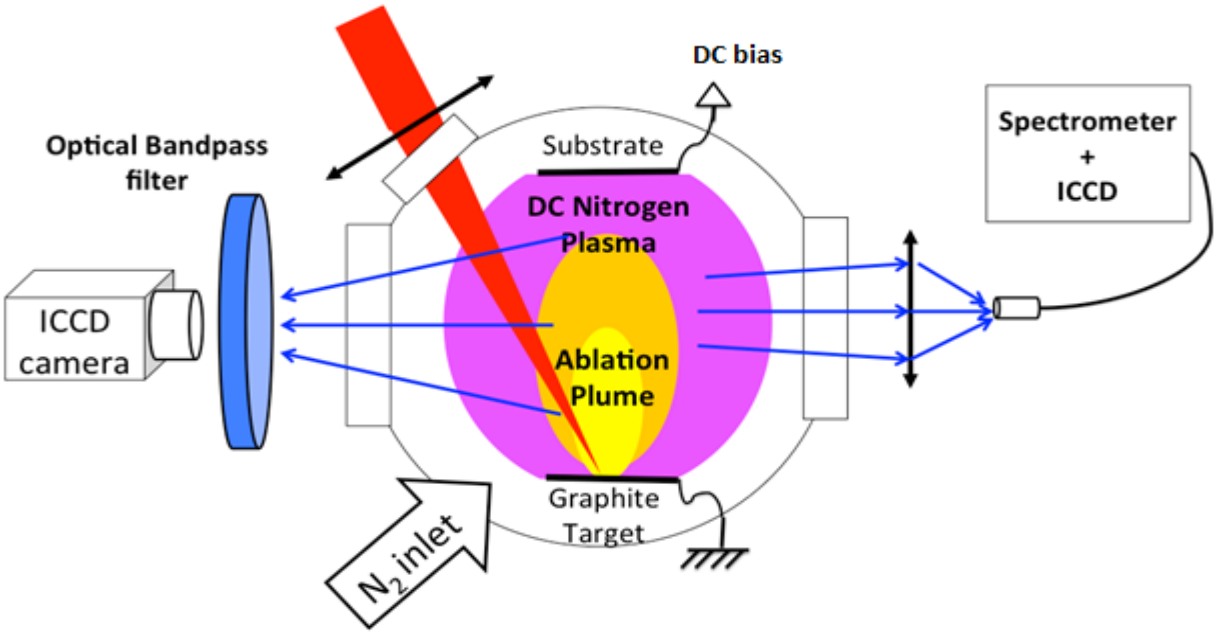

Figure 2. 6 Experimental setup used for the Optical emission spectroscopy and 2D imaging of the plasma.

2.3 Amorphous carbon nitride (a-C:N) film characterization techniques

In this section, we present the different characterization techniques which are used to characterize the amorphous carbon (a-C), amorphous carbon nitride (a-C:N) and N doped graphene thin films for their different properties. The films properties are studied by a wide variety of techniques: the surface morphology by Scanning Electron Microscopy (SEM) and Atomic Force Microscopy (Hubert Curien Laboratory), the microstructural properties by Multi-wavelength Raman

spectroscopy (Hubert Curien Laboratory, Saint Etienne), the chemical properties by X-ray Photoelectron Spectroscopy (XPS) (Ecole Des Mines, Saint Etienne) and Electron Energy Loss Spectroscopy (EELS) (ICMS, Spain), the electrochemical properties by Cyclic Voltammetry (CV) and Differential Pulse Anodic Stripping Voltammetry (DPASV) (ISA, Lyon) techniques.

2.3.1 Multi-wavelength Raman Spectroscopy

a. Raman spectra of amorphous carbon

The Raman spectroscopy is one of the most widely used characterization method for the carbon materials [2,3]. The advantages of using this technique is that it is fast, being a routine, non-destructive, vacuum and sample preparation steps are not required, it has a good lateral resolution (around 1 μm), and the area of sample is easily accessible for measurements. Generally, all the carbon materials show common features in their Raman spectra in the 800-2000 cm^{-1} region, so called G and D peak, which lie at around 1560 cm^{-1} and 1360 cm^{-1}, respectively for the visible excitation, and additionally T peak at around 1060 cm^{-1}, which is only seen for UV excitation [3–6]. The G peak is due to the bond stretching of all pairs of sp^2 atoms in both rings and chains. The D peak is due to the breathing modes of sp^2 atoms in rings, not in chains [5]. The Raman spectroscopy is the best way to obtain the detailed bonding structure of amorphous carbon (a-C) [5]. The Raman spectra of diamond, graphite, and some disordered carbons are shown in the Figure 2.7. The most disordered carbons are dominated by the G and D modes of graphite, like in all the carbon materials; even if they do not have any particular graphitic ordering [6].

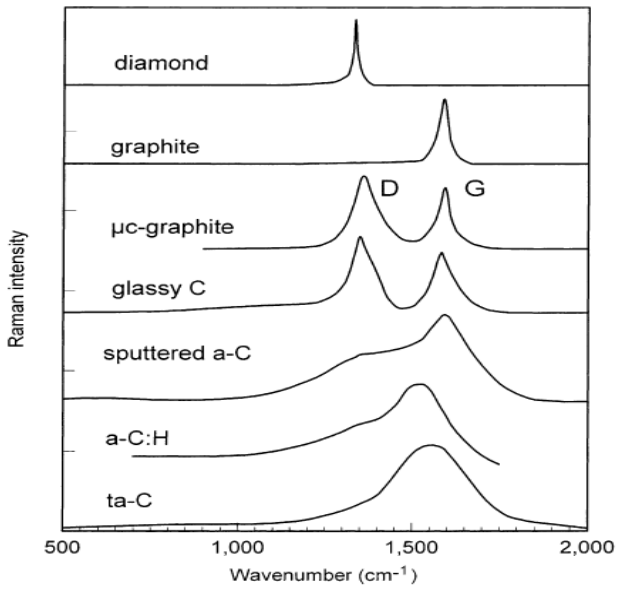

Figure 2. 7 Comparison of typical Raman spectra of carbons [6].

The Raman spectra of disordered carbons depends on the variety of parameters, such as the position of G peak, the intensity ratio of the D and G modes (I(D)/I(G)), Full Width Half Maximum (FWHM) of G peak and the shifting of G and D peaks.

The G peak is always present for any carbon at any excitation energy and it is the best-defined peak. The position of the G peak increases as the excitation wavelength decreases, from IR to UV range. The dispersion of the G peak is defined as, the rate of change of the G peak position as a function of the excitation wavelength. Empirically the G peak dispersion is defined as,

$$Disp\ (G)\left(cm^{-1}/_{nm}\right) = \frac{pos(G)@325 - pos(G)@633}{(633-325)nm} \tag{6}$$

where, Pos(G)@ wavelength indicates the G peak position measured at the specified wavelength. In a disordered carbon based compound, the G band dispersion occurs because there is a range of configurations with different local band gaps and different phonon modes. The dispersion arises from a resonant selection of sp^2 configurations or clusters with wider π band gaps and correspondingly with higher vibration frequencies. Such a dispersion is related to the topological disorder, which arises from the size and the shape distribution of the sp^2 clusters. Consequently,

the carbon compounds with a sp^2 phase entirely constituted of fully π-delocolized rings, does not show any G band dispersion. The G peak disperses only in disordered carbons. The G peak dispersion separates the materials into two parts, such material with only sp^2 rings, if the G peak dispersion saturates at maximum of 1600 cm^{-1}, and with sp^2 chains, if the G peak rises above the 1600 cm^{-1}.

The other two Raman parameters also effect the carbon bonding and the intensity ratio of the D and G peaks, I(D)/I(G), and the Full Width Half Maximum FWHM (G). In amorphous carbons, the I(D)/I(G) is a measure of the size of the sp^2 phase organized in rings. If I(D)/I(G) is negligible, then the sp^2 phase is mainly organized in chains, or even if rings are present, the pi-bonds are not fully delocalized on the rings [2,3]. The intensity ratio of the I(D)/I(G) is used to calculate the in-plane correlation length La or grain size of the graphite [2]. Tuinstra and Koening [7] proposed a relation, according to what, the I(D)/I(G) varies inversely with the in plane correlation length (L_a),

$$\frac{I(D)}{I(G)} = \frac{C_1(\lambda)}{L_a} \tag{7}$$

where, $C_1(\lambda)$ is constant depending on the laser wavelength. The above relation is valid only if the crystalline sizes are greater than 2 nm. According to Ferrari *et al*. [2], if the crystalline size is less than 2 nm, then the below equation is valid:

$$\frac{I(D)}{I(G)} = C_2(\lambda)L_a^2 \tag{8}$$

where, $C_2(\lambda)$ is constant depends on the laser wavelength. The equation 7 and 8 are represented in the Figure 2.8.

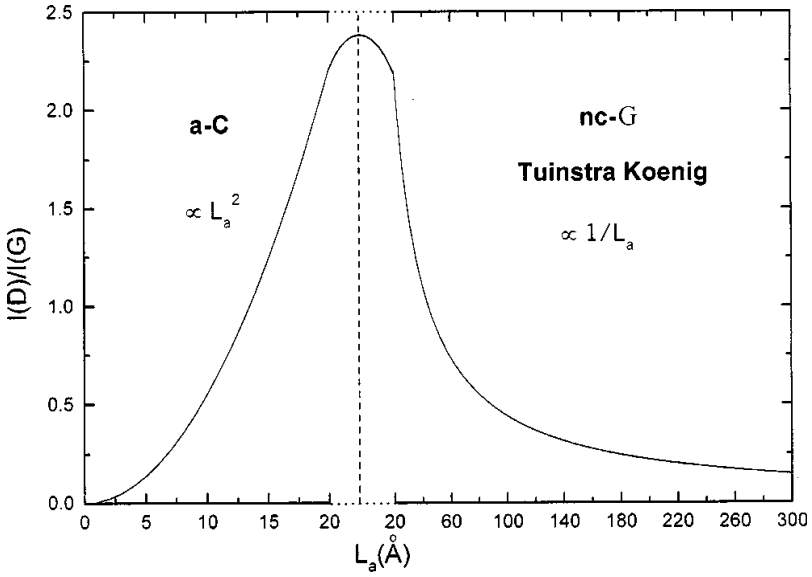

Figure 2. 8 Variation of intensity ratio of I(D)/I(G) with in plane correlation length L_a [2].

The FWHM (G) and Disp (G) both probe the disorder. However, the FWHM (G) is mainly sensitive to structural disorder. The structural disorder arises from bond angle and bond length distortions. FWHM (G) would be small if the clusters were defect free. For a given cluster size, higher bond length and bond angle disorder lead to a higher FWHM (G). The higher excitation energies are resonant with smaller clusters. This allows smaller differences between configurations and so the FWHM (G) decreases with the excitation energy [2,3,8].

J. Robertson [6] summarized and presented the schematic view to show the various factors leading to the shift of G and D peaks in either direction and alter their relative intensity, which is shown in the Figure 2.9. So, it is very important to know the precise position of G peak and D but the broad band in the region 800-2000 cm^{-1} in disordered carbon makes it is difficult get a precise value. To know the exact position and width of G and D band, we need to fit the spectra. A lot of fitting schemes were proposed. It is important to note how the spectra were fitted, as it affects the numerical values.

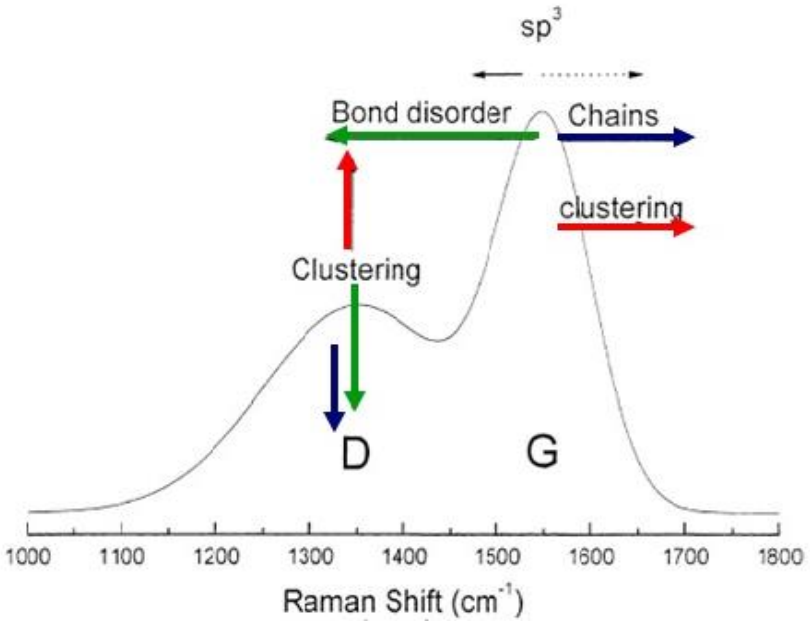

Figure 2. 9 Schematic of the factors affecting the position and heights of the Raman G and D peaks of disordered carbons [6].

b. Raman spectra deconvolution

The fitting of the Raman spectra allows us to find the exact position of G peak and D peak, the intensity ratio of D over G, full width at half maximum of G. There is no priority to choose a particular function to fit the spectrum. Empirically, the visible Raman spectra of amorphous carbon (a-C) shows one or two prominent features, the G and D peaks and some minor transitions, usually around 1100-1200 cm^{-1} and 1400-1500 cm^{-1}. The simplest fit consists of two functions, Lorentzian or Gaussian. The Lorentzian function could be used to measure the lifetime of the photoionization process, while the Gaussian function could be used to account for the instrumental energy resolution and chemical disorder [9,10]. However, Ferrari and Robertson reported that the Gaussian line shape is from the random distribution of phonon lifetime in disordered materials and Lorentzian fit is often used for crystal arising from finite life time broadening and it is normally used for disordered graphite [2]. Tamor *et al.*[11], mentioned that a two Gaussian peak fitting could faithfully explain that it is not necessary to study the Raman spectra by other more elaborate line shape fitting functions. Recently, F. C. Tai *et al.*[9], studied the effect of Raman parameters by fitting schemes, they tried nine sets of different fitting

functions on the Raman spectra of DLCH films. They found that the two peaks fitting methods with full Gaussian function tends to exhibit a higher G peak position shift and higher I(D)/I(G) ratio. They also tried with more complex four Gaussian function and found that the I(D)/I(G) ratio is close to that of a two peak fitting functions with mixture of BWF(G) and L(D) (BWF(G): Breit-Wigner-Fano (BWF) for G peak, and Lorentzian for D peak).

We systematically investigated the effect of fitting function on the Raman spectra of a-C film. The two peaks fitting of the Raman spectra was performed with six sets of combined fitting functions to decompose the Raman spectra of pure a-C film. The Raman spectra were obtained at 488 nm of Raman wavelength. The different fitting scheme is shown in the Table 2.2.

Combination of fitting functions
BWF (G) + L(D)
BWF (G) + G (D)
L(G) + L (D)
L (G) + G (D)
G (G) + L (D)
G(G) + G (D)

Table 2. 2 The combination of fitting functions, BWF: Breit-Wigner-Fano, L: Lorentzian, G: Gaussian, inside parenthesis G and D denotes that G: G peak, D: D peak.

We performed six set of different fitting combination tried on a-C films. We compared the G peak position from each spectra and compared it with the literature data [9]. The Figure 2.10 shows the comparison of G peak values (red points) with the literature data (as deposited: without annealing, as annealed: after deposition the samples were annealed) [9]. We found that the fitting with combination of Gaussian function shows a higher G peak position, whatever are the combinations of fitting functions, but the fitting with BWF for G peak and Lorentzian for D peak shows the closest value to the literature data. Therefore, the multi peak fitting revealed that there is a drastic difference by using different fitting functions but using the asymmetric functions with combination of symmetric function shows comparable values. Therefore, the fitting made in reference [9] is strictly valid to use as a reference. This is valited our fitting schemes.

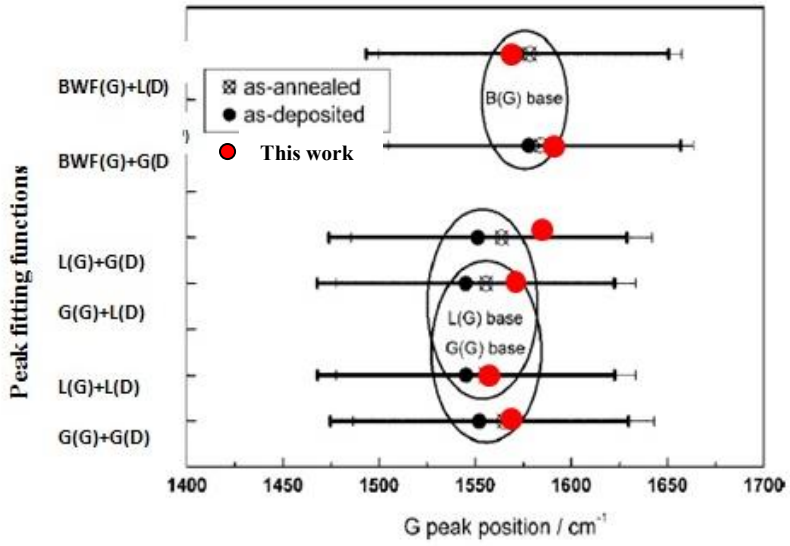

Figure 2. 10 G peak position values of a-C film obtained with different peak fitting function compared with literature data [9].

But in case of peak fitting accuracy, Ferrari *et al.*[6,8], thinks that simple two symmetric line fits (two Gaussian or two Lorentzian) are not always suitable to decompose the Raman spectra to characterize the D or G peaks, symmetric multi-peak fit or asymmetric Breit-Wigner-Fano (BWF) line shape combination can provide a better fit for Raman data. The most widely used alternative to a Gaussian fit is BWF line for G peak and Lorentzian for D peak. The BWF line has an asymmetric line shape, which arises from the coupling of a discrete mode to a continuum [6]. The BWF is given by,

$$I(\omega) = \frac{I_o[1+2(\omega-\omega_0)/Q\Gamma]^2}{1+[2(\omega-\omega_0)/\Gamma]^2} \tag{9}$$

where, I_o is the peak intensity, Γ is the full width half-maximum (FWHM) and Q^{-1} is the coupling or skewness coefficient. A symmetric Lorentzian corresponds to Q=∞. The maximum of the BWF occurs at,

$$\omega_{max} = \omega_0 + \frac{\Gamma}{2Q} \tag{10}$$

The above ω_{max} is going to be used as G peak maximum.

In amorphous carbon nitride (a-C:N) films, we have to consider the effect of the nitrogen on the Raman spectra. the vibration frequencies of solid carbon nitrides are expected to lie close to the modes of the analogous unsaturated CN molecules, which are 1500-1600 cm^{-1} for chain like molecules and 1300-1600 cm^{-1} for ring like molecules [12,13]. So, compared with amorphous carbon there is little difference in the G-D region between modes of a-C:N films due to C or N atoms. The modes in amorphous carbon nitride are also delocalized over both carbon and nitrogen sites because of the nitrogen tendency to sp^2 clustering. Therefore, there is a little difference between the Raman spectra of carbon nitride and N–free carbon films in the 1000-2000 cm^{-1} region. So, we analyzed the a-C:N films as N free amorphous carbons without needing extra peaks due to CN or NN modes [3,14,15].

In this work, we used the combination of asymmetric BWF function for G peak and symmetric Lorentzian function for D peak and the CN stretch, throughout the work for amorphous carbon nitrides [8]. We used symmetric Lorentzian function for the D, G and 2D peaks fitting of the graphene and N doped graphene [16,17].

c. Instrumentation of Multi-wavelength Raman spectroscopy

Multi-Wavelength (MW) unpolarized Raman spectroscopy has been performed using an Aramis Jobin Yvon spectrometer at four different laser excitation wavelengths, namely, 325 nm, 442 nm, 488 nm and 633 nm. The spectral resolution was 2 cm^{-1}. The laser beam were focused on the sample with a confocal objective 40 X in UV and 100 X in visible. The power on the sample was kept below 10 mW for 633 nm radiation, 3.2 mW for 488 nm radiation, 2.8 mW for 442 nm radiation and 2.2 mW for 325 nm radiation, to avoid the laser induced degradation of films. The Raman signals were acquired by a spectrometer equipped with a charge-coupled device (CCD) camera; all the spectra have been corrected by subtracting the normalized background spectrum with a similar silicon substrate. The Raman spectra were deconvoluted by a combination of an asymmetric Breit-Wigner-Fano (BWF) function for the G band, and a Lorentzian function for the D band and the C≡N stretch band observed in films.

The Raman spectroscopy was performed for graphene and N doped graphene at two different laser excitation wavelengths, namely, 442 nm and 633 nm. The laser beam was focused on the sample with a confocal objective 100 X in visible range. The power on the sample was kept

below 3 mW for 633 nm and 442 nm radiation, to avoid the laser induced degradation of films. The Raman signals were acquired by a spectrometer equipped with a charge-coupled device (CCD) camera; all the spectra were corrected by subtracting the normalized background spectrum of silicon substrate. The Raman spectrum was deconvoluted by a Lorentzian function for the D band, G band and 2D band, respectively.

The chemical structure analyses were studied by X-ray Photoelectron spectroscopy (XPS) and Electron Energy Loss Spectroscopy (EELS) of amorphous carbon nitride and N doped graphene.

2.3.2 X-ray Photoelectron Spectroscopy (XPS)

a. Basic Principle

X-ray photoelectron spectroscopy (XPS) is a surface sensitive technique. It provides the information about the chemical structure and the composition of a sample [18,19]. In order to characterize the carbon based thin films, particularly amorphous carbon nitride thin films, this technique has been used extensively in last decades [20–25]. XPS requires UHV conditions to remove the absorbed gasses, contamination and increase the mean free path of photoelectrons. The X-ray beams are usually monochromatic, either AlK_α of 1486.6 eV or MgK_α of 1253.6 eV are used to irradiate the sample surfaces. The photon energy (hν) is transferred to a core electron, a photoelectron is emitted as a result and its kinetic energy (KE) is measured. The photoelectron kinetic energy depends on the potential barrier. The energy barrier consists of two components, the core electron's binding energy (BE) and the work function (φ) of spectrometer [19,26,27].

$$BE = h\nu - KE - \varphi \tag{11}$$

The binding energy does not only depend on the specific element but it also depends on the chemical environment of the source atom (chemical structure). The valence band density changes as the chemical bond is formed, resulting in a binding energy shift. If the electrons are withdrawn from the atom by bond formation, then the binding energy of core electrons are increased. The XPS spectrum is a plot of the detected electrons quantity versus the binding energy of emitted electrons. Each chemical element produces a specific set of peaks at characteristics binding

energy and according to the peak position; it is possible to confirm the elements presence in the specimen. The observed peaks correspond with an electron configurations. By XPS, the depth analysis is very small, usually around 2-10 nm, depending on the chemical composition and density of the material. The XPS is also used to determinate the chemical states of the elements that are present within the material. As mentioned earlier, XPS is a surface sensitive technique. Due to that fact, the inelastic mean free path of the excited photoelectrons is in the order of 5-10 nm. This poses some issues about the analysis of sample surface chemistry results, often altered by the ambient armosphere. To overcome this problem several surface pretreatment techniques are possible: for example, the sputtering technique cleans the sample surfaces by bombarding the surfaces with high energies (by noble gases with energy ranges from 2 keV to 10 keV). It eliminates the undesired surface contaminations and this method is used for the sputter depth profiles in order to investigate the evolution of chemical composition. Other sputter cleaning techniques are also available. However, we should keep in mind that such procedures might lead to the structural damage or preferential sputtering. We did not perform any surface pretreatment on our films before XPS analysis, as sputtering leads to surface damage. Another concern in XPS measurements related to the conductivity of samples. Even moderately conducting films such as amorphous carbon nitride likely to charge during measurements; this is due to the continuous removal of photoelectrons that are not easily replaceable. Due to the charging effects, the spectra shift towards higher binding energies and broadening of the peaks may be observed. This can be compensated by using electron gun [28]. While performing the emission current, the charging balance of the electron gun is very important, otherwise it leads to broad and asymmetric peaks.

b. XPS spectra fitting scheme

The peak deconvolution and the peak assignment schemes are very important to investigate the chemical environment of carbon-based materials. During peak fitting, a set of components are crucial in order to validate the peak fitting such as expected number of different bands, chemical shifts, full width half maximum (FWHM) and type of fitting. The following considerations are taken into account in deconvolution of spectra of carbon based thin films. Such a suitable background type is very crucial in peak fitting. There are numerous background types available in XPS fitting. However, a linear or a Shirley type of background is widely used as background subtraction type. The applied background influences the choice of line shapes. Example, a

Shirley type background reduces the asymmetry of the components. In our work, we used the Shirley type background [[29]]. A suitable line shape is also important in order to fit the observed components of the core level spectra, different line shapes were used for the deconvolution of amorphous carbon (a-C) and amorphous carbon nitride films (a-C:N) [[28,30,31]]. In our work, we used the mixture of Gaussian and Lorentzian functions. The Lorentzian function could be used to measure the lifetime of photoionization process and the Gaussian function could be used to account for the instrumental resolution and chemical disorder. The combinations of Gaussian and Lorentzian line shapes are commonly used to fit the core level amorphous carbon nitride films [[28,30,32]]. The FWHM of each component should match to the instrumental and material expectations and as well as previously reported, the data and number of peak fit should be reasonable. The possible C1s and N1s assignments that were proposed by S.E. Rodil *et al.*[[33]] are presented in the Figure 2.11.

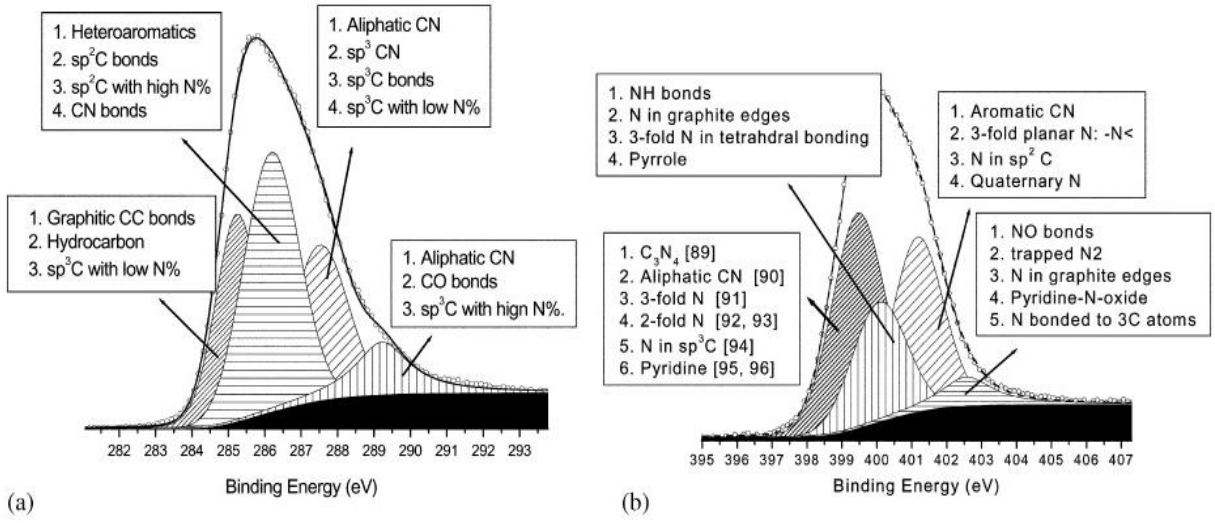

Figure 2. 11 Deconvolution of the core level lines using a maximum of four Gaussian and the common assignments found in the literature [[33]].

c. Instrumentation of XPS

In this work, the analysis were performed with a Thermo VG Thetaprobe spectrometer instrument with a focused monochromatic AlKα source (hν = 1486.68 eV, 400 µm spot size). The photoelectrons were analyzed using a concentric hemispherical analyzer operating in the

constant ΔE mode. The energy scale calibrated with sputter cleaned pure reference samples of Au, Ag and Cu in order that $Au4f_{7/2}$, $Ag3d_{5/2}$ and $Cu3p_{3/2}$ were positioned at binding energies of respectively 83.98, 386.26 and 932.67 eV. For all the samples analyzed, narrow scans were recorded for C1s, N1s and O1s with a step size of 0.1 eV and pass energy of 50 eV. This pass energy gives a width of the $Ag3d_{5/2}$ peak measured on a sputter clean pure Ag sample of 0.55 eV. Components in C1s and N1s peaks were adjusted by using line shape functions. In this work, we treated the data by using Avantage and CASA XPS software tools.

2.3.3 Electron Energy Loss Spectroscopy (EELS)

a. Basic Principle

The Electron Energy Loss Spectroscopy (EELS) is a spectroscopy technique, which is based essentially on the interaction of a beam of electrons with a sample and gives information about structural, chemical and electronic properties of the sample [34–36]. In the thesis, we used the transmission EELS (TEM/EELS). In transmission EELS, the electron beam passes through the sample and its energy loss is measured. The EELS technique probes the bulk properties of the sample. In that case, experiments are carried in a transmission electron microscope (TEM). The advantage of using TEM is the ability to use very fine probes with a diameter of the order of 1 A°, which provides information on atomic scales. EELS spectroscopy measures the distribution of inelastic scattered electrons, either as a function of energy loss and integrated over scattering angle or as a function of both energy loss and scattering angle. The Figure 2.12 shows a typical EELS spectrum with principal characteristics.

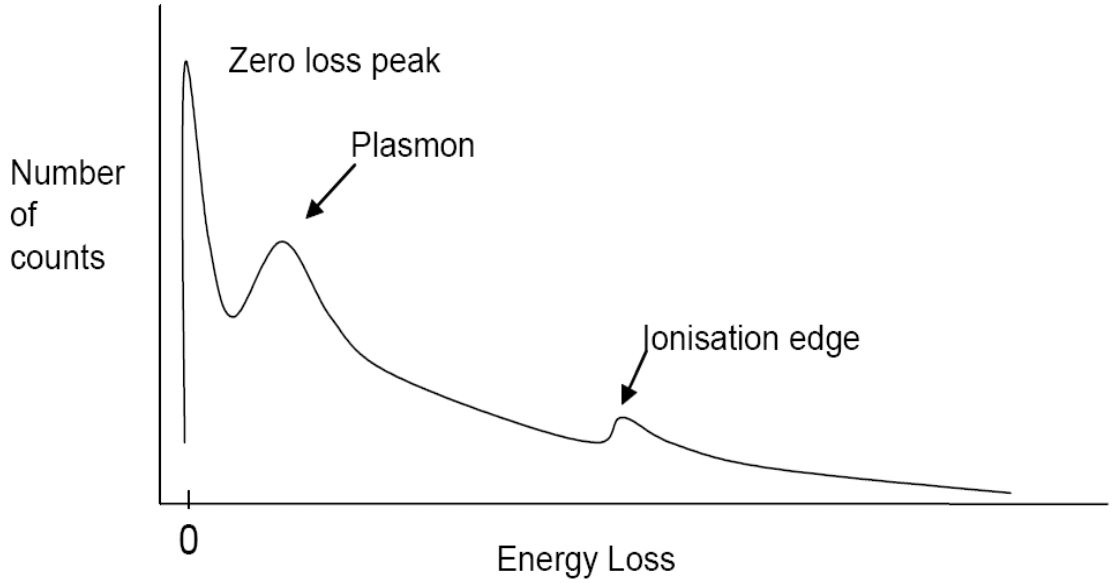

Figure 2. 12 Schematic of the EELS spectrum.

The largest signal occurs at energy loss zero in the Figure 2.12; the zero loss peaks contains all electrons that traversed the sample without losing any energy. Apart from the zero loss peak, the spectrum is divided into two parts, low loss region and core loss region. The separation between the two regions is arbitrary and typically taken to be at 50-100 eV energy loss. The most intense feature in the low loss region is typically an order of magnitude less intense than the zero loss peaks, situated at 5-50 eV energy loss, which corresponds to a collective excitation of electrons. In addition, the inter-band transitions are the excitation of valence electrons into the conduction band. They are often superposed on the plasmon peak or the zero loss peaks. The core loss region is characterized by atomic ionization, in which electrons are ejected from inner or core shell of the atom in the specimen. The presence of high loss region at a given energy loss in the spectrum allows a finger printing of qualitative identification of the chemical content of the sample. Analyzes of the chemical composition of sample is also possible, as the intensity of given edge in the spectrum is proportional to the amount of the elements present in the sample. The ionization edges are several orders of magnitude smaller than the zero loss peaks and superimposed on a background consisting of the tails of the zero loss peak and inelastic peaks. The core loss signal is one of the main challenges in EELS measurements and analysis. The EELS in a transmission electron microscope provides useful information regarding the bonding character of amorphous

carbon nitride (a-C:N) films [33]. In the low loss regime, the energy of the plasmon peak exhibits a significant shift to lower energies as the nitrogen content increases [37].

b. Instrumentation of EELS

In this work, we used the TEM/EELS. The TEM/EELS characterization was performed using a FEI FEG-TEM Tecnai G2 F30 S-Twin, equipped with a High Angle Annular Dark Field (HAADF) detector from Fischione Instruments, an SDD X-Max Energy-Dispersive X-ray spectrometer (EDX) detector from Oxford and a Imaging Filter EFTEM/EELS (GIF) model QUAMTUM SE. For EELS, the films were deposited onto NaCl substrates, which were dissolved in water before analysis.

2.3.4 Transmission Electron Microscopy (TEM)

a. Basic Principle

The Transmission Electron Microscope (TEM) provides the information of layered structures. The physicist Ernst Ruska constructed the first electron microscope in 1930. The TEM equipment requires a high set of equipments to achieve a high resolution in range of angstrom (A°). The electron microscope has three main important parts. The first is the electron gun and illumination system, where the electrons are thermionically emitted and focused onto a thin specimen, which should be thin enough to transmit the electrons by the electromagnetic lens system. The second is the sample stage and the objective lens, which is the heart of microscope. In order to form a signal in the transmission electron microscope an electron transparent sample is subject to the accelerated and focused electron beam and placed in front of electromagnetic objective lenses. The electron beam transmits the sample and the electrons undergo scattering process, which affects the provided information. The third is the image system; the image of the sample is projected onto the fluorescent screen, which converts the optical image into electronic image. It is also possible to observe diffraction patterns. The High Resolution Transmission Electron Microscope (HRTEM) is powerful enough to visualize the crystal structure and the resolution down to atomic scale.

b. Sample preparation

The TEM analysis requires an additional sample preparation step. The sample should be thinner than 50 nm. We use two types of sample preparation steps: Focused ion beam (FIB) and small angle cleavage technique, the FIB technique was used for samples prepared onto the Si substrates, and small angle cleavage technique for NaCl substrates. The FIB uses the high ion beam energy to mill a TEM specimen out of a specific sample preparation region. The advantage of this technique is the precise selection of the analysis area of specimen for TEM examination. Due to use of high-energy ions, it is possible to damage the sample and there is a high risk of contaminations. We used another technique, where the samples are deposited onto the brittle substrate (NaCl). For the sample preparation, the brittle substrates were rinsed in deionized water and collected on Cu grids. The advantage of this technique is the absence of structural damage.

c. Instrumentation of TEM

In this work, HRTEM characterization was performed using a FEI FEGTEM Tecnai G2 F30 S-Twin, equipped with a high angle annular dark field (HAADF) detector from Fischione Instruments, an SDD X-Max energy-dispersive X-ray spectrometer (EDX) detector from Oxford and an imaging filter EFTEM/EELS (GIF) model QUAMTUM SE. For HRTEM, the films were deposited onto NaCl substrates, which were dissolved in distilled water before observation.

2.3.5 Surface morphology characterization

a. Scanning Electron Microscopy (SEM)

The Scanning Electron Microscopy (SEM) was used to analyze the surface morphology of thin films. The SEM technique is a very simple technique compared with other microscope techniques. It is relatively easy, and there is no need of special sample preparation, it gives a wide area of scan and a high depth of focus. These characteristics make it a widely used technique for a large variety of materials. The SEM detects the secondary and backscattered electrons emitted from the specimen. An impact of electrons on the specimen surfaces can cause numerous processes shown in the Figure 2.13.

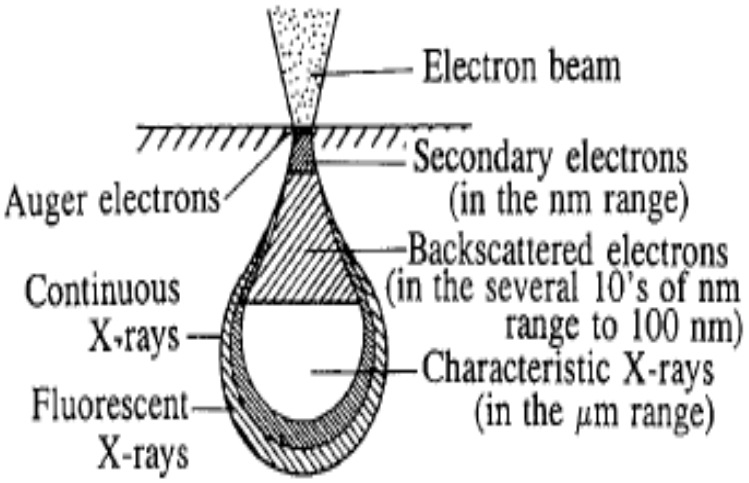

Figure 2. 13 Schematic illustration of signal generated from electron beam – specimen interaction [38].

The secondary and backscattered electrons used for an observation of the samples, and X-ray and auger electrons are usually used for the chemical analysis. The SEM works by focusing a source of electrons into a fine spot that can be scanned over the surface of the sample [38]. When the scanning electrons interact with the surface of the sample, they are imaged and several interactions occur. The images of the samples were generated by collecting the secondary electrons, the electrons from the material being imaged that are knocked out by the incident beam. The secondary electrons collected by a detector, where the information from the electrons is used to form the images of the films [38]. The images are obtained by detecting secondary electrons emitted from the surface of the sample. In this work, we used the microscope Nova NanoSEM 200 (MEB-FEG) and the resolution is 1 µm operates up to 30 kV.

b. Atomic Force Microscope (AFM)

Atomic Force Microscope (AFM) is used to analyze the topography of the films. AFM provides a three dimensional surface profile. Due to its high resolution, it is usually used for the determination of roughness of smooth surfaces. AFM is able to work in both contact and non-contact mode. It uses a sharp tip to scan the surface of a sample; the tip is mounted at the end of cantilever, which bends in respond to the forces exerted on the tip by the sample. As the tip is

brought close to the surface, the forces lead to the deflection of the cantilever. The deflection is measured by detecting the change in position of a laser beam from the end of the cantilever [39]. AFM reveals the information about the height and shape of topographic features with a very high resolution, around 0.1A°. The drawback of using AFM is limited to the area of scan. Most of the AFM are limited at around 100 mm^2. Different modes are possible depending on the type of interaction forces between the tip and the sample surfaces. In contact mode, there is a physical contact between the tip and the sample surface. The sample surface creates the deflection of the cantilever, which allows the measure of the film topography. In non-contact mode, the cantilever vibrates and the amplitudes are measured between the sample and the tip [40]. The AFM device used in this work is Agilent technologies 5500. The data were treated by Gwyddion software.

2.3.6 Electrochemical measurement

The measurement of electrochemical properties of the carbon based thin films is necessary for their future use as environmental analytical microsystems, for potential window and reactivity of carbon electrodes in the electrochemical sensors. An oxidation-reduction reaction is a type of chemical reaction that involves a transfer of electrons between two species. An oxidation reduction reaction is any chemical reaction in which the oxidation number of molecules, atoms, or ion changes by gaining or losing an electron.

Applying the potential difference between the two electrodes that are immersed in an electrolyte solution can cause a removal of electrons from molecules within the electrolyte. Then, the electrons move towards the positive electrode, while the ionized molecules (positively charged) are accelerating to the negative electrode. As a result, the dependence of current between the electrodes on the applied potential is observed.

a. Cyclic Voltammetry (CV) technique

Cyclic Voltammetry (CV) is an electrochemical technique, which measures the current that develops in an electrochemical cell. The CV is performing by cycling the potential of a working electrode and measuring the resulting current. The three-electrode system consists of a reference electrode, a counter electrode and a working electrode. The potential step varies linearly with time; this ramping is known as a scan rate. The potential is applied between the reference and the

working electrodes, and then the response is measured between the working and the counter electrodes. As shown in the Figure 2.14a, a typical reduction occurrs from (a) to (d) and an oxidation occurrs from (d) to (g). In the forward scan, the potential is first scanned negatively, starting from a greater potential (a) and ending at a lower potential (d). The potential extreme (d) is called the switching potential, and is the point where the voltage is sufficient to have cause an oxidation or reduction of an analyte. The reverse scan occurs from (d) to (g), and is where the potential scans positively. This cycle can be repeated many times during a single scan, and the scan rate can vary. The slope of the excitation signal gives the scan rate used [41,42].

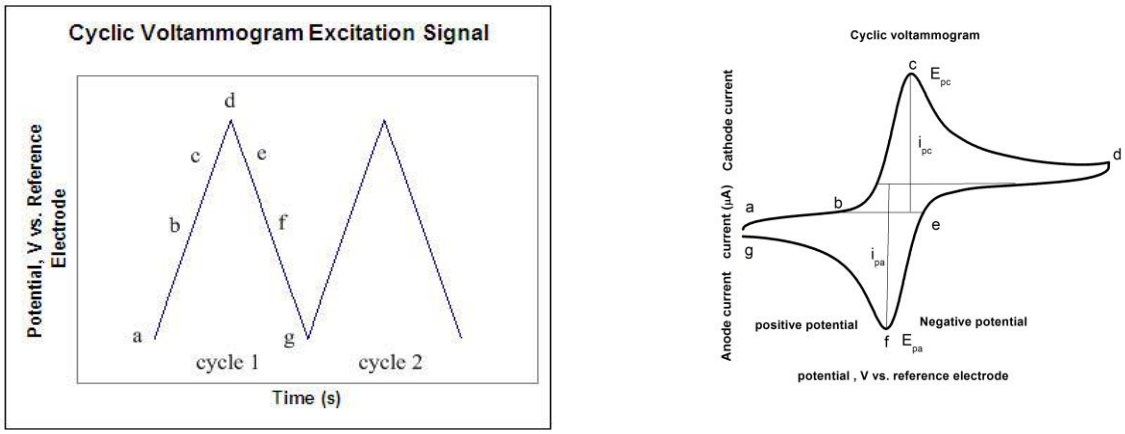

(a) **(b)**

Figure 2. 14 (a) A typical cyclic voltammetry potential waveform, and (b) cyclic voltammogram [41].

In the Figure 2.14b, the reduction process occurs from (a) the initial potential to (d) the switching potential. In this region, the potential is scanned negatively to cause a reduction. The resulting current is called cathodic current (i_{pc}). The corresponding peak potentials are occurring at (c), are called the cathodic peak potential (E_{pc}). The E_{pc} was reached when all of the substrate at the surface of the electrode was reduced. After that, the switching potential has been reached (d), the potential was scanned positively from (d) to (g), which resulted to anodic current (I_{pa}) and oxidation reaction. The peak potential at (f) is called the anodic peak potential (E_{pa}), and is reached when all the substrates at the surface of the electrode have been oxidized [41,42].

The separation between the two peaks potentials ΔE_p used to determine the electrochemcial reversibility for a redox couple, with [41]

$$\Delta E_p = 0.059/n \text{ [V] (at 298 K)} \quad (2.1)$$

This value is independent of the scan rate for fast electron transfer, increasing values of ΔEp as a function of increasing scan rate indicates the presence of electrochemcial irreversibility. The value of ΔE_p used in the calculation of the heterogeneous electron transfer rate constant (k_s) for the redox reaction.

b. Instrumentation of cyclic voltammetry (CV)

All the electrochemical measurements are carried out in a conventional one compartment-three electrodes cell in a Faraday cage with an internal volume of 3 mL (Verre Equipements, Collonges au Mont d'Or, France). The electrochemical cell is hermetically closed on one side with amorphous carbon (a-C) or amorphous carbon nitride (a-C:N) electrodes of thickness around 100 nm, and on the other side, a planar platinum electrode was used as the counter electrode. A KCl Saturated Calomel Electrode (SCE) from Radiometer Analytical (Villeurbanne, France) was used as a reference. The measurements are performed by using a multichannel potentiostat VMP3 (Bio-Logic Science Instruments, Pont de Claix, France). The electrochemical results are recorded and analysed using EC-Lab software from BioLogic Science Instruments. The electrochemical characterization of a-C and a-C:N films are studied by CV starting from -0.2 V vs SCE to 0.8 V vs SCE repeated 3 times in an aqueous solution containing $NaClO_4$ 0.1M as support electrolyte without any redox species in solution. Several scan rates were tested from 1V/s down to 5 mV/s and only the last cycles were used for data interpretations. After measurement, electrochemical cells containing all electrodes were rinsed with Milli-Q water and ethanol and the electrodes were kept 2-5 hours in water to ensure any physio-adsorbed species.

C. Differential Pulse Anodic Stripping Voltammetry (DPASV)

Stripping voltammetry is a sensitive electroanalytical technique for the determination of metals or metal complexes, especially heavy metals in water. The technique usually consist of a pre-concentration of the metals in the electrode surface, followed a potential sweep to dissolve pre-concentrated species of interest, making the quantification of them. Depending on the nature of the analyte, different modes of concentration analysis are used. The stripping step may consist of

a positive or a negative potential scan, creating either an anodic or a cathodic current respectively. Hence, Anodic Stripping Voltammetry (ASV) and Cathodic Stripping Voltammetry (CSV) are two specific stripping techniques. The most common is the Anodic Stripping Voltammetry (ASV). The stripping techniques have lower detection limit than any of the commonly used electrochemical techniques, and the preparation of the sample is low, in addition the sensitivity and the selectivity are excellent [[43]]. This procedure consist of three main steps: pre-concentraion step, this step provides different modes for preconcentration of the analyte on the working electrode, which can be summarized by two way, electrochemically (with or without potential stimulus) and by adsorptive. Thanks to this step is achieved the species concentration in volume very much smaller compared to the volume of the solution. To achieve reproducible results is necessary control the hydrodynamic parameters (pre-concentration time, stirring, temperature, electrode area and initial potential applied. The pre-concentration allows an increase of sensitivity of other 2 or 3 orders of magnitude, making it feasible to operate with analyte concentrations 10^{-10} M or even lower, sensitivities comparable with others techniques not electro-analytical characterized by high sensitivity. Step of Resting: After a time perfectly measured, stops electrolysis and stirring, but remains constant initial potential. During this time, is achieved the homogenizing of the substance on the electrode and recovering the diffusion regime. Step of Stripping: During this step, the deposited analyte is determined by a procedure voltammetric by stripping itself, through a potential sweep in the opposite direction to the initial. This sweep can be performed by various techniques (eg, differential pulse, square wave, linear sweep or staircase). The simplest technique is Linear Sweep Voltammetry (LSV) where the potential is scanned linearly as a function of time. Another commonly used technique is Differential Pulse Voltammetry (DPV), which has a lower detection limit than LSV. This is due to its pulsed waveform, which measures the current in pulses by taking two measurements and recording the difference as the potential is increased. This helps to reduce the background current. The waveforms from each pulse superimpose upon one another to form a staircase waveform since the pulse amplitude is constant while the potential increases in small increments.

2.4 Conclusions

In this chapter, we discussed the deposition chamber characteristics. We presented the femtosecond laser system and its characteristics, and the procedure of determination of laser fluence. We elaborate the deposition procedure of amorphous carbon (a-C) and amorphous carbon nitride (a-C:N) films by femtosecond pulsed laser deposition with and without DC bias assistance along with their deposition parameters. The characteristics of optical emission spectroscopy and spectral resolved 2D imaging were discussed, which were used to study the ablation plasma plume to understand the formation mechanism of thin films and address high nitrogen incorporation into the films. In the last part, we presented different characterization techniques which were used to characterize the films with their instrumentation and operation. Different characterization techniques are used to characterize the films for their surface morphology, physical chemical and electrochemical properties discussed.

References

(1) Liu, J. M. Simple Technique for Measurements of Pulsed Gaussian-Beam Spot Sizes. *Opt. Lett.* **1982**, *7*, 196.

(2) Ferrari, A. C.; Robertson, J. Interpretation of Raman Spectra of Disordered and Amorphous Carbon. *Phys. Rev. B* **2000**, *61*, 14095–14107.

(3) Donnet, C.; Erdemir, A. *Tribology of Diamond-like Carbon Films: Fundamentals and Applications*; Springer Science & Business Media, 2007.

(4) Ferrari, A. C.; Robertson, J. Resonant Raman Spectroscopy of Disordered, Amorphous, and Diamondlike Carbon. *Phys. Rev. B* **2001**, *64*, 75414.

(5) Ferrari, A. C.; Robertson, J. Raman Spectroscopy of Amorphous, Nanostructured, Diamond–like Carbon, and Nanodiamond. *Philos. Trans. R. Soc. Lond. Math. Phys. Eng. Sci.* **2004**, *362*, 2477–2512.

(6) Robertson, J. Diamond-like Amorphous Carbon. *Mater. Sci. Eng. R Rep.* **2002**, *37*, 129–281.

(7) Tuinstra, F.; Koenig, J. L. Raman Spectrum of Graphite. *J. Chem. Phys.* **1970**, *53*, 1126–1130.

(8) Ferrari, A. C.; Rodil, S. E.; Robertson, J. Interpretation of Infrared and Raman Spectra of Amorphous Carbon Nitrides. *Phys. Rev. B* **2003**, *67*, 155306.

(9) Tai, F. C.; Lee, S. C.; Chen, J.; Wei, C.; Chang, S. H. Multipeak Fitting Analysis of Raman Spectra on DLCH Film. *J. Raman Spectrosc.* **2009**, *40*, 1055–1059.

(10) Díaz, J.; Paolicelli, G.; Ferrer, S.; Comin, F. Separation of the sp3 and sp2 Components in the C1s Photoemission Spectra of Amorphous Carbon Films. *Phys. Rev. B* **1996**, *54*, 8064–8069.

(11) Tamor, M. A.; Vassell, W. C. Raman "'fingerprinting'" of Amorphous Carbon Films. *J. Appl. Phys.* **1994**, *76*, 3823–3830.

(12) Dollish, F. R., Fateley, W. G., Bentley, F. F. *Characteristic Raman Frequencies of Organic Compounds*; Wiley Interscience: New York, 1974.

(13) Katritzky, A. *Physical Methods in Heterocyclic Chemistry*; Elsevier, 2012.

(14) Rodil, S. E.; Muhl, S.; Maca, S.; Ferrari, A. C. Optical Gap in Carbon Nitride Films. *Thin Solid Films* **2003**, *433*, 119–125.

(15) Ferrari, A. C.; Rodil, S. E.; Robertson, J. Resonant Raman Spectra of Amorphous Carbon Nitrides: The G Peak Dispersion. *Diam. Relat. Mater.* **2003**, *12*, 905–910.

(16) Ferrari, A. C. Raman Spectroscopy of Graphene and Graphite: Disorder, Electron–phonon Coupling, Doping and Nonadiabatic Effects. *Solid State Commun.* **2007**, *143*, 47–57.

(17) Ferrari, A. C.; Meyer, J. C.; Scardaci, V.; Casiraghi, C.; Lazzeri, M.; Mauri, F.; Piscanec, S.; Jiang, D.; Novoselov, K. S.; Roth, S.; *et al.* Raman Spectrum of Graphene and Graphene Layers. *Phys. Rev. Lett.* **2006**, *97*, 187401.

(18) Brundle, C. R.; Evans, C. A.; Wilson, S. *Encyclopedia of Materials Characterization: Surfaces, Interfaces, Thin Films*; Gulf Professional Publishing, 1992.

(19) Barr, T. L. *Modern ESCAThe Principles and Practice of X-Ray Photoelectron Spectroscopy*; CRC Press, 1994.

(20) Pels, J. R.; Kapteijn, F.; Moulijn, J. A.; Zhu, Q.; Thomas, K. M. Evolution of Nitrogen Functionalities in Carbonaceous Materials during Pyrolysis. *Carbon* **1995**, *33*, 1641–1653.
(21) Ech-chamikh, E.; Essafti, A.; Ijdiyaou, Y.; Azizan, M. XPS Study of Amorphous Carbon Nitride (a-C:N) Thin Films Deposited by Reactive RF Sputtering. *Sol. Energy Mater. Sol. Cells* **2006**, *90*, 1420–1423.
(22) Ronning, C.; Feldermann, H.; Merk, R.; Hofsäss, H.; Reinke, P.; Thiele, J.-U. Carbon Nitride Deposited Using Energetic Species: A Review on XPS Studies. *Phys. Rev. B* **1998**, *58*, 2207–2215.
(23) Cappelli, E.; Orlando, S.; Trucchi, D. M.; Bellucci, A.; Valentini, V.; Mezzi, A.; Kaciulis, S. Carbon Nitride Films by RF Plasma Assisted PLD: Spectroscopic and Electronic Analysis. *Appl. Surf. Sci.* **2011**, *257*, 5175–5180.
(24) Tessier, P. Y.; Kre N'guessan, R.; Angleraud, B.; Fernandez, V.; Mubumbila, N.; Turban, G. Carbon Nitride Thin Films Deposited by Reactive Plasma Beam Sputtering. *Surf. Coat. Technol.* **2000**, *125*, 295–300.
(25) Sánchez-López, J. C.; Donnet, C.; Lefèbvre, F.; Fernández-Ramos, C.; Fernández, A. Bonding Structure in Amorphous Carbon Nitride: A Spectroscopic and Nuclear Magnetic Resonance Study. *J. Appl. Phys.* **2001**, *90*, 675–681.
(26) Watts, J. F.; Wolstenholme, J. *An Introduction to Surface Analysis by XPS and AES*; 2003.
(27) Heide, P. van der. *X-Ray Photoelectron Spectroscopy: An Introduction to Principles and Practices*; John Wiley & Sons, 2011.
(28) Le Normand, F.; Hommet, J.; Szörényi, T.; Fuchs, C.; Fogarassy, E. XPS Study of Pulsed Laser Deposited CNx Films. *Phys. Rev. B* **2001**, *64*, 235416.
(29) Shirley, D. A. High-Resolution X-Ray Photoemission Spectrum of the Valence Bands of Gold. *Phys. Rev. B* **1972**, *5*, 4709–4714.
(30) Ronning, C.; Feldermann, H.; Merk, R.; Hofsäss, H.; Reinke, P.; Thiele, J.-U. Carbon Nitride Deposited Using Energetic Species: A Review on XPS Studies. *Phys. Rev. B* **1998**, *58*, 2207–2215.
(31) Cappelli, E.; Orlando, S.; Trucchi, D. M.; Bellucci, A.; Valentini, V.; Mezzi, A.; Kaciulis, S. Carbon Nitride Films by RF Plasma Assisted PLD: Spectroscopic and Electronic Analysis. *Appl. Surf. Sci.* **2011**, *257*, 5175–5180.
(32) Marton, D.; Boyd, K. J.; Al-Bayati, A. H.; Todorov, S. S.; Rabalais, J. W. Carbon Nitride Deposited Using Energetic Species: A Two-Phase System. *Phys. Rev. Lett.* **1994**, *73*, 118–121.
(33) Rodil, S. E.; Muhl, S. Bonding in Amorphous Carbon Nitride. *Diam. Relat. Mater.* **2004**, *13*, 1521–1531.
(34) Egerton, R. *Electron Energy-Loss Spectroscopy in the Electron Microscope*; Springer Science & Business Media, 2011.
(35) Egerton, R. F. Electron Energy-Loss Spectroscopy in the TEM. *Rep. Prog. Phys.* **2009**, *72*, 16502.
(36) Ahn, C. C. *Transmission Electron Energy Loss Spectrometry in Materials Science and the EELS Atlas*; John Wiley & Sons, 2006.
(37) Waidmann, S.; Knupfer, M.; Fink, J.; Kleinsorge, B.; Robertson, J. Electronic Structure Studies of Undoped and Nitrogen-Doped Tetrahedral Amorphous Carbon Using High-Resolution Electron Energy-Loss Spectroscopy. *J. Appl. Phys.* **2001**, *89*, 3783–3792.

(38) Egerton, R. F. *Physical Principles of Electron Microscopy*; Springer US: Boston, MA, 2005.
(39) Binnig, G.; Quate, C. F.; Gerber, C. Atomic Force Microscope. *Phys. Rev. Lett.* **1986**, *56*, 930–933.
(40) Jean, M. S.; Hudlet, S.; Guthmann, C.; Berger, J. Van Der Waals and Capacitive Forces in Atomic Force Microscopies. *J. Appl. Phys.* **1999**, *86*, 5245–5248.
(41) Mabbott, G. A. An Introduction to Cyclic Voltammetry. *J. Chem. Educ.* **1983**, *60*, 697.
(42) Ramaley, L.; Krause, M. S. Theory of Square Wave Voltammetry. *Anal. Chem.* **1969**, *41*, 1362–1365.
(43) Barón-Jaimez, J.; Joya, M. R.; Barba-Ortega, J. Anodic Stripping Voltammetry – ASV for Determination of Heavy Metals. *J. Phys. Conf. Ser.* **2013**, *466*, 12023.

Chapter 3. a-C:N thin films: Results and Discussions

3.1 Introduction

In this chapter, we present the results and their analysis of amorphous carbon (a-C) and amorphous carbon nitride (a-C:N) thin films deposited by femtosecond pulsed laser deposition on Si and NaCl substrates at 5 J/cm^2 constant laser fluence. The detailed experimental procedure of thin films deposition and different characterization techniques along with their instrumentation and operational conditions were described in the chapter 2.

The results are obtained by using a wide variety of characterization techniques performed to study the surface morphology, chemical structure and microstructural properties of a-C and a-C:N thin films. As we know, the film properties are largely influenced by the deposition parameters, such as nitrogen partial pressure, plasma assistance and deposition technique. We studied the surface morphology by using Scanning Electron Microscopy (SEM) and Atomic Force Microscopy (AFM), the chemical composition and nitrogen quantification by using X-ray Photoelectron Spectroscopy (XPS) and Electron Energy Loss Spectroscopy (EELS), and the microstructural properties of films by using Multi-wavelength Raman spectroscopy.

In the first section, we analyze the results of the DC bias assistance effect on the films morphological, chemical and microstructural properties. The discussion is on the a-C, a-C:N deposited at 10 Pa P_{N2} pressure and 0 bias voltage, and biased a-C:N film deposited at 5 Pa P_{N2} pressure and 250 V bias assistance.

In the second part, we systematically study the effect of nitrogen partial pressure from 0-30 pa P_{N2} pressure on the films properties without using any DC bias assistance.

In the last part, the effect of different bias assistance on the films properties are presented and analyzed. The films are deposited by various DC bias voltages from 0-350V in range by keeping the nitrogen partial pressure as constant at 5 Pa.

3.2 Film thickness

The thicknesses of the films were measured by DekTak profilometry, the thickness values of different films were obtained in the 50-200 nm range. Different film thicknesses were used, depending on characterization techniques was used to study the chemical, structural and electrochemical properties of amorphous carbon nitride (a-C:N) films. In particularly, the 50 nm thickness films were used in X-ray photoelectron spectroscopy (XPS) technique, 100 nm thickness films was used in Raman spectroscopy and Cyclic Voltammetry (CV) technique, and 150-200 nm film thickness was used in Electron energy loss spectroscopy (EELS) measurements.

3.3 Surface morphology

The surface morphology of the films has been studied by using Scanning electron microscopy (SEM) and Atomic force microscopy (AFM) techniques.

3.3.1 Scanning Electron Microscopy (SEM)

The Figure 3.1 shows the SEM images of a-C and a-C:N films deposited by femtosecond PLD. The films were deposited at constant laser fluence of 5 J/cm^2. The deposition conditions are (a) a-C film deposited without nitrogen partial pressure and DC bias assistance, (b) a-C:N film deposited at 10 Pa N_2 pressure and without DC bias assistance, (c) the Biased a-C:N film deposited at 5 Pa N_2 pressure and 250 V bias assistance. The surface morphology of the deposited films was studied by scanning electron microscopy. All the films surfaces were found smooth and without cracks, and a low number of nanometer sized particles was observed. The nitrogen incorporated films (a-C:N) showed larger size nanoparticles than the pure a-C films, the nanoparticles density is increased in DC bias assistance deposited films (biased a-C:N). The particle formation is a very complex phenomenon, electrostatic forces, coulomb repulsion, atomization and spallation can be involved in particles formation as it is described in previous reports [1,2]. The nanoparticles are considered to arise from the condensation in the gas phase or direct sputtering from the liquid phase [2–4]. This kind of nanoparticles generation has been

observed in other experiments carried out by femtosecond pulsed laser deposition [5,6]. A similar surface morphology was observed for the films deposited at other deposition conditions.

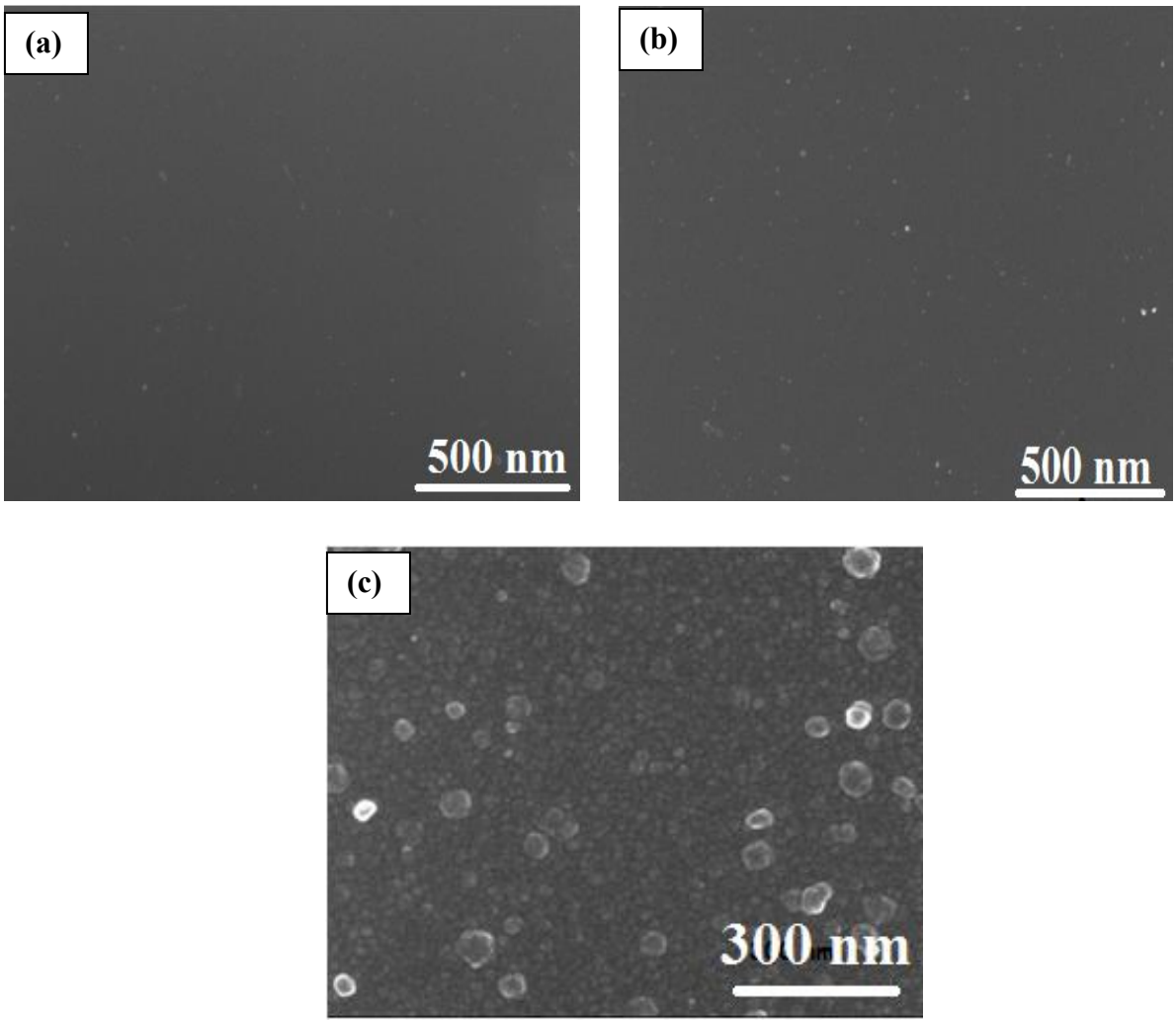

Figure 3. 1: SEM images of films deposited by femtosecond PLD with and without DC bias assistance at fluence 5 J/cm^2, (a) pure a-C film, (b) a-C:N film deposited at 10 Pa P_{N2} pressure, (c) Biased a-C:N film deposited at DC voltage 250 V and 5 Pa P_{N2} pressure.

3.3.2 Atomic Force Microscopy (AFM)

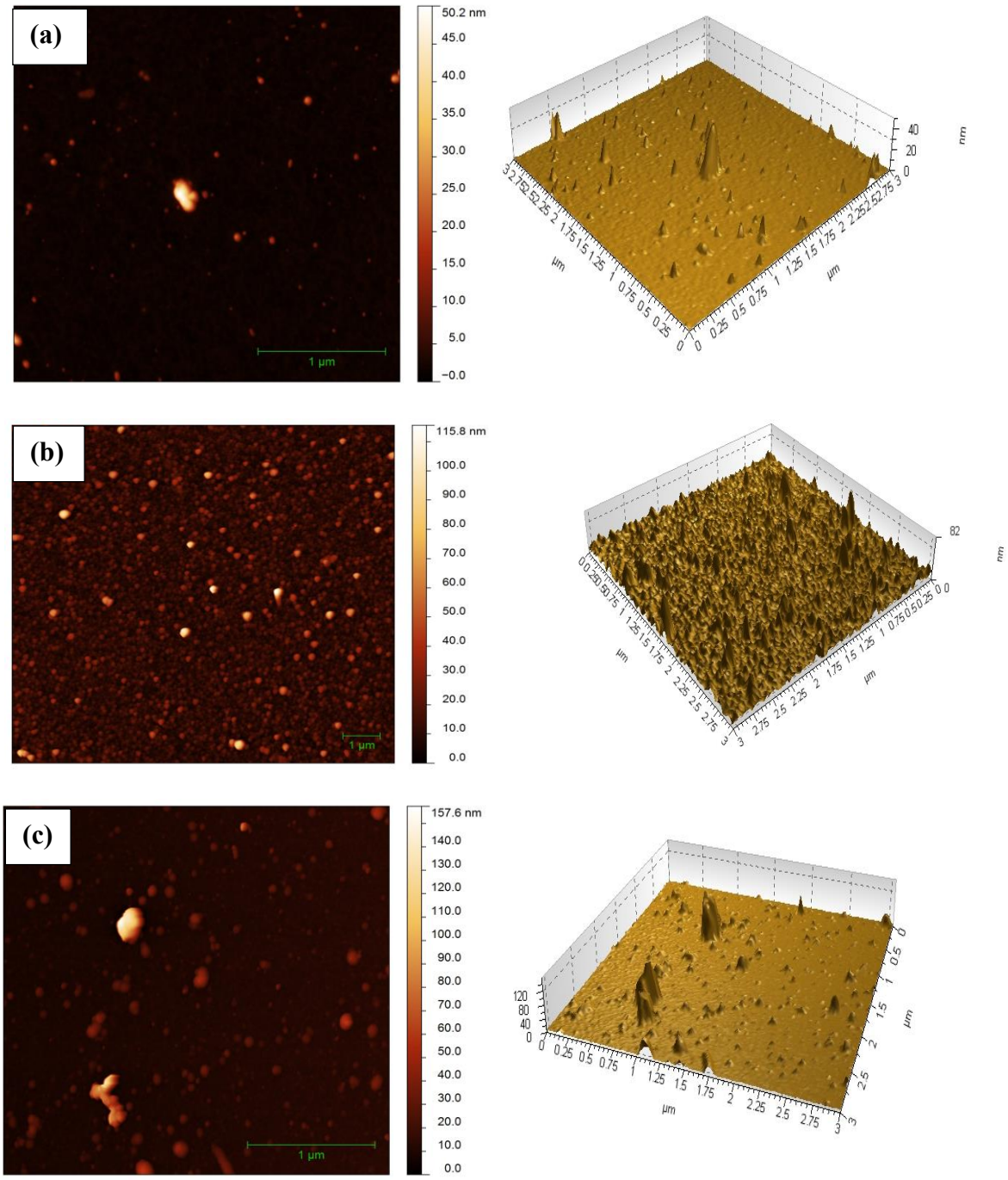

Figure 3. 2 2D and 3D images of films obtained by AFM, (a) pure a-C , (b) 16 % of N contain a-C:N film deposited at 10 Pa P_{N2} pressure, (C) 24 % of N contain biased a-C:N film deposited at DC voltage 250 V and 5 Pa P_{N2} pressure.

The Figure 3.2 shows the 3D and 2D images of a-C and a-C:N films. The a-C film deposited at 0 P_{N2} pressure and 0 DC bias voltage, and the a-C:N film with 16 % of nitrogen content is deposited at 10 Pa of P_{N2} pressure and 0 DC bias voltage, and the biased a-C:N film with 28 % of nitrogen content is deposited at 5 Pa P_{N2} pressure and 250 V DC bias voltage. The pure a-C and a-C:N films with N content 16 and 28 at.% films were analyzed by AFM. The roughness (Ra) of films was obtained at scan area of 3 µm x 3 µm. The roughness values of each film type was 2 nm (a-C), 6 nm (a-C:N) and 9 nm (biased a-C:N) respectively. The roughness values do not significantly increase with deposition conditions. The roughness value in biased a-C:N film was increased as compared to without bias assistance deposited films. The change of the roughness for biased a-C:N films with the substrate bias can be related to the change in the average energy of ions bombarding the film during film growth [7]. The substrate bias will cause the increase in ion energy, which affects the adhesion and roughness of films.

3.4 Chemical and microstructural analysis of a-C:N films

The chemical composition and atomic bonding of amorphous carbon and amorphous carbon nitride films were studied by using X-ray photoelectron spectroscopy (XPS), Electron energy loss spectroscopy (EELS) and Multi-wavelength Raman spectroscopy.

3.4.1 Nitrogen partial pressure effect on the chemical and microstructure of the a-C:N thin films

In this section, we studied the effect of nitrogen partial pressure on a-C:N films composition and structure by XPS, EELS and Raman spectroscopy techniques on the basis of the procedure described in the previous section.

a. X-ray photoelectron spectroscopy

The Figure 3.3 shows the evolution of nitrogen content in a-C:N films deposited at different nitrogen partial pressure. The N content is found to be 4 -18 at.% for the films with increasing of

nitrogen partial pressure from 0.5-30 Pa in range, respectively. The N content values are 0, 4, 10, 12, 16 and 18 at.% at 0, 0.5, 1, 5, 10 and 30 Pa of nitrogen partial pressures, respectively.

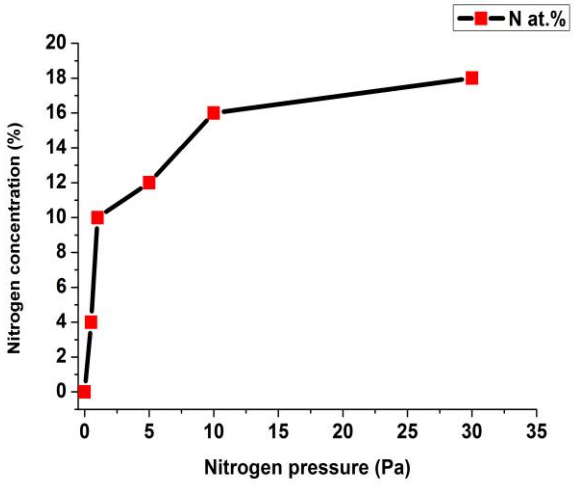

Figure 3. 3 Nitrogen concentration revealed by XPS as a function of nitrogen pressure.

The Figure 3.4 shows the normalized C1s and N1s spectra of our a-C:N films containing various nitrogen contents. One can see that the C1s peaks become broader and more asymmetric as a greater amount of nitrogen is incorporated into the films. The N1s spectra reveals a shift towards higher binding energy with higher nitrogen concentration. The oxygen was found to be very low in films which is in range 4 - 12 at.% mainly due to adventitious surface contamination. Usually in the literature, the C1s envelope of a-C:N films are deconvoluted using several components. To date the identification of local bonding states in C1s spectra is not definitive. Some authors proposed C1s fitting to three, four and five [8–16]. In this, The C1s spectra were fitted with three and four peaks respectively. The fitting with less number of peaks is less informative. The deconvoluted C1s and N1s spectra of a-C:N (4 at.% deposited at 0.5 Pa) and a-C:N (18 at.% deposited at 30 Pa) films are shown in the Figure 3.5. The C1s and N1s binding energy values are summarized in the Table 3.1, which are deduced from C1s and N1s deconvolution spectra. The pure a-C film binding energy values are at 284.92 eV, 285.89 eV and 287.16 eV assigned to Csp^2, Csp^3 and CO bonds respectively. The C1s and N1s spectra related to the a-C:N films were deposited at different nitrogen partial pressures summarized in the Table 3.1. The deconvoluted C1s and N1s spectra of a-C:N films (deposited at 0.5 Pa and 30 Pa) are shown in the Figure 3.5, they correspond to the films with the nitrogen content from low (4 %) to high (18 %) percentage

in films. The C1s binding energy values are in range at 284.52-284.97 eV, 285.05-285.84 eV, 286.02-286.86 eV, 287.04-287.80 and 288.38-288.96 eV peaks are assigned to Csp^2, Csp^3, sp^2 CN, sp^3 CN and CO bonds respectively [10,11,14,15,17–19]. A higher nitrogen content in the films lead to the shifting of the binding energy, which is clearly evidenced from above assignment and the Table 3.1 below. It is clear that by increasing the N content, the peaks located at low binding energy side disappear and the peaks were shifted to higher binding energy side, which means that the carbon bonding to N increases with the increasing of N content in films.

The Figure 3.5 shows the deconvoluted N1s spectra with four peaks, films are shown from low N content (deposited at 0.5 Pa) to high N content (deposited at 30 Pa). The nitrogen containing films exhibits four N1s contributions in the range between 398.90-398.91 eV, 399.17-399.99 eV, 400.29-400.77 eV, 401.04-401.68 eV and 402.03-402.26 eV respectively. The binding energy values are shift towards higher binding energies with the increase of nitrogen partial pressure. The chemical shift related to different N-bonding environments. The peak centered at 398.90-398.91 eV was assigned to N-sp^3C (N1), 399.17-399.99 eV was assigned to pyridinic-N (N2), and 400.29-400.77 eV was assigned to pyrrolic-N (N3), and 401.04-401.68 eV was assigned to quaternary-N (N4), and 402.03-402.26 eV was assigned to some NO (N5) respectively [13,16,19,20]. The N-sp^3C type bonding disappeared with the increasing of N content in films. The high N content films showed the existence of sp^2 CN type bonding. This confirms that the films are more graphite like structures as greater amounts of nitrogen is incorporated into the films during the deposition.

Film conditions	sp^2 C-C (eV)	sp^3C-C (eV)	sp^2C-N (eV)	sp^3C-N	CO (eV)	N1 (eV)	N2 (eV)	N3 (eV)	N4 (eV)	N5 (eV)
a-C	284.92	285.89	-	-	287.16	-	-	-	-	-
a-C: N (0.5 Pa)	284.89	285.84	286.86	-	288.39	398.91	399.94	400.77	-	402.03
a-C:N (1 Pa)	284.52	285.05	286.02	287.09	-	398.90	399.99	400.77	401.68	-
a-C:N (5 Pa)	284.97	285.75	286.43	287.59	-	398.91	399.74	400.68	401.52	-
a-C:N (10 Pa)	-	285.17	286.28	287.04	288.38	-	399.17	400.29	401.04	402.36
a-C:N (30 Pa)	-	285.19	286.39	287.80	288.96	-	399.35	400.51	401.13	402.27

Table 3. 1 The C1s and N1s binding energy values of XPS spectra of a-C:N films deposited at different nitrogen partial pressure.

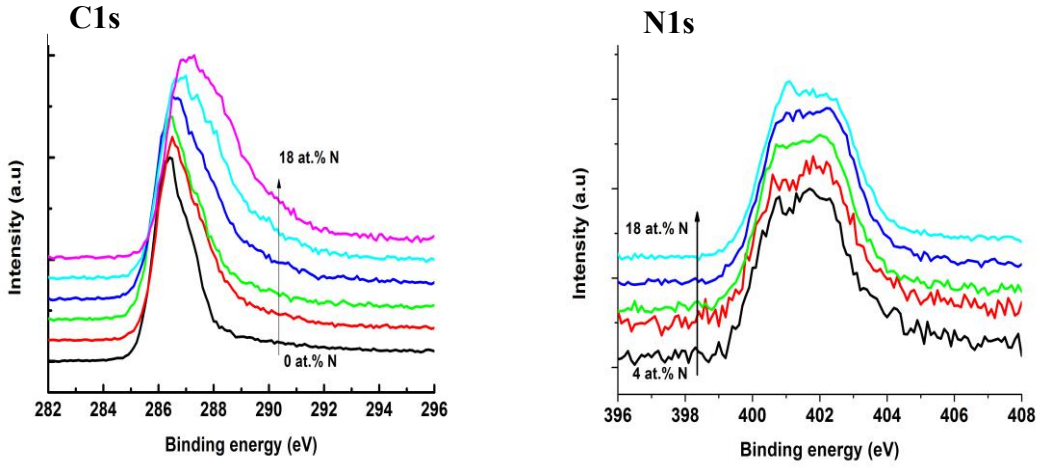

Figure 3. 4 C1s and N1s XPS signals, depending on the N content values from 0, 4, 10, 12 , 16 and 18 at.% .

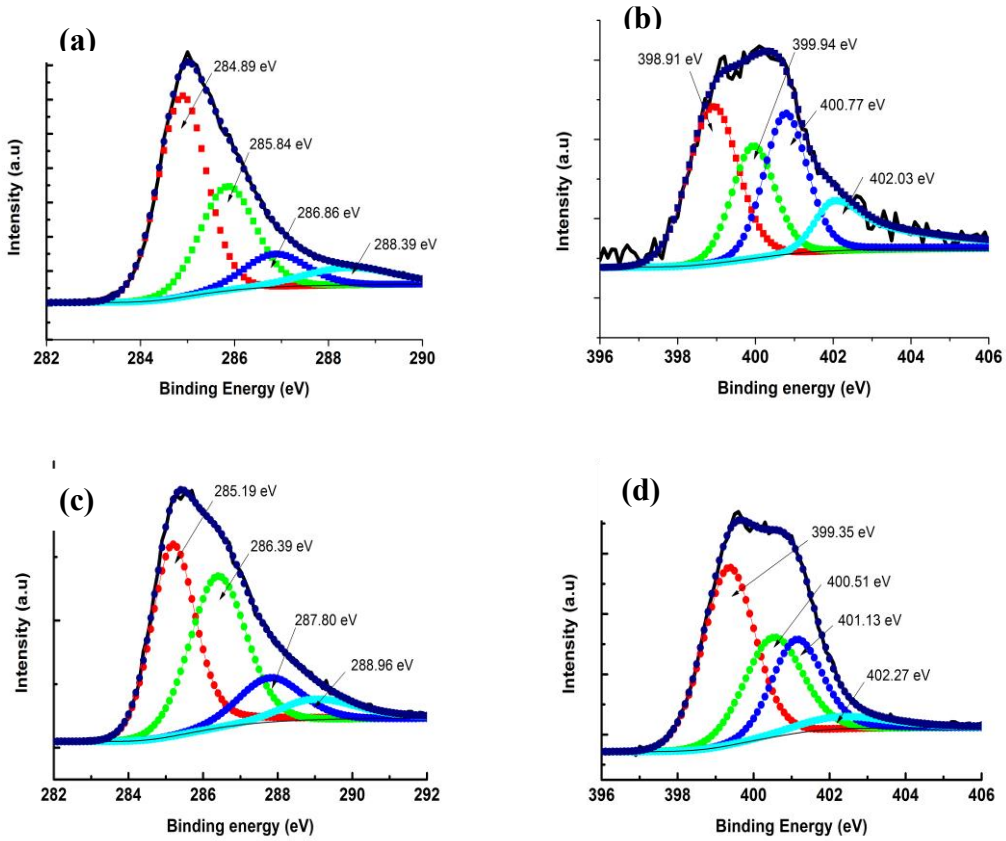

Figure 3. 5 Deconvolution of the C1s and N1s spectra of a-C:N films at different nitrogen concentrations, (a) and (b) at 4 % N film deposited at 0.5 Pa of P_{N2} pressure, (c) and (d) at 18 % N film deposited at 30 Pa of P_{N2} pressure.

From the Figures 3.4 and 3.5, one can clearly see that the peaks of our XPS spectra systematically shifted to higher binding energies with N content. The C1s spectra deposited at lower nitrogen partial pressure showed the Csp^2 contribution, by increasing the deposition pressure the Csp^2 contribution was shifted to sp^2 CN, and the intensity of the sp^2 CN contribution was increased with the increase of nitrogen partial pressure. This can be explained due to the increase in the nitrogen incorporation in films, which increases the intensity of the CN peak at the expense of the CC peak. In summary, it is worth emphasizing the following points from the XPS analysis. The C1s peak fitting revealed the formation of CN bonds at the expense of CC bonds as a function of the nitrogen partial pressure increase. The N1s peak fitting confirmed the existence

of different N bonding types, which is pyridinic, pyrrolic or quaternary type of N bonding types in a-C:N films.

b. Electron Energy Loss Spectroscopy (EELS)

The C-K edge and N-K edge of the EELS spectrum of the amorphous carbon nitride films deposited at nitrogen partial pressures at 1 Pa and 5 Pa is depicted at the Figure 3.6 in comparison with amorphous carbon films with their π* and σ* regions. The evolution of C-K edge binding energy with nitrogen partial pressure was shown in the Figure 3.7c. The main features are observed in the spectra was at 283.6-285.5 eV due to transitions from the orbital 1s to π* states and a broad band centered at 295 eV due to the 1s to σ* transitions. By incorporation of nitrogen into a-C films, the peak due to 1s to π* transition shifts from 283.6 eV in a-C to 284 eV in a-C:N with 10 at.%, and 285.5 eV in a-C:N with 15 at.% N content. At first, the transition was increased from 283.6 eV to 284 eV in a-C to a-C:N with 10 % of N, and then showed the increasing value from 284 eV to 285.5 eV by increasing the N in films from 10 to 15 %. The shift of 1s-π* transition to higher energy loses due to nitrogen incorporation in π bonds enhancement the π* resonance and this caused due to higher electronegativity of nitrogen (N: C – 3.0: 2.5) that decreases the electronic density around carbon atoms [9,24]. It is clear that the existence of π* and absence of plasmon losses at higher energy (295 eV) side are the characteristics of non-existence of tetrahedral bonded CN materials with Csp^3-N bonds. The above features strongly suggest the predominance of sp^2 hybridized C bonded to N exist in the present a-C:N films [9,21,22,25–27].

The N-K edge spectra of films are shown in the Figure 3.6. The N-K edge spectrum is similar to the C-K edge spectrum. The 1s-π* and 1s-σ* transitions are at 397.18 eV and 405.35 eV in a-C:N film with 10 % of N, and 398.53 eV and 407.03 eV in a-C:N film with 15 % of N content respectively. The transition 1s-π* and 1s-σ* are shifted to higher energy losses with higher N content in a-C:N films, which indicates that the N atoms in our film are mostly sp^2 hybridized in agreement with the conclusion from C-K edge. However, according to Rodil *et al*. the interpretation of N-K edge is more elusive since there are different bonding environments are associated with N [9,19]. The whole EELS analysis suggest that the formation of a majority amorphous CN phase is similar to amorphous carbon in which nitrogen has substituted carbon.

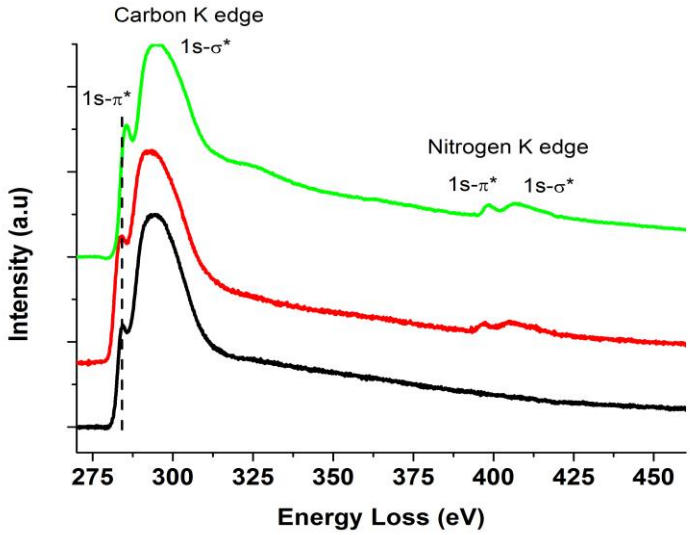

Figure 3. 6 EELS spectrum of carbon and nitrogen K edges of a-C and a-C:N films with different nitrogen content at 10 and 15 at.%

The EELS spectroscopy derived nitrogen content, Ep, C-K edge and π/σ ratio values of pure a-C and a-C:N films are shown in Figure 3.7. The Figure 3.7a shows the N content evaluation with nitrogen pressure. The nitrogen content values are 10 at.% for the film deposited at 1 Pa N_2 pressure and 15 at.% for film deposited at 5 Pa N_2 pressure. The increasing of nitrogen content was observed with the increase of deposition pressure; in agreement with XPS data. The Figure 3.7b shows the bulk plasmon peak (Ep) values with nitrogen partial pressure. The bulk plasmon values are located around 24 eV respectively. The Ep values shifts 1.6 eV with N incorporation into the films. The bulk plasmon peak shifts from pure graphite at 25.5 eV to 22.5 eV in amorphous carbon and to 24.4 eV in both the a-C:N films. The σ+π did not show any significant variation in all the films deposited at different nitrogen partial pressures. The σ+π peak shift from pure a-C to a-C:N, which indicates the increasing of ordered structures with increment of nitrogen content. The obtained values are far from the standard diamond Ep value is at 33.3 eV, which is confirming that the lower sp^3 hybridized carbon [21–23]. We observed that the Ep values are lower in a-C:N and in a-C films than the crystalline graphite films, which confirms that the structural order depends on the plasmon energy values in carbonaceous compounds. The a-C:N films with different nitrogen content did not show any structural ordering but structural changes are observed compared to a-C films. Also, from the Figure 3.7d, the increase of π/σ ratio in the

low loss region with the increase of the N content showed the existence of more ordered graphitic domains in a-C:N films with N incorporation. We observed structural changes by incorporation of nitrogen but there is no appreciable change with different content of N in films. We noticed that the nitrogen incorporation in a-C films have showed the structural changes in films.

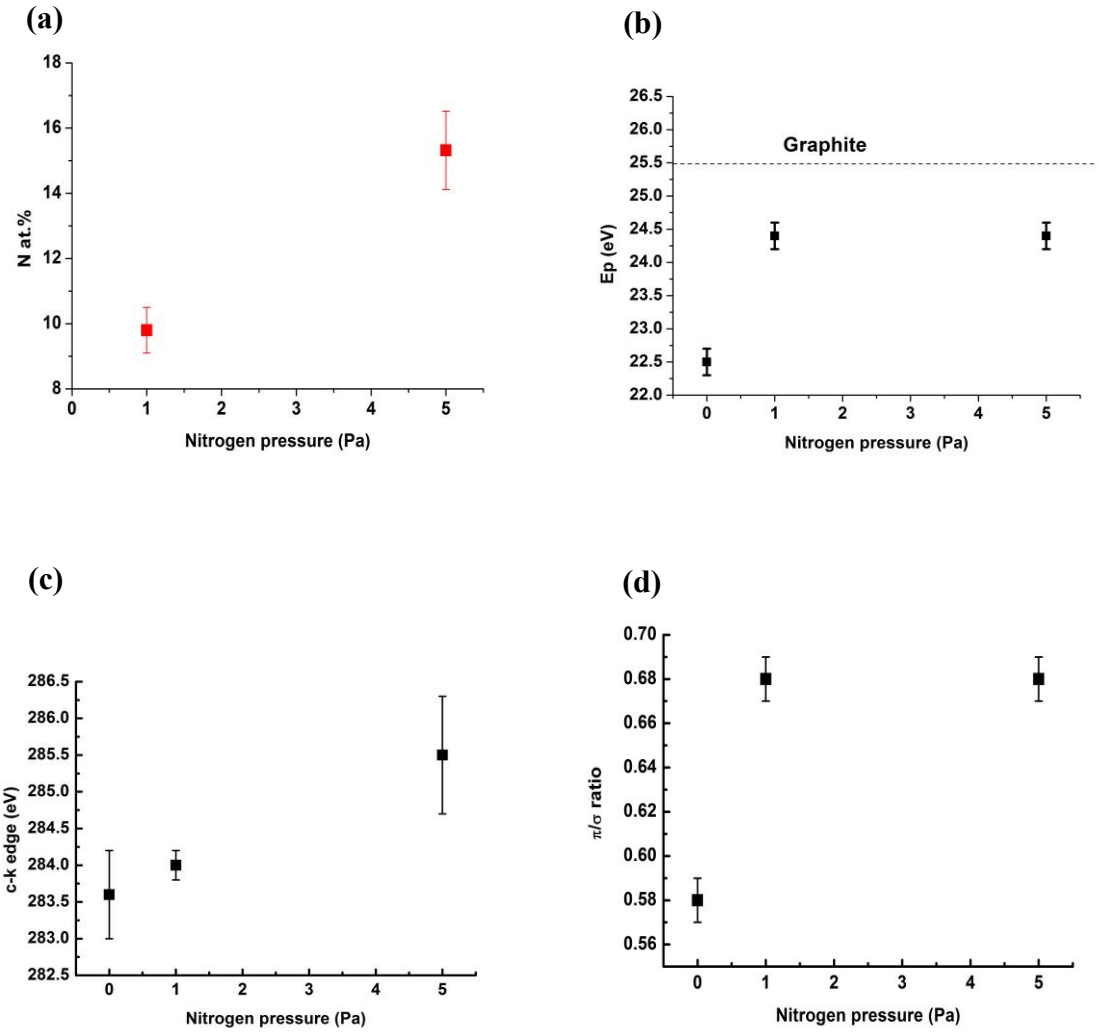

Figure 3. 7 (a) N content of a-C:N films deposited at 1 Pa and 5 Pa, (b) bulk plasmon losses with nitrogen partial pressure. (c) EELS C-K edge energy loss with nitrogen partial pressures in a-C:N films, (d) EELS π/σ ratio vs nitrogen partial pressure.

c. MW-Raman spectroscopy

The Figure 3.8 shows the Raman spectra as a function of nitrogen pressure. The Table 3.2 summarizes the fitting parameters of Raman spectra obtained at laser wavelength 325 nm

wavelength for films deposited at different nitrogen partial pressures. The spectra have been normalized to allow for the visualization of changes in the position and shape of the D and G band in Raman spectra of a-C and a-C:N films**.** It is clear that as a greater amount of nitrogen is incorporated into the films, the spectra become more asymmetric and a prominent D peak is observed at nitrogen content above 10 %. This is suggesting that the film have more sp^2 content. A band at 2225 cm^{-1} has been observed with UV excitation wavelength in a-C:N films having N content above 10 %, which is not available in films with less nitrogen content, while it is barely detectable at higher wavelengths. This band corresponds to terminal nitrogen triple bonded to carbon (C≡N), in agreement with literature [28]. This confirms that a minimum threshold of nitrogen is required to observe the C≡N band at 2225 cm^{-1}. The intensity ratio of I(CN)/I(G) available for a-C:N films with high N content, greater than 10 %. The Figure 3.9a shows the variation of I(D)/I(G) ratio as a function of N content at 325 nm excitation wavelength. The I(D)/I(G) ratio is used to give a qualitative assessment of the induced disorder in the sp^2 domains and is also related to the clustering of sp^2 phase. We can see that as the nitrogen content increases within the films the I(D)/I(G) ratio also increases until 16 % after that it decreases with the increase of N content above 16 %. The increase in the I(D)/I(G) ratio relates to an increase in the number and size of disordered sp^2 sites [28]. According to the relation proposed by Ferrari *et al*. correlation between I(D)/I(G) relates to correlation length L_a. The relation is valid for crystalline size smaller than 2 nm.

$$\frac{I(D)}{I(G)} = C_2(\lambda) L_a^2 \qquad (1)$$

$C_2(\lambda)$ is a constant which depends on the laser wavelength [29]. According to the above relation, we calculate the cluster size. From our calculation, the cluster size increased from 0.23 nm to 0.31 nm as the nitrogen content increased from 0 % to 16 %. However, when the correlation length is greater than 2 nm the I(D)/I(G) ratio decreases and the Tuinstra and Koening relationship is valid, according to this relation the I(D)/I(G) varies inversely proportional to the L_a [28,30,31].

$$\frac{I(D)}{I(G)} = \frac{C_2(\lambda)}{L_a} \qquad (2)$$

The above case is valid for a-C:N film deposited at 30 Pa P_{N2} partial pressure, which shows a decrease of I(D)/I(G) intensity ratio.

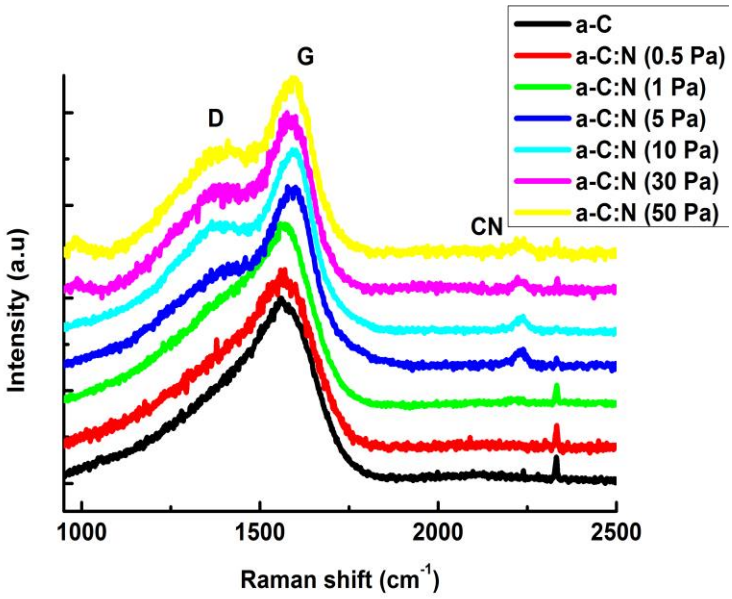

Figure 3. 8 Raman spectra at 325 nm excitation of films prepared at different nitrogen pressures (showed in inset).

The Figure 3.9a shows the variation in G position as a function of N content at 325 nm excitation wavelength. The G peak is shifted to higher value with the increase of N content, the increase in G position agrees with the previously reported data. The Figure 3.9b shows the variation of FWHM and dispersion of G positions as a function of N content. The increment in G position represents an increase in the sp^2 content. The dispersion of G band (disp(G)) is related to the topological disorder. The dispersion of G values increased until N content is at 16 %, further increasing in N content the dispersion values decreases to lower number. The lower disp(G) means ordering of the films structure.

N_2 pressure (Pa)	G position (cm^{-1})	D position (cm^{-1})	CN position (cm^{-1})	I(D)/I(G)	I(CN)/I(G)	FWHM(G) (cm^{-1})	Disp(G) (cm^{-1}/nm)	N at.% (XPS)
0 Pa /	1573	1386	-	0.32	-	208	0.23	0
0.5 Pa	1574	1385	-	0.40	-	198	0.15	4
1 Pa	1576	1391	-	0.44	-	167	0.18	10
5 Pa	1592	1371	2219	0.44	0.09	151	0.23	12
10 Pa	1593	1369	2232	0.51	0.11	137	0.19	16
30	1590	1373	2230	0.42	0.08	146	0.21	18
50 Pa	1591	1376	2230	0.47	0.1	144	-	17

Table 3. 2 Characteristics of Raman spectra at 325 nm of a-C and a-C:N films with different nitrogen pressure.

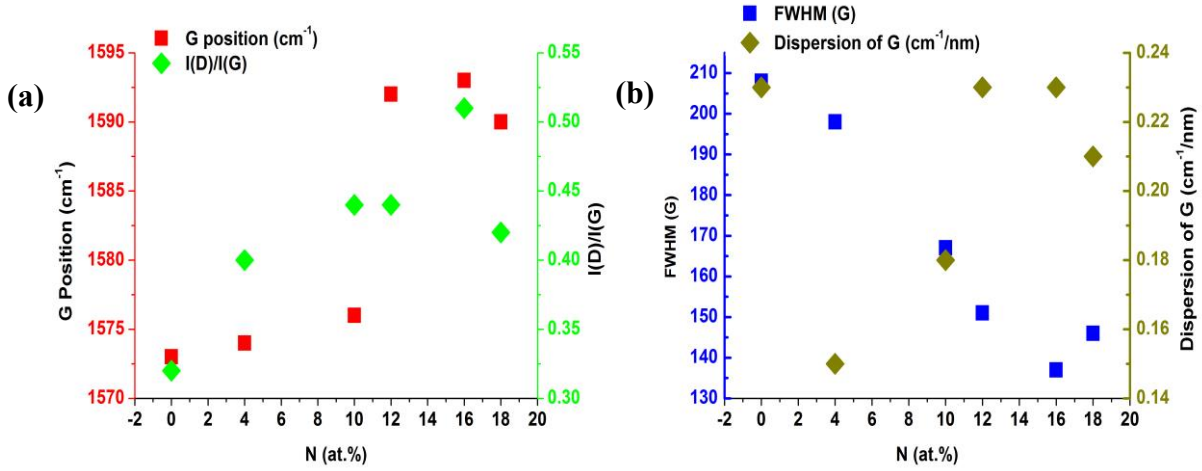

Figure 3. 9 (a) Variation of G position and I(D)/I(G) ratio, (b) G peak dispersion and FWHM (G) versus n content deduced from Raman measurements at 325 nm.

The Figure 3.9b shows the variation in FWHM position as a function of N content at 325 nm excitation wavelength. The width of G band is related to the structural disorder, which corresponds to the bond length and bond angle disorder at the Csp^2 sites. We observe a decrease of FWHM (G) when the nitrogen content increases, which is consistent with a substantial loss of bond length and bond angle distortions of the clusters when the nitrogen is high at 16 %, but FWHM (G) increases for a nitrogen content in films above 16 % of N. which is consistent with

previously observed results [32]. The clusters size decreases with nitrogen content higher than 16 %.

In conclusion, our results on nitrogen partial pressure effect on a-C:N films, the chemical bonding structure of the films was investigated by XPS, EELS and Raman spectroscopy. XPS studies of our films revealed that an increase of nitrogen content with increasing of nitrogen partial pressure from 4 to 18 % with nitrogen pressure 0.5 to 30 Pa, which also increases the CN sites at the expenses of CC bonded carbon sites as nitrogen content increased in films. The I(D)/I(G) ratio and G peak position increased as a function of nitrogen content whereas FWHM of G peak decreased. This is indicative of an increase either in the size or in number of sp^2 sites.

3.4.2 Effect of different DC bias voltage on a-C:N film properties

In this section, we study the effect of DC bias on structural and chemical composition of a-C:N films by Raman spectroscopy, XPS , EELS and HRTEM techniques.

a. X-ray Photoelectron Spectroscopy

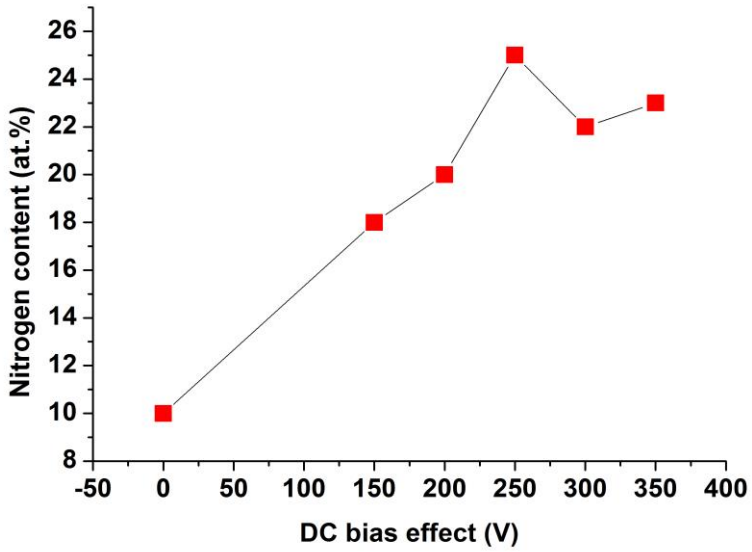

Figure 3. 10 Nitrogen content in a-C:N films vs negative substrate bias voltages.

The Figure 3.10 shows the nitrogen content within a-C:N films as the function of DC bias voltages. The N content was found to be 10-25 at.% for the films with the DC bias effect. The order of nitrogen content increases until a certain bias voltage, after what it starts decreasing. This confirms that certain values of bias are favorable to attain high content of nitrogen in a-C:N films. The Figure 3.11 shows the deconvolution of C1s and N1s spectra of films with different bias effects at 0V, -150V, -200V, -250V, -300V and -350V and at constant 5 Pa P_{N2} pressure. The binding energy values deduced from C1s and N1s deconvolution spectra are summarized in the Table 3.3. The pure a-C film binding energy values are at 284.92 eV, 285.89 eV and 287.16 eV assigned to Csp^2, Csp^3 and CO bonds respectively. The deconvoluted C1s and N1s spectra of a-C:N films deposited at different bias voltages are shown in the Figure 3.11, The C1s spectra deconvoluted with mixture of Gaussian and Lorentzian profiles with five components. The C1s binding energy values are in range at C1: 284.73-284.99 eV, C2: 285.24-285.82 eV, C3: 286.03-286.88 eV, C4: 287.03-287.71 eV and C5: 288.18-288.68 eV peaks are assigned to $CCsp^2$, $CCsp^3$, sp^2CN, sp^3CN and CO bonds respectively [[8,10,14,15,17–19,32]]. Higher nitrogen contents lead to the shifting of the binding energies, which is clearly evidenced from the above assignments and the Table 3.3 below. It has shown that by increasing the N content, the peaks located at low binding energy side disappear and the peaks are shifting to higher binding energy side, which means the C bonded to N increases with increasing of N content. The C1s spectra binding energy increases with bias until 250 V, and then it shows shifting to lower binding energy, which is consistent with nitrogen content.

The Figure 3.11 shows the deconvoluted N1s spectra with four peaks. The a-C:N films exhibits four N1s contributions in the range between N1: 398.63-398.91 eV, N2: 399.32-399.82 eV, N3: 400.36-400.70 eV, N4: 401.14-401.71 eV and N5: 402.09-402.44 eV respectively. There is a shift towards higher binding energies, which is observed until a certain bias voltage and further increasing in bias then it shifting to lower binding energy side. The chemical shift is related to different N-bonding environments. The peak N1 was assigned to N-sp^3C, N2 was assigned to pyridinic-N, N3 was assigned to pyrrolic-N, N4 was assigned to quaternary-N, and N5 was assigned to some NO respectively [[13,16,19,20]]. The N-sp^3C type bonding decreases as bias increases up to 250 V with increasing of N content, further increase in bias the N content showed a decreasing trend and the shifting of lower binding energy values are observed in films with

higher bias voltages. The high N content film showed the existence of sp^2 CN type bonding only. From the above analysis, one can conclude that the films are more graphite like structures as greater amounts of nitrogen incorporated into films with bias voltages are in range from 0 V to 250 V.

Film conditions (V)	C1 (eV)	C2 (eV)	C3 (eV)	C4 (eV)	C5 (eV)	N1 (eV)	N2 (eV)	N3 (eV)	N4 (eV)	N5 (eV)
0	284.97	285.75	286.43	287.59	-	398.91	399.74	400.68	401.52	-
-150	284.71	285.82	286.64	287.71	-	398.63	399.82	400.67	-	402.71
-200	284.99	285.88	286.36	-	288.18	-	399.32	400.36	401.14	402.09
-250	-	285.31	286.35	287.28	288.68	-	399.41	400.66	401.44	402.49
-300	-	285.24	286.03	287.03	288.40	-	399.50	400.70	401.58	402.36
-350	284.73	285.68	286.35	287.64	-	398.54	399.43	400.46	401.37	-

Table 3. 3 XPS C1s and N1s contributions in the a-C:N films deposited at different bias voltages and at 5 Pa constant pressure.

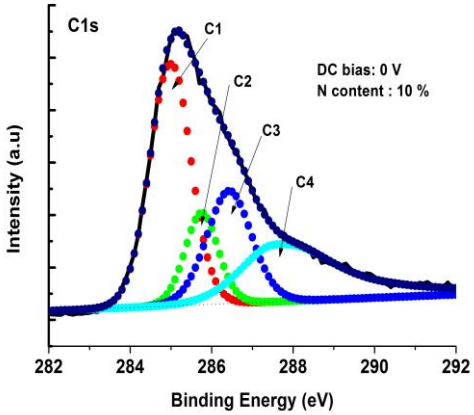

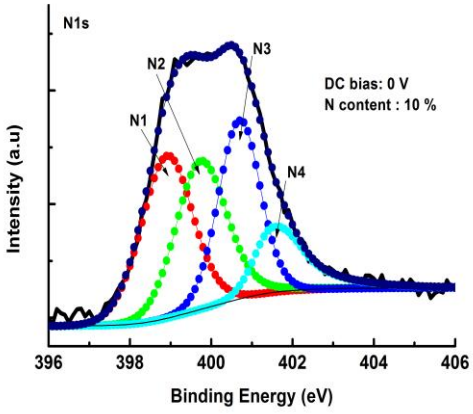

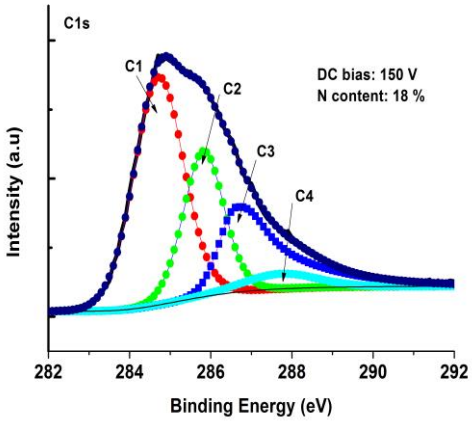
C1s
C1
C2
C3
C4
DC bias: 150 V
N content: 18 %
Intensity (a.u)
282
284
286
288
290
292
Binding Energy (eV)

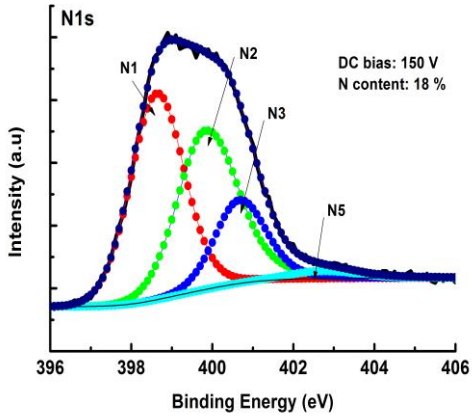
N1s
N1
N2
N3
N5
DC bias: 150 V
N content: 18 %
Intensity (a.u)
396
398
400
402
404
406
Binding Energy (eV)

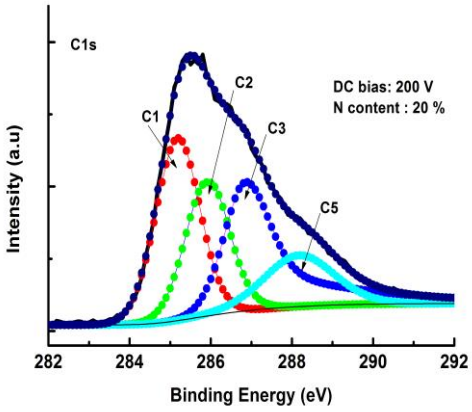
C1s
C1
C2
C3
C5
DC bias: 200 V
N content : 20 %
Intensity (a.u)
282
284
286
288
290
292
Binding Energy (eV)

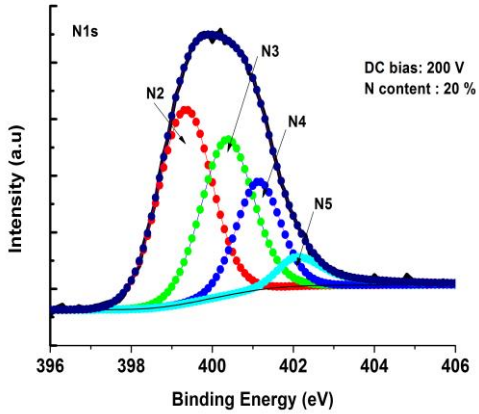
N1s
N2
N3
N4
N5
DC bias: 200 V
N content : 20 %
Intensity (a.u)
396
398
400
402
404
406
Binding Energy (eV)

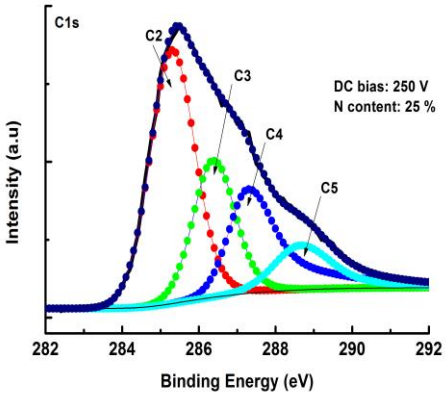
C1s
C2
C3
C4
C5
DC bias: 250 V
N content: 25 %
Intensity (a.u)
282
284
286
288
290
292
Binding Energy (eV)

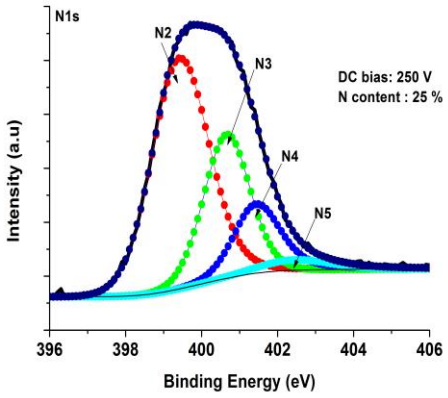
N1s
N2
N3
N4
N5
DC bias: 250 V
N content : 25 %
Intensity (a.u)
396
398
400
402
404
406
Binding Energy (eV)

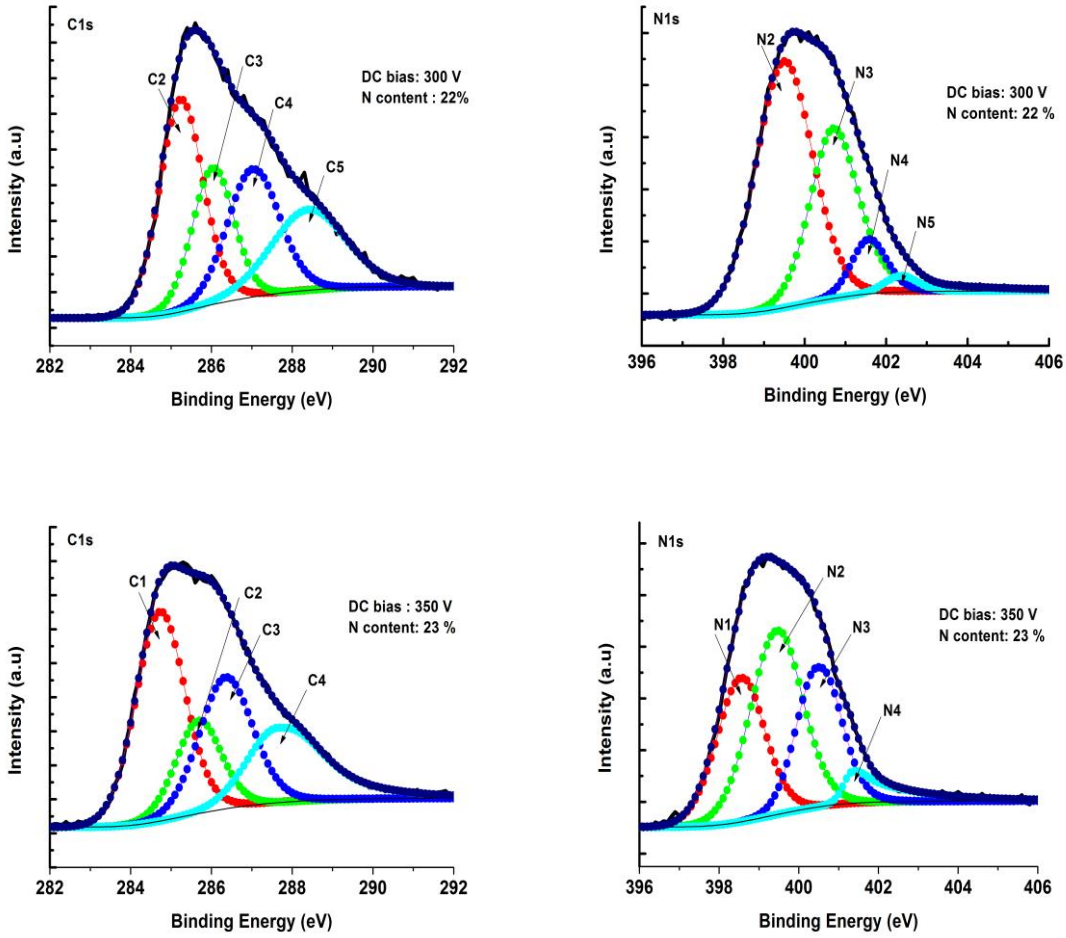

Figure 3. 11 Deconvolution of the C1s and N1s spectra of a-C:N films at different nitrogen concentrations deposited at different DC bias voltages (inset) and constant P_{N2} pressure of 5 Pa.

b. Electron energy loss spectroscopy (EELS)

The nitrogen contents of the a-C:N films obtained by EELS quantification are depicted in the Figure 3.12a as a function of the deposition conditions. The increment of the nitrogen partial pressure from 1 to 5 Pa led to a rise of the nitrogen incorporation, from 10 to 15 at.%. Maintaining the pressure at 5 Pa, the application of an additional DC bias to the samples produced another significant increase up to 19 (-150 V) and 21 at.% (-250 or -350 V) respectively. The π^*/σ^* ratios deduced from the intensity of the $1s \rightarrow \pi^*$ and $1s \rightarrow \sigma^*$ transitions in the C-K core-loss regions of the EELS spectra are depicted in the Figure 3.12b versus the nitrogen content. This parameter provides an immediate evaluation of the sp^2 character of a

specimen. The increase of the π^* features as the nitrogen incorporated in the film grows is clearly evidenced. This phenomenon has been already observed in CN_x films [33] and attributed mainly to the formation of additional C=N bonds (trigonal sp^2 hybridization) although C≡N bonding (diagonal sp^1 hybridization) cannot be ruled out at the highest nitrogen contents, as stated previously by Raman analysis. Moreover, above 7 at.%, N plays a more substitutional role whereby nitrogen and carbon tend to bond in a sp^2 configuration in an under-constrained C-N network, which is thermodynamically more stable [34]. The most intense feature within the low-loss part of the EELS spectra corresponds to collective excitations of valence electrons (plasmon peak) and may be correlated to the nature of the carbon bonds ($\pi+\sigma$) [21,22,26]. The plasmon energy is dependent upon the square root of the valence electron density and may be affected by crystal size effects. The Figure 3.12c shows the dependence of the bulk plasmon peaks (Ep) versus the deposition conditions. This represents a measure of the degree of the graphitic character. The incorporation of nitrogen in the films deposited at 0V supposed an increase from 22.6 to 24.4 eV. These values are smaller than the corresponding Ep for crystalline graphite (marked as a dashed line) at 25.5 eV due to the significant structural and bonding disorder in respect to the perfect crystal structure. Nevertheless, the increment of Ep for a-C:N versus a-C can be explained by the increase in the valence electron density provided by the incorporation of nitrogen atoms. The application of bias led a reduction of about 1 eV without significant differences between -150 and -350 V. This fact correlates well with the topological disorder induced by the ion bombardment during nitrogen plasma assistance. Our Ep values are far from the characteristic value of diamond, confirming the non-predominance of sp^3 hybridized carbons, as previously observed [35].

(a)

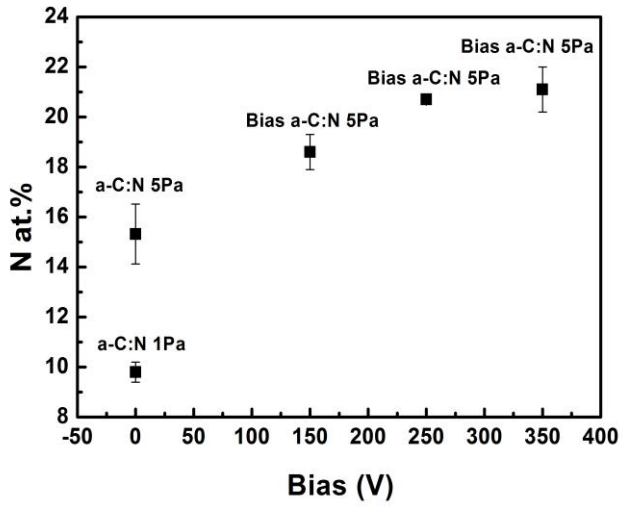
N at.%
Bias (V)
Bias a-C:N 5Pa
Bias a-C:N 5Pa
Bias a-C:N 5Pa
a-C:N 5Pa
a-C:N 1Pa
24
22
20
18
16
14
12
10
8
-50
0
50
100
150
200
250
300
350
400

(b)

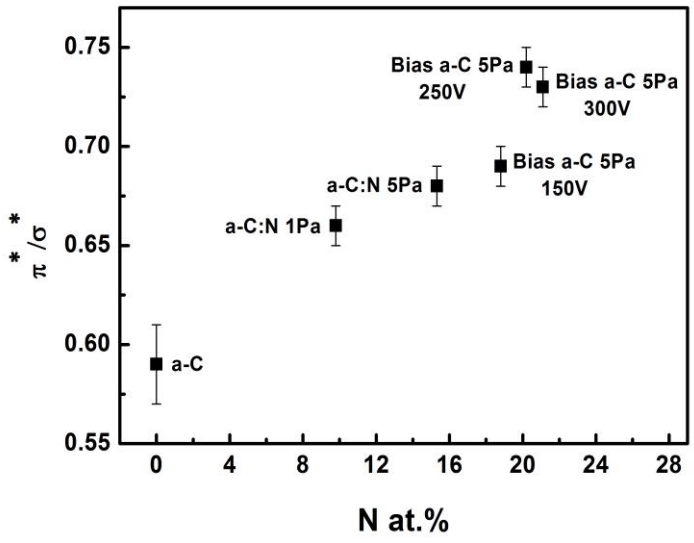
π* /σ*
N at.%
Bias a-C 5Pa
250V
Bias a-C 5Pa
300V
Bias a-C 5Pa
150V
a-C:N 5Pa
a-C:N 1Pa
a-C
0.75
0.70
0.65
0.60
0.55
0
4
8
12
16
20
24
28

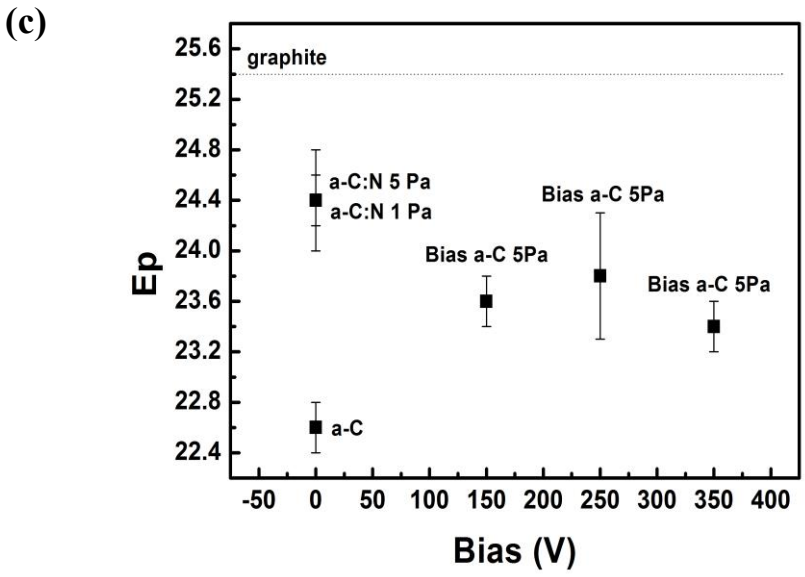

Figure 3. 12 EELS investigations of the a-C:N films: a) nitrogen content, b) π/σ ratio and c) plasmon value. The dashed line is the reference values related to crystalline graphite.

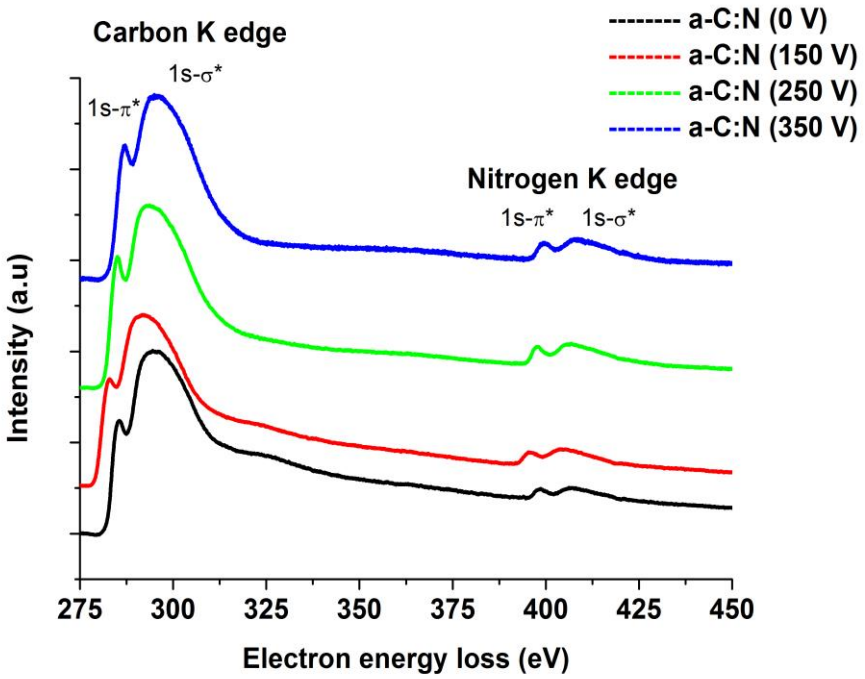

Figure 3. 13 EELS spectra of C-K edge and N-K edge of a-C:N films with different bias voltages.

The C-K edge and N-K edge of the EELS spectrum of the amorphous carbon nitride films deposited at different bias voltages were shown in the Figure 3.13. The main features are observed in the spectra at 283.7-286.8 eV due to transitions from the orbital 1s to π* states and a broad band centered at 295 eV due to the 1s to σ* transitions. By changing the nitrogen incorporation into the a-C:N films with the help of bias voltages from 0-350 V, the 1s-π* transition shifts from 285.5 ±0.8 eV in film with 0 V bias to 283.7±0.9 eV in with bias 150 V to 285±0.5 eV in with bias 250 V to 286.8±0.2 eV in with bias 350 V. The nitrogen content increased with the increase of bias voltages, which shows an increase of carbon K edge energy losses. The energy losses shift to lower values when bias increased from 0 V to 150 V, from 285.5 eV to 283.7 eV, and further increasing of bias to higher values showed the energy losses shifts to higher values from 283.7 eV to 286.8 eV. The shift of 1s-π* transition to higher energy loses due to nitrogen incorporation in π bonds enhancement the π* resonance and this caused due to higher electronegativity of nitrogen that decreases the electronic density around carbon atoms [9,24]. It is clear that the existence of π* and the absence of plasmon losses at higher energy (295 eV) side are the characteristics of non-existence of tetrahedral bonded CN materials with Csp^3-N bonds. The above features strongly suggest the predominance of sp^2 hybridized C bonded to N exist in the present a-C:N films [9,21,22,25–27]. The N-K edge spectra of films are shown in the Figure 3.13. The N-K edge spectrum is similar to the C-k edge spectrum. The 1s-π* and 1s-σ* transitions are at 398.73 eV and 407.23 eV at 0V, 395.90 eV and 404.67 eV at 150 V, 397.78 eV and 406.25 eV at 250 V, and 399.67 eV and 408.44 eV at 350 V. The energy losses are shifts to higher with the increase of bias from 0 V to 350 V. The transition 1s-π* and 1s-σ* are shifts to higher energy losses with higher N content in a-C:N films with increasing of bias voltage, which indicates that the N atoms in our film are mostly sp^2 hybridized in agreement with the conclusion from C-K edge. However, according to Rodil *et al*. the interpretation of N-K edge is more elusive since there are different binding environments associated with N [9,19]. The whole EELS analysis suggest that the formation of a majority amorphous CN phase is similar to amorphous carbon in which nitrogen has substituted carbon.

c. High Resolution Transmission Electron Microscopy (HRTEM)

The high-resolution structure deduced from HRTEM images of the films deposited at 5 Pa of N_2 at negative bias of 0, -150, -250 and -350 V is illustrated in the Figure 3.14. The pictures

confirmed a highly disordered carbon structure for all the conditions. Similar kind of structures were observed by previous articles on a-C:N films [36,37]. EELS analysis, however, pointed out an enhanced disorder when bias was applied by downshifting the energy of the plasmon but no differences could be observed from the micrographs.

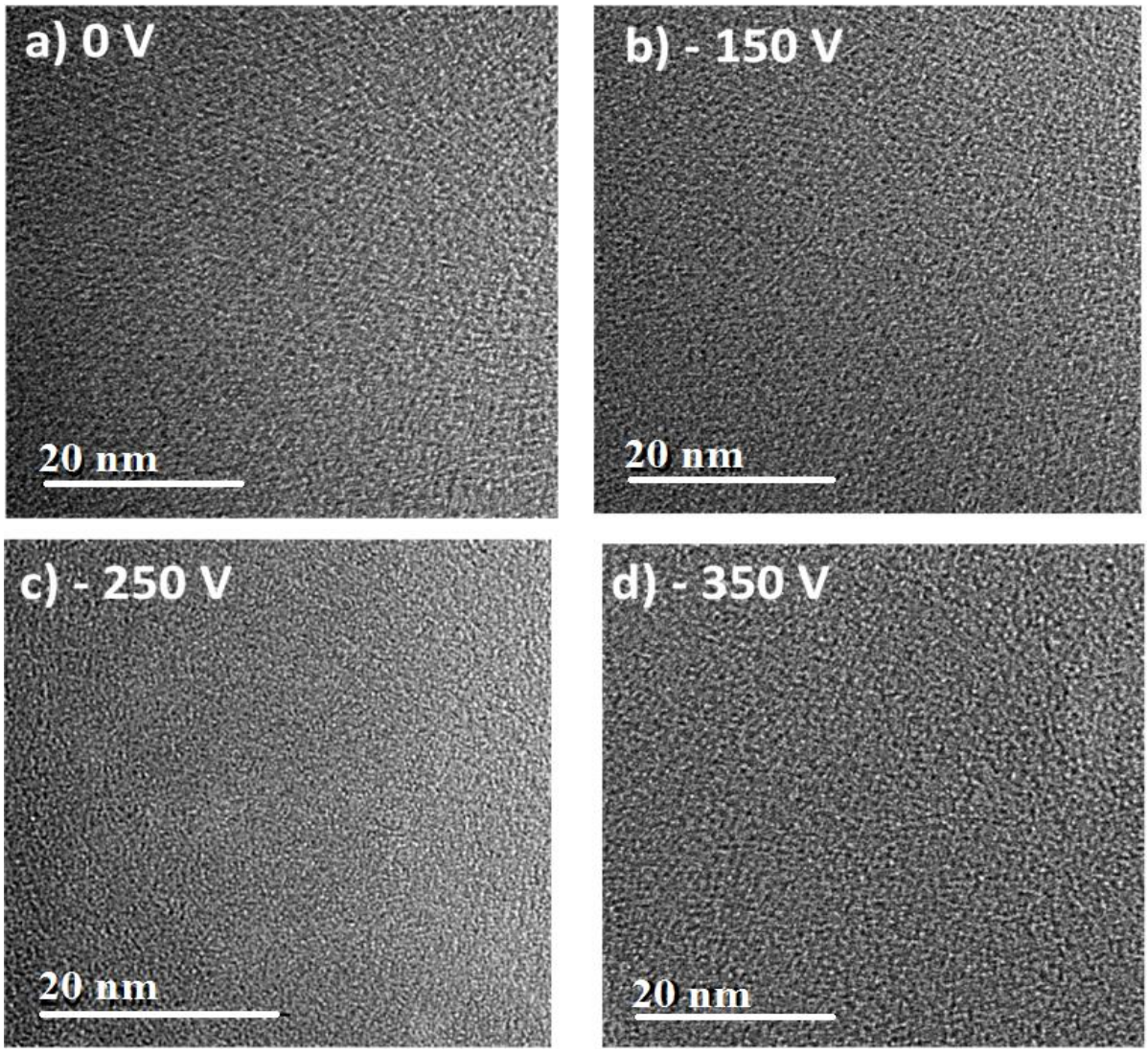

Figure 3. 14 HRTEM of the a-C:N and bias a-C:N films deposited with a N_2 pressure of 5 Pa, at various DC bias (shown inset).

d. Raman spectroscopy

The Figure 3.15 shows the comparison of Raman spectra of a-C:N films deposited at constant nitrogen pressure 5 Pa and different DC bias voltages with an Raman excitation wavelength 325

nm. The Table 3.4 summarizes the fitting parameters of Raman spectra at 325 nm wavelength of all the films deposited at different DC biases and constant nitrogen pressure was at 5 Pa. The Figure 3.15 shows the D peak position is prominent in films with DC bias voltages increases from 0 V to -350 V indicating higher sp^2 content films. The Raman spectra were fitted with three peaks with combination of BWF and Lorentzian functions. The Raman parameters are obtained from the fitting of Raman spectra at 325 nm excitation wavelength that are shown in the Figure 3.16 below. It clearly shows the evaluation of I(D)/I(G) ratio and FWHM of G with bias assistance. The N content in film up to 25 % the I(D)/I(G) ratio increases and FWHM of G decreases, and I(D)/I(G) and FWHM of G showed the reverse trend when N content decreases in films, which is shown in the Figure 3.16 and the Table 3.4. Other than D and G bands, a third band at 2220 cm^{-1} has been observed for all the films at 325 nm wavelength. This band corresponds to a terminal nitrogen triple bonded to carbon (C≡N) [28]. We deduced the intensity of I(CN)/I(G) for all the films at 325 nm. The I(CN)/I(G) ratio decreases with bias voltages increases.

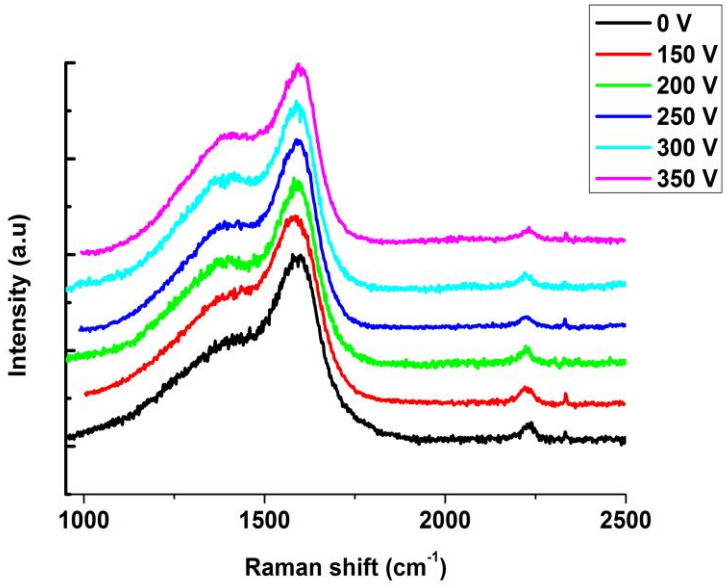

Figure 3. 15 Comparison of Raman spectra of a-C:N films deposited at different bias voltages and 5 Pa N_2 pressure at Raman wavelength 325 nm, bias voltages are shown in inset.

Bias (V)	G position (cm^{-1})	D position (cm^{-1})	CN position (cm^{-1})	I(D)/I(G)	I(CN)/I[G]	FWHM(G) (cm^{-1})	Disp(G) (cm^{-1}/nm)	N at.% (XPS)
0 V	1592	1371	2219	0.44	0.09	151	0.23	10±2
150 V	1586	1384	2222	0.46	0.1	148	0.19	18
200 V	1591	1379	2223	0.43	0.07	128	-	10
250 V	1597	1391	2230	0.47	0.058	131	0.17	25
300 V	1595	1393	2222	0.48	0.06	124	-	22
350 V	1590	1378	2222	0.43	0.052	145	0.15	23

Table 3. 4 Characteristics of Raman spectra related to different bias voltages and at constant pressure at 5 Pa.

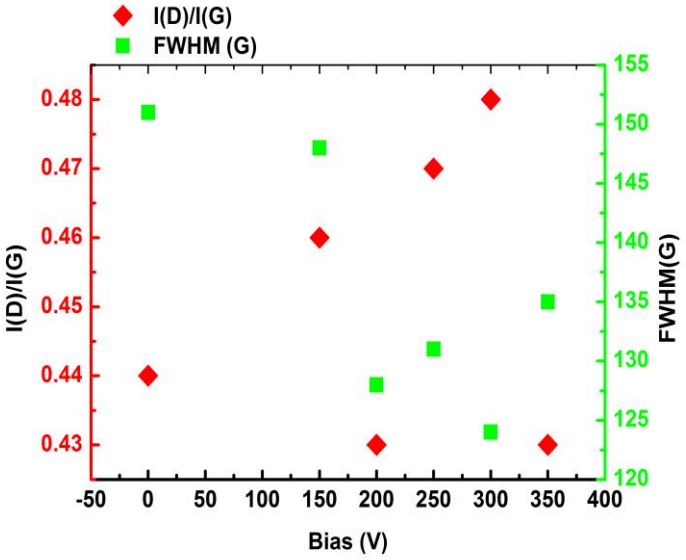

Figure 3. 16 Variation of I(D)/I(G) and FWHM versus bias effect deduced from Raman spectra at 325 nm.

The Figure 3.16 shows the evolution of Raman parameters with bias voltages. The increase of I(D)/I(G) ratio and the decrease of FWHM of G of the bias assisted films indicates the increase of the sp^2 content [32]. The decreasing trend of I(D)/I(G) ratio and the increase of the FWHM of G at the higher biases are mainly attributed to the larger cluster size [32]. In the present study, the I(D)/I(G) ratio increases with the increase of N content in films when the bias voltages increase

up to 0 - 250 V. When the bias voltages increase from 250 V - 350 V, the N content decreases, which is attributed to the decrease of I(D)/I(G) ratio and G line width. The increase trend of I(D)/I(G) ratio relates to an increase in the number and size of graphitic clusters [19,28,32]. The correlation length L_a is calculated according to the relation proposed by Ferrari *et al*. According to the Eq 1, we estimated a correlation length L_a of films, and the L_a values showed a decreasing trend with the increase bias voltages. The L_a values increased from 0.3 nm to 0.4 nm as nitrogen content increases. The Eq 1 is valid for crystalline sizes smaller than 2 nm. However, when the crystalline sizes are greater than 2 nm, the I(D)/I(G) ratio decreases. The Eq.2 is valid when the ratio of peak intensity varies inversely with L_a. The film deposited at -350 V bias showed the decrease of intensity ratio, so we calculated the correlation length La by using Eq.2. According to that relation, the L_a value is about 6.02 nm. This is attributed to increase of crystalline size. The G peak position did not have a well-defined trend with increase of bias assistance. From The Figure 3.16 and the Table 3.4, it was clearly evidenced that the FWHM of G band decreasing with the increase of N content. The FWHM of G relates with N content in films, which is increased with the increase of N content. The dispersion of G band decreasing with increasing of N content in films from 0.23 to 0.15 cm^{-1}/nm. The lowering of dispersion of G relates to the ordering of the film structure.

3.4.3 Plasma assistance deposition effect on a-C:N films

In this section, we studied the use of plasma assistance deposited a-C:N films and investigate its chemical bonding states and micro structures by XPS, EELS and Multi-wavelength (MW) Raman spectroscopy, respectively.

a. X- ray Photoelectron Spectroscopy (XPS)

XPS investigations allow the estimation of the chemical composition, including the carbon and nitrogen chemical environments at the topmost surface. The N content is found to be 14 for the a-C:N film deposited at 10 Pa of P_{N2} pressure and without DC bias assistance and 28 at.% for the biased a-C:N film deposited at 5 Pa P_{N2} pressure and 250 V DC bias, respectively. The range of N content values was obtained for the films deposited by without bias assistance and with bias assistance will detail in next sections. The N/C ratio of this deposited film is much higher than

previously reported values obtained with nanosecond pulsed laser deposition with bias assistance [38]. Oxygen ranges between 8 and 12 at.% mainly due to adventitious surface contamination. The deconvoluted C1s and N1s spectra of pure a-C, a-C:N (10 Pa and 0 V) and biased a-C:N (5 Pa and 250 V) films are shown in Figure 3.17 The binding energy values deduced from the C1s and N1s deconvolution spectra are summarize in Table 3.5. The spectra depicted in Figure 3.17 and Table 3.5 is present the typical deconvolution process used for the a-C, a-C:N (10 Pa) and biased a-C:N (5 Pa and 250 V) films and results depending on other deposition conditions are presented in next sections. The pure a-C film shown in the Figure 3.17a exhibits two C1s components: C1 at 284.2 eV and C2 at 285.1 eV. A small shoulder at higher binding energy may be attributed to CO bonds due to adventitious surface contamination. Its low intensity does not allow proposing any significant fit to this contribution. The C1s and N1s spectra related to the a-C:N film (deposited at P_{N2} =10 Pa without any plasma assistance) are shown in Figures 3.17b and 3.17d respectively. Two C1s components, at 284.3 and 285.3 eV, correlate well the C1 and C2 contributions found in pure a-C film. The intensity ratio of C1/C2 is significantly lower in the a-C:N compared to the pure a-C film. Additionally a C3 component centered at 287.3 eV may be attributed to CN bonds, due to the high electronegativity of nitrogen atoms. This contribution was may be attributed to CO bonds, but its intensity is significantly higher when nitrogen is introduced into the film, compared to the pure a-C film. Even if the CO contribution exists, it remains weak and weakly overlaps the CC and CN contributions. Therefore, it is ignored in the following discussion. The biased a-C:N film, deposited using DC plasma at P_{N2}= 5 Pa and a DC voltage of 250 V, exhibits C1s and N1s signal depicted in Figures 3.17c and 3.17e respectively. The introduction of a bias, consistent with nitrogen plasma assistance during the deposition, leads to subsequent decrease of the C1/C2 intensity ratio, along with a significant shift of 1 eV of the C1, C2 and C3 contributions. In addition, it is observed that the intensity of C3 strongly increases compared to the conventional a-C:N film. This is in favor to the attribution of the C3 component to CN bonds. The DC plasma assistance is clearly responsible for a multiplication by a factor two of the nitrogen content at a lower P_{N2} (5 Pa) compared to the film deposited in N_2 atmosphere with no DC assistance at higher P_{N2} (10 Pa).

The nitrogen containing films exhibit three N1s contributions labeled N1, N2 and N3. The binding energy values for the different films are very similar, independently of the use or not of

the plasma assistance, even if a small chemical shift of about 0.2-0.5 eV towards higher binding energies is observed with the DC plasma assistance. It is worth mentioning that the chemical shift related to different N-bonding environments is soundly lower than the chemical shift related to the C1s for the two-nitrogenated films. N1 is centered at 398.2 – 398.7 eV, N2 is centered at 399.9 – 400.2 eV and N3 is centered at 402.6 – 401.7 eV. With plasma assistance, the N1/N2 ratio significantly decreases, whereas the N3 intensity slightly increases.

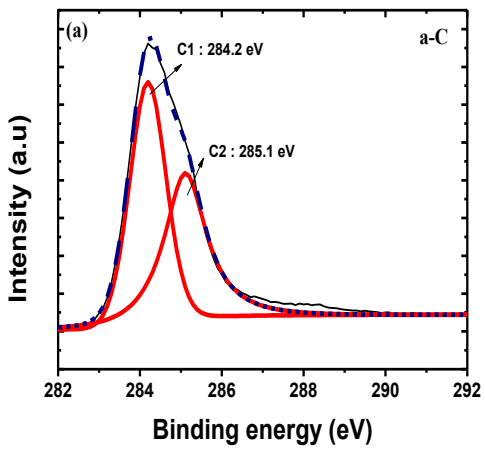

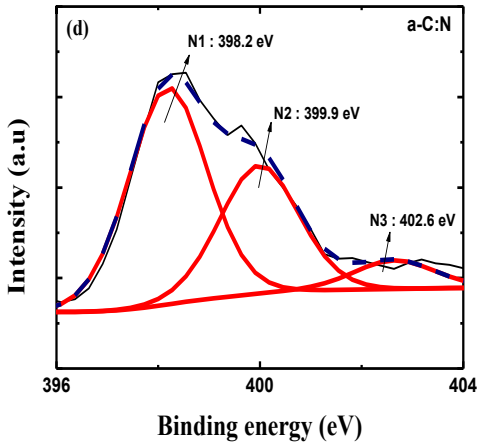

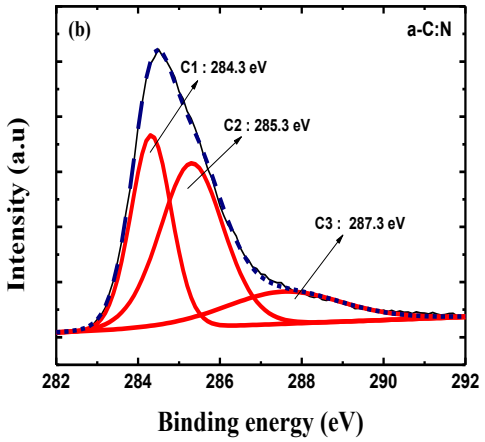

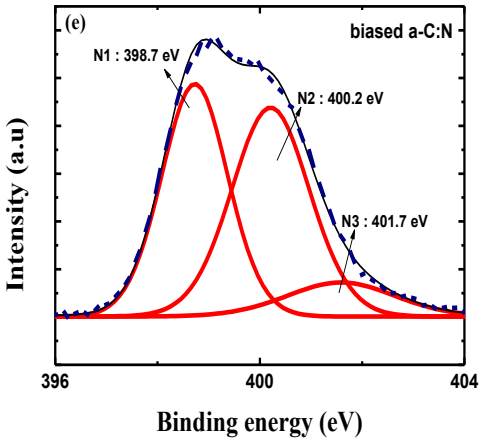

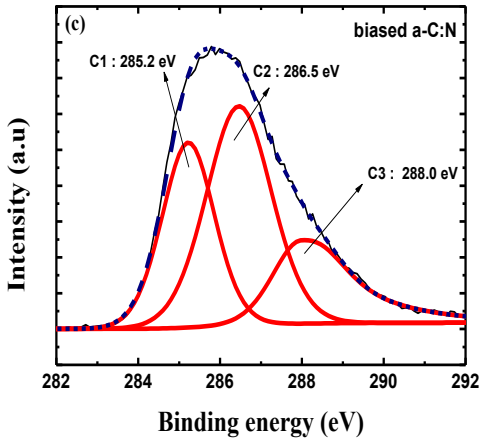

Figure 3. 17 XPS deconvoluted C1s spectra of (a) a-C (b) a-C:N film deposited at 10 Pa (c) biased a-C:N film deposited 5 Pa and 250 V bias, and N1s spectra of (d) a-C:N deposited at 10 pa, (e) biased a-C:N film deposited at 5 pa and 250 V bias.

	$P(N_2)$ (Pa)	DC voltage (V)	C1 (eV)	C2 (eV)	C3 (eV)	N1 (eV)	N2 (eV)	N3 (eV)	N/C Ratio	N (XPS) (at.%)
a-C	-	-	284.2	285.1	-	-	-	-	-	0
a-C:N	10	-	284.3	285.3	287.3	398.2	399.9	402.6	0.16	14
biased a-C:N	5	250	285.2	286.5	288.0	398.7	400.2	401.7	0.38	28

Table 3. 5 XPS C1s and N1s contributions in the a-C, a-C:N (10 Pa) and biased a-C:N (5 pa and 250 V) films and N/C ratio and N at.% deduced from XPS.

Since the sp^3, sp^2 and sp^1 hybridizations can exist for both C and N atoms, at least nine different bonding configurations can exist in carbon nitride films. Unambiguous interpretation of XPS is not possible by considering the literature data. Rodil *et al.* [19] have published a sound compilation of XPS data related to various CN films. The Figure 3.18 shows their conclusions on which our results have been superimposed.

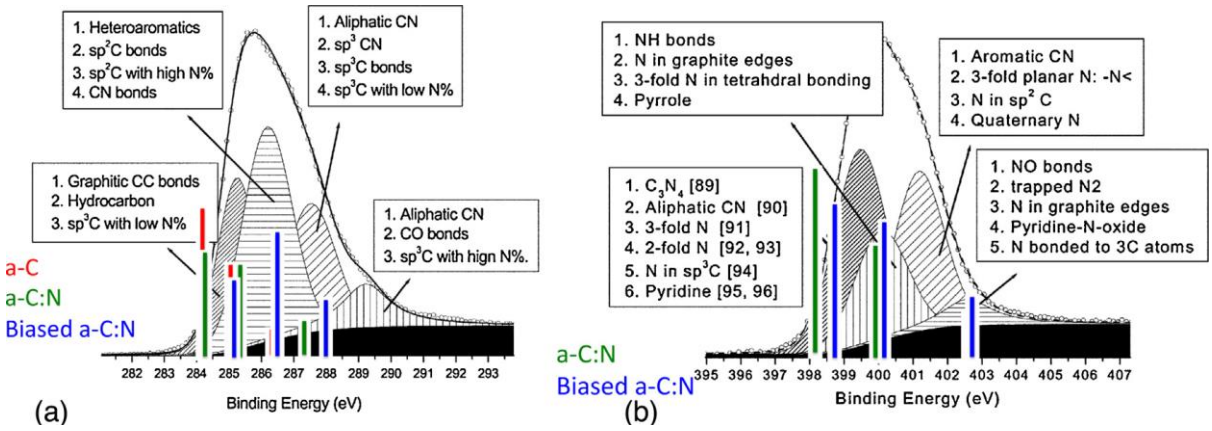

Figure 3. 18 Chemical shifts of the C1s (a) and N1s (b) XPS spectra of a-C, a-C:N (10 Pa) and biased a-C:N (5 pa and 250 V) films superimposed on the compilation of Rodil *et al.*[[19]].

From the Figure 3.18, one can observe that the peaks of our XPS spectra are slightly but systematically shifted to lower binding energies, compared to the compilation of data from literature. This may be due to differences in energy calibration and charge shifts from one experimental configuration to another one. Such a shift does not prevent to go further in the discussion, since the acquisition has been performed in similar experimental conditions for all films. The a-C and a-C:N (14 at.%) have rather similar C1s contributions. According to the compilation published by Rodil *et al.*[[19]], the C1 peak may be affected mainly to carbon-carbon bonds (mainly Csp^2), but also to some Csp^3 bonds with low N concentration for the a-C:N film. Indeed it is known that our pure a-C films deposited by femtosecond PLD have Csp^2 content in the 60-70% range, compared to a-C films deposited by nanosecond PLD with a Csp^2 content in the 15-25% range [[39]]. The C2 contribution may be assigned to CN bonds in various possible configurations, including heteroaromatic rings containing N atoms for the a-C:N film. However, this C2 contribution is observed also in the pure a-C film, which is attributed by some authors to Csp^3 bonds. A chemical shift of less than 1 eV between two XPS peaks with a rather complex chemistry as for carbon is controversial. This indicates that a conventional attribution of the lowest energy contribution C1 only to CC bonds, and the higher energy contribution C2 only to CN bonds, in spite of a higher N electronegativity compared to C, cannot fully explain the results. However the C1/C2 intensity ratio decreases when nitrogen is introduced, which is consistent with some possible assignations mentioned above: CN bonds can definitely explain part of the C2 contribution of the a-C:N film. The C3 peak may correspond to Csp^3 bonds in both films,

including with low amounts of nitrogen, as well as aliphatic CN bonds. The three C1s contributions of the biased a-C:N film (28 at.%) are significantly shifted towards higher binding energies. The C1 may correspond to carbon aromatic bonds, whereas the C2 should correspond to Csp^2 bonded to nitrogen. The increase of the C2 component is consistent with the increase of the nitrogen content up to 28 at.% due to plasma assistance. The C3 contribution can relate to Csp^3 bonds as well as aliphatic CN (including Csp^3-N bonds) or even CO bonds. Compared to the a-C film, the C2 and C3 contributions progressively increase from the a-C:N to the biased a-C:N films, consistent with their assignment to various types of CN bonds. The three nitrogen contributions N1, N2 and N3 are very similar for both nitrogenated films, with a decrease of N1 at the expense of N2 when DC plasma assistance is used. The interpretations compiled by Rodil *et al*. [19] indicate a sound difficulty to assess unambiguously the three nitrogen contributions. Schematically, the lowest N contribution was may be attributed to Nsp^3-C bonds, whereas higher binding energies may be assigned rather to Nsp^2-C bonds. Such interpretations are consistent with a global increase of the aromatic character of our films when the nitrogen concentration is increased by bias assistance, with nitrogen predominantly incorporated inside aromatic carbon rings. Due to an important controversy related to the interpretations of XPS data of CN films in the literature, one concludes that XPS alone is not sufficient to elucidate exactly the bonding states and their dependence versus the N content. The EELS spectra allow going further by probing the whole film thickness.

b. Electron Energy Loss Spectroscopy (EELS)

The EELS spectra of low and core-loss regions of pure a-C, a-C:N film at 10 Pa P_{N2} pressure and biased a-C:N film at 5 Pa P_{N2} pressure and 250 V DC bias assistance deposited films are shown in the Figure 3.19. The low-loss part of the EELS spectra corresponds to collective excitations of valence electrons and may be correlated to the nature of the carbon bonds [21,22,26]. The Figure 3.19a shows the π-plasmon and the bulk plasmon peaks (Ep) located around 5.4 and 23 eV respectively. While the π-π* transition is almost invariable, the E_p value shifts about 1 eV when including N in the film composition. The E_p is known to vary from 33.3 eV for diamond, down to 25.5 eV for crystalline graphite and much lower for amorphous a-C with a predominance of sp^2 hybridization [39]. In the present study, the positions of the bulk plasmon peak shifts from 22.5 eV in pure a-C to 23.6 eV in both a-C:N or biased a-C:N samples, indicating an increased

ordering of the amorphous Csp^2-bonded structures with the increment of the nitrogen content. These values are far from the characteristic value of diamond, confirming the non-predominance of sp^3 hybridized carbons [21,26,35]. We also observe that the values are lower than those published for crystalline graphite. This is consistent with a strong dependence of the plasmon energy values with the structural order in carbonaceous compounds. Also from the Figure 3.19a, the increase in intensity of the π-plasmon peak in the low-loss energy region with increasing the N content is consistent with more-ordered sp^2 graphitic domains.

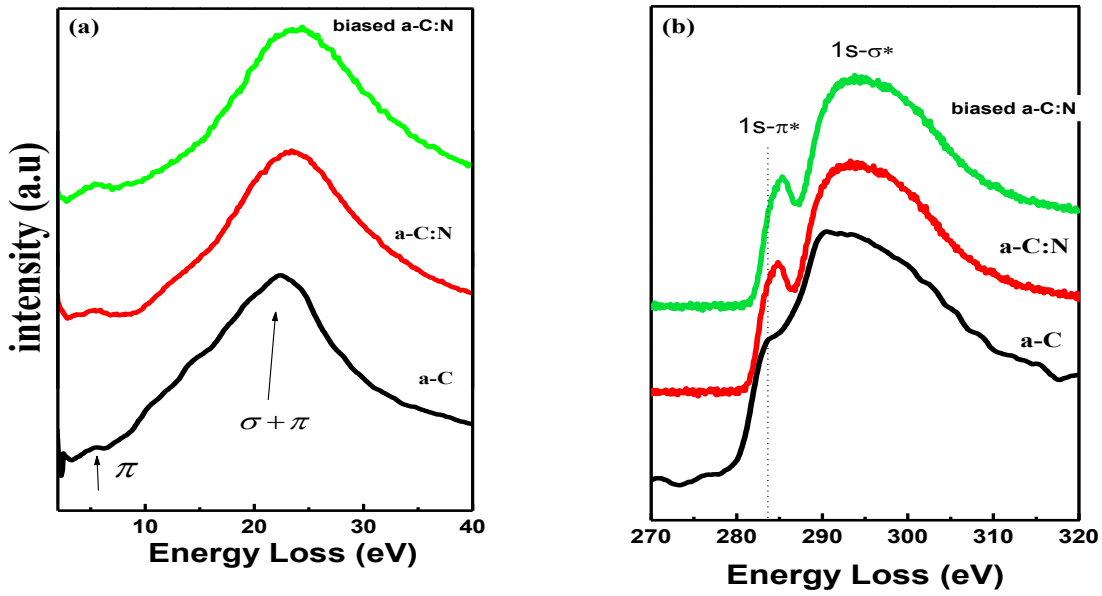

Figure 3. 19 EELS spectra of the a-C, a-C:N (deposited at 10 Pa) and biased a-C:N (deposited at 5 pa and 250 V) films: (a) low loss spectra, (b) C-K edge spectra.

The C-K edge of the EELS spectra along with their π* and σ* regions of a-C, a-C:N and biased a-C:N films are shown in the Figure 3.19b. By increasing the N content, the peak due to C1s→π* transition is more defined and shifts from 283.6 eV in a-C to 284.7 eV in a-C:N, and 285.3 eV in biased a-C:N. The corresponding N contents deduced by EELS are 0, 17 and 24 at.%, respectively, in agreement with the XPS data reported in the Table 3.5. This shift is attributed to a decrease of the electron density around carbon atoms originated by the higher electronegativity of nitrogen [40]. In general, π* peaks are not observed in tetrahedral bonded CN materials whose Csp^3-N bonds are denoted by the existence of small peaks at energy losses higher than 295 eV

[40,41]. The π* peak and the absence of peaks above 295 eV in the present CN films strongly suggest the predominance of sp^2 hybridized C bonded to N [26,33,35,40,41], whereas no direct evidence of a Csp^2 increase due to the incorporation of nitrogen can be demonstrated by EELS investigations. The N-K edge spectra (not shown) are consistent with the 1s→π* and 1s→σ* transitions at 397.7 and 407.0 eV, respectively. According to the Rodil *et al*. [19], the interpretation of the N-K edge would be difficult due to the different configurations associated with N [19].

c. Microstructure characterization of a-C:N films: Multi-wavelength Raman spectroscopy

The Figure 3.20 a-c show the MW-RAMAN analysis excited at four different wavelengths (325, 442, 488, 633 nm), for the a-C, a-C:N film deposited at 10 Pa P_{N2} pressure and biased a-C:N film deposited at 5 Pa P_{N2} pressure and 250 V DC bias assistance deposited films respectively. The Figure 3.20d superimposes the spectra of the three films with an irradiation at 325 nm. The Table 3.6 summarizes the fitting parameters of all Raman spectra obtained at the four laser wavelengths for the three films. The D and G bands are characteristic of amorphous carbon based films and their positions are not clearly affected by the nitrogen content in the film, in agreement with [42]. In all the films, an increase of the G band position is observed with a decrease of the laser wavelength.

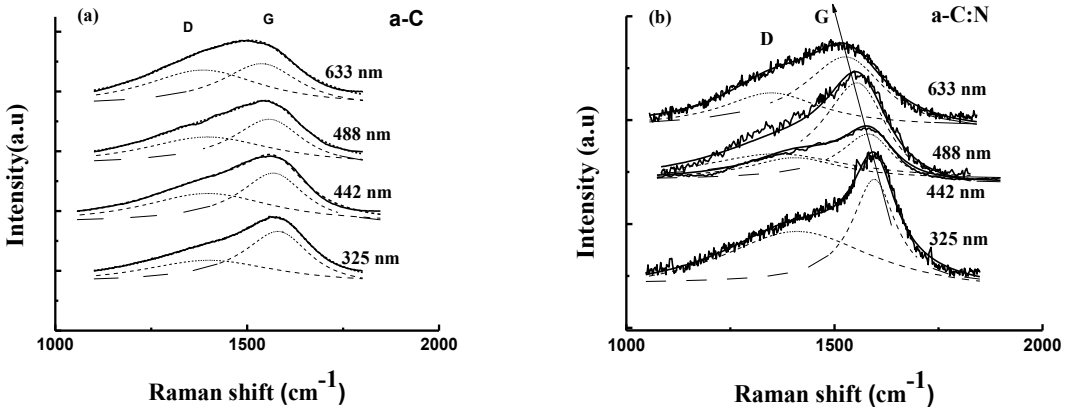

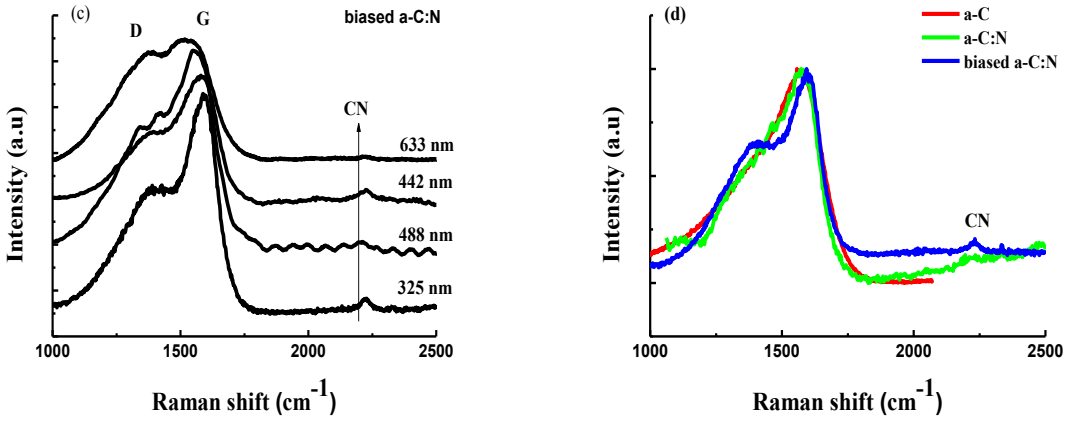

Figure 3. 20 Raman spectra of (a) a-C, (b) a-C:N (10 Pa) and (c) biased a-C:N (5 Pa and 250 V) obtained at four wavelength, (d) superimposed Raman spectra of the three films at 325 nm.

A band at 2225 cm^{-1} has been observed only with biased a-C:N film mainly for UV excitation, while it is barely detectable at higher wavelengths. This band corresponds to a terminal nitrogen triple bonded to carbon (C≡N), in agreement with the literature [42]. Even though it is not shown in the Figure 3.20b, the C≡N stretch band is not detected in a-C:N whatever the laser wavelength. The intensity ratio I(CN)/I(G) is only available for the biased a-C:N film, at 325 nm, 442 nm and 488 nm laser excitations. Indeed the 633 nm wavelength does not provide enough C≡N signal intensity to fit correctly the band. According to [42], a I(CN)/I(G) near 0.10 may correspond to nitrogen contents within 17-25 at% with some uncertainties. This order of magnitude is consistent with the composition of our biased a-C:N film. Indeed, it is worth mentioning that a minimum threshold of nitrogen is required to observe the C≡N band at 2225 cm^{-1}. This may indicate a kind of saturation in the incorporation ability of nitrogen in the carbonaceous network, leading to C≡N terminal groups at the highest nitrogen concentration. In the present study, this threshold is between 14 at.% and 28 at.%.

Sample	a-C				a-C:N				biased a-C:N			
Laser	633	488	442	325	633	488	442	325	633	488	442	325
Wavelength(nm)												
G position (cm^{-1})	1510	1556	1567	1573	1538	1565	1586	1595	1544	1563	1584	1597
G FWHM (cm^{-1})	300	227	206	208	197	159	146	139	190	154	140	136
D position (cm^{-1})	1362	1396	1397	1382	1386	1407	1441	1409	1361	1383	1403	1391
I(D)/I(G)	0.45	0.62	0.60	0.30	0.68	0.53	0.55	0.40	1.36	0.55	0.45	0.47
I(CN)/I(G)	-	-	-	-	-	-	-	-	-	0.08	0.12	0.06
Disp(G)(cm^1/nm)	0.21				0.19				0.17			

Table 3. 6 Characteristics of MW Raman spectra related to the a-C, a-C:N and biased a-C:N films, a-C:N film deposited at 10 Pa P_{N2} pressure and biased a-C:N film deposited at 5 Pa P_{N2} pressure and 250 V DC bias assistance.

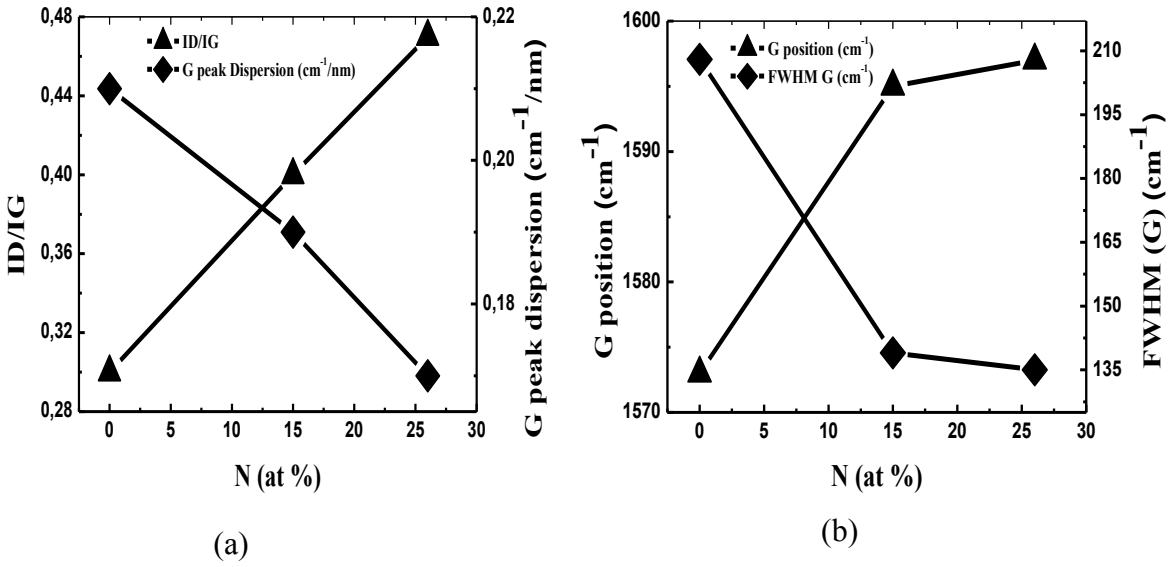

Figure 3. 21 (a) Variation of I(D)/I(G) ratio and FWHM (G); (b) G peak position and G Peak dispersion versus N content deduced from RAMAN measurement at 325 nm.

The following discussion is mainly based on our results summarized in the Figure 3.21, considering the compilation of data interpretation proposed by Ferrari *et al.*[42]. The maximum values are recorded at 325 nm. No G band position exceeds 1600 cm^{-1}, which is consistent with a

predominance of Csp^2 rings in all films. In our previous study related to the pure a-C films, we observe a similar result with femtosecond PLD, whereas the films obtained by nanosecond PLD had a predominance of Csp^2 chains [39]. The G band shifts to higher values with increasing N content in agreement with previously reported data [32,43]. This increment of G position together with an increase of D band intensity is attributed to an increase of Csp^2 clustering when the nitrogen content increases. The dispersion of the G band (Disp(G)) is related to the topological disorder, which corresponds to the size and shape distribution of rings. The dispersion of the G band is decreasing with the increase of N content in films, from 0.21 to 0.17. These values are consistent with those obtained with other CN films, as reported on the Figure 3.22. A low Disp(G) always means that the film structure is ordered, which is consistent with the conclusion deduced from the increase of the G position with N content, as discussed above.

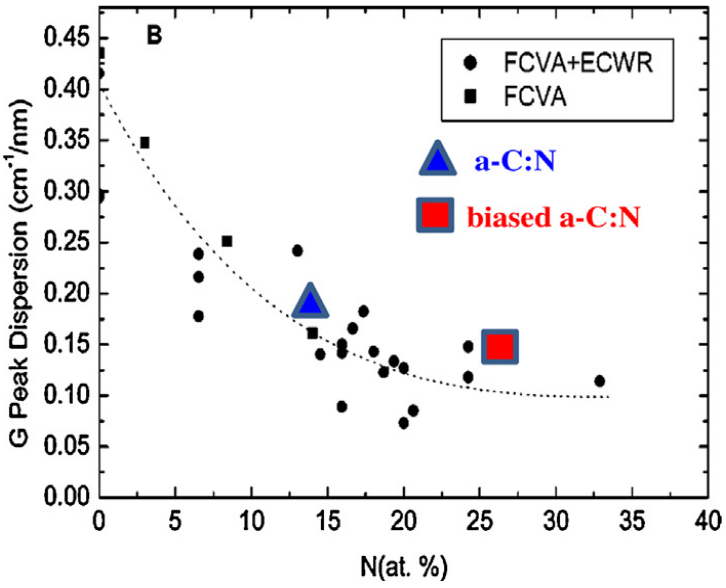

Figure 3. 22 Dispersion of the G peak versus N content (already published data from [42]).

The FWHM of the G band is related to the structural disorder, which corresponds to the bond length and bond angle distortion of Csp^2 clusters. It is well known that FWHM(G) decreases when the excitation wavelength decreases. It is more interesting to observe a decrease of FWHM(G) when the nitrogen content increases, which is consistent with a substantial loss of bond length and bond angle distortions of the clusters when the nitrogen content is high. The

I(D)/I(G) ratio increases with the increase the N content for all excitation wavelengths. The increasing trend of I(D)/I(G) ratio is related to an increase in the proportion of graphitic clusters [19,42,44]. Ferrari *et al*. [45] have proposed a relation between I(D)/I(G) ratio and the correlation length L_a, which is valid for crystallize size smaller than 2 nm.

$$I(D)/I(G) = C_2(\lambda)L_a^2 \qquad (1)$$

C_2 (λ) is a constant which depends on the laser wavelength [29]. According to this reference, the value of C_2 (633 nm) is 8.2 nm. From the above relation, we estimated a correlation length L_a of 0.23 nm for a-C, 0.29 nm for a-C:N and 0.41 nm for biased a-C:N. The increase of aromatic cluster size with N content is consistent with reported data [32,42,46] as well as with other Raman parameters discussed above.

We can conclude an increase of the nitrogen content from 14 at.% (XPS) – 17 at.% (EELS), for the a-C:N film, to 28 at.% (XPS) – 24 at.% (EELS) for the biased a-C:N film. The increase of N content is associated to an increase of the clustering of the sp^2 phase in ordered rings of the CN films, developing more ordered graphitic clusters both in terms of structural and topological order. The correlation length L_a of the clusters increases from 0.23 nm with no nitrogen incorporation, to 0.29 nm and 0.41 nm for the a-C:N and biased a-C:N films.

3.5 Conclusions

The femtosecond pulsed laser ablation of graphite target in an atmosphere of nitrogen without and with DC polarized substrate effect on the structure and composition of the a-C:N film have been investigated in this study. The main conclusions are summarized as follows:

- In this study a-C:N film with nitrogen content up to 18 at.% was grown by ultrafast pulsed laser deposition as a function of nitrogen partial pressure without any DC bias assistance.
- The C1s XPS spectra showed the increase of CN bonds at the expense of CC bonds with the increase of nitrogen content in the films, with the increase of the nitrogen partial pressure.

- The ID/IG ratio and G peak position increased while the FWHM of G band decreased, which showed an increase of the size of the number of sp^2 sites in films when the nitrogen partial pressure increases.
- Up to 28 at.% of nitrogen has been introduced in the a-C:N film by combining femtosecond laser ablation of graphite with a DC bias applied on the substrates. Such a high percentage has never been obtained by fs-PLD process.
- By comparing our XPS results with XPS data compilations, the exact interpretations of the C1s and N1s components are controversial due to rather complex chemistry of CN compounds with rather limited chemical shifts in the 1-2 eV range for both elements.
- By combining XPS, EELS and RAMAN results, the increase of nitrogen content can be associated to an increase of the aromatic character of the carbon network, by increasing the structural and topological orders of the graphitic clusters, which certainly contain incorporated nitrogen.
- No clear and unambiguous evidence of Csp^2:Csp^3 dependence with the N content can be deduced.
- The effect of different DC bias assistance on a-C:N film have been studied successfully, the increase of the DC bias assistance increases the N content until a certain bias assistance after what the N content starts to decrease .
- The high N contents are consisted with an increase of the sp^2 character and higher correlation lengths of the graphitic clusters. However, DC bias induces an increase of the structural disorder, as well as a substantial increase of the nitrile group in films.

At the highest nitrogen concentration, terminal C≡N groups are incorporated in the film, which are observed only for plasma assisted-PLD, as already observed with longer laser pulse duration.

References

(1) Lorazo, P.; Lewis, L. J.; Meunier, M. Thermodynamic Pathways to Melting, Ablation, and Solidification in Absorbing Solids under Pulsed Laser Irradiation. *Phys. Rev. B* **2006**, *73*, 134108.

(2) Lescoute, E.; Hallo, L.; Hébert, D.; Chimier, B.; Etchessahar, B.; Tikhonchuk, V. T.; Chevalier, J.-M.; Combis, P. Experimental Observations and Modeling of Nanoparticle Formation in Laser-Produced Expanding Plasma. *Phys. Plasmas 1994-Present* **2008**, *15*, 63507.

(3) Amoruso, S.; Ausanio, G.; Bruzzese, R.; Vitiello, M.; Wang, X. Femtosecond Laser Pulse Irradiation of Solid Targets as a General Route to Nanoparticle Formation in a Vacuum. *Phys. Rev. B* **2005**, *71*, 33406.

(4) Amoruso, S.; Bruzzese, R.; Spinelli, N.; Velotta, R.; Vitiello, M.; Wang, X.; Ausanio, G.; Iannotti, V.; Lanotte, L. Generation of Silicon Nanoparticles via Femtosecond Laser Ablation in Vacuum. *Appl. Phys. Lett.* **2004**, *84*, 4502–4504.

(5) Eliezer, S.; Eliaz, N.; Grossman, E.; Fisher, D.; Gouzman, I.; Henis, Z.; Pecker, S.; Horovitz, Y.; Fraenkel, M.; Maman, S.; *et al.* Synthesis of Nanoparticles with Femtosecond Laser Pulses. *Phys. Rev. B* **2004**, *69*, 144119.

(6) Perrière, J.; Boulmer-Leborgne, C.; Benzerga, R.; Tricot, S. Nanoparticle Formation by Femtosecond Laser Ablation. *J. Phys. Appl. Phys.* **2007**, *40*, 7069.

(7) Li, J.; Zheng, W. T.; Jin, Z.; Lu, X.; Gu, G.; Mei, X.; Dong, C. Influence of Substrate Dc Bias on Chemical Bonding, Adhesion and Roughness of Carbon Nitride Films. *Appl. Surf. Sci.* **2002**, *191*, 273–279.

(8) Cappelli, E.; Orlando, S.; Trucchi, D. M.; Bellucci, A.; Valentini, V.; Mezzi, A.; Kaciulis, S. Carbon Nitride Films by RF Plasma Assisted PLD: Spectroscopic and Electronic Analysis. *Appl. Surf. Sci.* **2011**, *257*, 5175–5180.

(9) Sánchez-López, J. C.; Donnet, C.; Lefèbvre, F.; Fernández-Ramos, C.; Fernández, A. Bonding Structure in Amorphous Carbon Nitride: A Spectroscopic and Nuclear Magnetic Resonance Study. *J. Appl. Phys.* **2001**, *90*, 675–681.

(10) Ronning, C.; Feldermann, H.; Merk, R.; Hofsäss, H.; Reinke, P.; Thiele, J.-U. Carbon Nitride Deposited Using Energetic Species: A Review on XPS Studies. *Phys. Rev. B* **1998**, *58*, 2207–2215.

(11) Marton, D.; Boyd, K. J.; Al-Bayati, A. H.; Todorov, S. S.; Rabalais, J. W. Carbon Nitride Deposited Using Energetic Species: A Two-Phase System. *Phys. Rev. Lett.* **1994**, *73*, 118–121.

(12) Bhattacharyya, S.; Hong, J.; Turban, G. Determination of the Structure of Amorphous Nitrogenated Carbon Films by Combined Raman and X-Ray Photoemission Spectroscopy. *J. Appl. Phys.* **1998**, *83*, 3917–3919.

(13) Cheng, Y. H.; Qiao, X. L.; Chen, J. G.; Wu, Y. P.; Xie, C. S.; Wang, Y. Q.; Xu, D. S.; Mo, S. B.; Sun, Y. B. Dependence of the Composition and Bonding Structure of Carbon Nitride Films Deposited by Direct Current Plasma Assisted Pulsed Laser Ablation on the Deposition Temperature. *Diam. Relat. Mater.* **2002**, *11*, 1511–1517.

(14) Cappelli, E.; Trucchi, D. M.; Kaciulis, S.; Orlando, S.; Zanza, A.; Mezzi, A. Effect of Deposition Temperature on Chemical Composition and Electronic Properties of

Amorphous Carbon Nitride (a-CNx) Thin Films Grown by Plasma Assisted Pulsed Laser Deposition. *Thin Solid Films* **2011**, *519*, 4059–4063.

(15) Pels, J. R.; Kapteijn, F.; Moulijn, J. A.; Zhu, Q.; Thomas, K. M. Evolution of Nitrogen Functionalities in Carbonaceous Materials during Pyrolysis. *Carbon* **1995**, *33*, 1641–1653.

(16) Cheng, Y. H.; Sun, Z. H.; Tay, B. K.; Lau, S. P.; Qiao, X. L.; Chen, J. G.; Wu, Y. P.; Xie, C. S.; Wang, Y. Q.; Xu, D. S.; *et al.* Influence of Deposition Pressure on the Composition and Structure of Carbon Nitride Films Deposited by Direct Current Plasma Assisted Pulsed Laser Ablation. *Appl. Surf. Sci.* **2001**, *182*, 32–39.

(17) Das, D.; Chen, K. H.; Chattopadhyay, S.; Chen, L. C. Spectroscopic Studies of Nitrogenated Amorphous Carbon Films Prepared by Ion Beam Sputtering. *J. Appl. Phys.* **2002**, *91*, 4944–4955.

(18) Le Normand, F.; Hommet, J.; Szörényi, T.; Fuchs, C.; Fogarassy, E. XPS Study of Pulsed Laser Deposited CNx Films. *Phys. Rev. B* **2001**, *64*, 235416.

(19) Rodil, S. E.; Muhl, S. Bonding in Amorphous Carbon Nitride. *Diam. Relat. Mater.* **2004**, *13*, 1521–1531.

(20) Cheng, Y. H.; Qiao, X. L.; Chen, J. G.; Wu, Y. P.; Xie, C. S.; Wang, Y. Q.; Xu, D. S.; Mo, S. B.; Sun, Y. B. Effect of Laser Fluences on the Structure of Carbon Nitride Films Deposited by Direct Current Plasma Assisted Pulsed Laser Ablation. *Surf. Coat. Technol.* **2002**, *160*, 269–276.

(21) E. Riedo; F. Comin; J. Chevrier; A. M. Bonnot. Composition and Chemical Bonding of Pulsed Laser Deposited Carbon Nitride Thin Films. *J. Appl. Phys.* **2000**, *88*, 4365–4370.

(22) G Soto. Electron Spectroscopic Identification of Carbon Species on CNx Films. *Mater. Lett.* **2001**, *49*, 352–356.

(23) E. Riedo; F. Comin; J. Chevrier; F. Schmithusen; S. Decossas; M. Sancrotti. Structural Properties and Surface Morphology of Laser-Deposited Amorphous Carbon and Carbon Nitride Films. *Surf. Coat. Technol.* **2000**, *125*, 124–128.

(24) Jiangtao Hu; Peidong Yang; Charles M. Lieber. Nitrogen Driven Structural Transformation in Carbon Nitride Materials. *Appl. Surf. Sci.* **1998**, *127–129*, 569–573.

(25) A. Fernández; J. C. Sánchez-López; G. Lassaletta. Characterisation of Carbon Nitride Thin Films Prepared by Reactive Magnetron Sputtering. *Carbon* **1998**, *36*, 761–764.

(26) C. Spaeth; M. Kühn; F. Richter; U. Falke; M. Hietschold; R. Kilper; U. Kreissig. A Comparative Study of Elastic Recoil Detection Analysis (ERDA), Electron Energy Loss Spectroscopy (EELS) and X-Ray Photoelectron Spectroscopy (XPS) for Structural Analysis of Amorphous Carbon Nitride Films. *Diam. Relat. Mater.* **1998**, *7*, 1727–1733.

(27) G Soto; E. C Samano; R Machorro; M. H Farías; L Cota-Araiza. Study of Composition and Bonding Character of CNx Films. *Appl. Surf. Sci.* **2001**, *183*, 246–258.

(28) Ferrari, A. C.; Rodil, S. E.; Robertson, J. Interpretation of Infrared and Raman Spectra of Amorphous Carbon Nitrides. *Phys. Rev. B* **2003**, *67*, 155306.

(29) Matthews, M. J.; Pimenta, M. A.; Dresselhaus, G.; Dresselhaus, M. S.; Endo, M. Origin of Dispersive Effects of the Raman D Band in Carbon Materials. *Phys. Rev. B* **1999**, *59*, R6585–R6588.

(30) Ferrari, A. C.; Robertson, J. Resonant Raman Spectroscopy of Disordered, Amorphous, and Diamondlike Carbon. *Phys. Rev. B* **2001**, *64*, 75414.

(31) Robertson, J. Diamond-like Amorphous Carbon. *Mater. Sci. Eng. R Rep.* **2002**, *37*, 129–281.

(32) McCann, R.; Roy, S. S.; Papakonstantinou, P.; McLaughlin, J. A.; Ray, S. C. Spectroscopic Analysis of a-C and a-CNx Films Prepared by Ultrafast High Repetition Rate Pulsed Laser Deposition. *J. Appl. Phys.* **2005**, *97*, 73522.
(33) Sánchez-López, J. C.; Donnet, C.; Lefèbvre, F.; Fernández-Ramos, C.; Fernández, A. Bonding Structure in Amorphous Carbon Nitride: A Spectroscopic and Nuclear Magnetic Resonance Study. *J. Appl. Phys.* **2001**, *90*, 675–681.
(34) D.A. Zeze, S.R.P. Silva, S. Haq and S.J. Harris. *Phil Mag B 83 1937-1947* **2003**.
(35) C. Donnet; J. M. Martin; J. Fontaine; J. C. Sánchez-López; C. Quirós; E. Elizalde; J. M. Sanz; T. C. Rojas; A. Fernández. The Role of CN Chemical Bonding on the Tribological Behaviour of CNx Coatings. *Surf. Coat. Technol.* **1999**, *120–121*, 594–600.
(36) Bakoglidis, K. D.; Schmidt, S.; Garbrecht, M.; Ivanov, I. G.; Jensen, J.; Greczynski, G.; Hultman, L. Low-Temperature Growth of Low Friction Wear-Resistant Amorphous Carbon Nitride Thin Films by Mid-Frequency, High Power Impulse, and Direct Current Magnetron Sputtering. *J. Vac. Sci. Technol. A* **2015**, *33*, 05E112.
(37) Radnóczi, G.; Kovács, I.; Geszti, O.; Bíró, L. P.; Sáfrán, G. Structure of Amorphous Carbon-Nitride Thin Films. *Surf. Coat. Technol.* **2002**, *151–152*, 133–137.
(38) Cheng, Y. H.; Qiao, X. L.; Chen, J. G.; Wu, Y. P.; Xie, C. S.; Wang, Y. Q.; Xu, D. S.; Mo, S. B.; Sun, Y. B. Dependence of the Composition and Bonding Structure of Carbon Nitride Films Deposited by Direct Current Plasma Assisted Pulsed Laser Ablation on the Deposition Temperature. *Diam. Relat. Mater.* **2002**, *11*, 1511–1517.
(39) A. Sikora; F. Garrelie; C. Donnet; A. S. Loir; J. Fontaine; J. C. Sanchez-Lopez; T. C. Rojas. Structure of Diamondlike Carbon Films Deposited by Femtosecond and Nanosecond Pulsed Laser Ablation. *J. Appl. Phys.* **2010**, *108*, 113516.
(40) J. C Sánchez-López; C Donnet; M Belin; T Le Mogne; C Fernández-Ramos; M. J Sayagués; A Fernández. Tribochemical Effects on CNx Films. *Surf. Coat. Technol.* **2000**, *133–134*, 430–436.
(41) A. Fernández; P. Prieto; C. Quirós; J. M. Sanz; J.-M. Martin; B. Vacher. Characterization of Carbon Nitride Thin Films Prepared by Dual Ion Beam Sputtering. *Appl. Phys. Lett.* **1996**, *69*, 764–766.
(42) Ferrari, A. C.; Rodil, S. E.; Robertson, J. Interpretation of Infrared and Raman Spectra of Amorphous Carbon Nitrides. *Phys. Rev. B* **2003**, *67*, 155306.
(43) S. Prawer; K. W. Nugent; Y. Lifshitz; G. D. Lempert; E. Grossman; J. Kulik; I. Avigal; R. Kalish. Systematic Variation of the Raman Spectra of DLC Films as a Function of sp2:sp3 Composition. *Diam. Relat. Mater.* **1996**, *5*, 433–438.
(44) Wang, P.; Takeno, T.; Fontaine, J.; Aono, M.; Adachi, K.; Miki, H.; Takagi, T. Effects of Substrate Bias Voltage and Target Sputtering Power on the Structural and Tribological Properties of Carbon Nitride Coatings. *Mater. Chem. Phys.* **2014**, *145*, 434–440.
(45) A. C. Ferrari; J. Robertson. Interpretation of Raman Spectra of Disordered and Amorphous Carbon. *Phys. Rev. B* **2000**, *61*, 14095–14107.
(46) Bing Zhou; Xiaohong Jiang; A. V. Rogachev; Ruiqi Shen; Dongping Sun; D. G. Piliptsou; Lude Lu. A Comparison Study between Atomic and Ionic Nitrogen Doped Carbon Films Prepared by Ion Beam Assisted Cathode Arc Deposition at Various Pulse Frequencies. *Appl. Surf. Sci.* **2013**, *287*, 150–158.

Chapter 4. Spectroscopic studies of graphite ablation plume under nitrogen gas and plasma assistance

4.1 Introduction

The dynamics and the quantities of the various laser-ablated plume species strongly affect the deposition process, which in turn determines the properties of the deposited thin films [1–4]. When the deposition is performed in a reactive atmosphere, the chemical reactions of the ablated species with the ambient gas are a key factor for the thin film composition and structure. Especially, when the films are deposited by nitrogen doping into amorphous carbon, the nitrogen forms different CN bonds and nitrogen contents into the films. In order to address and understand the formation of CN bonding and N content incorporation into films produced by nitrogen ambient gas and DC bias assistance fs-PLD during the ablation, transfer or deposition on the substrate, we need *in-situ* spectroscopy techniques.

There are several techniques for the characterization of the laser-ablated plume, such as Optical Emission Spectroscopy (OES) [5–7], spectrally resolved direct ultrafast imaging [8–10], time of flight mass spectroscopy [11], and laser induced fluorescence spectroscopy [12]. Those allow finding out the correlation between plasma parameters and deposited film properties. Among those techniques, Optical Emission Spectroscopy is one of the fundamental plasma diagnostic methods. OES is effective for *in situ* studies of the plume dynamics and its interaction with a reactive gas, particularly to observe where chemical bonding take place and how the generated species carry on their path to the deposition substrate [5,11,13,14].

In this chapter, we present the results of the identification of plume components and expansion dynamics of the ablated plumes produced from the graphite target by ultrafast laser ablation in vacuum, nitrogen atmosphere and DC bias nitrogen plasma. The plumes were analyzed via ultrafast Optical Emission Spectroscopy (OES) technique and Spectrally resolved ultrafast 2D-imaging, coupled with ICCD camera, in order to address and understand the bonding formation and high N content incorporation in DC bias assistance deposited a-C:N thin films. In addition, we studied the films chemical and microstructure properties to link *in situ* observations of the

ablation plume, the samples are deposited on silicon by PLD in the four selected conditions for which ablation plumes are studied. The detailed experimental procedure of thin films deposition and operation of emission spectroscopy and plume imaging, along with thin film characterization techniques were described in the chapter 2.

4.2 Optical characterization of the ablation plumes

4.2.1 Identification of the plume components

The Optical Emission Spectroscopy (OES) was used to study the plasma plume emission at different deposition conditions. We prepared a set of samples just allowing the carbon plume expanding in a N_2 atmosphere at 1 and 10 Pa, and a set of conditions have been obtained with the carbon plume expanding in a 250 V DC polarized substrate in a N_2 pressure 1 Pa and 10 Pa. We chose those conditions to see both plasma and N_2 pressure effects. All the films were deposited at constant laser fluence of 5 J/cm^2. We compared the optical emission spectra of plumes expanding in vacuum or nitrogen atmosphere, with or without the DC bias. The Figure 4.1 shows the spectra obtained at a pressure of 10 Pa with and without DC bias at 250 V and with vacuum, by integrating all the emitted light from 20 ns up to 50 µs after interaction. These delays are chosen to avoid the initial bremsstrahlung before 20 ns and because no notable emission can be recorded past 50 µs.

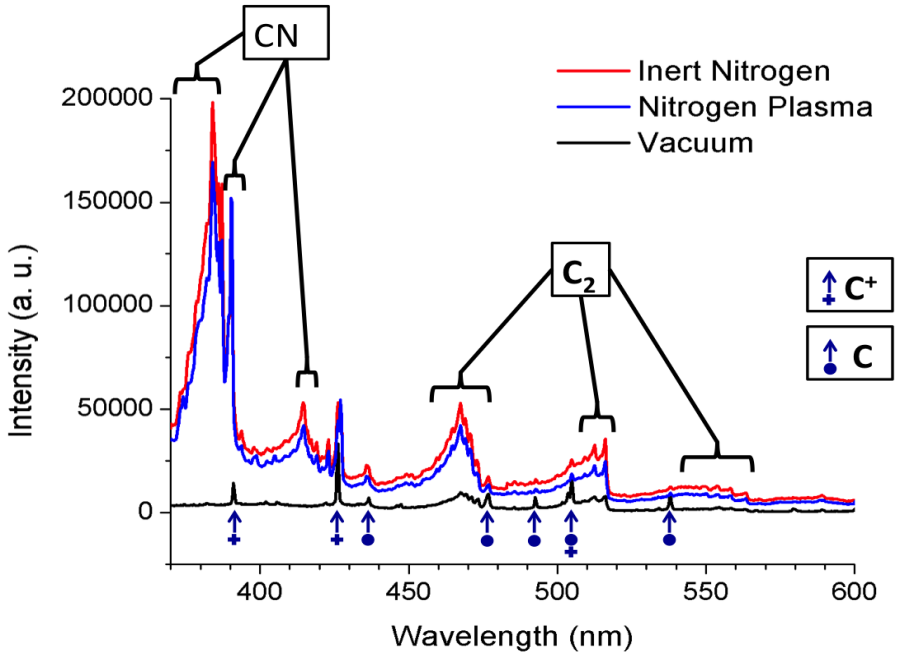

Figure 4. 1 Optical emission spectra of graphite ablation plumes expanding in vacuum and various gas conditions at 10 Pa with and without bias assistance at 250V was recorded from 20 ns to 50 µs after interaction.

Numerous emission lines and bands can be observed. All emission lines correspond to either C II or C I spectroscopic lines, indicating the emission of C^+ ions and neutral C atoms, respectively. None can be attributed to pure nitrogen species, due to the low-resolution optical emission spectroscopy. A deeper insight and detailed analysis should be carried on to extending the investigated region toward the spreading of the spectrum, which means high resolution grating, in order to achieve a better resolution and identification of the peaks belonging to the various species. In vacuum, C II lines are visible during few hundred nanoseconds after interaction, and C I during 1 µs. In nitrogen, these emissions almost disappear after 200 ns. The observation of C II and C I in vacuum is in agreement with the previous detailed studies of femtosecond ablation of graphite [[15,16]].

The emission bands observed in vacuum correspond accurately to the well-known Swan Bands [[17]] emitted by C_2 molecules, with main heads at 466.8 nm, 516.5 nm, and 554.0 nm (visible only when zoomed). These relatively large bands appear in all recorded spectra, with different

intensities. They have already been well observed and detailed in vacuum [18,19]. They can be observed up to few µs after interaction in vacuum, and few tens of µs after interaction in inert nitrogen and nitrogen plasma.

The most notable feature of these spectra is the three huge bands in the short wavelength region, which appear only in nitrogen ambient. All of them can be associated to the Violet System [17] emitted by CN molecules vibrational transition. The widest one belongs to the main system, and consists of three heads at 385.1 nm, 385.5 nm and 386.2 nm. The thinner ones belong to the tail bands, with heads at 391.0 nm and 407.9 nm. The former can be distinguished over time from the C II line appearing in vacuum and centered at 391.9 nm [18]. This emission is clearly visible after initial bremsstrahlung (20 ns after interaction), and is maximal in the first 100 ns after interaction. The emission from CN behaves quite similarly to C_2 in nitrogen ambient, existing during 30 µs after interaction.

Similar species are observed at similar times when using a pressure of 1 Pa. These observations only concern a section of the plume close to the target, and give no idea of the species dynamics. The spectral position and bandwidths of the different species emission allow using spectral band pass optical filters in order to select species for 2-D imaging of the plume to locate the species, and to determine their quantity when they reach the substrate during PLD.

4.2.2 Expansion dynamics of the plume during the deposition

The plasma plume was imaged by a gated intensified CCD camera in the UV-Visible range. Several optical band pass filters are used to select the emission of the different species. Filters going from 375 to 385 nm and 387 to 397 nm allow assessing CN emissions. A filter going from 425 to 435 nm allows recording C II emission. C_2 bands are observed through filters going from 455 to 465 and 515 to 525 nm. C I emission is recorded in the range of 535-545 nm. Ambiguities can only appear for the recorded lines, for which the emission can be convoluted with broader molecular bands, but are minored by two facts. First, C I and C II emissions only exist for less than 200 ns in nitrogen. Second, spatial segregation between ions, atoms and molecules has been evidenced in vacuum [16], and might be expected here.

The images recorded with the C I and C II filters always contain a component ahead of the main plume, which is not recorded using the filters selected for CN and C_2. This indicates that the spatial segregation still exist in nitrogen ambient. Additionally, the observations confirm the fast disappearing of these components. They have the same behavior, quantity and speed whether or not DC bias is used, and cannot be observed more than a centimeter away from the target. The most striking feature is the behavior of the CN and C_2 components because of the predominance of C_2 for amorphous carbon films growth [16] and the incorporation of nitrogen in the films through plasma reactions and CN bonding. Here, the study will be separated between the 1 and 10 Pa pressure conditions. The Figure 4.2 presents CN and C_2 emissions in 1 Pa of either inert nitrogen or nitrogen plasma, recorded at a) 1000-1200 ns after laser interaction and b) 2500-3000 ns after laser interaction. The emission is normalized to the maximum of the four images in each case.

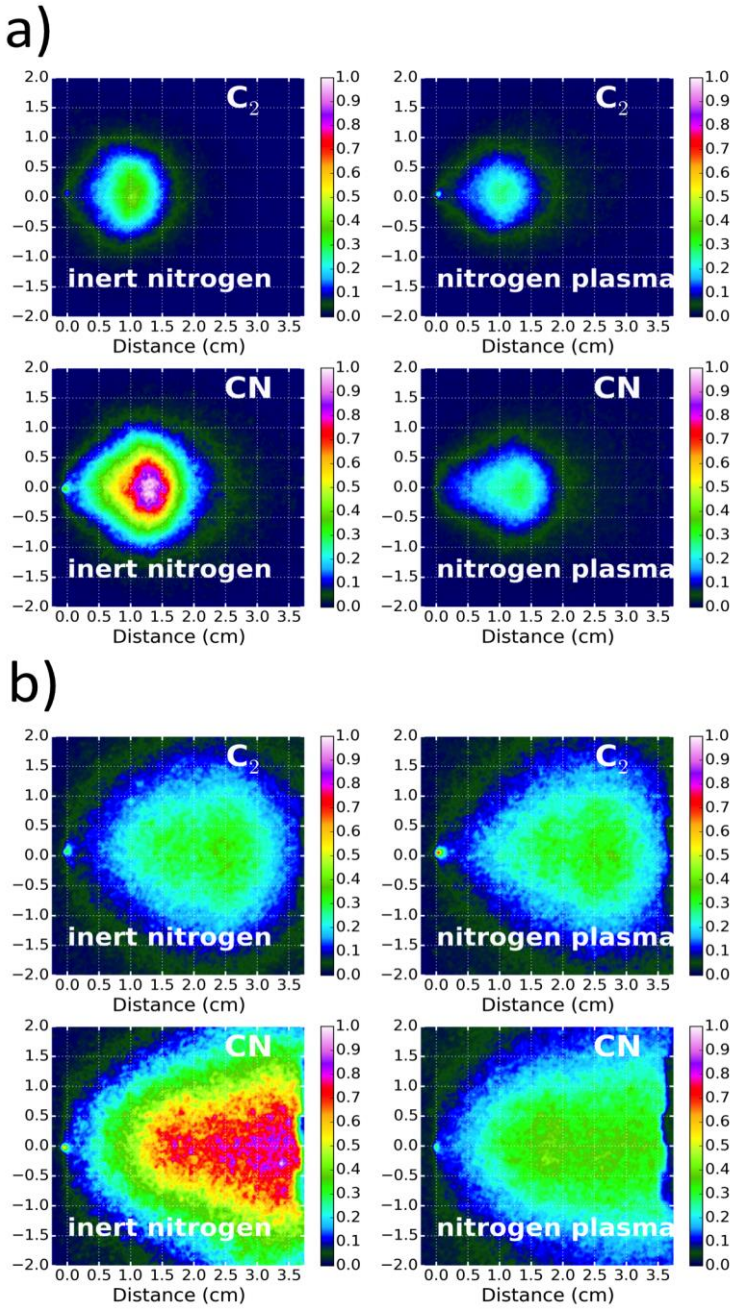

Figure 4. 2 Spectrally resolved emission from CN (375-385 nm) and C_2 (455-465 nm) of fs laser-induced carbon plasma plume expansion in 1 Pa of inert N_2 gas or of nitrogen plasma recorded at a) 1000 to 1200 ns b) 2500 to 3000 ns after laser interaction.

The plume expands while its center of mass progresses normally along the ejection axis, with the major part of the plume making contact with the substrate in any case. Indeed, as it can be seen at delay 2500 to 3000 ns after interaction, the substrate (at 3.6 cm from target) is "showered" by the

C_2 and CN molecules. The use of DC bias to induce nitrogen plasma does not modify the quantity of emission due to C_2 molecules. However, the emission due to CN is considerably higher in the case of inert nitrogen ambient rather than plasma. This is confirmed by the Figure 4.3, which features a summation of the emission shown in the Figure 4.2 along the ejection axis. Here, the quantity of C_2 emission is always quite comparable, while CN emission is much stronger in the case of plasma ambient nitrogen.

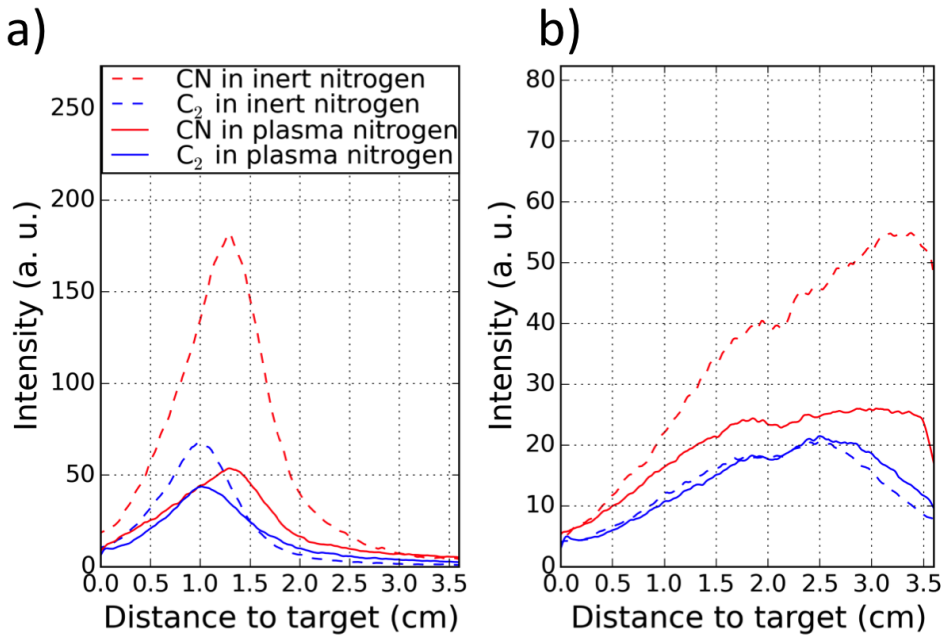

Figure 4. 3 Emission from CN and C_2 molecules summed along the ejection axis in 1 Pa of N_2 inert gas or nitrogen plasma a) from 1000 to 1200 ns and b) from 2500 to 3000 ns after laser interaction.

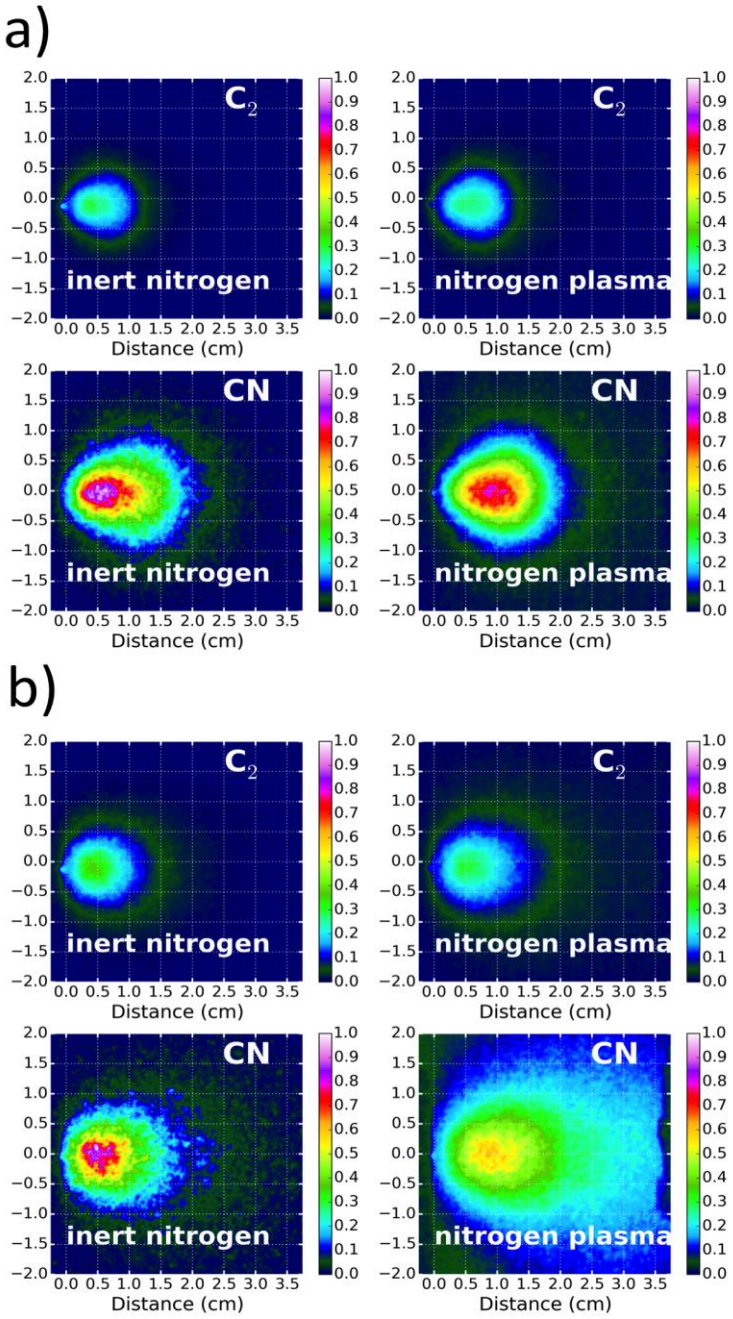

Figure 4. 4 Spectrally resolved emission from CN (375-385 nm) and C_2 (455-465 nm)) of fs laser-induced carbon plasma plume expansion in 10 Pa of N_2 inert gas or nitrogen plasma (250 V bias assistance) at a) 1000 to 1200 ns b) 2500 to 3000 ns after interaction.

An important fact to notice is that, however limited the effect is, in every case, the CN emission always appears slightly further from the target compared to C_2 emission, even if the two

components are mixed. Finally, it is observed that when using nitrogen plasma, both CN and C_2 molecules seem to progress faster and further than their respective counterpart in inert nitrogen. The same observations are carried with 10 Pa of ambient gas, as presented in the Figure 4.4. The same delays and filters as the Figure 4.2 are used, in order to observe C_2 and CN between 1000 and 1200 ns and 2500 and 3000 ns after laser interaction. The first important difference with preceding observations is that the quantities of the various species are not dramatically changed by the use of DC bias. In particular, during 1000-1200 ns, the plume emissions look quantitatively similar. In contrast to what happens at 1 Pa, the plume center of mass presents a very weak evolution between the two different delays. This is confirmed by the Figure 4.5, which sums the emission recorded in the Figure 4.4 along with the ejection axis. Even when studied at longer delays, until the plume no longer emits, the bulk of the emitting plasma plume under 10 Pa never makes contact with the substrate. Only the front of the plume expands enough to reach the substrate.

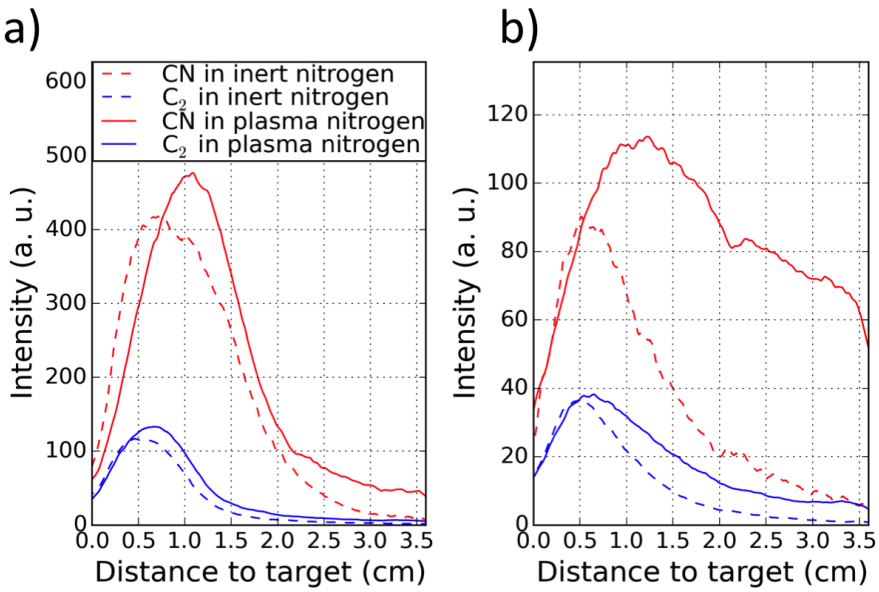

Figure 4. 5 Emission from CN and C_2 molecules summed along the ejection axis in 10 Pa of N_2 inert gas or nitrogen plasma at 250 V from a) 1000 to 1200 ns b) 2500-3000 ns after laser interaction.

Despite these differences, we can still observe the CN emission, which is always further than C_2, even though the various components are still very intermixed. Similarly, to the 1 Pa pressure

case, CN and C_2 plume components progress slightly further when expanding in plasma rather than inert ambient gas. It means that more species from the plume front can make contact with the substrate in the plasma ambient case. These two different pressures with or without DC bias induce different plasma plumes, with the DC bias inducing quite different effects depending on the N_2 pressure. In particular, CN and C_2 species impinging on the substrate may authorize different growth conditions during the deposition. This should lead to different N contents in the deposited a-C:N films.

4.2.3 Comparison with ex-situ thin film analysis

The detailed microstructural and chemical properties of a-C and a-C:N films were investigated and discussed in the chapter 3. Here, we give corresponding N content values of films that were used in plasma plume studies. The variations in nitrogen content of amorphous carbon nitride films produced at different nitrogen partial pressures with and without DC bias assistance are presented in the Table 4.1. In inert nitrogen surrounding gas, at the highest pressure 10 Pa, the N content value of the film increases with pressure from 13 to 16 at.%. At low pressure (1 Pa) the DC bias (-250 V) induces a decrease of the N contents from 13 to 10 at.%, while at high pressure (10 Pa), it induces an increase of the N content, from 16 up to 25 at.%. The pressure and the DC bias on the laser induced ablation plume induce a difference in the thin films nitrogen content.

Pressure (Pa)	Bias (V)	N contents (at.%)
1	0	13
1	-250	10
10	0	16
10	-250	25

Table 4. 1 Nitrogen contents from a-C:N films deposited by femtosecond laser deposition with various bias and nitrogen pressure conditions.

As we know, the microstructural properties of a-C:N films also affect the films properties. The microstructural property of films was studied by Raman spectroscopy.

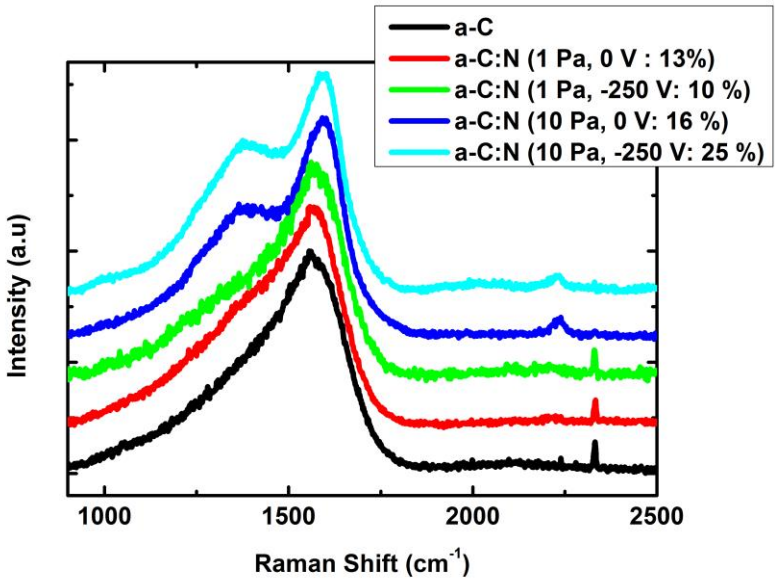

Figure 4. 6 Raman spectra of a-C and a-C: N films deposited at different nitrogen pressures and DC bias along with their N content values (showed in legend).

The detailed Raman spectroscopy measurements and analysis were discussed in the previous chapters 2 and 3. Here, we present the evaluation of Raman spectra with N content in films, which have been used in plasma plume investigations. The Figure 4.6 shows the superimpose of the Raman spectra of the films deposited at different nitrogen pressure and DC bias voltages with a 325 nm Raman wavelength. It appears that the samples with lower nitrogen content (0-13 at.%) does not reveal the presence unambiguously attributed to the formation of CN, while the films with higher N content (16-25 at.%) show a clear evidence of a chain terminating C≡N bond around 2200 cm^{-1}. We can clearly see from the Figure 4.6 that the increase of nitrogen in films resemble to the increase of D band intensity, which relates to the increase of sp^2 phase organized in films [20,21]. Based on all our results, we present in the next section a sound discussion on the plasma plume obtained by optical emission spectroscopy and 2D imaging technique.

4.3 Plasma dynamics impacts an a-C:N thin films structures

Contrary to the rest of the plume, ions and neutrals seem to be relatively unaffected by the use of DC-bias. Their quantity remains constant, and within the few hundred nanoseconds during which they are visible, they always appear to progress faster in the plume. It is possible that they reach the substrate in a non-radiative state. Anyway, they disappear at centimetric distance from the target and ahead of the main CN/C_2 plume, that is to say that any recombination process between C^+, C and the nitrogen ambient, with or without DC bias, will be excluded here. This is different to what has been observed previously in [10], where higher pressure was used (more than 40 Pa). Thus, it can be expected that at higher pressure, the C^+ and C components are squeezed between expanding C_2 and ambient gas.

The CN emission appearing after only a few tens of nanosecond after plume interaction indicates that the CN bonding takes place during the very first few nanosecond of plume expansion, when the plume is a hot optically thick plasma [19,22]. Molecular dynamics studies have shown that a huge part of the ablated matter, in the case of graphite ablation, remain in the form of molecules from the first picoseconds after interaction [23,24]. This should mean that CN are expected to form from the interaction between N_2 and C_2 at high temperature via $C_2 + N_2 \rightarrow 2$ CN, as it has been suggested for nanosecond interaction [9]. Note that from the end of bremsstrahlung to the disappearance of most species or their collection on the substrate, the ratio of CN emission over C_2 emission remains almost constant. That is to say that the chemical reaction leading to CN bonding does not occur after the first few tens of nanoseconds after interaction. When we use different pressures (1 and 10 Pa) and the laser fluence (5 J/cm^2), the formation of CN is due only to the interaction between the hot plume and the ambient gas or plasma at the beginning of the expansion. As expected, in all cases, the CN and C_2 components appear really intermixed, with the CN center of mass slightly ahead of the C_2 one.

At a lower pressure (1 Pa), the use of a DC bias strongly reduces CN component quantity, while affecting weakly C_2 formation. A key factor in the ablation plume dynamics in ambient gas is the atomic weight of gas molecules [25]. The dissociation of molecules in the nitrogen plasma should reduce the average atomic weight of the surrounding gas encountered by the expanding plume. Thus, C_2 molecules will have an easier way to flow towards the substrate through the plasma.

This will reduce the number of C_2/N_2 interactions necessary to trigger the $C_2 + N_2 \rightarrow 2$ CN reactions. From a hydrodynamic viewpoint, the faster expansion of the plume reduces the duration for which it is hot and dense enough to trigger the chemical reaction. Another explanation could be the lack of N_2 in the nitrogen plasma, since the same should be true in the 10 Pa pressure conditions, where no decrease of CN component is observed when using a DC bias. The easier penetration of the plume in the nitrogen plasma was confirmed by the observation of the CN and C_2 center of mass being slightly further at the same acquisition times in plasma than in inert nitrogen surrounding atmosphere.

The laser-induced plasma plume then propagates to the substrate where it is deposited as a-C:N layer. It appears only logical that with a lower proportion of CN in the plume using a DC bias, one obtains a lower N content in the deposited thin films. The observed plume contents and dynamics correlate then very well to the thin films properties at low pressure.

At the highest pressure, the emitted plume center of mass does not reach the substrate anymore; only its front makes contact with it. Moreover, the plume front is richer in CN, due to their formation location, the center of mass of the CN component being slightly ahead of the C_2. Despite almost the same overall ratio between CN and C_2 emission in inert gas at both pressures, a higher N content is obtained in the thin films at the higher pressure. This happens by limiting the substrate contact to the CN richer part of the plume, yielding an increase in nitrogen ratio from 13 to 16 at.%.

Contrary to lower pressure condition, DC bias increases the CN component emission at 10 Pa. This is related to the fact that at this pressure, the N^+ rich nitrogen plasma remains strong enough to prevent expansion and favor the temperature and pressure become high enough to trigger CN formation in the first tens of nanosecond after interaction. Moreover, the nitrogen plasma lets CN and C_2 flowing more easily than the inert nitrogen surrounding gas. It ensures an even better, in particular faster, contact between the substrate and plume front. This is especially clear in Figure 4.5, where one can observe a contact with the CN plume as early as at 1 µs after interaction when using DC bias. Note that the C_2 contact with the plume is favored too, but only later, when the CN emission on the substrate is half its maximum along the ejection axis. Thus, a higher contact

with the CN rich part of the plume is ensured when using the DC bias, as confirmed by the very high N contents of the thin films deposited in these conditions.

In summary, the use of both optical emission spectroscopy and spectrally resolved 2D imaging, coupled with intensified CCD temporal resolution, allowed to precisely follow such species of the plume as CN and C_2 molecules from their emerging to their deposition on the substrate. The results showed that the carbon and nitrogen bonding arise at the early time of expansion with little changes in quantity thereafter. The key role of the DC bias is in lowering the molecular weight of the ambient gas, thus easing molecules way towards the target and interfere with the chemical reaction for CN generation. Depending on the ambient pressure, these processes have drastic effects on the thin films properties.

4.4 Conclusions

The graphite ultrafast ablation plume expanding in nitrogen at various pressures (1 and 10 Pa) with only a nitrogen-surrounding atmosphere or in presence of nitrogen plasma between target and PLD substrate is studied through optical emission spectroscopy and spectrally resolved ultrafast imaging. The results are correlated to a-C:N deposited thin films through their N contents evaluated with XPS spectroscopy, and microstructural properties studied by Raman spectroscopy.

The DC bias assistance has been found to have a detrimental or enhancing effect on the N contents of the a-C:N thin films depending on the pressure used. This is related to an easier flow of laser-ablated molecules in an N^+ rich ambient gas rather than inert N_2. At low pressure, this reduces CN contents in the plume due to less interaction between C_2 and N_2, with the whole plume contacting the substrate, inducing lower N contents in the film. On the opposite, a high pressure was sufficient to trigger a strong CN formation reaction, while limiting the plume/substrate interaction to the CN rich plume front only. The DC bias thus could enhance N contents of a-C:N thin films from 16 to 25 at.% at 10 Pa.

Considering the high potential of N-rich a-C:N alloy thin films as active sensors for bio pollutants or heavy metals detectors, this study shows how very high N contents of such films can be

obtained. Indeed by studying the optical emission from the plume, one can optimize pressure and bias conditions for which strong CN formation is triggered, and ablation plume front and substrate interaction is favored. The maximum nitrogen incorporation into a-C:N films was 25 at.% at pressure about 10 Pa and DC bias -250 V, which matched well with maximum excited CN radicals near the substrate and with the higher sp^2 sites. A deeper insight and detailed analysis should be carried on to extending the investigated region toward the spreading of the spectrum, which means high resolution grating, in order to achieve a better resolution and identification of the peaks belonging to the various species.

.

References

(1) Fuge, G. M.; Ashfold, M. N. R.; Henley, S. J. Studies of the Plume Emission during the Femtosecond and Nanosecond Ablation of Graphite in Nitrogen. *Journal of Applied Physics* **2006**, *99*, 014309.

(2) Cappelli, E.; Orlando, S.; Trucchi, D. M.; Bellucci, A.; Valentini, V.; Mezzi, A.; Kaciulis, S. Carbon Nitride Films by RF Plasma Assisted PLD: Spectroscopic and Electronic Analysis. *Applied Surface Science* **2011**, *257*, 5175–5180.

(3) Itoh, M.; Suda, Y.; Bratescu, M. A.; Sakai, Y.; Suzuki, K. Amorphous Carbon Nitride Film Preparation by Plasma-Assisted Pulsed Laser Deposition Method. *Appl Phys A* **2004**, *79*, 1575–1578.

(4) Thareja, R. K.; Dwivedi, R. K.; Ebihara, K. Interaction of Ambient Nitrogen Gas and Laser Ablated Carbon Plume: Formation of CN. *Nuclear Instruments and Methods in Physics Research Section B: Beam Interactions with Materials and Atoms* **2002**, *192*, 301–310.

(5) Yamagata, Y.; Sharma, A.; Narayan, J.; Mayo, R. M.; Newman, J. W.; Ebihara, K. Comparative Study of Pulsed Laser Ablated Plasma Plumes from Single Crystal Graphite and Amorphous Carbon Targets. Part I. Optical Emission Spectroscopy. *Journal of Applied Physics* **2000**, *88*, 6861–6867.

(6) Yamagata, Y.; Sharma, A.; Narayan, J.; Mayo, R. M.; Newman, J. W.; Ebihara, K. Optical Emission Study of Ablation Plasma Plume in the Preparation of Diamond-like Carbon Films by KrF Excimer Laser. *Journal of Applied Physics* **1999**, *86*, 4154–4159.

(7) Harilal, S. S.; Issac, R. C.; Bindhu, C. V.; Gopinath, P.; Nampoori, V. P. N.; Vallabhan, C. P. G. Time Resolved Study of CN Band Emission from Plasma Generated by Laser Irradiation of Graphite. *Spectrochimica Acta Part A: Molecular and Biomolecular Spectroscopy* **1997**, *53*, 1527–1536.

(8) Loir, A.-S.; Garrelie, F.; Subtil, J.-L.; Goutaland, F.; Belin, M.; Le Harzic, R.; Donnet, C.; Ouerdane, Y.; Rogemond, F.; Laporte, P. Study of Plasma Expansion Induced by Femtosecond Pulsed Laser Ablation and Deposition of Diamond-like Carbon Films. *Applied Surface Science* **2003**, *208–209*, 553–560.

(9) Voevodin, A. A.; Jones, J. G.; Zabinski, J. S.; Hultman, L. Plasma Characterization during Laser Ablation of Graphite in Nitrogen for the Growth of Fullerene-like CNx Films. *Journal of Applied Physics* **2002**, *92*, 724–735.

(10) Al-Shboul, K. F.; Harilal, S. S.; Hassanein, A. Spatio-Temporal Mapping of Ablated Species in Ultrafast Laser-Produced Graphite Plasmas. *Applied Physics Letters* **2012**, *100*, 221106.

(11) Kokai, F.; Koga, Y.; Heimann, R. B. Magnetic Field Enhanced Growth of Carbon Cluster Ions in the Laser Ablation Plume of Graphite. *Applied Surface Science* **1996**, *96–98*, 261–266.

(12) Voevodin, A. A.; Laube, S. J. P.; Walck, S. D.; Solomon, J. S.; Donley, M. S.; Zabinski, J. S. Pulsed Laser Deposition of Diamond-like Amorphous Carbon Films from Graphite and Polycarbonate Targets. *Journal of Applied Physics* **1995**, *78*, 4123–4130.

(13) Voevodin, A. A.; Laube, S. J. P.; Walck, S. D.; Solomon, J. S.; Donley, M. S.; Zabinski, J. S. Pulsed Laser Deposition of Diamond-like Amorphous Carbon Films from Graphite and Polycarbonate Targets. *Journal of Applied Physics* **1995**, *78*, 4123–4130.
(14) Riascos, H.; Franco, L. M.; Pérez, J. A. Optical Spectroscopy of Emission from CN Plasma Formed by Laser Ablation. *Phys. Scr.* **2008**, *2008*, 014020.
(15) Amoruso, S.; Ausanio, G.; Vitiello, M.; Wang, X. Infrared Femtosecond Laser Ablation of Graphite in High Vacuum Probed by Optical Emission Spectroscopy. *Appl. Phys. A* **2004**, *81*, 981–986.
(16) Bourquard, F.; Tite, T.; Loir, A.-S.; Donnet, C.; Garrelie, F. Control of the Graphite Femtosecond Ablation Plume Kinetics by Temporal Laser Pulse Shaping: Effects on Pulsed Laser Deposition of Diamond-Like Carbon. *J. Phys. Chem. C* **2014**, *118*, 4377–4385.
(17) Pearse, R. W. B.; Gaydon, A. G. *The Identification of Molecular Spectra*; Chapman and Hall LTD, 1965.
(18) Striganov, A. R.; Sventitskii, N. S. *Tables of Spectral Lines of Neutral and Ionized Atoms*; Springer US: Boston, MA, 1968.
(19) M. Guillermin; J. P. Colombier; S. Valette; E. Audouard; F. Garrelie; R. Stoian. Optical Emission and Nanoparticle Generation in Al Plasmas Using Ultrashort Laser Pulses Temporally Optimized by Real-Time Spectroscopic Feedback. *Phys. Rev. B* **2010**, *82*, 035430.
(20) Rodil, S. E.; Muhl, S. Bonding in Amorphous Carbon Nitride. *Diamond and Related Materials* **2004**, *13*, 1521–1531.
(21) Ferrari, A. C.; Rodil, S. E.; Robertson, J. Interpretation of Infrared and Raman Spectra of Amorphous Carbon Nitrides. *Phys. Rev. B* **2003**, *67*, 155306.
(22) F. Bourquard; J. -P. Colombier; M. Guillermin; A. -S. Loir; C. Donnet; R. Stoian; F. Garrelie. Temporal Pulse Shaping Effects on Aluminium and Boron Ablation Plumes Generated by Ultrashort Pulsed Laser Ablation and Analyzed by Time- and Space-Resolved Optical Spectroscopy. *Applied Surface Science* **2012**, *258*, 9374–9378.
(23) Jeschke, H. O.; Garcia, M. E.; Bennemann, K. H. Theory for the Ultrafast Ablation of Graphite Films. *Phys. Rev. Lett.* **2001**, *87*.
(24) Garcia, M. E.; Jeschke, H. O. Theoretical Approach to the Laser-Induced Melting of Graphite under Different Pressure Conditions. *Applied Surface Science* **2003**, *208–209*, 61–70.
(25) Garrelie, F.; Champeaux, C.; Catherinot, A. Study by a Monte Carlo Simulation of the Influence of a Background Gas on the Expansion Dynamics of a Laser-Induced Plasma Plume. *Appl Phys A* **1999**, *69*, 45–50.

Chapter 5. Amorphous carbon nitride thin film electrodes for analytical microsystems

5.1 Introduction

The sensor is defined as a device, which brings out some quantitative information about the real world. An electrochemical sensor is a device that transforms electrochemical information into an analytically useful signal. Electrochemical sensors are usually composed of two basic components, a chemical (molecular) recognition system, which is the most important part of a sensor and a physicochemical transducer, which is a device that converts the chemical response into a signal that can be detected by electrical instrument [1,2]. All the processes depend on the electrodes materials and their quality. The next important function related to the topic of electrode material (a-C:N), is the passivation resistance in an aggressive working environment. Owing to it, the testing of new prospective materials with electrochemical stability in a wide scale of applied potential (wide potential window), fast electron transfers (higher reactivity) and with a high resistance to passivation (enable to reuse) is necessary. The carbon-based materials showed a big potential in this area, and now the research is focused on the investigation of such film properties (microstructure, surface character, chemical composition, and electrochemical properties), are appropriate for their applications in sensors [3]. Amorphous carbon nitride (a-C:N) films are very interesting electrode materials, due to their wide potential window, which allowed a wide number of transfer reactions without decomposition of reactants in water due to reduction or oxidation reactions in various electrolytes [4]. Although, the boron-doped diamond (BDD) is still more common in industry applications, and the amorphous carbon nitride films could be aspirate to be a better substitution of BDD in near future. The electrochemical properties of both electrodes (BDD and a-C:N) are comparable, but the a-C:N films are cost effective, can be deposited at low temperature and without using any toxic gas during elaboration.

In this work, we investigate the electrochemical properties of the amorphous carbon nitride (a-C:N) electrodes, which are deposited by femtosecond pulsed laser deposition with and without DC plasma assistance. The detailed deposition procedures are described in the Chapter 2. The

aim is to find the ideal a-C:N electrode for the electrochemical applications. We also performed the detection of heavy metal and showed the ability to functionalize the surface to increase the sensitivity of a-C:N electrode to biomolecules detection in future.

5.2 Electrochemical properties of a-C:N films

5.2.1 Chemicals

Ferrocene dimethanol (Sigma-Aldrich), sodium perchlorate anhydrous (Alfa Aesar), sodium nitrite, 97% (Sigma-Aldrich), hydrochloric acid, 97% (Sigma-Aldrich), 4-ethynylaniline, 97% (Sigma-Aldrich), Tris[(1-benzyl-1H-1,2,3-triazol-4-yl)methyl]amine or TBTA (Sigma-Aldrich), cupper(II) sulfate, anhydrous (Sigma-Aldrich), dimethyl sulfoxide (DMSO) ,99%, ethanol, 99% were commercially available and used without any purification. Aqueous buffers and electrolytes were made with deionized water purified through a Milli-Q system (Millipore, Bedford, MA). 2-azidoethyl ferrocene (Fc-Azide) was synthesized as described by Ripert *et al*.[5].

The plasma assistance deposited films showed delamination due to their poor adhesion to the substrate. The films that have been deposited with plasma assistance showed delamination problems due to the poor adhesion to the Si_3N_4 substrate. To overcome this problem, we chose the Si substrate. The film adhesion to the Si substrate by femtosecond pulsed laser was performed by one of our group members [6]. The films deposited with plasma assistance were tested in the water for the delamination problem before testing their electrochemical properties. We did not observe any delamination problem. We chose a wide range of N content a-C:N films for the electrochemical measurements, from 0 to 21 at.% in range (N content from EELS). The film deposition conditions are at 10 at.% of N deposited at 1 Pa P_{N2} pressure and 15 at.% of N deposited at 5 Pa P_{N2} pressure, and 21 at.% of N deposited at 5 Pa P_{N2} pressure and at 250 V DC bias voltage. However, DC bias induces an increase of the structural disorder, as well as a substantial increase of the nitrile group in the films. Therefore, we chose an optimized DC bias voltage for the electrochemical performance.

5.3 Cyclic voltammetry (CV) of a-C:N electrode

The Figure 5.1 shows a background cyclic voltammetric *i-E* curves (CV) in 0.1 M $NaClO_4$ of amorphous carbon (a-C) and amorphous carbon nitride (a-C:N) (deposited at 10 Pa P_{N2} pressure) films at scan rate 100 mV/s at room temperature. The voltammograms covers a wide potential range allowing determination of the working potential window from -0.2 to +0.6 V, where no electrochemical activity of the a-C:N films is observed.

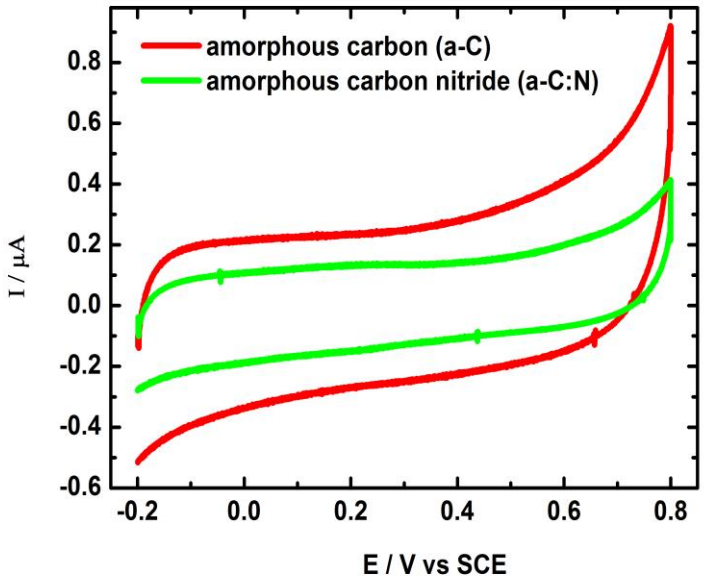

Figure 5. 1 Background cyclic voltammetric i-E curves for a-C and a-C:N (deposited at 10 Pa P_{N2} pressure) electrodes in 0.1 M $NaClO_4$, at room temperature, scan rate 100 mV/s.

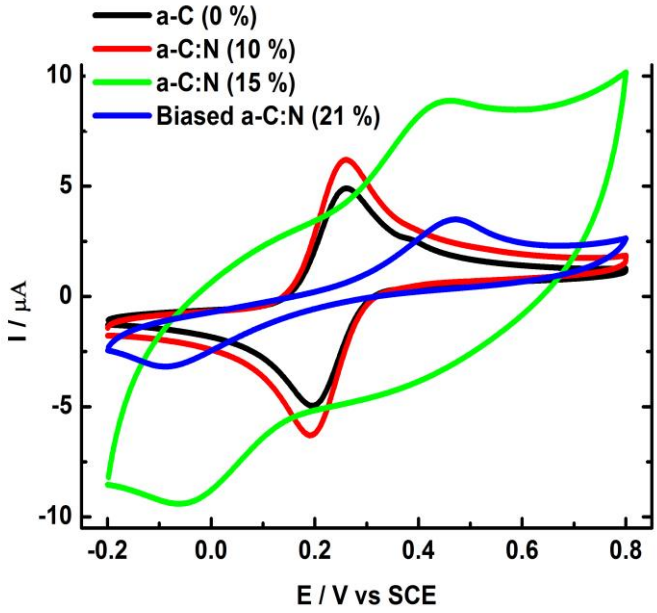

Figure 5. 2 Cyclic voltammetry of 0.5 mM ferrocene di-methanol in 0.1M $NaClO_4$ solution, on a-C, a-C:N and bias a-C:N films, scan rate 100 mV/s.

The Figure 5.2 shows the cyclic voltammetry (CV) obtained with the a-C film, the a-C:N(10 at.%) film deposited at 1 Pa, the a-C:N(15 at.%) film deposited at 5 Pa, and the 250 V biased a-C:N(21 at.%) film deposited at 5 Pa, in presence of ferrocene di-methanol. Although all electrodes exhibit ferrocene detection, the peak-to-peak potential separation depends considerably on the nitrogen content. The CV data are presented in the Table 5.1 for a single scan rate of 100 mV/s. The I_p^{ox}/I_p^{red} current intensity ratios of all films are close to unit for the films without nitrogen and with a nitrogen content of 10 at.%. The peak-to-peak potential separation ΔE_p for the a-C and a-C:N(10 %) electrodes are close to the theoretical value of 59 mV [7], according to the equation 2.1 stated in chapter 2. Higher nitrogen contents exhibit very larger potential difference ΔE_p values, due to more insulating properties.

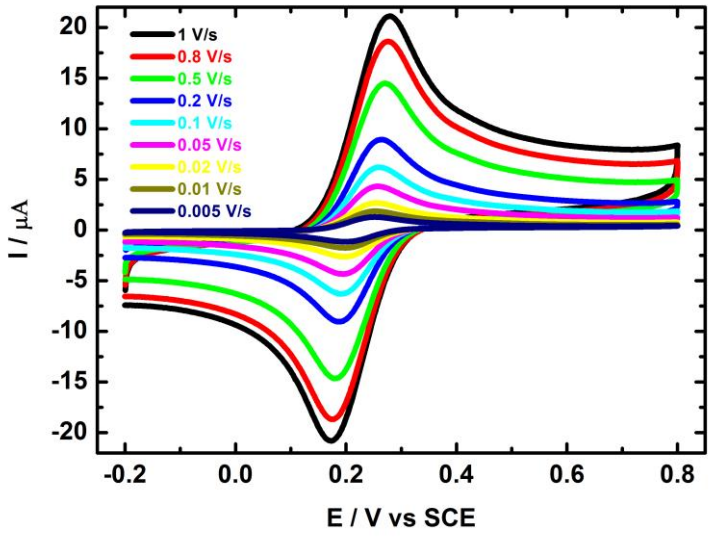

Figure 5. 3 Cyclic voltammograms (CV) of a-C:N (10 % of N deposited at 1 Pa P_{N2} pressure) electrode in 0.5 mM $Fc(CH_2OH)_2$ in 0.1 M $NaClO_4$ at different scan rates (showed in inset).

The Figure 5.3 shows the scan rate dependence of cyclic voltammograms for the ferrocene di-methanol redox reaction on the a-C:N(10%) electrode. The anodic to cathodic peak current ratio are close to one and the peak-to-peak potential separation ΔE_p increases as the scan rate increases (Table 5.1). The films showed a reproducible peak potential after 3 weeks of storage. The electron transfer kinetics depicted in Table 5.1 were calculated for a-C and a C:N(10 at.%) films by using Nicholson method [[8]]. The diffusion coefficient of $Fc(CH_2OH)_2$ was 6.4×10^{-6} cm^2/s [[9]], and the electron transfer coefficient (α) was equal to 0.5 for scan rate below 20 mV/s. Full details of the Nicholson method can be found in the Appendix A. The film electrode showed a quasi-reversible electron transfer with a heterogeneous rate constant k^o value in the order of 7.85×10^{-2} cm/s and 5.12×10^{-2} cm/s respectively for a-C and a-C:N(10 at.%) films. The obtained k^0 values are quite close to the value of k^o measured by scanning electron microscopy on a single layer graphene electrode with ferrocene di-methanol, 2.0×10^{-2} cm/s [[10]]. The above results indicates that the ferrocene is adapted as a future redox probe for amorphous carbon nitride (a-C:N) electrodes. The ferrocene di-methanol redox probe is showing faster electron transfer kinetics than the ferri/ferrocyanide (10^{-5} to 10^{-3} cm/s), the quinone/hydroquinone (10^{-7} cm/s), and the

hexaamineruthenium (10^{-5} to 10^{-4} cm/s). The ferrocene di-methanol redox probe transfer kinetics is comparable to the hexachloroiodate (2 x 10^{-2} to 5 x 10^{-2} cm/s) [11–14].

P_{N2} pressure (Pa)	N content (at.%)	ΔEp (mV)	I_p^{ox} / I_p^{red}	k°/cm s^{-1}
a-C (0 Pa)	0 %	63	1.04	7. 85 x 10^{-2}
a-C:N (1 Pa)	10 %	65	1.01	5. 12 x 10^{-2}
a-C:N (5 Pa)	15 %	397	1.5	-
Biased a-C:N (5 Pa, -250 V)	21 %	528	1.85	-

Table 5. 1 Potential difference values ΔEp, ratio of anodic to cathodic peak currents (Ipox/Ipred) and apparent rate constant data k° of different films, at a scan rate 100 mV/s.

5.4 Influence of film properties on electrochemical performances of a-CN electrodes

Generally, the electrochemical properties of films depend on the films microstructure, chemical composition and N content respectively. We systematically studied the relation between film microstructures and electrochemical properties of films. The film microstructures and chemical compositions were studied by Raman spectroscopy and X-ray photoelectron spectroscopy (XPS). The detailed structural and chemical analyses were described in the chapter 3. In this section, we tried to correlate the electrochemical properties with its microstructure and chemical properties of a-C:N films.

5.4.1 Effect of microstructural properties of a-C:N films on electrochemical performances

The Figure 5.4 shows the relation between film microstructure (I(D)/I(G) and La) and the electrochemical potential values (ΔEp). The dominance of I(D)/I(G) ratio increases the potential values and show the slow transfer kinetics. From the correlation, the high nitrogen content films increase the I(D)/I(G) ratio and the cluster sizes, which cause the decrease of the electrochemical

properties of films performance. That confirms that the bigger cluster size and the high intensity ratio containing films are not suitable for electrochemical applications, and the good electrodes need a fine tuning of the I(D)/I(G) ratio along with the cluster size (La).

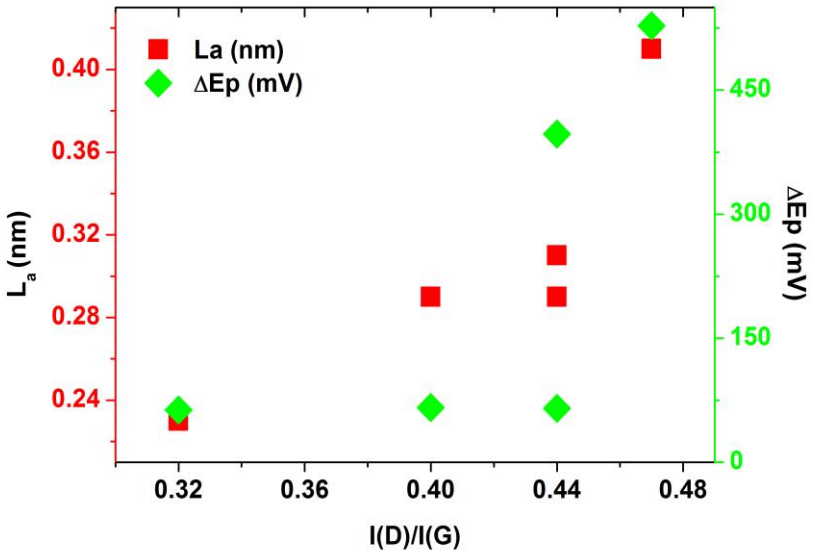

Figure 5.4 The correlation between the Raman parameters and electrochemical properties.

5.4.2 Chemical composition of a-C:N films on electrochemical properties

XPS analysis is used to determine the chemical composition and the relative concentration of the chemical bonding configurations in the films. The detailed chemical analyses of films were described in the chapter 3. In this section, we tried to correlate the relation between the chemical properties and the electrochemical properties of a-C:N electrodes.

The a-C:N films deposited at a higher nitrogen content showed more graphitic like structure and higher nitrogen bonding atoms. From a practical point of view, the ideal nitrogen concentration and the type of bonds are required for a good electrode material in electrochemistry applications [[15]]. The Figure 5.5 shows the correlation between the nitrogen content and the potential difference values. From our XPS results, it is evident that the films with the lowest nitrogen contents and a more graphitic like structures show a better electrochemical performance.

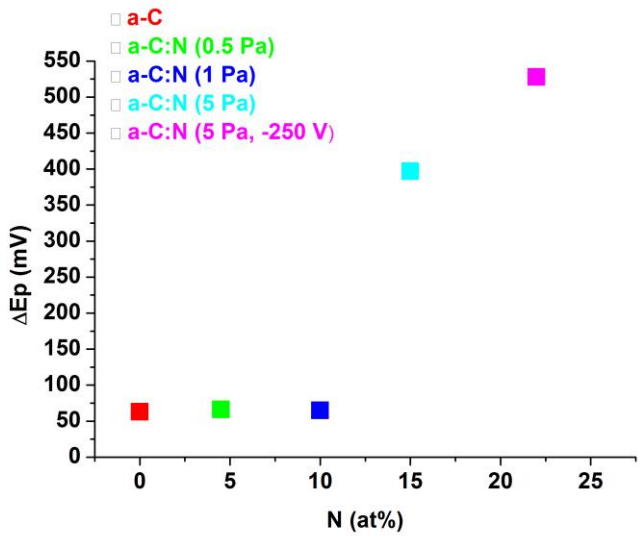

Figure 5.5 The influence of nitrogen content on electrochemical properties.

Based on our above analysis of results, we chose amorphous carbon nitride deposited at 1 Pa N_2 partial pressure without DC bias as an ideal electrode for electrochemical applications. The a-C:N film with 10 at.% of nitrogen shows different chemical bonding sites, less disordered clustered rings, a low potential difference value, and mainly fast redox transfer kinetics. We performed the detection and functionalization of surface on the a-C:N film with 10 at.% of nitrogen deposited at 1 Pa nitrogen pressure electrode to show ability of heavy metals detection and surface functionalization for bio molecules attachment on the surface.

5.5 Detection of heavy metals by an a-C:N (10 at.%) electrode

In our industrial society, pollution by highly toxic heavy metals, with very low toxicity limits induces urgent needs to develop both curative and detection technologies. The environmental impacts and health consequences are important and are global scourge. The precise and selective detection of these ions in wastewater is thus a primary health priority [16–18]. Many techniques have been developed for the *in-situ* quantification of pollutants prior to industrial or public wastewater treatment [19–23]. To quantify the heavy metals in solutions, some electrochemical detection techniques have been developed in the last decades taking advantages of mercury based electrodes (hanging mercury drop or thin mercury fil electrodes), which have been widely

employed [24]. However, because of the toxicity and the inconvenient disposal of mercury, many studies have been conducted aiming to design mercury free or environmentally friendly electrodes. Towards this motivation, Wang *et al*. have built up bismuth electrodes presenting performances similar to that of thin mercury film. However, bismuth film electrodes are relatively having low chemical stability [25,26]. Another alternative that has been developed during last years, carbon based electrodes for electrochemical detection [20,25,27–31]. Thus, boron doped diamond [19,32,33], boron doped nanocrystalline diamond thin film [29], modified glassy carbon electrode [34,35], and amorphous carbon nitride [36,37] films were demonstrated as good candidates for industrial applications aiming to detection of different types of pollutants. Unlike diamond based materials, amorphous carbon nitride thin films present mainly sp^2 carbon [37–41], and are far easier and considerably cheaper to develop. Furthermore, their properties could be adjusted easily by varying doping concentration and chemical compositions.

The electrochemical behavior of several a-C:N electrodes with different N concentrations was tested (presented in the last section), from those results the films presenting the best electron exchange reversibility (higher heterogeneous rate constant k^o) and low potential difference value electrode has been selected for detection of Pb^{2+} and the covalent surface functionalization through diazonium electrografting.

Detection of single Lead ion (Pb^{2+})

The Lead ion (Pb^{2+}) detection was carried out by the Differential Pulse Anodic Stripping Voltammetry (DPASV) at low concentration, measurements were performed using a Palm-Sens sensor PC system (Eindhoven, The Nederlands) was used to apply to the a-C:N (10 at.%) electrode, being connected to the PC computer with a specific software. The electrochemical cell was a 100 µL cylindrical shaped one, having a circular neck opening one side, allowing the solution to be in contact with a-C:N electrode and a O-ring rubber was placed to ensure the sealing. The detection was studied by using the Differential pulse anodic stripping voltammetry (DPASV) method. In this method, the potential of accumulation was chosen usually at -1.7 vs SCE for 20 s. The potential scan was performed from -1.7 to + 0.3 V/ SCE with a scan rate of 50 mV/s.

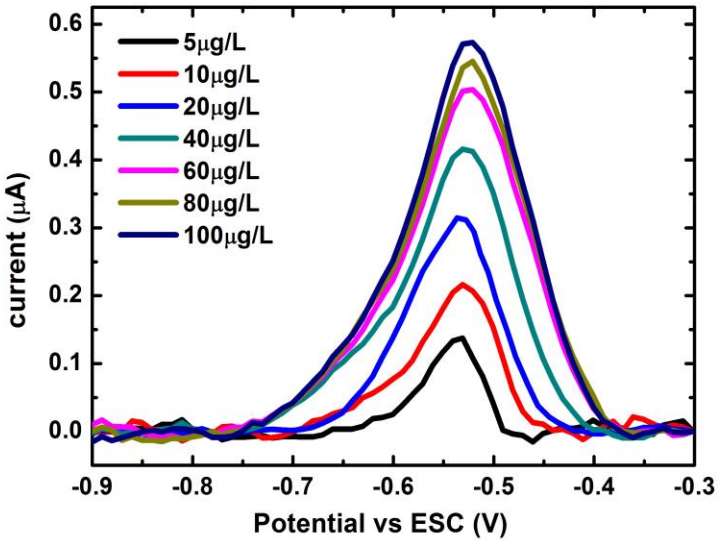

Figure 5.6 Voltammograms of a-C:N (10 at.%) electrode in 0.1 M potassium citrate and HCl buffer PH 2 for different Pb concentrations, Deposition potential is -1.7 V vs. SCE, Potential step 10 mV, scan rate 50 mV/s.

The Figure 5.6 shows the DPASV voltammograms obtained for increasing lead (Pb^{2+}) concentrations ranging from 5 to 100 µg/L in 0.1 M acetate buffer solution, using the a-C:N(10 %) film as electrode. The Pb dissolution peak was found around -0.55 V vs. SCE. There was a slight shift of the peaks for higher concentration values, which might be predicted by Nernst's equation as the concentration increases. The Figure 5.7 shows the plot of peak current as a function of the Pb^{2+} ion concentration. The corresponding calibration plot reveals that the peak current increases with Pb concentration, the linear range being from 5 to 40 µg/L. A saturation effect appears for concentrations higher than 60 µg/L. The limit of detection (LOD) values was found to be 5 µg/L and 1.5 µg/L. LOD, smallest measured content, from which it is possible to deduce the presence of the analyte with reasonable statistical certainty. The limit of detection is numerically equal to three times the standard deviation of the mean of the blank determinations. These analytical characteristics are close to those obtained on BDD electrodes [42].

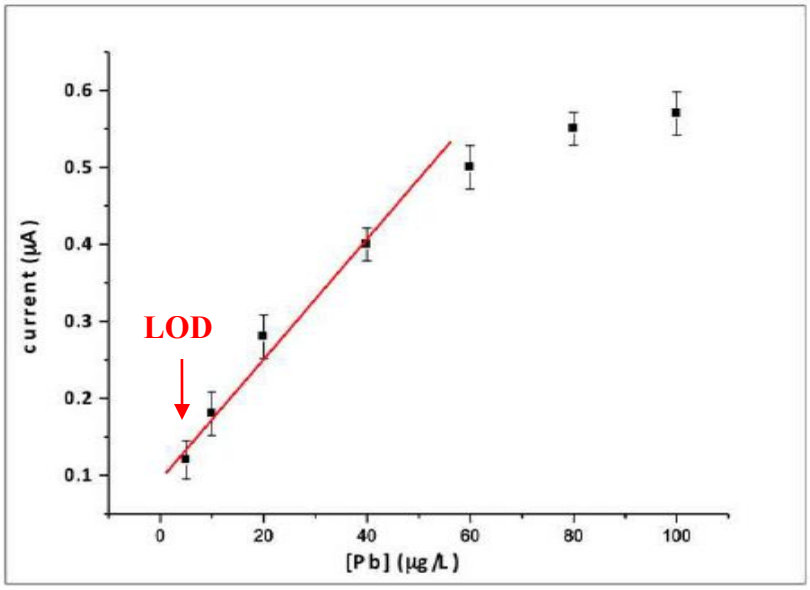

Figure 5.7 Evolution of the peak current as a function of Pb concentration for a-C:N (10 at.%) electrode deposited at 1 Pa, scan rate 50 mV/s.

5.6 Electrochemical functionalization of a-C:N (10 at.%) electrode

The functionalization of surfaces at the molecular level, with biological, redox/active, or photo chemical sensitive molecules is of central interest in the development of molecular electronics [43,44], energy conversion [45] and chemical and biological sensing [46,47]. The electrografting has been to characterize the electrochemical reactions that permit binding of organic layers to a solid conducting surface [48]. Here, we propose a covalent modification of amorphous carbon electrode (a-C:N) through the "aryldiazonium salt chemistry" to introduce alkyne functionalities of a-C:N electrode surface further modification through the click chemistry. The diazonium salt chemistry has been studied on various advanced carbon materials [49] like Glassy carbon electrode [50], Boron doped diamond [51] and graphene [52,53]. The reduction of in situ generated diazonium salts by cyclic voltammetry (CV) offers several advantages in order to modify the carbon electrodes i.e., strong linkage low cost, fast preparation and easy control of grafted molecules. Click chemistry provides a highly selective and quantitative reaction, which is well suited for electrode surface functionalization. For instant, Ripert *et al*.[5] used the click chemistry to address an azido-modified ferrocene onto gold electrode previously functionalized with alkyne functions. Yeap *et*

al.[51] reported a grafting strategy on BDD surface coupling an alkynyl-ferrocene derivatives on azido-modified BDD. The 4-ethynylphenyl diazonium salt and electrografting and subsequent click reaction with ferrocene on amorphous carbon nitride electrode not yet been reported.

5.6.1 In-situ generation of diazonium salt and grafting of 4-ethynylphenyl group

The surface functionalization of a-C:N electrodes was carried out at 4°C in a solution degassed with nitrogen of 0.1M HCl containing 40mM $NaNO_2$ and 2 mM 4-ethynylaniline. The 4-ethynylaniline was first dissolved in HCl 0.1M and $NaNO_2$ was added just before grafting. The electrochemical cell was degassed with nitrogen before grafting. The electrochemical grafting of the *in-situ* generated diazonium salt was performed by CV starting from the 0.4V vs SCE to -0.8V vs SCE with a scan rate of 0.1V/s repeated by 3 times. After the functionalization, the electrochemical cells containing all the electrodes were rinsed thoroughly with a Milli-Q water, ethanol and kept 2 hours in each solvent to ensure the removal of any adsorbed species.

5.6.2 Click reaction of ferrocene-azide with 4-ethynylphenyl modified a-C:N electrode

The 4-ethynylphenyl functionalized a-C:N electrodes were treated 16 hours at ambient temperature with a DMSO:H_2O 1:1 solution containing 1mM of Fc-Azide, 5mM of sodium ascorbate, 1mM of TBTA and 2.5 mM of copper(II) sulfate. The copper (II) sulfate was added just before starting the reaction. After the functionalization, the electrochemical cells containing all the electrodes were thoroughly rinsed with Milli-Q water and ethanol and the electrode was kept (or immersed) 16 hours in water to ensure the complete elimination of any physisorbed species.

5.6.3 Electrochemical characterization of functionalized a-C:N electrode

The electrochemical characterization of a-C:N electrodes has been done by CV starting from -0.2 V vs SCE to 0.8 V vs SCE repeated 3 times in an aqueous solution containing $NaClO_4$ 0.1M as support electrolyte without any redox species in the solution. Several scan rates have been tested from 1 V s^{-1} down to 50 mV s^{-1}. Only the last cycles have been used for data interpretations. The

amount of grafted ferrocene has been calculated by the integration of oxidation and reduction peaks, the average of both values were used for the grafted ferrocene amount determination.

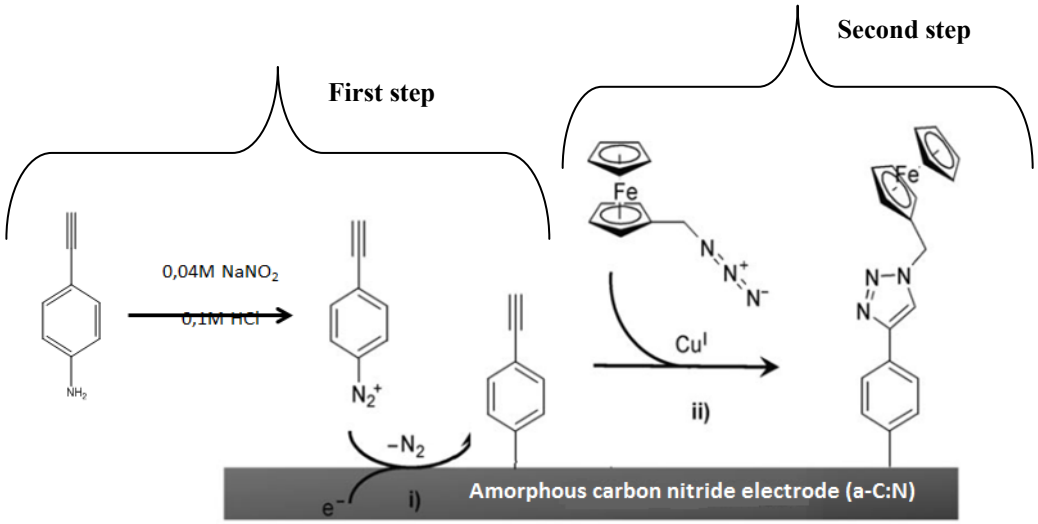

Figure 5.8 Schematic of synthetic route used for the synthesis of grafted molecules.

The functionalization of a-C:N (10 at.%) electrode is shown in the Figure 5.8, the functionalization of a-C:N with a ferrocene derivative was performed in two steps. The first step (shown in the Figure 5.8) consisted in modifying the self-organized a-C:N electrode with alkyne function through an electrografting of 4-ethynyl diazonium salt under reduction potential applied through a cyclic voltammogram. The diazonium derivative was in situ generated from the 4-ethynyl aniline upon adding hydrochloric acid and sodium nitrite in the solution. The second step (shown in the Figure 5.8) is a Cu^{1} catalyzed Huisgen 1,3-dipolar cycloaddition between the 4-ethynylphenyl grafted electrode and Fc-Azide. The grafting behavior is shown in the Figure 5.9. The first scan (blue curve in the Figure 5.9) is characteristic for diazonium reduction. The reduction peak at -0.18 V vs SCE can be related to the formation of the 4-ethynylphenyl diazonium salt and its reduction at the electrode forms the radical that reacts to form a covalent bound between a-C:N electrode and the phenyl ring. The two subsequent cycles show passivation of the electrode by the electrochemical grafted layer, which blocks the access of the diazonium salt. This electrochemical behavior is characteristic and indicates that the a-C:N electrode surface was well functionalized with 4-ethynylphenyl groups. Similar results with 4-ethynylaniline were obtained on glassy carbon and pyrolytic graphite electrodes [[50]]. The redox probe was chosen as a

model to optimize the experimental conditions of grafting and to prove that this method was an easy route for a-C:N functionalization. The attachment of ferrocene group after electrografting and click reaction was studied by using CV at various scan rates. The analysis of the peak currents as a function of scan rates showed a linear relationship, which indicated the ferrocene was bounded to the electrode (Figure 5.10).

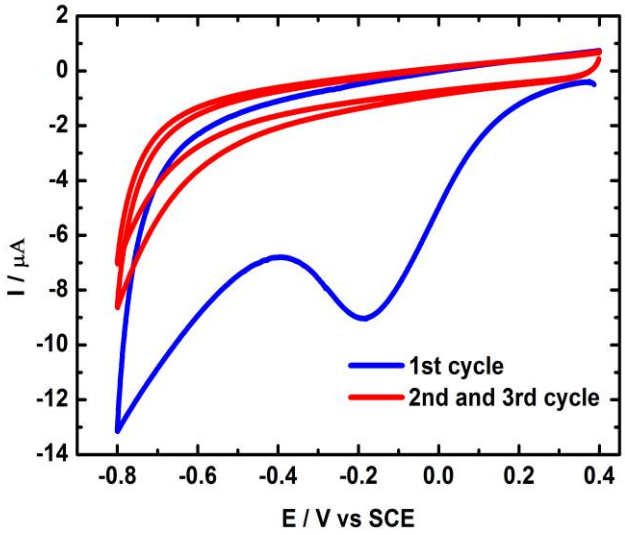

Figure 5.9 Cyclic voltammogram (CV) of the in-situ generated 4-ethynylphenyl diazonium salt on a-C:N (10 at.% of N) electrodes at 0.1V/s in HCl 0.1M containing 40 mM $NaNO_2$ and 2 mM 4-ethynylaniline. The solution is at 4°C and degassed with N_2. In blue are shown the first CV scan, than in red the two consecutive scans.

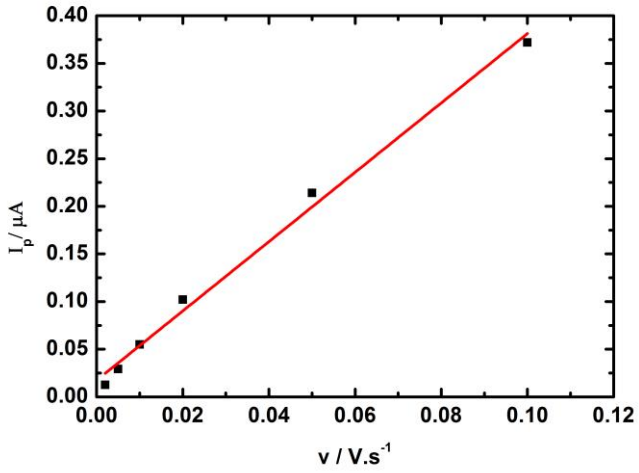

Figure 5.10 The anodic peak currents as a function of scan rates after ferrocene attachment to the a-C:N (10 at.%) electrode deposited at 1 Pa P_{N2} pressure.

The linearity confirms the efficient grafting of the ferrocene onto the electrode. The bell-shaped CV (Figure 5.11) and the linear relationship of anodic peak current versus scan rate (Figure 5.10) are characteristic of grafted redox probe on the a-C:N electrode.

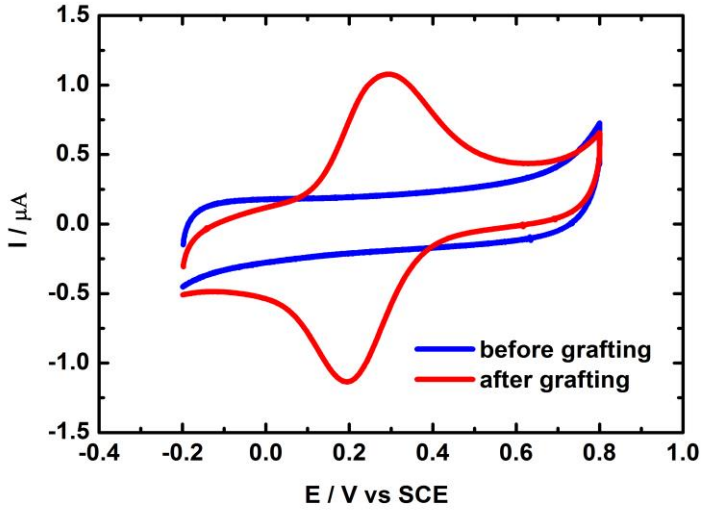

Figure 5.11 Voltammograms in 0.1 M $NaClO_4$ at 0.1 V/s of a a-C:N electrode, the data in blue shows a voltammogram of the bare a-C:N electrode before electrografting and click reaction procedure. The data in red shows a voltammogram of the Fc-modified self-organized a-C:N electrode performed by electrografting and click reactions procedure.

The high signal stability overtime (21 days) was another strong indication of a covalent grafting of ferrocene at the electrode. The ferrocene coverage (Γ in mol/cm^2) on the a-C:N electrode was estimated from the coverage of the charge (Q) of the anodic and cathodic peaks on the voltammograms and by assuming a one-electron transfer with the following equation.

$$\Gamma = Q/nFS$$

in which n=1 is the number of electrons involved during the redox event, F is the Faraday's constant, and S is the area of the exposed electrode (0.07 cm^2).

The ferrocene coverage was estimated to be 3.9x10^{-10} mol. cm^{-2}. The ferrocene coverage on our amorphous carbon nitride (a-C:N) electrode is higher than the amount grafted on glassy carbon (GC) [50] and BDD electrodes [51] modified by similar techniques using aryl diazonium salt and click chemistry to link ferrocene to the a-C:N electrode. To conclude from the electrochemical characterization of a-C:N electrode, The amount grafting on a-C:N electrode is higher than the BDD and GC electrodes [50,54] and the value is close to the dense packed monolayer of ferrocene [55]. We successfully grafted higher ferrocene molecules (3.9x10^{-10} mol/cm^2) on a-C:N electrode than the recently published one (3.7x10^{-10} mol/cm^2) [56]. The higher amount of grafted molecules gives the advantages of higher sensitivity for further sensing applications.

5.7 Conclusions

The a-C:N films have been synthetized by femtosecond pulsed laser ablation in various conditions of N_2 pressure and DC bias, thus allowing to explore the structure of the films as well as their electrochemical properties within a nitrogen concentration range from 0 to 21 at.%. The main conclusions are the following:

1. The a-C:N electrodes were shown as good electrochemical properties, such as wide potential window, fast electron transfer kinetics and lower potential difference values. These properties make them as good electrodes in electrochemical sensors.
2. The electrochemical results are consistent with the film structures. The a-C:N films deposited with DC bias exhibit a less conductive behavior compared to the films obtained

without DC bias. The increase of the structural disorder in the films is detrimental to their electrochemical behavior.

3. The best electrochemical performance has been obtained with the low nitrogen containing films. The a-C:N electrode containing 10 at.% of nitrogen, deposited at 1 Pa of N_2 without DC bias assistance showed the best electrochemical performance.
4. The potential difference values of the a-C:N(10 at.%) are close to the theoretical value, and lower compared to the CVs obtained in ferri-ferrocyanide of glassy carbon (GC) electrode .
5. The a-C:N(10 at.%) electrode shows faster electron transfer kinetics (10^{-2} cm/s) than the other carbon based electrodes such as GC, BDD and a-C:N electrodes in ferri/ferrocyanide and quinone/hydroquinone, and close to transfer kinetics of graphene in hexachlororidate.
6. The a-C:N (10 at.%) electrode shows a good ability to detect lead ions in the 5-40 µg/L concentration range, with a limit of detection of 1.5 µg/L.
7. The surface coverage of the a-C:N(10%) electrode is higher than the BDD and glassy carbon electrodes, and close to the dense packed monolayer of ferrocene. We have shown the ability to achieve a surface coverage of 3.9×10^{-10} mol/cm^2. This method allows a simple, robust and cost effective functionalization compared to other grafting methods.

The present contribution shows that the nitrogen content and the film nanostructure (in terms of cluster size and order) is a paramount parameter for a-C:N films to exhibit a promising electrochemical detection of electroactive pollutants as well as bio pathogen molecules after surface grafting of the specific affinity receptor. It is expected to be an alternative to boron doped diamond (BDD) electrodes in the near future. Particularly, its room temperature deposition, no specific surface treatment and no catalyst for deposition are the significant advantages over diamond electrodes. These advantages makes a-C:N electrode compatible in semiconductor technology to fabricate micro sensors, which can be easily integrated into microfluidic channels to invent lab-on-chip devices.

References

(1) Kimmel, D. W.; LeBlanc, G.; Meschievitz, M. E.; Cliffel, D. E. Electrochemical Sensors and Biosensors. *Anal. Chem.* **2012**, *84*, 685–707.

(2) Bakker, E.; Qin, Y. Electrochemical Sensors. *Anal. Chem.* **2006**, *78*, 3965–3984.

(3) Zhang, W.; Zhu, S.; Luque, R.; Han, S.; Hu, L.; Xu, G. Recent Development of Carbon Electrode Materials and Their Bioanalytical and Environmental Applications. *Chem. Soc. Rev.* **2016**, *45*, 715–752.

(4) Durand-Drouhin, O.; Benlahsen, M.; Clin, M.; Bouzerar, R. Deposition Mechanism of Sputtered Amorphous Carbon Nitride Thin Film. *Appl. Surf. Sci.* **2004**, *223*, 269–274.

(5) Ripert, M.; Farre, C.; Chaix, C. Selective Functionalization of Au Electrodes by Electrochemical Activation of the "click" Reaction Catalyst. *Electrochimica Acta* **2013**, *91*, 82–89.

(6) Loir, A. S.; Garrelie, F.; Donnet, C.; Rogemond, F.; Subtil, J. L.; Forest, B.; Belin, M.; Laporte, P. Towards the Deposition of Tetrahedral Diamond-like Carbon Films on Hip Joints by Femtosecond Pulsed Laser Ablation. *Surf. Coat. Technol.* **2004**, *188–189*, 728–734.

(7) Allen J. Bard, Larry R. Faulkner.pdf.

(8) Nicholson, R. S. Theory and Application of Cyclic Voltammetry for Measurement of Electrode Reaction Kinetics. *Anal. Chem.* **1965**, *37*, 1351–1355.

(9) Zhang, W.; Gaberman, I.; Ciszkowska, M. Effect of the Volume Phase Transition on Diffusion and Concentration of Molecular Species in Temperature-Responsive Gels: Electroanalytical Studies. *Electroanalysis* **2003**, *15*, 409–413.

(10) Velický, M.; Bradley, D. F.; Cooper, A. J.; Hill, E. W.; Kinloch, I. A.; Mishchenko, A.; Novoselov, K. S.; Patten, H. V.; Toth, P. S.; Valota, A. T.; *et al.* Electron Transfer Kinetics on Mono- and Multilayer Graphene. *ACS Nano* **2014**, *8*, 10089–10100.

(11) Xu, J.; Chen, Q.; Swain, G. M. Anthraquinonedisulfonate Electrochemistry: A Comparison of Glassy Carbon, Hydrogenated Glassy Carbon, Highly Oriented Pyrolytic Graphite, and Diamond Electrodes. *Anal. Chem.* **1998**, *70*, 3146–3154.

(12) Ferreira, N. G.; Silva, L. L. G.; Corat, E. J.; Trava-Airoldi, V. J. Kinetics Study of Diamond Electrodes at Different Levels of Boron Doping as Quasi-Reversible Systems. *Diam. Relat. Mater.* **2002**, *11*, 1523–1531.

(13) Ramesham, R. Determination of Flatband Potential for Boron Doped Diamond Electrode in 0.5 M NaCl by AC Impedance Spectroscopy. *Thin Solid Films* **1998**, *322*, 158–166.

(14) Y. U. Evstefeeva. *Russ J Electrochem* **1998**, *34, 934*.

(15) Zeng, A.; Neto, V. F.; Gracio, J. J.; Fan, Q. H. Diamond-like Carbon (DLC) Films as Electrochemical Electrodes. *Diam. Relat. Mater.* **2014**, *43*, 12–22.

(16) Newman, M. C.; McIntosh, A. W. *Metal Ecotoxicology Concepts and Applications*; CRC Press, 1991.

(17) Nriagu, J. O.; Pacyna, J. M. Quantitative Assessment of Worldwide Contamination of Air, Water and Soils by Trace Metals. *Nature* **1988**, *333*, 134–139.

(18) Seck, S. M.; Charvet, S.; Fall, M.; Baudrin, E.; Lejeune, M.; Benlahsen, M. Detection of Cadmium and Copper Cations Using Amorphous Nitrogenated Carbon Thin Film Electrodes. *Electroanalysis* **2012**, *24*, 1839–1846.

(19) El Tall, O.; Jaffrezic-Renault, N.; Sigaud, M.; Vittori, O. Anodic Stripping Voltammetry of Heavy Metals at Nanocrystalline Boron-Doped Diamond Electrode. *Electroanalysis* **2007**, *19*, 1152–1159.
(20) Manisankar, P.; Vedhi, C.; Selvanathan, G.; Arumugam, P. Differential Pulse Stripping Voltammetric Determination of Heavy Metals Simultaneously Using New Polymer Modified Glassy Carbon Electrodes. *Microchim. Acta* **2008**, *163*, 289–295.
(21) Babyak, C.; Smart, R. B. Electrochemical Detection of Trace Concentrations of Cadmium and Lead with a Boron-Doped Diamond Electrode: Effect of KCl and KNO3 Electrolytes, Interferences and Measurement in River Water. *Electroanalysis* **2004**, *16*, 175–182.
(22) Khadro, B.; Sikora, A.; Loir, A.-S.; Errachid, A.; Garrelie, F.; Donnet, C.; Jaffrezic-Renault, N. Electrochemical Performances of B Doped and Undoped Diamond-like Carbon (DLC) Films Deposited by Femtosecond Pulsed Laser Ablation for Heavy Metal Detection Using Square Wave Anodic Stripping Voltammetric (SWASV) Technique. *Sens. Actuators B Chem.* **2011**, *155*, 120–125.
(23) Buffle, J.; Tercier-Waeber, M.-L. Voltammetric Environmental Trace-Metal Analysis and Speciation: From Laboratory to in Situ Measurements. *TrAC Trends Anal. Chem.* **2005**, *24*, 172–191.
(24) Tölg, G. Stripping Analysis. Principles, Instrumentation, and Applications. Von J. Wang. VCH Verlagsgesellschaft, Weinheim 1985. VIII, 160 S., Geb DM 120.00 – ISBN 3-527-26192-3. *Angew. Chem.* **1986**, *98*, 764–764.
(25) Wang, J.; Lu, J.; Hocevar, S. B.; Farias, P. A. M.; Ogorevc, B. Bismuth-Coated Carbon Electrodes for Anodic Stripping Voltammetry. *Anal. Chem.* **2000**, *72*, 3218–3222.
(26) Bučková, M.; Gründler, P.; Flechsig, G.-U. Adsorptive Stripping Voltammetric Detection of Daunomycin at a Bismuth Bulk Electrode. *Electroanalysis* **2005**, *17*, 440–444.
(27) Jovanovski, V.; Hrastnik, N. I.; Hočevar, S. B. Copper Film Electrode for Anodic Stripping Voltammetric Determination of Trace Mercury and Lead. *Electrochem. Commun.* **2015**, *57*, 1–4.
(28) Dragoe, D.; Spătaru, N.; Kawasaki, R.; Manivannan, A.; Spătaru, T.; Tryk, D. A.; Fujishima, A. Detection of Trace Levels of Pb2+ in Tap Water at Boron-Doped Diamond Electrodes with Anodic Stripping Voltammetry. *Electrochimica Acta* **2006**, *51*, 2437–2441.
(29) Sonthalia, P.; McGaw, E.; Show, Y.; Swain, G. M. Metal Ion Analysis in Contaminated Water Samples Using Anodic Stripping Voltammetry and a Nanocrystalline Diamond Thin-Film Electrode. *Anal. Chim. Acta* **2004**, *522*, 35–44.
(30) Nagles, E.; Arancibia, V.; Rojas, C.; Segura, R. Nafion–mercury Coated Film Electrode for the Adsorptive Stripping Voltammetric Determination of Lead and Cadmium in the Presence of Pyrogallol Red. *Talanta* **2012**, *99*, 119–124.
(31) Wang, J.; Tian, B. Screen-Printed Stripping Voltammetric/potentiometric Electrodes for Decentralized Testing of Trace Lead. *Anal. Chem.* **1992**, *64*, 1706–1709.
(32) Zhao, G.; Tong, X.; Hu, Z.; Xiao, X.; Li, D. Electrochemical Costripping Models and Mutual Interferences of Mutli-Transition Metal Systems on the Surface of Boron-Doped Diamond. *Electrochimica Acta* **2008**, *53*, 4283–4292.
(33) Becker, D.; Jüttner, K. Influence of Surface Inhomogeneities of Boron Doped CVD-Diamond Electrodes on Reversible Charge Transfer Reactions. *J. Appl. Electrochem.* **2003**, *33*, 959–967.

(34) McGaw, E. A.; Swain, G. M. A Comparison of Boron-Doped Diamond Thin-Film and Hg-Coated Glassy Carbon Electrodes for Anodic Stripping Voltammetric Determination of Heavy Metal Ions in Aqueous Media. *Anal. Chim. Acta* **2006**, *575*, 180–189.
(35) Dai, X.; Compton, R. G. Detection of As(iii) via Oxidation to As(v) Using Platinum Nanoparticle Modified Glassy Carbon Electrodes: Arsenic Detection without Interference from Copper. *The Analyst* **2006**, *131*, 516.
(36) Lagrini, A.; Deslouis, C.; Cachet, H.; Benlahsen, M.; Charvet, S. Elaboration and Electrochemical Characterization of Nitrogenated Amorphous Carbon Films. *Electrochem. Commun.* **2004**, *6*, 245–248.
(37) Tamiasso-Martinhon, P.; Cachet, H.; Debiemme-Chouvy, C.; Deslouis, C. Thin Films of Amorphous Nitrogenated Carbon a-CNx: Electron Transfer and Surface Reactivity. *Electrochimica Acta* **2008**, *53*, 5752–5759.
(38) Ferrari_PRB2003.pdf.
(39) Kimura, T.; Nishimura, R. Formation of Amorphous Carbon Nitride Films by Reactive Ar/N $_2$ High-Power Impulse Magnetron Sputtering. *Jpn. J. Appl. Phys.* **2015**, *54*, 01AD06.
(40) Benlahsen, M.; Cachet, H.; Charvet, S.; Debiemme-Chouvy, C.; Deslouis, C.; Lagrini, A.; Vivier, V. Improvement and Characterization of the Electrochemical Reactivity of Amorphous Carbon Nitride Electrodes. *Electrochem. Commun.* **2005**, *7*, 496–499.
(41) Lagrini, A.; Charvet, S.; Benlahsen, M.; Debiemme-Chouvy, C.; Deslouis, C.; Cachet, H. Microstructure and Electronic Investigations of Carbon Nitride Films Deposited by RF Magnetron Sputtering. *Thin Solid Films* **2005**, *482*, 41–44.
(42) Amel Sbartai; Philippe Namour; Abdelhamid Errachid; Jan Krejči; Romana Šejnohová; Louis Renaud; Mohamed Larbi Hamlaoui; Anne-Sophie Loir; Florence Garrelie; Christophe Donnet; *et al.* Electrochemical Boron-Doped Diamond Film Microcells Micromachined with Femtosecond Laser: Application to the Determination of Water Framework Directive Metals. *Anal. Chem.* **2012**, *84*, 4805–4811.
(43) Aswal, D. K.; Lenfant, S.; Guerin, D.; Yakhmi, J. V.; Vuillaume, D. Self Assembled Monolayers on Silicon for Molecular Electronics. *Anal. Chim. Acta* **2006**, *568*, 84–108.
(44) James, D. K.; Tour, J. M. Self-Assembled Molecular Electronics. In *Nanoscale Assembly*; Huck, W. T. S., Ed.; Nanostructure Science and Technology; Springer US, 2005; pp. 79–98.
(45) Grätzel, M. Solar Energy Conversion by Dye-Sensitized Photovoltaic Cells. *Inorg. Chem.* **2005**, *44*, 6841–6851.
(46) Willner, null; Katz, null. Integration of Layered Redox Proteins and Conductive Supports for Bioelectronic Applications. *Angew. Chem. Int. Ed Engl.* **2000**, *39*, 1180–1218.
(47) Willner, I.; Katz, E. Redoxproteinschichten Auf Leitenden Trägern – Systeme Für Bioelektronische Anwendungen. *Angew. Chem.* **2000**, *112*, 1230–1269.
(48) Bélanger, D.; Pinson, J. Electrografting: A Powerful Method for Surface Modification. *Chem. Soc. Rev.* **2011**, *40*, 3995–4048.
(49) McCreery, R. L. Advanced Carbon Electrode Materials for Molecular Electrochemistry. *Chem. Rev.* **2008**, *108*, 2646–2687.
(50) Evrard, D.; Lambert, F.; Policar, C.; Balland, V.; Limoges, B. Electrochemical Functionalization of Carbon Surfaces by Aromatic Azide or Alkyne Molecules: A

Versatile Platform for Click Chemistry. *Chem. Weinh. Bergstr. Ger.* **2008**, *14*, 9286–9291.

(51) Yeap, W. S.; Murib, M. S.; Cuypers, W.; Liu, X.; van Grinsven, B.; Ameloot, M.; Fahlman, M.; Wagner, P.; Maes, W.; Haenen, K. Boron-Doped Diamond Functionalization by an Electrografting/Alkyne–Azide Click Chemistry Sequence. *ChemElectroChem* **2014**, *1*, 1145–1154.

(52) Huang, P.; Jing, L.; Zhu, H.; Gao, X. Diazonium Functionalized Graphene: Microstructure, Electric, and Magnetic Properties. *Acc. Chem. Res.* **2013**, *46*, 43–52.

(53) Bekyarova, E.; Itkis, M. E.; Ramesh, P.; Berger, C.; Sprinkle, M.; de Heer, W. A.; Haddon, R. C. Chemical Modification of Epitaxial Graphene: Spontaneous Grafting of Aryl Groups. *J. Am. Chem. Soc.* **2009**, *131*, 1336–1337.

(54) Downard, A. J. Electrochemically Assisted Covalent Modification of Carbon Electrodes. *Electroanalysis* **2000**, *12*, 1085–1096.

(55) Lee, L.; Leroux, Y. R.; Hapiot, P.; Downard, A. J. Amine-Terminated Monolayers on Carbon: Preparation, Characterization, and Coupling Reactions. *Langmuir* **2015**, *31*, 5071–5077.

(56) Jribi, S.; Cordoba de Torresi, S. I.; Augusto, T.; Cachet, H.; Debiemme-Chouvy, C.; Deslouis, C.; Pailleret, A. Determination of Surface Amine Groups on Amorphous Carbon Nitride Thin Films Using a One Step Covalent Grafting of a Redox Probe. *Electrochimica Acta* **2014**, *136*, 473–482.

Chapter 6. N doped graphene: The future material for advanced technology

6.1 Introduction

Carbon materials have been investigated very intensively due to their extraordinary properties, which makes them very useful in various applications. In this work, the amorphous carbon nitride materials were studied as potential candidates to be used as electrodes in electrochemical sensors. Although the amorphous carbon nitride thin films showed good electrochemical properties (wide potential window, fast electron transfer, grafting with ferrocenedimethanol), according to the theoretical and pilot studies, graphene is the best currently known material with excellent properties [1–3]. Graphene has attracted tremendous attention in the fields of electronics, catalysis, energy storage, sensors and in many more potential applications [1,4–6]. Graphene presents unique physical and chemical properties, such as high surface area (~2630 m^2/g) [2,3,7], excellent conductivity, ease of functionalization and production [8,9]. It is widely used for the design of electrochemical electrodes because of their relatively wide working potential window, low background current, better electron transfer kinetics and relative chemical inertness in most electrolyte solutions, this has opened a new window to the electrochemical biosensors research [3,7,10–15]. These properties stimulated an intense activity between the researchers and scientists. Many researches have been focused on developing routes for the controllable growth of high quality graphene. Historically, the graphene can be produced via micromechanical cleavage and SiC decomposition methods [1,16]. In order to meet even higher requirements, such as a good crystallinity, less impurities and large area coverage, the present most successful fabrication technique focuses on chemical vapor deposition (CVD) on copper [16,17]. Some other graphene growth methods have also been reported in the recent years including growth of graphene from solid carbon source, graphene synthesis by ion implantation, and graphene formation by decomposition of C_{60} [18]. Apart from these, pulsed laser deposition (PLD) is one of the unique physical vapor deposition (PVD) methods, which is a new fabrication method of graphene from solid carbon source.

Until now, there are only a few studies on PLD based graphene. Indeed, such method used in graphene fabrication originates from the growth of carbon thin film by PLD technique. If a single carbon layer with aromatic ring structure in plane can be obtained, it gives results of a single layer graphene. For the PLD method, the amorphous C layer can be easily deposited at room temperature. However, in order to fabricate C layer or graphene with desirable crystalline quality by PLD, some other conditions are required. For example, high substrate temperature, vacuum level inside PLD chamber, appropriate laser operation conditions (i.e. laser fluence and repetition rate) and choice of catalytic metal are to be properly chosen. Wang, *et al*. [19] has demonstrated that few layer graphene that is bi-layer to multi-layer graphene can be fabricated on catalytic nickel (Ni) thin film by PLD system. The number of graphene layers is found depending on the laser ablation time, and the crystallinity of the graphene depends on the substrate temperature during laser ablation. During the graphene formation, it involves several steps, such as C atoms adsorption, precipitation, segregation and recrystallization. All these processes happen due to the interaction between C atoms and metals. The formation of the graphene on the metal surface was first observed during the preparation of platinum (Pt) and ruthenium (Ru) single crystal surfaces [20,21]. In fact, the study of the interaction of the C atom and the metals has a long history. However, the graphene fabricated by PLD method is realized in recent years. By comparing with a conventional CVD method, which usually involves high processing temperature (<1100^{o}C) and chemical reactive hydrocarbon gas flow, PLD can reach the same goal at relatively lower temperatures. Koh, *et al.*,[22] have demonstrated that few layer graphene can be fabricated at 750^{o}C on Ni plate. Recently, Tite *et al*.,[23] presented the successful growth of graphene by PLD and demonstrated its potential use in SERS applications. Apart from temperature issue, they also showed that the cooling rate and laser energy are crucial parameters in fabricating such graphene layers. In this chapter, we will present the growth mechanisms of N doped graphene from amorphous carbon nitride thin films.

Metal induced crystallization method, also known as metal mediated or metal catalyzed crystallization method, is a crystalline technique to fabricate mono or polycrystalline materials via the inter diffusion, precipitation, segregation and recrystallization of two materials upon thermal annealing. One of them performs as the catalyst. It is usually a metal, such as aluminum (Al), gold (Au), platinum (Pt), nickel (Ni), cobalt (Co) [21,24–26], while the other chosen is a

semiconductor material, such as germanium (Ge) and silicon (Si). This technique has been widely explored in past years, in particularly for the polycrystalline Si thin film based solar cell investigation [27]. It has been proposed and experimentally demonstrated in fabricating high crystalline quality and large area polycrystalline Si thin film on various kinds of substrates at low temperature. For both CVD and PVD method used for graphene fabrication, metal induced crystallization method acts as a dominating role during the graphitization process at elevated temperature. One way to realize this method in graphene growth is that amorphous C layer can be easily changed to crystalline graphene layer based on thermal annealing process. This process uses solid carbon sources. In this approach, the carbon was introduced in the amorphous phase with the Ni thin film forming bi-layer stack. Upon high temperature annealing, the C atoms from the a-C layer would dissolve into the Ni layer and be expelled from solution after cooling below the solid solubility limit. By comparing with previous studies about metal-induced Si crystallization, similar mechanism is involved. The driving force for crystallization is thermodynamic stability of the crystalline C and Si phases relative to the amorphous phase.

Graphene is a zero bandgap material and it shows a metallic behavior for many electronic applications. However, its electrical conductivity is not completely controlled like a classical semiconductor. Theoretical and experimental studies have revealed that substitutional doping can alter the Fermi level and introduce a metal to semiconductor transition in graphene [28–30]. Therefore, we concentrate on N doped graphene synthesis, characterization and its possible future potential applications. This chapter focuses on a new synthesis route of N doped graphene.

6.2 Nitrogen doped graphene

Doping is the most feasible method to control the semiconducting properties in the conventional semiconductor community. The B and N atoms are the natural candidates for doping in carbon based materials such as amorphous carbon and graphene, because of their similar atomic size as that of C and of their hole acceptor and electron donor characters for substitutional B- and N-doping, respectively.

Among possible chemical choices for carbon modification, nitrogen functionalization has long been a natural and widely studied option. Nitrogen-containing carbon structures have attracted

great attention in large part because of their abundance, accessibility, and low health risk. In recent years, the study of carbon and nitrogen has expanded into the sub-stoichiometric regime of nitrogen-modified carbons. This modification allows for the beneficial properties of the carbon to be utilized while finely tuning the final electrical, morphological, and chemical properties of the functionalized carbon network [31–33].

Nitrogen is the natural choice for efficient and beneficial modification due to three specific reasons. Firstly, N is one neighbor away from C on the periodic table and by replacing one C with N in the carbon network the total number of electrons in the system can be tailored one electron at a time. Secondly, N has an atomic radius similar to that of C, thereby preventing significant lattice mismatch. Thirdly, N-doping can induce an n-type electronic modification to the carbon structure, in analogy to typical semiconducting materials, which enables the potential use of these C–N structures in multiple important applications. The substitutional doping is also a useful method to open bandgap of graphene as proved by the theoretical work about B-, N- and bi-doping in graphene [34,35]. Through first-principles density functional theory (DFT) and *ab initio* calculations, the effect of substitutional doping on the structure of graphene as well as on the electronic properties was studied [36]. The results reveal that the linearity in the dispersion of electronic bands within 1 eV of the Fermi energy is almost unchanged with B- and N-doping, indicating that the doped graphene exhibits the band structure with a linear dispersion relation similar to the band structure of pristine graphene. Nevertheless, bandgap is opened in graphene after substitutional doping with B and N atoms, and the Fermi level lies in valence and conduction band, respectively, showing ideal *p*- and *n*-type semiconducting electronic properties for potential applications of graphene in electronic devices.

Many research works on N doped graphene (NG) have emerged in recent years. Recently, a number of approaches have been proposed to synthesize nitrogen doped graphene by direct synthesis [37–40] and post treatment [41–43]. The various synthesis approaches and characterization techniques have been explored to obtain N-graphene. The Figure 6.1 shows the overview of different deposition methods, characterization techniques have been used to study the N doped graphene, and it shows possible potential applications. However, the method for production of large-scale N graphene is still lacking. Moreover, synthesizing N-graphene meets problems similar to those encountered during the fabrication of N-CNT. First, controlling the nitrogen type and distribution is unresolved. Second, to achieve nitrogen doping at specific positions on

nitrogen atom in the C network and with precise control of doping content is still a challenge, thus new synthesis methods need to be developed [30].

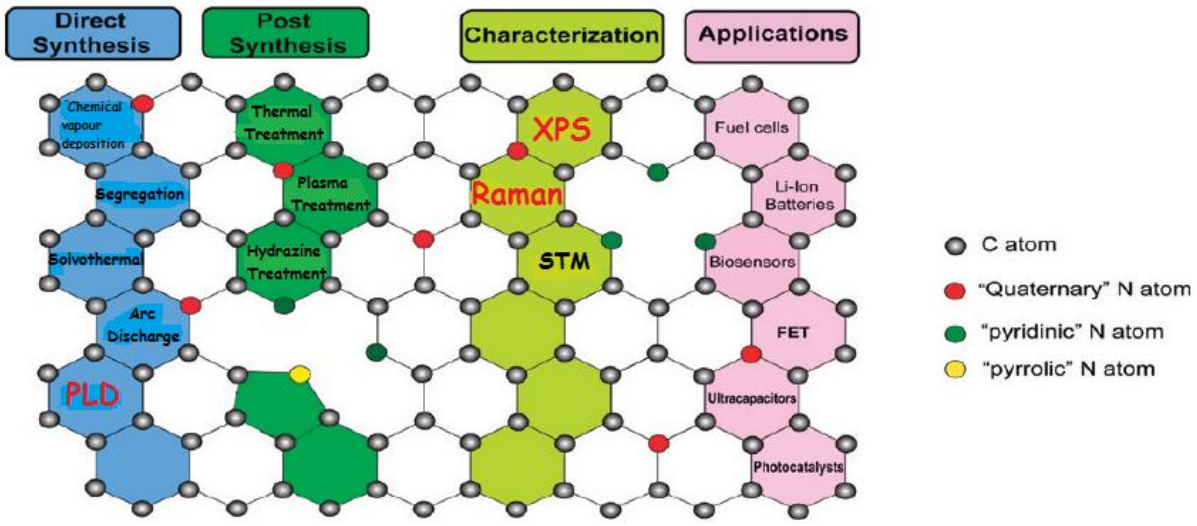

Figure 6. 1 Various synthesis methods to introduce N doping and various characterization techniques used for the examination of N doping extracted from [30], our N doped graphene synthesis approach and characterization techniques are included.

We have developed a simple and fast processing technique based on fs-pulsed laser deposition (PLD) to grow few layer graphene and N doped graphene (NG) at reduced temperatures of 780^{o}C. We choose Ni as catalyst. The Ni has received great attention as catalyst for graphene and N doped graphene growth. We chose Ni because it is inexpensive and is a standard material for wide range of applications [44,45]. Here, we report a new approach, which makes use of amorphous carbon nitride films deposited over a metal substrate to prepare N doped graphene. The concerns are mainly on the deposited amorphous carbon and the amorphous carbon nitride layers thickness. Our approach is the utilization of a common segregation phenomenon to turn trace amount of amorphous carbon (a-C) and amorphous carbon nitride (a-C:N) dissolved in bulk metals through vacuum annealing process. We synthesized the graphene and the N doped graphene films by femtosecond pulsed laser deposition route of carbonaceous films. This approach provides a simple, fast, cost effective, and low temperature synthesis route, and the open possibility to control the N doping content in graphene.

6.3 Experimental procedure for N doped graphene synthesis

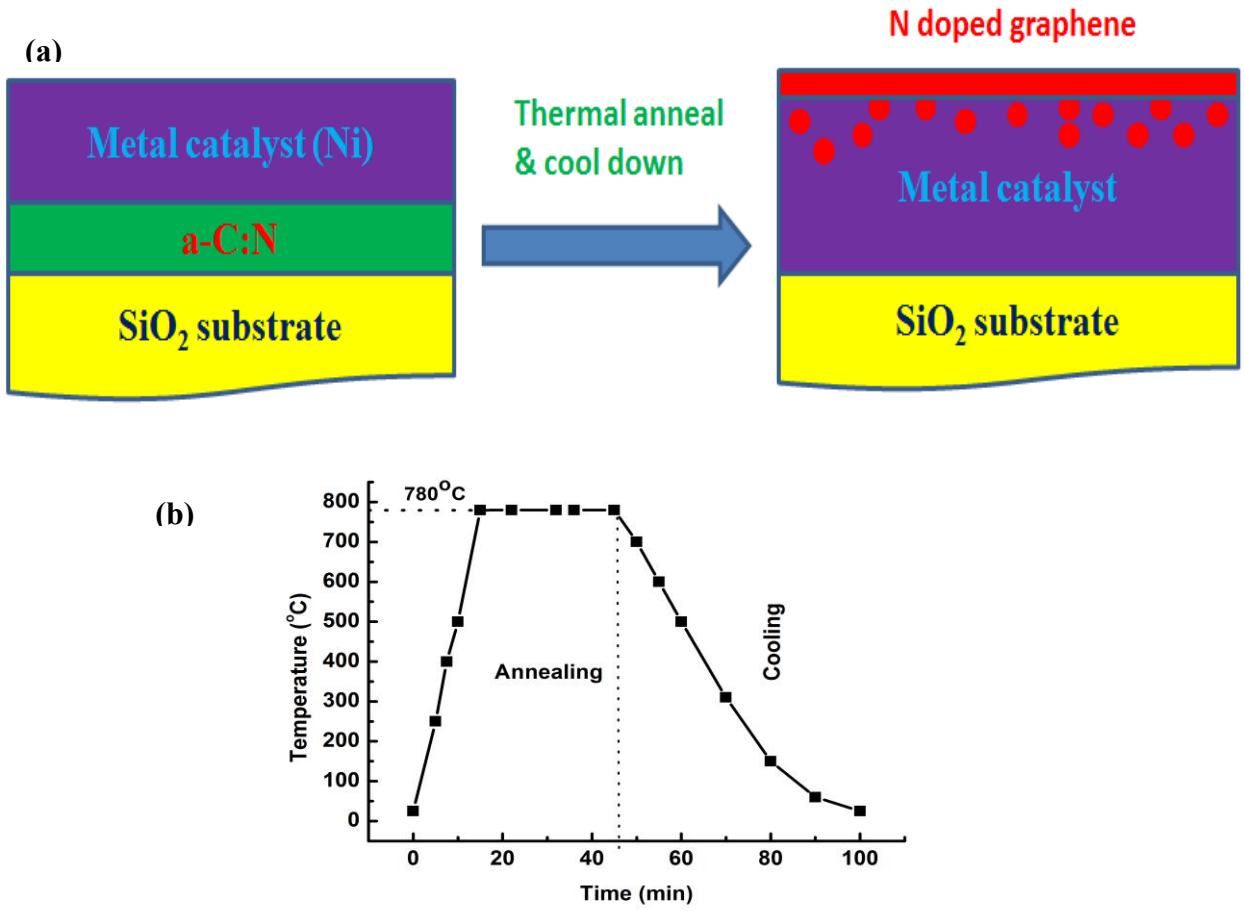

Figure 6. 2 (a) Schematic representation of N doped graphene growth from amorphous carbon nitride (a-C:N) thin film deposited by fs-PLD, (b) shows a temperature profile of N doped graphene.

The Figure 6.2a shows the synthesis procedure of N doped graphene (NG) from sandwich type of substrate. Our graphene and N doped graphene are synthesized through vacuum annealing of a sandwiched Ni(153nm)/a-C(10nm)/SiO_2 (or) Ni(153nm)/a-C:N(10nm)/SiO_2 substrate at low temperatures. The Figure 6.2b shows the temperature ramp and the cooling conditions of N doped graphene. A thin amorphous carbon (a-C) or amorphous carbon nitride (a-C:N) thin films were prepared by femtosecond pulsed laser deposition (fs-PLD). The deposition of films is performed at room temperature by ablating a graphite target onto SiO_2 substrates. The N content was 16 at.% in a-C:N films.

The detailed deposition procedure of a-C and a-C:N films were described in chapter 2. The thickness of the a-C and a-C:N films, measured by a profilometer (Vecco Dektak), is controlled by the deposition time. The experimental parameters are shown in Table 6.1.

	a-C	a-C:N
Laser source	Ti: sapphire 800 nm	
Pulse width	60 fs	
Pulse energy	1 mJ	
Repetition rate	1 kHz	
Fluence	5 J/cm²	
Deposition rate	10 nm/min	2.5 nm/min
N_2 pressure	-	10 Pa
N content	-	16 at.%
Catalyst thickness (Ni)	153 nm	
Annealing temp (°C)	780°C	
Cooling Rate	5°C /min	
Annealing time (min)	30 min	

Table 6. 1 Experimental conditions for femtosecond PLD of a-C and a-C:N films, catalyst film thickness and annealing conditions.

6.4 Results and Discussions

The films have been characterized by various techniques; microstructural and chemical composition have been studied by Raman spectroscopy, and X-ray photoelectron spectroscopy, and the surface morphology has been studied by Scanning electron microscopy (SEM) and Atomic force microscopy(AFM), respectively.

6.4.1 Microstructural properties of N doped graphene: Raman spectroscopy

The characterization and quantitative studies of graphene and N doped graphene mainly relay on fast and nondestructive Raman spectroscopy [46–48]. In the past decades, it has been witnessed that Raman spectroscopy plays an important role in characterizing pyrolytic graphite, glassy carbon, graphitic foams, carbon fibers and carbon nanotubes. Owing to the presence of sp^2 bonds in graphene, Raman spectroscopy gives plenty of inspired information about crystallite size, the

introduction of chemical impurities, the optical energy gap, the elastic constant, the doping defects, the crystal disorder, the strain and number of graphene layers. With this respect, the discussion about fs-PLD fabricated graphene and N doped graphene will be addressed.

a) Graphene

The Figure 3 shows the Raman spectra of Ni/a-C/SiO_2 samples before and after being annealed at 780^{o}C for 30 min in vacuum. The a-C films deposited at room temperature without any annealing show broad peaks at 1100-1800 cm^{-1} and 2500-3500 cm^{-1} indicating amorphous nature of the samples (Figure 6.3, black curve). After thermal annealing at 780^{o}C the spectra showed sharp peaks (Figure 6.3, red curve). The annealed samples showed the characteristics of graphene fingerprints of D, G and 2D peaks [47,49]. The presence of well-defined D, G and 2D features observed at ~1380 cm^{-1}, ~1587 cm^{-1} and ~2740 cm^{-1} in the present study reveals the formation of graphene layers. No shoulder was observed on the low frequency side of the 2D peak, suggesting that the stacking between the layers is not AB stacking (without turbostratic graphite) and the interlayer coupling is rather weak [23].

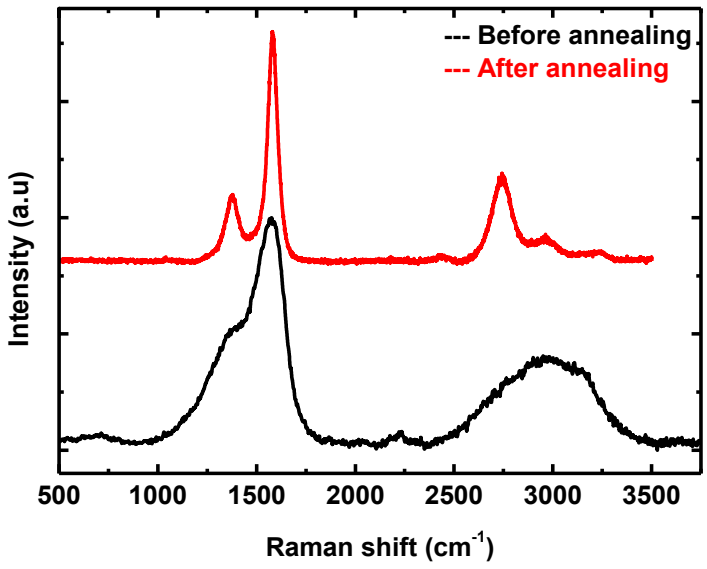

Figure 6. 3 Raman spectra at 442 nm of Ni/a-C (10 nm)/SiO_2 before annealing (black curve), and after annealing at 780oC (red curve).

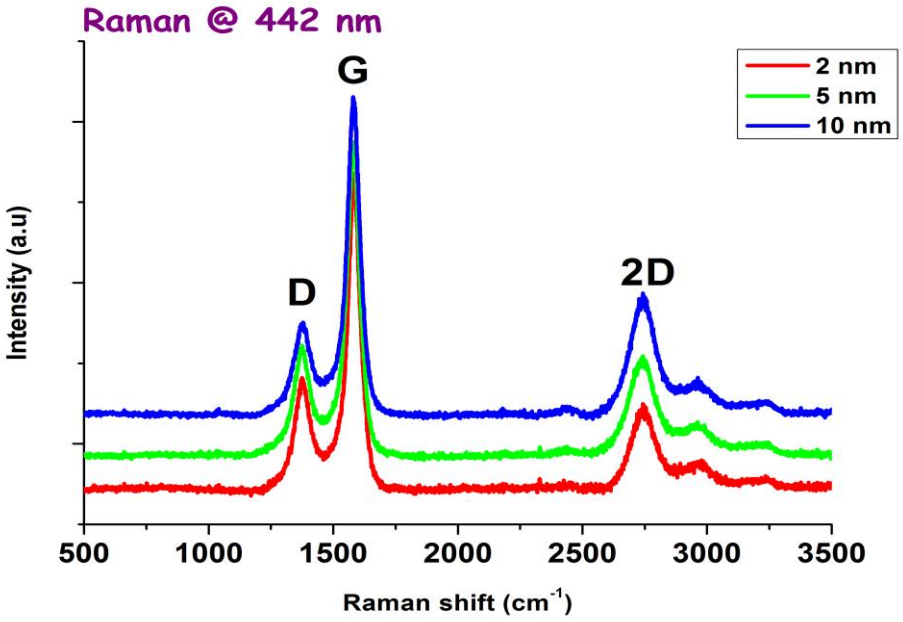

Figure 6. 4 Raman spectra of graphene deposited at different amorphous carbon (a-C) thicknesses Ni/a-C (2nm, 5 nm, 10 nm)/ SiO_2 at 442 nm.

The G peak is due to the doubly degenerate zone center E_{2g} vibrational mode, D peak is related to the defects and the 2D peak is due to a second order of the D peak, which originates via a participation of two phonons with opposite wave vectors leading to momentum conservation [16,47]. From graphene spectra by determining the I_{2D}/I_G, I_D/I_G ratio and full width half maximum (FWHM) of 2D peak, one can inform the quality of graphene layers [16,47,49,50]. The intensity ratio of I_{2D}/I_G is ~0.4, which indicates the formation of few layer graphene [23,49,51]. This synthesis route has been inspired by the work of Tite *et al.,* [23] in our laboratory. They have synthesized grapheme layers from a-C films elaborated by ns-PLD and have shown the interest of such graphene as robust platform for SERS applications.

The Figure 6.4 shows the thickness dependent Raman spectra of graphene at a Raman wavelength of 442 nm. In this scheme, we found the number of graphene layers and the intensity ratio of D and 2D bands to G band greatly affected by the thickness of the a-C layer. The D band is less intensive and the 2D band is greater among those three spectra when the thickness of the a-C layer is at 10 nm. The most notable feature is the appearance of 2D peak, whose position and

shape revealed the formation of bilayer or few layer graphene (FLG) [47,49]. The film with 10 nm of a-C thickness shows a very prominent 2D band compared to the other a-C thicknesses (2 and 5 nm). Then we chose the optimization thickness of C layer at 10 nm, throughout the deposition of a-C and a-C:N films.

The formation of graphene on nickel substrate was explained by the diffusion and the segregation process [26,52]. First carbon atoms diffuse into the nickel lattice while annealing at the temperature 780^{o}C and form solid solutions. While cooling, the carbon atom segregates onto the surface of nickel substrate and forms an atomic layer thick graphene. The important conclusion is the improvement of the results compared with the previously reported data by ns-PLD [53] and moreover a comparable intensity ratio of I_{2D}/I_G with those obtained by filtered cathodic vacuum arc technique and standard reduced graphene oxide [17,54]. As we know, there is more sp^2 content when a-C is grown by fs-PLD than by ns-PLD [55], more sp^2 content a-C is favorable to fast grow graphene and require less annealing time. The quality and the number of graphene layers depend on the thickness of a-C film. In our case, we grew the graphene by fs-PLD at a lower a-C thickness of 10 nm, which is less compared to some already reported graphene growth techniques, so we expect that we can grow good quality and few layer graphene by fs-PLD at low annealing temperature and time. The graphene obtained from a-C grown by fs-PLD presents less defective sites since the I_{2D}/I_D is lower in our case. More reduced thicknesses of a-C films of 2-5 nm and characterization techniques are required to comment precisely on the quality and the number of graphene layers.

b) N doped graphene

Raman spectroscopy is an effective tool to detect the doping effect of Graphene [30,44,47,56]. The Figure 6.5 shows the comparison between Raman spectra of graphene and N doped graphene at a wavelength of 633 nm. From the Figure 6.5, we can clearly see that the 2D band intensity of N doped graphene decreased (clearly showed in inset) with the nitrogen doping compared to the intensity of graphene 2D band, which confirms the insertion of nitrogen in graphene network [57,58].

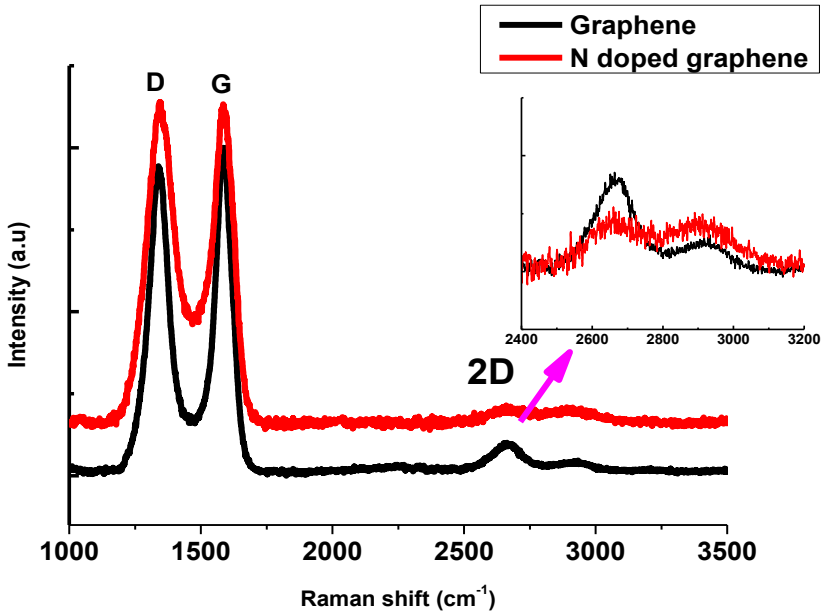

Figure 6. 5 Raman spectra of graphene (Ni/a-C(10 nm)/SiO_2) and N doped graphene (Ni/a-C:N(10 nm)/SiO2), where D, G and 2D denote the characteristic D band, G band and 2D band of graphene, at Raman wavelength 633 nm (inset shows the enlarged 2D zone).

The Figure 6.6a shows the typical Raman spectra of N doped graphene at 442 nm excitation wavelength. The Figure 6.6b shows the Raman mapping of N doped graphene. The NG present three intense Raman features, which are assigned to D, G and 2D peaks at ~1378 cm^{-1}, 1582 cm^{-1} and 2737 cm^{-1} in NG, respectively. The D peak is located at ~1370 cm^{-1}, which is activated by defects, *i.e*., in plane substitution, heteroatoms, vacancies or grain boundary edges [56,59], through an inter-valley double resonance Raman process, in which the defects provide the missing momentum in order to satisfy the resonant process.

The D peak in graphene and N doped graphene is due to the activation of defects. By doping of nitrogen atoms in the graphene network, the intensity of D peak rises in N-doped graphene rapidly, the defects may include bonding disorder and vacancies in graphene lattice by nitrogen doping.

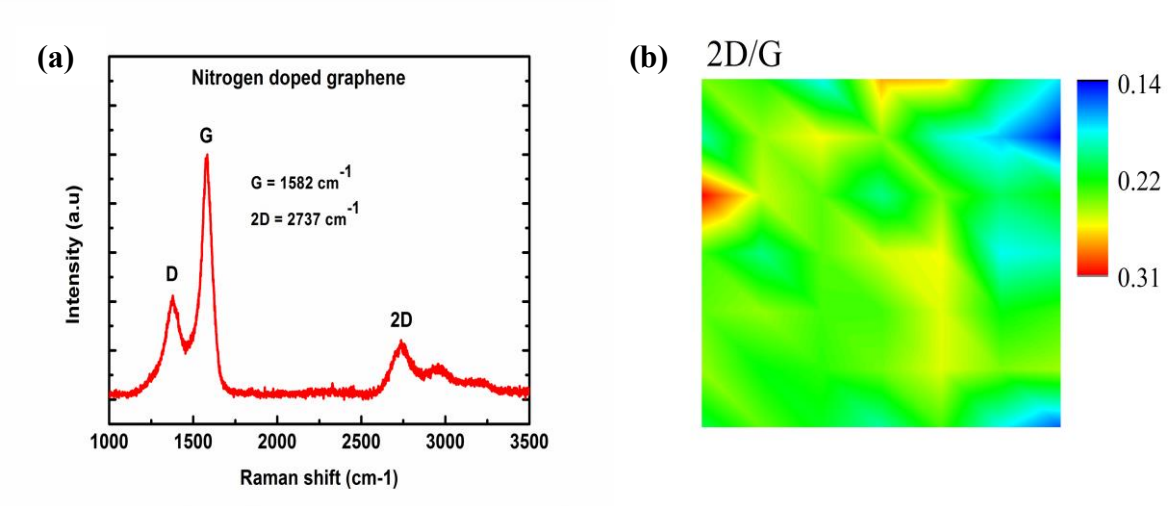

Figure 6. 6 Raman spectra of (a) N doped graphene deposited at Ni(153nm)/a-C:N(10nm)/SiO_2, (b) Raman map showing the variation in 2D/G peak intensity ratio over a 30 µm x 30 µm area of N doped graphene sample, at Raman wavelength of 442 nm.

The different Raman parameters were listed in Table 6.2, deduced from deconvolution of Raman spectra of graphene and N doped graphene. One can clearly see from the Table 6.2 that the intensity ratio I_D/I_G of graphene (I_D/I_G=0.38) and N doped graphene (I_D/I_G=0.63), is increased by N doping. This is the indication that doping of graphene, will introduce defects. The 2D peak originates from the two phonon double resonant process and it does not need defects to fulfil the resonant condition [56,59]. The intensity of 2D peak is strongly affected by the electron/hole scattering rate [56,6039,61].

Previous studies revealed that the intensity of 2D peak is sensitive to the lattice defects and doping in graphene [60]. The I_{2D}/I_G ratio of N doped graphene is smaller than the graphene (Table 6.2). The decrease of the intensity of the 2D peak in NG is shown by Raman mapping (Figure 6.6b). The Raman mapping also confirms the homogenous doping in graphene.

Raman @ 442 nm	D (cm^{-1})	G (cm^{-1})	2D (cm^{-1})	I(D)/I(G)	I(2D)/I(G)	La (nm)
Graphene	1375	1578	2742	0.38	0.38	24
N-doped graphene	1378	1582	2737	0.63	0.2	14

Table 6. 2 Raman parameters deduced from deconvolution of Raman spectra at 442 nm of graphene and N doped graphene.

The 2D to G intensity ratio (I_{2D}/I_G) in N doped graphene which is at value of 0.2, is much lower than the reported value of 0.6, which corresponds to a doping level of $> 4 \times 10^{13}$ cm^{-2} [57].

We observed a small shifting of G and 2D peak in NG compared to the graphene. The amount of blue shift is 4 cm^{-1} and red shift 5 cm^{-1} for G and 2D peak in N doped graphene compared to the graphene respectively. There are several possible origins for the shifting of Raman peaks, including effect of doping and strain [57,62]. The shifting of G and 2D peak values are comparable with previous reported data [63]. The electron/hole doping in graphene affects the interaction between optical phonons and the Dirac fermions transitions across the zero bandgap of graphene. Hence, the G band phonon shows a stiffening as well as bandwidth sharpening with doping. For 2D peak, the influence of dynamic effects is very weak and it is only affected by the modification of the equilibrium lattice parameters with a consequent stiffening/softening of the phonons, with the hole doping resulting in a blue shift, and the opposite is true for electron doping [57]. Nitrogen doping was found to introduce n-doping in graphene and carbon nanotubes [39,64,65], and hence should cause a blue shift of G peak and red shift of 2D peak [65] or no obvious 2D peak shift as presented by Das *et al*., [57]. Therefore, the blue shift of G and red shift of 2D peak in our system confirm the doping is a n–type doping even though a very small shift of G and 2D peak was observed.

The width of D, G and 2D peaks in N doped graphene are broadened in contrast to the graphene, which can be attributed to the various bonding structures and defects after doping. The ratio of D

to G bands integrated intensities (I_D/I_G) can be used to estimate the crystallite size (L_a) of graphene [46,47]. We calculated La of graphene according to the following equation [66].

$$L_a(nm) = (2.4X10^{-10})\lambda^4 \left(\frac{I_D}{I_G}\right)^{-4} \qquad (1)$$

where, λ is Raman excitation wavelength (λ=442 nm).

The I_D/I_G ratio of graphene and N doped graphene are taken at 0.38 and 0.63, which corresponds to crystallite sizes of 24 nm and 14 nm, respectively. Therefore, with the nitrogen doping the crystallite size decreases. It confirmed the doping in the graphene network.

The surface also plays a very important role in different applications and it shows the quality of the films. The surface was examined by Scanning electron microscopy (SEM) and Atomic force microscopy (AFM) techniques.

6.4.2 Surface morphology (SEM and AFM)

The Figures 6.7a and 6.7b show the typical SEM micrograph of few layer graphene and N doped graphene.

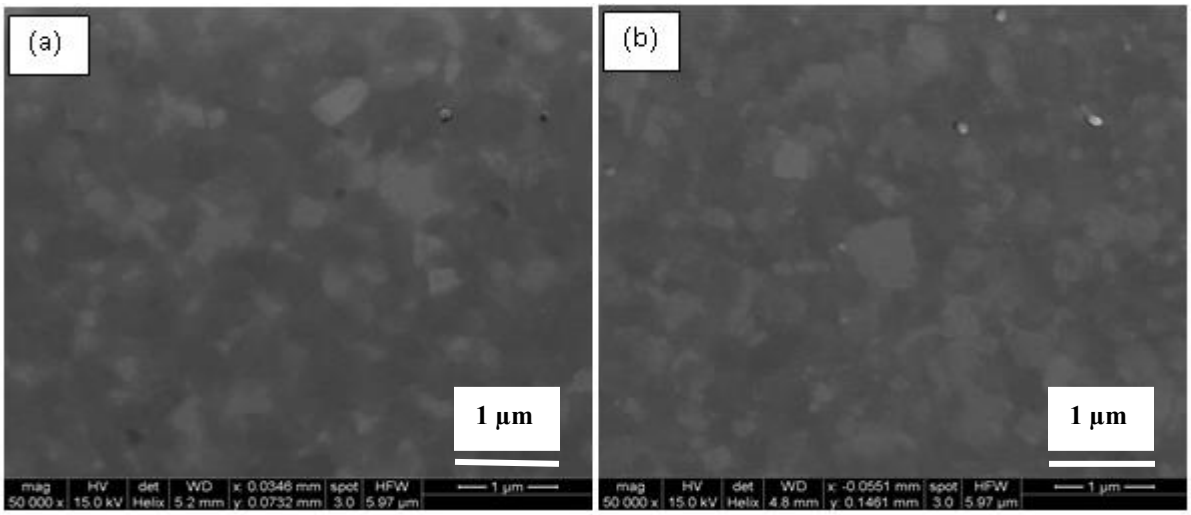

Figure 6. 7 Typical SEM images (a) graphene from Ni/a-C(10 nm)/SiO_2, (b) N doped graphene from Ni/a-C:N(10 nm)/SiO_2 after thermal annealing at 780°C during 30 min.

It is evident from the micrograph that the graphene and the N doped graphene films are uniform. One can clearly see the formation of layer structures in both the films. No appreciable difference was observed between the films.

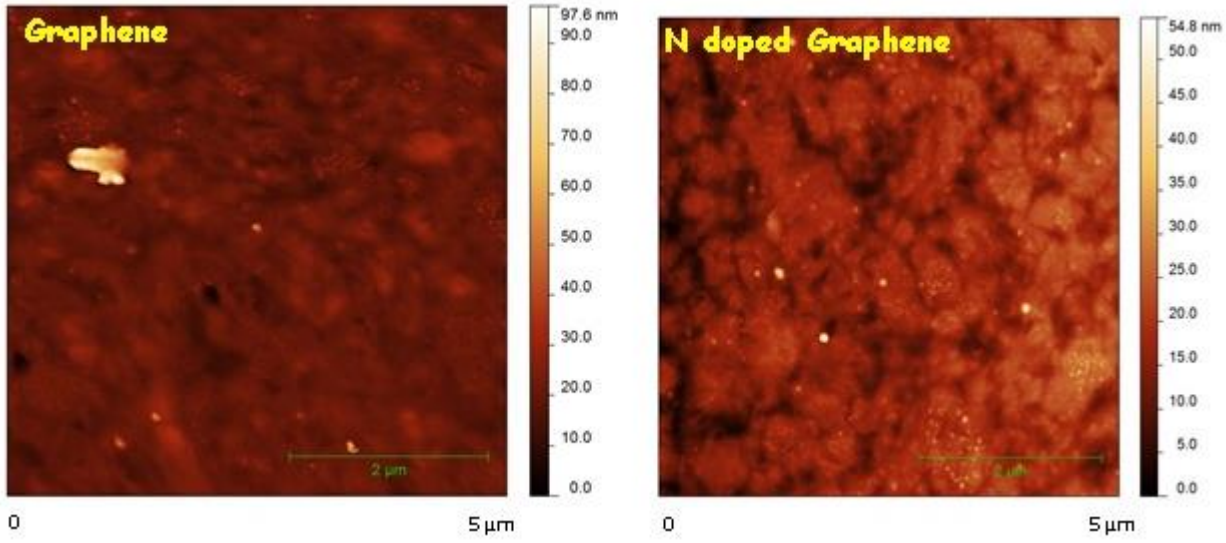

Figure 6. 8 AFM images of graphene (Ni/a-C(10 nm)/SiO_2) and N doped graphene (Ni/a-C:N(10 nm)/SiO_2).

The Figure 6.8 shows the AFM images of graphene and N doped graphene. The roughness values (Ra) were calculated for both the graphene and N doped graphene films; we observed a very small difference, though negligible as the roughness values of graphene is at 9 nm and N doped graphene is at 6 nm.

Even though we have got the evidence of doping by Raman spectroscopy, we need to confirm the doping and address information on chemical bonding information in N doped graphene. Therefore, we used the X-ray photoelectron spectroscopy technique to study the nitrogen evidence and content, chemical composition and bonding between carbon and nitrogen in N doped graphene.

6.4.3 Chemical composition in N doped graphene: X-ray photoelectron spectroscopy (XPS)

A large variety of nitrogen-containing functional groups can be introduced in graphene network by nitrogen doping, such as pyridinic, pyrrolic, amine, and quaternary nitrogen (Q-N) as reported in Figure 6.1. The type of nitrogen containing functional groups plays an important role is the various properties of N doped graphene. The accurate assignments and the introduction of aimed single nitrogen containing functional groups are essential for the future of graphene. X-ray photoelectron spectroscopy (XPS) is among the most commonly used analytical technique for the identification of functional groups in graphene [[30]]. Owing to the efforts of many researchers, the assignments of nitrogen containing functional groups have been revealed experimentally. For example, Ishitani *et al*. analyzed the carbon fibers and assigned four types of peak shifts such as sp^3C-CN (400 eV), pyridinic (so called N-6, 399 eV), imino (401 eV) and nitroso (403 eV) groups [[67]]. Proctor *et al*. assigned a peak at 400 eV as an amine group [[68]], Pels *et al*. [[69]] and Jansen *et al*. [[70]] added various nitrogen containing functional groups as pyrrolic and pyridine-like groups (so called N-5) and quaternary nitrogen (Q-N). These assignments are probably among the most used ones to analyze the multiple nitrogen containing functional groups. However, many problems still exist to assign nitrogen containing functional groups. The problem is the unclarity of C1s shifts with nitrogen containing functional groups. Some research groups have used two types of C-N bonding such as sp^2C-N and sp^3C-N for C1s shifts from 0.6 to 1.5 eV and from 1.6 to 3.0 eV, respectively [[38,40,43]]. However, most research groups explain only N1s spectra without clear explanation of C1s spectra. One of the reasons for the difficulties is the insufficient references of C1s spectra of nitrogen containing functional groups, and a lack of appropriate model compounds to obtain accurate assignments. Another reason should be the presence of oxygen-containing functional groups for most carbon materials. Even for oxygen containing functional groups, the assignments are complicated [[71]]. Thus, the assignments of C1s spectra including both oxygen and nitrogen containing functional groups are extremely challenging.

XPS is a standard technique to study the nitrogen doping in graphene. The Figure 6.9 shows the typical XPS general scan spectra of graphene and N doped graphene on nickel surface after growth. In the XPS spectrum of N doped graphene the peaks appearing at about 398.00 eV and

284.00 eV corresponds to the N1s and C1s respectively. The N doped graphene shows an obvious N1s peak whereas there is no detectable N peak in pure graphene, which confirms the nitrogen doping of graphene. The oxygen (O1s peak) was observed in both graphene and N doped graphene, which is possibly due to physisorbed oxygen on the graphene surface. The higher peak intensity ratio of O1s and C1s in N doped graphene suggests stronger oxygen adsorption ability on N doped graphene surface.

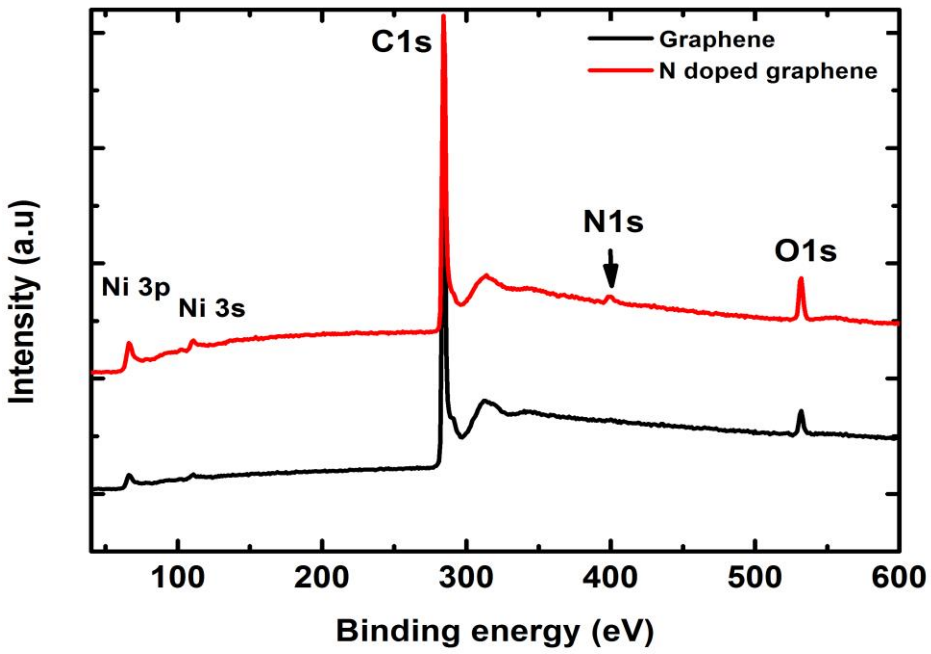

Figure 6. 9 XPS general spectra of graphene (Ni/a-C/SiO_2) and nitrogen doped graphene (Ni/a-C:N/SiO_2), both films were annealed at 780°C.

The Figure 6.10a shows the comparison of C1s spectra of graphene and N doped graphene. We can clearly see that the C1s spectra of N doped graphene shifts to higher binding energies and is broadened by nitrogen doping. The broadened spectra reveal the C atoms bonded to different N functionalities, as detailed later. The Figure 6.10b shows the N1s spectra of N doped graphene. This clearly evidenced of N incorporation in the graphene network.

To study the possible hybridization of C and N in N doped graphene, the C1s and N1s spectra of N doped graphene have been deconvoluted into different components, as reported in Figure 6.11a and 6.11b. The deconvolution scheme was stated in the experimental section in the chapter 2.

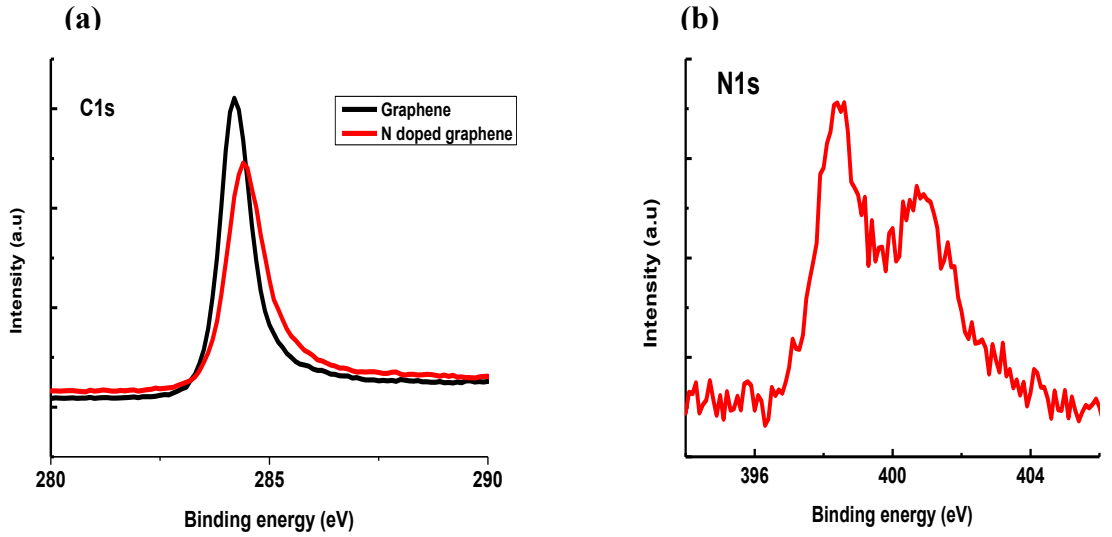

Figure 6. 10 (a) XPS C1s spectra of graphene and N doped graphene (b) N1s spectra of N doped graphene.

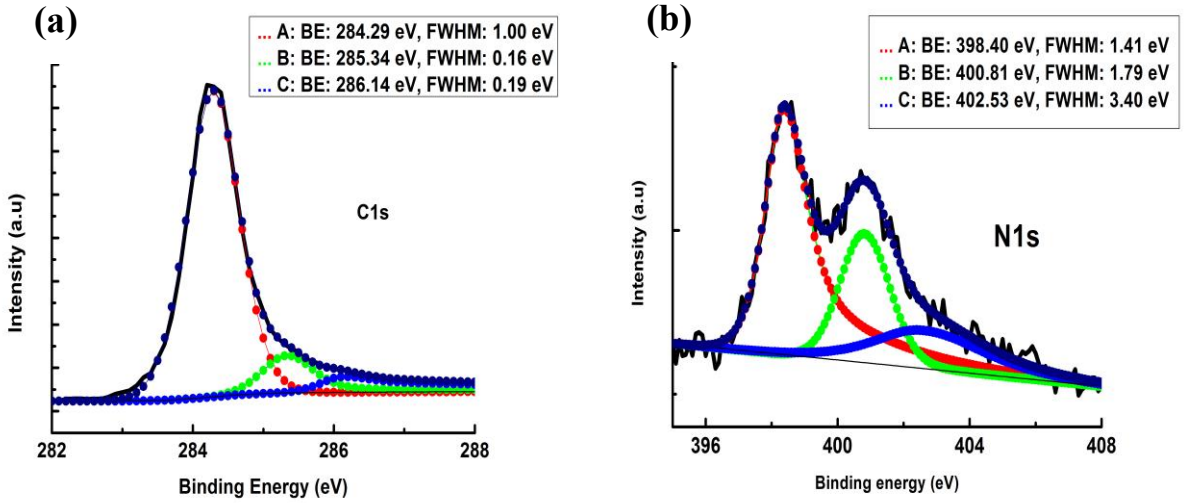

Figure 6. 11 Deconvoluted (a) C1s spectra, (b) N1s spectra of N doped graphene.

The nitrogen content in N doped graphene is deduced at 3 at.%. The N1s and C1s spectra of N doped graphene were deconvoluted into three components. The C1s spectra of N doped graphene shows three components at 284.29 eV, 285.34 and 286.14 eV, which are assigned to the graphitic-like sp^2, N-sp^2C and N-sp^3C, respectively, originating from the substitutional doping of graphene [38]. The N1s peak in N doped graphene is deconvoluted into three components centered at 398.40 eV, 400.81 eV and 402.51 eV, corresponding to pyridinic-N, pyrrolic-N, and graphitic-N [38,72], respectively. The pyridinic-N type of functionality is dominating in our N doped graphene film, consistent with theoretical prediction that N atoms are more thermodynamically stable at the edges of graphene lattice [41].

In the pyridinic-N, the nitrogen atoms are at the edges of the graphene planes, they are bounded to two carbon atoms and they donate one p electron to the aromatic π-system. As previously stated, the graphitic-N promotes the oxygen reduction reaction (ORR) activity, whereas pyridinic-N suppresses the ORR activity. As claimed by some researchers [73], the density functional theory (DFT) modeling shows that graphitic-N lowers the adsorption energy of oxygen and facilitates the first electron transfer. However, the ORR is catalyzed through a ring-opening process of the cyclic C-N bond, resulting in the formation of pyridinic-N [74]. In contrast, many other papers stated that pyridinic-N does not suppress but facilitates the ORR activity [75–80]. The DFT calculations show that pyridinic-N enhances the O_2 adsorption on the neighboring carbon atoms by inducing high spin density and positive atomic charge density to the neighboring carbon atoms, and thus, it promotes a four-electron process of ORR [81,82]. According to the recent study, the pyridinic-N type dominance is highly active and stable electrocatalyst for oxygen reduction activity [82]. The Pt is a widely used catalyst in ORR activity, but due to shortage and susceptibility to CO poising [83,84], replacing it became a big concern. Our prydinic-N dominance N doped graphene could be the catalyst in near future.

Recently, the laser-grown graphene electrode elaborated in our group showed a very high electrochemical performance and a great capability to electrochemical functionalization [15]. We are expecting that our N doped graphene will be an excellent electrode in electrochemical sensors and functionalization of surface by biomolecules in near future.

Opening and tuning the energy gap in graphene is possible by heteroatom doping and it is central to many electronic applications [85]. With our N doped graphene, it is expected that the tuning of nitrogen content in a-C:N films will affect N doped graphene by leading to different N contents, which will tune the bandgap in graphene. It is expected that our N doped graphene could be a promising material in many electronic applications in future.

6.5 Conclusions

We developed a simple and efficient method to synthesize N doped graphene layers. Our N doped graphene was synthesized through vacuum annealing of a sandwiched Ni/a-C:N(10 nm)/SiO_2 substrate at a low temperature by the utilization of common segregation phenomenon. The amorphous carbon nitride and nickel layers have been deposited on SiO_2 substrate by femtosecond pulsed laser deposition and thermal evaporation techniques, respectively. The N doping has been confirmed by Raman spectroscopy and XPS. By doping, the 2D band intensity ratio decreased compared to the graphene and Raman mapping confirmed the homogeneous quality of N doped graphene. The C-N bonding configuration is found to be pyridine N type bonding with a high N concentration at 3 at.%. With our simple and fast approach, useable at low temperature, we can obtain the desired types of N bonding and a high N concentration. It is expected that it will be possible to tune the N content values. This type of N-doped graphene could be a promising material for electrochemical sensors, electrochemical energy devices, and bioelectronics and biosensors applications.

References

(1) Novoselov, K. S.; Geim, A. K.; Morozov, S. V.; Jiang, D.; Zhang, Y.; Dubonos, S. V.; Grigorieva, I. V.; Firsov, A. A. Electric Field Effect in Atomically Thin Carbon Films. *Science* **2004**, *306*, 666–669.

(2) Geim, A. K. Graphene: Status and Prospects. *Science* **2009**, *324*, 1530–1534.

(3) Geim, A. K.; Novoselov, K. S. The Rise of Graphene. *Nat. Mater.* **2007**, *6*, 183–191.

(4) Bunch, J. S.; Zande, A. M. van der; Verbridge, S. S.; Frank, I. W.; Tanenbaum, D. M.; Parpia, J. M.; Craighead, H. G.; McEuen, P. L. Electromechanical Resonators from Graphene Sheets. *Science* **2007**, *315*, 490–493.

(5) Nair, R. R.; Blake, P.; Grigorenko, A. N.; Novoselov, K. S.; Booth, T. J.; Stauber, T.; Peres, N. M. R.; Geim, A. K. Fine Structure Constant Defines Visual Transparency of Graphene. *Science* **2008**, *320*, 1308–1308.

(6) Wallace, P. R. The Band Theory of Graphite. *Phys. Rev.* **1947**, *71*, 622–634.

(7) Novoselov, K. S.; Geim, A. K.; Morozov, S. V.; Jiang, D.; Katsnelson, M. I.; Grigorieva, I. V.; Dubonos, S. V.; Firsov, A. A. Two-Dimensional Gas of Massless Dirac Fermions in Graphene. *Nature* **2005**, *438*, 197–200.

(8) Brownson, D. A. C.; Kampouris, D. K.; Banks, C. E. Graphene Electrochemistry: Fundamental Concepts through to Prominent Applications. *Chem. Soc. Rev.* **2012**, *41*, 6944–6976.

(9) Mao, M.; Hu, J.; Liu, H. Graphene-Based Materials for Flexible Electrochemical Energy Storage. *Int. J. Energy Res.* **2015**, *39*, 727–740.

(10) Pumera, M. Graphene in Biosensing. *Mater. Today* **2011**, *14*, 308–315.

(11) Pumera, M. Electrochemistry of Graphene: New Horizons for Sensing and Energy Storage. *Chem. Rec.* **2009**, *9*, 211–223.

(12) Pumera, M. Graphene-Based Nanomaterials for Energy Storage. *Energy Environ. Sci.* **2011**, *4*, 668–674.

(13) Pumera, M.; Ambrosi, A.; Bonanni, A.; Chng, E. L. K.; Poh, H. L. Graphene for Electrochemical Sensing and Biosensing. *TrAC Trends Anal. Chem.* **2010**, *29*, 954–965.

(14) Allen, M. J.; Tung, V. C.; Kaner, R. B. Honeycomb Carbon: A Review of Graphene. *Chem. Rev.* **2010**, *110*, 132–145.

(15) Philippe Fortgang; Teddy Tite; Vincent Barnier; Nedjla Zehani; Chiranjeevi Maddi; Florence Lagarde; Anne-Sophie Loir; Nicole Jaffrezic-Renault; Christophe Donnet; Florence Garrelie; *et al.* Robust Electrografting on Self-Organized 3D Graphene Electrodes. *ACS Appl. Mater. Interfaces* **2015**.

(16) Reina, A.; Jia, X.; Ho, J.; Nezich, D.; Son, H.; Bulovic, V.; Dresselhaus, M. S.; Kong, J. Large Area, Few-Layer Graphene Films on Arbitrary Substrates by Chemical Vapor Deposition. *Nano Lett.* **2009**, *9*, 30–35.

(17) Li, X.; Cai, W.; An, J.; Kim, S.; Nah, J.; Yang, D.; Piner, R.; Velamakanni, A.; Jung, I.; Tutuc, E.; *et al.* Large-Area Synthesis of High-Quality and Uniform Graphene Films on Copper Foils. *Science* **2009**, *324*, 1312–1314.

(18) Sun, Z.; Yan, Z.; Yao, J.; Beitler, E.; Zhu, Y.; Tour, J. M. Growth of Graphene from Solid Carbon Sources. *Nature* **2010**, *468*, 549–552.

(19) Wang, K.; Tai, G.; Wong, K. H.; Lau, S. P.; Guo, W. Ni Induced Few-Layer Graphene Growth at Low Temperature by Pulsed Laser Deposition. *AIP Adv.* **2011**, *1*, 022141.
(20) Hamilton, J. C.; Blakely, J. M. Carbon Segregation to Single Crystal Surfaces of Pt, Pd and Co. *Surf. Sci.* **1980**, *91*, 199–217.
(21) Grant, J. T.; Haas, T. W. A Study of Ru(0001) and Rh(111) Surfaces Using LEED and Auger Electron Spectroscopy. *Surf. Sci.* **1970**, *21*, 76–85.
(22) Koh, A. T. T.; Foong, Y. M.; Chua, D. H. C. Cooling Rate and Energy Dependence of Pulsed Laser Fabricated Graphene on Nickel at Reduced Temperature. *Appl. Phys. Lett.* **2010**, *97*, 114102.
(23) Tite, T.; Donnet, C.; Loir, A.-S.; Reynaud, S.; Michalon, J.-Y.; Vocanson, F.; Garrelie, F. Graphene-Based Textured Surface by Pulsed Laser Deposition as a Robust Platform for Surface Enhanced Raman Scattering Applications. *Appl. Phys. Lett.* **2014**, *104*, 041912.
(24) Hamilton, J. C.; Blakely, J. M. Carbon Segregation to Single Crystal Surfaces of Pt, Pd and Co. *Surf. Sci.* **1980**, *91*, 199–217.
(25) Saenger, K. L.; Tsang, J. C.; Bol, A. A.; Chu, J. O.; Grill, A.; Lavoie, C. In Situ X-Ray Diffraction Study of Graphitic Carbon Formed during Heating and Cooling of Amorphous-C/Ni Bilayers. *Appl. Phys. Lett.* **2010**, *96*, 153105.
(26) Zheng, M.; Takei, K.; Hsia, B.; Fang, H.; Zhang, X.; Ferralis, N.; Ko, H.; Chueh, Y.-L.; Zhang, Y.; Maboudian, R.; *et al.* Metal-Catalyzed Crystallization of Amorphous Carbon to Graphene. *Appl. Phys. Lett.* **2010**, *96*, 063110.
(27) Wang, K.; Wong, K. H. Growth of Large Grain Polycrystalline Silicon Thin Film on Soda-Lime Glass at Low Temperature for Solar Cell Applications. In *Symposium A – Amorphous and Polycrystalline Thin-Film Silicon Science and Technology*; MRS Online Proceedings Library; 2011; Vol. 1321.
(28) Deifallah, M.; McMillan, P. F.; Corà, F. Electronic and Structural Properties of Two-Dimensional Carbon Nitride Graphenes. *J. Phys. Chem. C* **2008**, *112*, 5447–5453.
(29) Shao, Y.; Zhang, S.; Engelhard, M. H.; Li, G.; Shao, G.; Wang, Y.; Liu, J.; Aksay, I. A.; Lin, Y. Nitrogen-Doped Graphene and Its Electrochemical Applications. *J. Mater. Chem.* **2010**, *20*, 7491–7496.
(30) Wang, H.; Maiyalagan, T.; Wang, X. Review on Recent Progress in Nitrogen-Doped Graphene: Synthesis, Characterization, and Its Potential Applications. *ACS Catal.* **2012**, *2*, 781–794.
(31) Knittle, E.; Kaner, R. B.; Jeanloz, R.; Cohen, M. L. High-Pressure Synthesis, Characterization, and Equation of State of Cubic C-BN Solid Solutions. *Phys. Rev. B* **1995**, *51*, 12149–12156.
(32) Liu, A. Y.; Cohen, M. L. Prediction of New Low Compressibility Solids. *Science* **1989**, *245*, 841.
(33) Weng-Sieh, Z.; Cherrey, K.; Chopra, N. G.; Blase, X.; Miyamoto, Y.; Rubio, A.; Cohen, M. L.; Louie, S. G.; Zettl, A.; Gronsky, R. Syntehsis of BxCyNz Nanotubules. *Phys. Rev. B* **1995**, *51*, 11229–11232.
(34) Ci, L.; Song, L.; Jin, C.; Jariwala, D.; Wu, D.; Li, Y.; Srivastava, A.; Wang, Z. F.; Storr, K.; Balicas, L.; *et al.* Atomic Layers of Hybridized Boron Nitride and Graphene Domains. *Nat. Mater.* **2010**, *9*, 430–435.
(35) Lee, S. Y.; Duong, D. L.; Vu, Q. A.; Jin, Y.; Kim, P.; Lee, Y. H. Chemically Modulated Band Gap in Bilayer Graphene Memory Transistors with High On/Off Ratio. *ACS Nano* **2015**, *9*, 9034–9042.

(36) Panchakarla, L. S.; Subrahmanyam, K. S.; Saha, S. K.; Govindaraj, A.; Krishnamurthy, H. R.; Waghmare, U. V.; Rao, C. N. R. Synthesis, Structure, and Properties of Boron- and Nitrogen-Doped Graphene. *Adv. Mater.* **2009**, *21*, 4726–4730.
(37) Qu, L.; Liu, Y.; Baek, J.-B.; Dai, L. Nitrogen-Doped Graphene as Efficient Metal-Free Electrocatalyst for Oxygen Reduction in Fuel Cells. *ACS Nano* **2010**, *4*, 1321–1326.
(38) Wei, D.; Liu, Y.; Wang, Y.; Zhang, H.; Huang, L.; Yu, G. Synthesis of N-Doped Graphene by Chemical Vapor Deposition and Its Electrical Properties. *Nano Lett.* **2009**, *9*, 1752–1758.
(39) Zhao, L.; He, R.; Rim, K. T.; Schiros, T.; Kim, K. S.; Zhou, H.; Gutiérrez, C.; Chockalingam, S. P.; Arguello, C. J.; Pálová, L.; *et al.* Visualizing Individual Nitrogen Dopants in Monolayer Graphene. *Science* **2011**, *333*, 999–1003.
(40) Reddy, A. L. M.; Srivastava, A.; Gowda, S. R.; Gullapalli, H.; Dubey, M.; Ajayan, P. M. Synthesis Of Nitrogen-Doped Graphene Films For Lithium Battery Application. *ACS Nano* **2010**, *4*, 6337–6342.
(41) Wang, X.; Li, X.; Zhang, L.; Yoon, Y.; Weber, P. K.; Wang, H.; Guo, J.; Dai, H. N-Doping of Graphene through Electrothermal Reactions with Ammonia. *Science* **2009**, *324*, 768–771.
(42) Wang, Y.; Shao, Y.; Matson, D. W.; Li, J.; Lin, Y. Nitrogen-Doped Graphene and Its Application in Electrochemical Biosensing. *ACS Nano* **2010**, *4*, 1790–1798.
(43) Lin, Y.-C.; Lin, C.-Y.; Chiu, P.-W. Controllable Graphene N-Doping with Ammonia Plasma. *Appl. Phys. Lett.* **2010**, *96*, 133110.
(44) Zhang, C.; Fu, L.; Liu, N.; Liu, M.; Wang, Y.; Liu, Z. Synthesis of Nitrogen-Doped Graphene Using Embedded Carbon and Nitrogen Sources. *Adv. Mater.* **2011**, *23*, 1020–1024.
(45) Orofeo, C. M.; Ago, H.; Hu, B.; Tsuji, M. Synthesis of Large Area, Homogeneous, Single Layer Graphene Films by Annealing Amorphous Carbon on Co and Ni. *Nano Res.* **2011**, *4*, 531–540.
(46) Ferrari, A. C.; Rodil, S. E.; Robertson, J. Interpretation of Infrared and Raman Spectra of Amorphous Carbon Nitrides. *Phys. Rev. B* **2003**, *67*, 155306.
(47) Ferrari, A. C.; Meyer, J. C.; Scardaci, V.; Casiraghi, C.; Lazzeri, M.; Mauri, F.; Piscanec, S.; Jiang, D.; Novoselov, K. S.; Roth, S.; *et al.* Raman Spectrum of Graphene and Graphene Layers. *Phys. Rev. Lett.* **2006**, *97*, 187401.
(48) Ferrari, A. C. Raman Spectroscopy of Graphene and Graphite: Disorder, Electron–phonon Coupling, Doping and Nonadiabatic Effects. *Solid State Commun.* **2007**, *143*, 47–57.
(49) Omvir Singh Panwar; Ajay Kumar Kesarwani; Sanjay Rangnath Dhakate; Bhanu Pratap Singh; Rajib Kumar Rakshit; Atul Bisht; Sreekumar Chockalingam. Few Layer Graphene Synthesized by Filtered Cathodic Vacuum Arc Technique. *J. Vac. Sci. Technol. B* **2013**, *31*, 040602.
(50) Hao, Y.; Wang, Y.; Wang, L.; Ni, Z.; Wang, Z.; Wang, R.; Koo, C. K.; Shen, Z.; Thong, J. T. L. Probing Layer Number and Stacking Order of Few-Layer Graphene by Raman Spectroscopy. *Small Weinh. Bergstr. Ger.* **2010**, *6*, 195–200.
(51) Chao Yan; Jeong Ho Cho; Jong-Hyun Ahn. Graphene-Based Flexible and Stretchable Thin Film Transistors. *Nanoscale* **2012**, *4*, 4870–4882.

(52) Zhang, Y.; Gomez, L.; Ishikawa, F. N.; Madaria, A.; Ryu, K.; Wang, C.; Badmaev, A.; Zhou, C. Comparison of Graphene Growth on Single-Crystalline and Polycrystalline Ni by Chemical Vapor Deposition. *J. Phys. Chem. Lett.* **2010**, *1*, 3101–3107.

(53) Angel T. T. Koh; Yuan Mei Foong; Daniel H. C. Chua. Comparison of the Mechanism of Low Defect Few-Layer Graphene Fabricated on Different Metals by Pulsed Laser Deposition. *Diam. Relat. Mater.* **2012**, *25*, 98–102.

(54) C. Petridis; Y.-H. Lin; K. Savva; G. Eda; E. Kymakis; T. D. Anthopoulos; E. Stratakis. Post-Fabrication, in Situ Laser Reduction of Graphene Oxide Devices. *Appl. Phys. Lett.* **2013**, *102*, 093115.

(55) Sikora, A.; Garrelie, F.; Donnet, C.; Loir, A. S.; Fontaine, J.; Sanchez-Lopez, J. C.; Rojas, T. C. Structure of Diamondlike Carbon Films Deposited by Femtosecond and Nanosecond Pulsed Laser Ablation. *J. Appl. Phys.* **2010**, *108*, 113516.

(56) Zafar, Z.; Ni, Z. H.; Wu, X.; Shi, Z. X.; Nan, H. Y.; Bai, J.; Sun, L. T. Evolution of Raman Spectra in Nitrogen Doped Graphene. *Carbon* **2013**, *61*, 57–62.

(57) Das, A.; Pisana, S.; Chakraborty, B.; Piscanec, S.; Saha, S. K.; Waghmare, U. V.; Novoselov, K. S.; Krishnamurthy, H. R.; Geim, A. K.; Ferrari, A. C.; *et al.* Monitoring Dopants by Raman Scattering in an Electrochemically Top-Gated Graphene Transistor. *Nat. Nanotechnol.* **2008**, *3*, 210–215.

(58) Zhang, C.; Fu, L.; Liu, N.; Liu, M.; Wang, Y.; Liu, Z. Synthesis of Nitrogen-Doped Graphene Using Embedded Carbon and Nitrogen Sources. *Adv. Mater.* **2011**, *23*, 1020–1024.

(59) Malard, L. M.; Pimenta, M. A.; Dresselhaus, G.; Dresselhaus, M. S. Raman Spectroscopy in Graphene. *Phys. Rep.* **2009**, *473*, 51–87.

(60) Venezuela, P.; Lazzeri, M.; Mauri, F. Theory of Double-Resonant Raman Spectra in Graphene: Intensity and Line Shape of Defect-Induced and Two-Phonon Bands. *Phys. Rev. B* **2011**, *84*, 035433.

(61) Lv, R.; Li, Q.; Botello-Méndez, A. R.; Hayashi, T.; Wang, B.; Berkdemir, A.; Hao, Q.; Elías, A. L.; Cruz-Silva, R.; Gutiérrez, H. R.; *et al.* Nitrogen-Doped Graphene: Beyond Single Substitution and Enhanced Molecular Sensing. *Sci. Rep.* **2012**, *2*.

(62) Ni, Z. H.; Yu, T.; Lu, Y. H.; Wang, Y. Y.; Feng, Y. P.; Shen, Z. X. Uniaxial Strain on Graphene: Raman Spectroscopy Study and Band-Gap Opening. *ACS Nano* **2008**, *2*, 2301–2305.

(63) Shinde, S. M.; Kano, E.; Kalita, G.; Takeguchi, M.; Hashimoto, A.; Tanemura, M. Grain Structures of Nitrogen-Doped Graphene Synthesized by Solid Source-Based Chemical Vapor Deposition. *Carbon* **2016**, *96*, 448–453.

(64) Wang, X.; Li, X.; Zhang, L.; Yoon, Y.; Weber, P. K.; Wang, H.; Guo, J.; Dai, H. N-Doping of Graphene through Electrothermal Reactions with Ammonia. *Science* **2009**, *324*, 768–771.

(65) Maciel, I. O.; Anderson, N.; Pimenta, M. A.; Hartschuh, A.; Qian, H.; Terrones, M.; Terrones, H.; Campos-Delgado, J.; Rao, A. M.; Novotny, L.; *et al.* Electron and Phonon Renormalization near Charged Defects in Carbon Nanotubes. *Nat. Mater.* **2008**, *7*, 878–883.

(66) Cançado, L. G.; Takai, K.; Enoki, T.; Endo, M.; Kim, Y. A.; Mizusaki, H.; Jorio, A.; Coelho, L. N.; Magalhães-Paniago, R.; Pimenta, M. A. General Equation for the Determination of the Crystallite Size La of Nanographite by Raman Spectroscopy. *Appl. Phys. Lett.* **2006**, *88*, 163106.

(67) Ishitani, A. Application of X-Ray Photoelectron Spectroscopy to Surface Analysis of Carbon Fiber. *Carbon* **1981**, *19*, 269–275.
(68) Proctor, A.; Sherwood, P. M. A. X-Ray Photoelectron Spectroscopic Studies of Carbon Fibre surfaces—II. *Carbon* **1983**, *21*, 53–59.
(69) Pels, J. R.; Kapteijn, F.; Moulijn, J. A.; Zhu, Q.; Thomas, K. M. Evolution of Nitrogen Functionalities in Carbonaceous Materials during Pyrolysis. *Carbon* **1995**, *33*, 1641–1653.
(70) Jansen, R. J. J.; van Bekkum, H. XPS of Nitrogen-Containing Functional Groups on Activated Carbon. *Carbon* **1995**, *33*, 1021–1027.
(71) Yamada, Y.; Yasuda, H.; Murota, K.; Nakamura, M.; Sodesawa, T.; Sato, S. Analysis of Heat-Treated Graphite Oxide by X-Ray Photoelectron Spectroscopy. *J. Mater. Sci.* **2013**, *48*, 8171–8198.
(72) Marton, D.; Boyd, K. J.; Al-Bayati, A. H.; Todorov, S. S.; Rabalais, J. W. Carbon Nitride Deposited Using Energetic Species: A Two-Phase System. *Phys. Rev. Lett.* **1994**, *73*, 118–121.
(73) Niwa, H.; Horiba, K.; Harada, Y.; Oshima, M.; Ikeda, T.; Terakura, K.; Ozaki, J.; Miyata, S. X-Ray Absorption Analysis of Nitrogen Contribution to Oxygen Reduction Reaction in Carbon Alloy Cathode Catalysts for Polymer Electrolyte Fuel Cells. *J. Power Sources* **2009**, *187*, 93–97.
(74) Kim, H.; Lee, K.; Woo, S. I.; Jung, Y. On the Mechanism of Enhanced Oxygen Reduction Reaction in Nitrogen-Doped Graphene Nanoribbons. *Phys. Chem. Chem. Phys.* **2011**, *13*, 17505–17510.
(75) Yadav, R. M.; Wu, J.; Kochandra, R.; Ma, L.; Tiwary, C. S.; Ge, L.; Ye, G.; Vajtai, R.; Lou, J.; Ajayan, P. M. Carbon Nitrogen Nanotubes as Efficient Bifunctional Electrocatalysts for Oxygen Reduction and Evolution Reactions. *ACS Appl. Mater. Interfaces* **2015**, *7*, 11991–12000.
(76) Vikkisk, M.; Kruusenberg, I.; Joost, U.; Shulga, E.; Kink, I.; Tammeveski, K. Electrocatalytic Oxygen Reduction on Nitrogen-Doped Graphene in Alkaline Media. *Appl. Catal. B Environ.* **2014**, *147*, 369–376.
(77) Chen, Z.; Higgins, D.; Tao, H.; Hsu, R. S.; Chen, Z. Highly Active Nitrogen-Doped Carbon Nanotubes for Oxygen Reduction Reaction in Fuel Cell Applications. *J. Phys. Chem. C* **2009**, *113*, 21008–21013.
(78) Rao, C. V.; Cabrera, C. R.; Ishikawa, Y. In Search of the Active Site in Nitrogen-Doped Carbon Nanotube Electrodes for the Oxygen Reduction Reaction. *J. Phys. Chem. Lett.* **2010**, *1*, 2622–2627.
(79) Wu, G.; Mack, N. H.; Gao, W.; Ma, S.; Zhong, R.; Han, J.; Baldwin, J. K.; Zelenay, P. Nitrogen-Doped Graphene-Rich Catalysts Derived from Heteroatom Polymers for Oxygen Reduction in Nonaqueous Lithium–O2 Battery Cathodes. *ACS Nano* **2012**, *6*, 9764–9776.
(80) Chang, D. W.; Choi, H.-J.; Baek, J.-B. Wet-Chemical Nitrogen-Doping of Graphene Nanoplatelets as Electrocatalysts for the Oxygen Reduction Reaction. *J. Mater. Chem. A* **2015**, *3*, 7659–7665.
(81) Zhang, L.; Xia, Z. Mechanisms of Oxygen Reduction Reaction on Nitrogen-Doped Graphene for Fuel Cells. *J. Phys. Chem. C* **2011**, *115*, 11170–11176.
(82) Wu, J.; Ma, L.; Yadav, R. M.; Yang, Y.; Zhang, X.; Vajtai, R.; Lou, J.; Ajayan, P. M. Nitrogen-Doped Graphene with Pyridinic Dominance as a Highly Active and Stable

Electrocatalyst for Oxygen Reduction. *ACS Appl. Mater. Interfaces* **2015**, *7*, 14763–14769.

(83) Gasteiger, H. A.; Kocha, S. S.; Sompalli, B.; Wagner, F. T. Activity Benchmarks and Requirements for Pt, Pt-Alloy, and Non-Pt Oxygen Reduction Catalysts for PEMFCs. *Appl. Catal. B Environ.* **2005**, *56*, 9–35.

(84) Wu, J.; Yang, H. Platinum-Based Oxygen Reduction Electrocatalysts. *Acc. Chem. Res.* **2013**, *46*, 1848–1857.

(85) Guo, B.; Liu, Q.; Chen, E.; Zhu, H.; Fang, L.; Gong, J. R. Controllable N-Doping of Graphene. *Nano Lett.* **2010**, *10*, 4975–4980.

Conclusions and future perspectives

Conclusions

This manuscript is a contribution to a multi-laboratory research program dedicated to the synthesis and characterization of nitrogen containing carbon-based films, deposited by femtosecond pulsed laser ablation. Considering the wide bibliography already published on such kind of films, we have focused our contribution to a deeper and continuous collaboration between a less explored deposition process (femtosecond pulsed laser deposition, with DC plasma assistance), complementary surface analysis and electrochemical investigations of the films, up to the electrochemical functionalization of a CN electrode by organic molecules for future experiment dedicated to the detection of pathogen agents. Direct synthesis of nitrogen doped graphene by femtosecond PLD has also been explored.

The main scientific conclusions are the following:

A. <u>Influence of nitrogen partial pressure on the a-C:N films properties</u>

- Amorphous carbon nitride (a-C:N) films with a nitrogen content up to 18 at.% were grown on by conventional femtosecond pulsed laser deposition as a function of nitrogen partial pressure without using any bias assistance.
- The C1s XPS showed that the CN bonds increases at the expense of CC bonds with the increase of N content in films.

B. <u>Influence of DC bias assistance on the a-C:N films properties</u>

- With DC bias assistance femtosecond pulsed laser deposition, higher N content up to 28 at.% have been obtained in a-C:N films.
- High N contents are associated to more ordered sp^2 rich graphitic clusters in terms of both structural and topological order.
- The evidence of bonding dependence on N content was not fully understood.

- There are clear agreements between the XPS, EELS and MW Raman spectroscopy.

C. Effect of different DC bias on the a-C:N films

- The highest N content (about 28 at.%) has been obtained with DC bias assistance (0-350V) at a nitrogen pressure of 5 Pa.
- High nitrogen contents are consistent with an increase of the sp^2 character and higher correlation lengths of the graphitic clusters. However, DC bias induces an increase of the structural disorder, as well as a substantial increase of nitrile group in the films

D. Plasma plume properties of a-C:N films

- Plasma plume diagnostic allows to correlate the process with the film composition. DC bias induces better CN incorporation from the plasma into the growing film

E. Amorphous carbon nitride (a-C:N) films electrochemical properties

- The a-C:N electrodes showed extraordinary electrochemical properties, a wide potential window, fast electron transfer kinetics and low potential difference values.
- The electrochemical properties of a good electrode need a balance between chemical and microstructural properties.
- The electrochemical results are consistent with the film structures. The a-C:N films deposited with DC bias assistance exhibit a less conductive behavior compared to the films obtained without DC bias. The best electrochemical performance has been obtained with the film containing 10 at.% of nitrogen.

- The potential difference values of the a-C:N (10 %) electrode are close to the theoretical value and low compared to the cyclic voltammetry obtained in ferri-ferrocyanide of glassy carbon electrode.
- The a-C:N electrode shows faster electron transfer kinetics (10^{-2} cm/s) than the other carbon based electrodes such as boron doped diamond, glassy carbon and amorphous carbon nitride electrodes in ferri/ferrocyanide and quinone/hydroquinone, and is close to the transfer kinetics of graphene in hexachlororidate.
- The a-C:N(10%) electrode shows a good ability to detect lead (Pb) ions in the low concentration range.
- The surface coverage of the a-C:N(10%) electrode is higher than the BDD and glassy carbon electrodes, and is close to the dense packed monolayers of ferrocene.
- We have shown the ability to achieve a high surface coverage of 3.9×10^{-10} mol/cm^2.

F. N doped graphene

- We successfully synthesized the few layer graphene and N doped graphene by amorphous carbon nitride (a-C:N) deposited by fs-PLD.
- On doping, the intensity of 2D peak decreases, which confirms the doping of the nitrogen in graphene network.
- We obtained the high N content 3 at.%.
- Pyridinic-N type is dominating in our N doped graphene.
- Our approach is simple, fast, cost effective, and allows selective types of bonding and may be the possibility of controlling the doping content.

Future Perspectives

In this section, we present works that are potentially interesting to be performed in near future as a direct perspective of this work.

We successfully synthesised a-C:N films by femtosecond pulsed laser deposition technique, elaborated its physical, chemical and electrochemical properties and studied its potential use in electrochemical sensors applications.

As a direct perspective to this work, we propose some interesting studies,

- In thin films deposition, the substrate plays a vital role in many potential environmental friendly applications. It would be interesting to study the deposition of amorphous carbon nitride by fs-PLD on flexible substrate (polymer) in analytical microsystems to study the detection of heavy metals, bio pathogens and contaminants in flow water. The functionalization of surfaces, and attachment of DNA molecules will improve the sensitivity of electrode in bio sensors applications.

- It would also be interesting to study the dependence of the temperature on the a-C:N films deposited by conventional fs-PLD and reactive fs-PLD and to study the effect on its physical, chemical and electrochemical properties.

- As a-C:N electrodes showed great electrochemical properties, si it would be very interesting to develop nitrogen doped amorphous carbon in analytical microsystem by micro/nano matching with a femtosecond lasers. Thus, developed microsystems are very promising in micro-fluidic channels, lab on chip devices, and bio sensor applications.

- We successfully showed the ability of the grafting on a-C:N electrodes to increase the sensitivity of electrode. An extension of this work could lead to attach bio molecules like DNA onto a-C:N electrode to be used as bio sensors in many biological applications.

- When films are doped with heteroatoms, their properties are altered, especially electrical properties. It would be interesting to study electrical properties of a-C:N films by four

probe method as it will explain the good performance of electrodes used in electrochemical sensors. This would help to develop more sensitive and selective electrodes for future development in analytical microsystems and replace the toxic mercury and boron doped diamond electrode in analytical microsystems.

- The films behavior would be better understood by a further study of in-depth characterization a by the development of the theoretical models.

- We need higher resolution optical emission spectroscopy techniques to understand better the nitrogen plume diagnostics, and get a more precise understanding of the effects of N_2 pressures and DC bias assistance on film microstructural and chemical properties.

- We showed the successful deposition of graphene by fs-PLD technique. We need to do perform more experiments and characterization techniques to comment on the quality and the number graphene layers. It is also necessary to transfer the graphene on flexible substrate as it is required to study its electrical properties and its potential use in environmental, energy storage and conversion applications.

- We developed the new synthesis route to grow the N doped graphene by fs-PLD technique from direct conversion of a-C:N films by ex-situ annealing. We need to do more experiments to see if it would be possible to tune different N contents and study its properties by more sophisticated material characterization techniques, such as STM and HRTEM for knowing the number of layers and its electrical properties.

- It would be important to develop the theoretical model to understand better the growth mechanism of N doped graphene from a-C:N films by fs-PLD technique.

- The nitrogen doping in graphene tunes its energy gap. So it is needed to study electrical properties of N doped graphene to know its band gap as it is promising material for many electronic applications. Before studying its electrical properties, we need to transfer the N doped graphene on desired types of substrate.

- It is necessary to study the characteristics of pyridinic-N type, as the growth of pyridine dominance N doped graphene films would be useful in electrochemical, catalyst in ORR activity, and biosensors applications.

- Direct writing of graphene patterns on insulating substrates under ambient conditions can be achieved by femtosecond laser direct writing (LDW) process without needing extra transfer to produce the patterns. This provides a facile and cost effective way to fabricate the complex and high quality graphene patterns directly onto the target substrate, which opens a door for the fabrication of various advanced future functional devices.

- As the interest in laser matter interaction is growing, the new synthesis routes are highly accessible in industry to develop simpler, cost effective, and environmental friendly devices. It would be possible to synthesis the N doped carbon nanotubes (N-CNT) by fs-PLD technique. The N-CNT has a big potential in a wide variety of applications in sensors, biomedical, solar cells, hydrogen storage, super capacitors, water treatment and microelectronics.

List of Figures

Figure 1. 1 Schematic of a biosensor with electrochemical transducer [3]. 15

Figure 1. 2 Important aspects for choosing electrochemical sensors for environmental monitoring. 16

Figure 1. 3 Ternary phase diagram of different amorphous carbon types [54]. 20

Figure 1. 4 Ternary phase diagram of amorphous carbon nitride (a-C:N) alloys, without hydrogen (left) and with hydrogen (right) showing sp^3, sp^2 and N content [99]. 23

Figure 1. 5 (a) The chemical bonding in C_3N_4 phase, (b) Different CN_x bonding configurations, paired bonds are depicted as lines, unpaired electrons are represented by one dot and paired electrons in non-bonding lone pair as two dots [100]. 25

Figure 1. 6 Schematic diagram of laser ablation process., (a) Initial absorption of laser radiation, melting and vaporization begin, (b) Melt front propagates into the solid, vaporization continues and laser plume interactions start to become important, (c) Absorption of incident laser radiation by the plume, and plasma formation, (d) Melt front recedes leading to eventual re-solidification [150]. 29

Figure 1. 7 The energy absorption and laser ablation process in nanosecond and femtosecond at approximate time scales along with various process [240]. 33

Figure 2. 1 Schematic view of the film deposition vacuum chamber in fs-PLD. 56

Figure 2. 2 Schematic of chirped pulse amplification (CPA) of femtosecond laser system. 57

Figure 2. 3 Size of the laser spot on graphite target according to the position of the focusing lens. 59

Figure 2. 4 Snapshot of nitrogen plasma under DC bias. 61

Figure 2. 5 Schematic view of the deposition configuration, a) Without bias assistance, b) with bias assistance. 62

Figure 2. 6 Experimental setup used for the Optical emission spectroscopy and 2D imaging of the plasma. 64

Figure 2. 7 Comparison of typical Raman spectra of carbons [6]. 66

Figure 2. 8 Variation of intensity ratio of I(D)/I(G) with in plane correlation length L_a [2]. 68

Figure 2. 9 Schematic of the factors affecting the position and heights of the Raman G and D peaks of disordered carbons [6]. 69

Figure 2. 10 G peak position values of a-C film obtained with different peak fitting function compared with literature data [9]. 71

Figure 2. 11 Deconvolution of the core level lines using a maximum of four Gaussian and the common assignments found in the literature [33]. 75

Figure 2. 12 Schematic of the EELS spectrum. 77

Figure 2. 13 Schematic illustration of signal generated from electron beam – specimen interaction [38]. 80

Figure 2. 14 (a) A typical cyclic voltammetry potential waveform, and (b) cyclic voltammogram [41]....82

Figure 3. 1: SEM images of films deposited by femtosecond PLD with and without DC bias assistance at fluence 5 J/cm^2, (a) pure a-C film, (b) a-C:N film deposited at 10 Pa P_{N2} pressure, (c) Biased a-C:N film deposited at DC voltage 250 V and 5 Pa P_{N2} pressure. 91

Figure 3. 2 2D and 3D images of films obtained by AFM, (a) pure a-C , (b) 16 % of N contain a-C:N film deposited at 10 Pa P_{N2} pressure, (C) 24 % of N contain biased a-C:N film deposited at DC voltage 250 V and 5 Pa P_{N2} pressure. 92

Figure 3. 3 Nitrogen concentration revealed by XPS as a function of nitrogen pressure. 94

Figure 3. 4 C1s and N1s XPS signals, depending on the N content values from 0, 4, 10, 12 , 16 and 18 at.% 96

Figure 3. 5 Deconvolution of the C1s and N1s spectra of a-C:N films at different nitrogen concentrations, (a) and (b) at 4 % N film deposited at 0.5 Pa of P_{N2} pressure, (c) and (d) at 18 % N film deposited at 30 Pa of P_{N2} pressure. 97

Figure 3. 6 EELS spectrum of carbon and nitrogen K edges of a-C and a-C:N films with different nitrogen content at 10 and 15 at.% 99

Figure 3. 7 (a) N content of a-C:N films deposited at 1 Pa and 5 Pa, (b) bulk plasmon losses with nitrogen partial pressure. (c) EELS C-K edge energy loss with nitrogen partial pressures in a-C:N films, (d) EELS π/σ ratio vs nitrogen partial pressure. 100

Figure 3. 8 Raman spectra at 325 nm excitation of films prepared at different nitrogen pressures (showed in inset). 102

Figure 3. 9 (a) Variation of G position and I(D)/I(G) ratio, (b) G peak dispersion and FWHM (G) versus n content deduced from Raman measurements at 325 nm. 103

Figure 3. 10 Nitrogen content in a-C:N films vs negative substrate bias voltages. 104

Figure 3. 11 Deconvolution of the C1s and N1s spectra of a-C:N films at different nitrogen concentrations deposited at different DC bias voltages (inset) and constant P_{N2} pressure of 5 Pa. 108

Figure 3. 12 EELS investigations of the a-C:N films: a) nitrogen content, b) π/σ ratio and c) plasmon value. The dashed line is the reference values related to crystalline graphite. 111

Figure 3. 13 EELS spectra of C-K edge and N-K edge of a-C:N films with different bias voltages. 111

Figure 3. 14 HRTEM of the a-C:N and bias a-C:N films deposited with a N_2 pressure of 5 Pa, at various DC bias (shown inset). 113

Figure 3. 15 Comparison of Raman spectra of a-C:N films deposited at different bias voltages and 5 Pa N_2 pressure at Raman wavelength 325 nm, bias voltages are shown in inset. 114

Figure 3. 16 Variation of I(D)/I(G) and FWHM versus bias effect deduced from Raman spectra at 325 nm. 115

Figure 3. 17 XPS deconvoluted C1s spectra of (a) a-C (b) a-C:N film deposited at 10 Pa (c) biased a-C:N film deposited 5 Pa and 250 V bias, and N1s spectra of (d) a-C:N deposited at 10 pa, (e) biased a-C:N film deposited at 5 pa and 250 V bias. 119

Figure 3. 18 Chemical shifts of the C1s (a) and N1s (b) XPS spectra of a-C, a-C:N (10 Pa) and biased a-C:N (5 pa and 250 V) films superimposed on the compilation of Rodil *et al*.[[19]]. 120

Figure 3. 19 EELS spectra of the a-C, a-C:N (deposited at 10 Pa) and biased a-C:N (deposited at 5 pa and 250 V) films: (a) low loss spectra, (b) C-K edge spectra. 122

Figure 3. 20 Raman spectra of (a) a-C, (b) a-C:N (10 Pa) and (c) biased a-C:N (5 Pa and 250 V) obtained at four wavelength, (d) superimposed Raman spectra of the three films at 325 nm. 124

Figure 3. 21 (a) Variation of I(D)/I(G) ratio and FWHM (G); (b) G peak position and G Peak dispersion versus N content deduced from RAMAN measurement at 325 nm. 125

Figure 3. 22 Dispersion of the G peak versus N content (already published data from [[42]]). 126

Figure 4. 1 Optical emission spectra of graphite ablation plumes expanding in vacuum and various gas conditions at 10 Pa with and without bias assistance at 250V was recorded from 20 ns to 50 µs after interaction. 135

Figure 4. 2 Spectrally resolved emission from CN (375-385 nm) and C_2 (455-465 nm) of fs laser-induced carbon plasma plume expansion in 1 Pa of inert N_2 gas or of nitrogen plasma recorded at a) 1000 to 1200 ns b) 2500 to 3000 ns after laser interaction. 138

Figure 4. 3 Emission from CN and C_2 molecules summed along the ejection axis in 1 Pa of N_2 inert gas or nitrogen plasma a) from 1000 to 1200 ns and b) from 2500 to 3000 ns after laser interaction. 139

Figure 4. 4 Spectrally resolved emission from CN (375-385 nm) and C_2 (455-465 nm)) of fs laser-induced carbon plasma plume expansion in 10 Pa of N_2 inert gas or nitrogen plasma (250 V bias assistance) at a) 1000 to 1200 ns b) 2500 to 3000 ns after interaction. 140

Figure 4. 5 Emission from CN and C_2 molecules summed along the ejection axis in 10 Pa of N_2 inert gas or nitrogen plasma at 250 V from a) 1000 to 1200 ns b) 2500-3000 ns after laser interaction. 141

Figure 4. 6 Raman spectra of a-C and a-C: N films deposited at different nitrogen pressures and DC bias along with their N content values (showed in legend). 143

Figure 5. 1 Background cyclic voltammetric i-E curves for a-C and a-C:N (deposited at 10 Pa P_{N2} pressure) electrodes in 0.1 M $NaClO_4$, at room temperature, scan rate 100 mV/s. 153

Figure 5. 2 Cyclic voltammetry of 0.5 mM ferrocene di-methanol in 0.1M $NaClO_4$ solution, on a-C, a-C:N and bias a-C:N films, scan rate 100 mV/s. 154

Figure 5. 3 Cyclic voltammograms (CV) of a-C:N (10 % of N deposited at 1 Pa P_{N2} pressure) electrode in 0.5 mM $Fc(CH_2OH)_2$ in 0.1 M $NaClO_4$ at different scan rates (showed in inset).... 155

Figure 5.5 The correlation between the Raman parameters and electrochemical properties. 157

Figure 5.6 The influence of nitrogen content on electrochemical properties. 158

Figure 5.7 Voltammograms of a-C:N (10 at.%) electrode in 0.1 M potassium citrate and HCl buffer PH 2 for different Pb concentrations, Deposition potential is -1.7 V vs. SCE, Potential step 10 mV, scan rate 50 mV/s. 160

Figure 5.8 Evolution of the peak current as a function of Pb concentration for a-C:N (10 at.%) electrode deposited at 1 Pa, scan rate 50 mV/s. 161

Figure 5.9 Schematic of synthetic route used for the synthesis of grafted molecules. 163

Figure 5.10 Cyclic voltammogram (CV) of the in-situ generated 4-ethynylphenyl diazonium salt on a-C:N (10 at.% of N) electrodes at 0.1V/s in HCl 0.1M containing 40 mM $NaNO_2$ and 2 mM 4-ethynylaniline. The solution is at 4°C and degassed with N_2. In blue are shown the first CV scan, than in red the two consecutive scans. 164

Figure 5.11 The anodic peak currents as a function of scan rates after ferrocene attachment to the a-C:N (10 at.%) electrode deposited at 1 Pa P_{N2} pressure. 165

Figure 5.12 Voltammograms in 0.1 M $NaClO_4$ at 0.1 V/s of a a-C:N electrode, the data in blue shows a voltammogram of the bare a-C:N electrode before electrografting and click reaction procedure. The data in red shows a voltammogram of the Fc-modified self-organized a-C:N electrode performed by electrografting and click reactions procedure. 165

Figure 6. 1 Various synthesis methods to introduce N doping and various characterization techniques used for the examination of N doping extracted from [30], our N doped graphene synthesis approach and characterization techniques are included. 177

Figure 6. 2 (a) Schematic representation of N doped graphene growth from amorphous carbon nitride (a-C:N) thin film deposited by fs-PLD, (b) shows a temperature profile of N doped graphene. 178

Figure 6. 3 Raman spectra at 442 nm of Ni/a-C (10 nm)/SiO_2 before annealing (black curve), and after annealing at 780oC (red curve). 180

Figure 6. 4 Raman spectra of graphene deposited at different amorphous carbon (a-C) thicknesses Ni/a-C (2nm, 5 nm, 10 nm)/ SiO_2 at 442 nm. 181

Figure 6. 5 Raman spectra of graphene (Ni/a-C(10 nm)/SiO_2) and N doped graphene (Ni/a-C:N(10 nm)/SiO2), where D, G and 2D denote the characteristic D band, G band and 2D band of graphene, at Raman wavelength 633 nm (inset shows the enlarged 2D zone). 183

Figure 6. 6 Raman spectra of (a) N doped graphene deposited at Ni(153nm)/a-C:N(10nm)/SiO_2, (b) Raman map showing the variation in 2D/G peak intensity ratio over a 30 µm x 30 µm area of N doped graphene sample, at Raman wavelength of 442 nm. 184

Figure 6. 7 Typical SEM images (a) graphene from Ni/a-C(10 nm)/SiO_2, (b) N doped graphene from Ni/a-C:N(10 nm)/SiO_2 after thermal annealing at 780°C during 30 min. 186

Figure 6. 8 AFM images of graphene (Ni/a-C(10 nm)/SiO_2) and N doped graphene (Ni/a-C:N(10 nm)/SiO_2). 187

Figure 6. 9 XPS general spectra of graphene (Ni/a-C/SiO_2) and nitrogen doped graphene (Ni/a-C:N/SiO_2), both films were annealed at 780°C. 189

Figure 6. 10 (a) XPS C1s spectra of graphene and N doped graphene (b) N1s spectra of N doped graphene. 190

Figure 6. 11 Deconvoluted (a) C1s spectra, (b) N1s spectra of N doped graphene. 190

List of Tables

Table 1. 1 Literature review presentation of different PLD deposited CN films presenting the highest N content. 32

Table 2. 1 The deposited films along with their deposition rate, and with the different experimental parameters of DC bias and N_2 pressure values. 62

Table 2. 2 The combination of fitting functions, BWF: Breit-Wigner-Fano, L: Lorentzian, G: Gaussian, inside parenthesis G and D denotes that G: G peak, D: D peak. 70

Table 3. 1 The C1s and N1s binding energy values of XPS spectra of a-C:N films deposited at different nitrogen partial pressure. 96

Table 3. 2 Characteristics of Raman spectra at 325 nm of a-C and a-C:N films with different nitrogen pressure. 103

Table 3. 3 XPS C1s and N1s contributions in the a-C:N films deposited at different bias voltages and at 5 Pa constant pressure. 106

Table 3. 4 Characteristics of Raman spectra related to different bias voltages and at constant pressure at 5 Pa. 115

Table 3. 5 XPS C1s and N1s contributions in the a-C, a-C:N (10 Pa) and biased a-C:N (5 pa and 250 V) films and N/C ratio and N at.% deduced from XPS. 119

Table 3. 6 Characteristics of MW Raman spectra related to the a-C, a-C:N and biased a-C:N films, a-C:N film deposited at 10 Pa P_{N2} pressure and biased a-C:N film deposited at 5 Pa P_{N2} pressure and 250 V DC bias assistance. 125

Table 4. 1 Nitrogen contents from a-C:N films deposited by femtosecond laser deposition with various bias and nitrogen pressure conditions. 142

Table 5. 1 Potential difference values ΔEp, ratio of anodic to cathodic peak currents (Ipox/Ipred) and apparent rate constant data k° of different films, at a scan rate 100 mV/s. 156

Table 6. 1 Experimental conditions for femtosecond PLD of a-C and a-C:N films, catalyst film thickness and annealing conditions. 179

Table 6. 2 Raman parameters deduced from deconvolution of Raman spectra at 442 nm of graphene and N doped graphene. 185

Appendix

Supplementary Information

Structure, electrochemical properties and electrografting of amorphous CN films deposited by femtosecond pulsed laser ablation

Nicholson Method for k° determination in diffusive system.

A quasi reversible electron transfer process results in a peak-to-peak separation (ΔE_p) that increases with the scan rate (v) and this effect allows one to calculate a heterogeneous electron transfer rate (k°) using the commonly used Nicholson method [1] :

$$\psi = k^\circ \left(\frac{D_O}{D_R}\right)^{\alpha/2} \sqrt{\frac{RT}{\pi n F D_O v}} \qquad \text{(eq. S1)}$$

where ψ is the dimensionless kinetic parameter determined from ΔE_p, α the electron transfer coefficient, n the number of electrons transferred during the redox event, D_O and D_R are respectively the diffusion coefficient of the oxidized and reduced forms of the redox mediator, F the Faraday constant, R the gas constant value and T the temperature. In the case of ferrocene redox probe, D_O and D_R are assumed to be equal and that the reduction and the oxidation kinetics are symmetrical, i.e., α ≈ 0.5 so that eq. S1 can be simplified to

$$\psi = k^\circ \sqrt{\frac{RT}{\pi n F D v}} \qquad \text{(eq. S2)}$$

ψ is calculated using an empirically determined working function [2] for a given ΔE_p:

$$\psi = \frac{(-0.6288 + 0.0021 n \Delta E_p)}{(1 - 0.017 n \Delta E_p)} \qquad \text{(eq. S3)}$$

where ΔE_p is given in mV and limited to values below ca. 220mV.

V in V/s	ΔE_p in mV	ψ
0.1	63	6.993
0.2	68	3.115
0.5	80	1.28
0.8	87	1
1	91	0.800

Table S1A. Empirically determined value of ψ calculated from ΔE_p value beyond 59mV (quasi-reversible behavior) for a-C film.

V in V/s	ΔE_p in mV	ψ
0.1	65	4.689
0.2	71	2.317
0.5	86	0.970
0.8	96	1
1	103	0.549

Table S1B. Empirically determined value of ψ calculated from ΔE_p value beyond 59mV (quasi-reversible behavior) for a-C:N (10%) film.

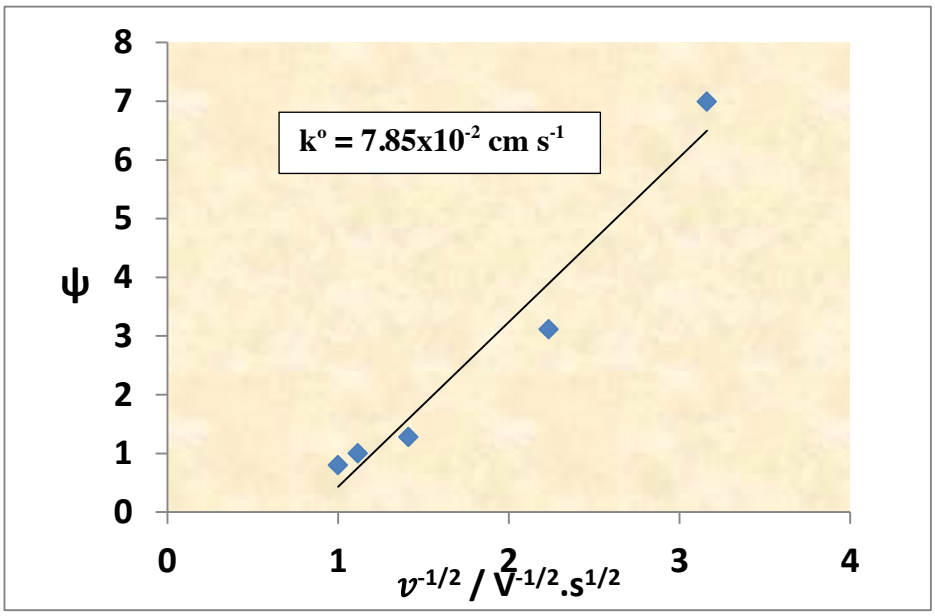

Figure S1A. Variation of ψ with the scan rate using for k° determination from the slope of the $\psi = f(v^{-\frac{1}{2}})$ dependence for a-C film.

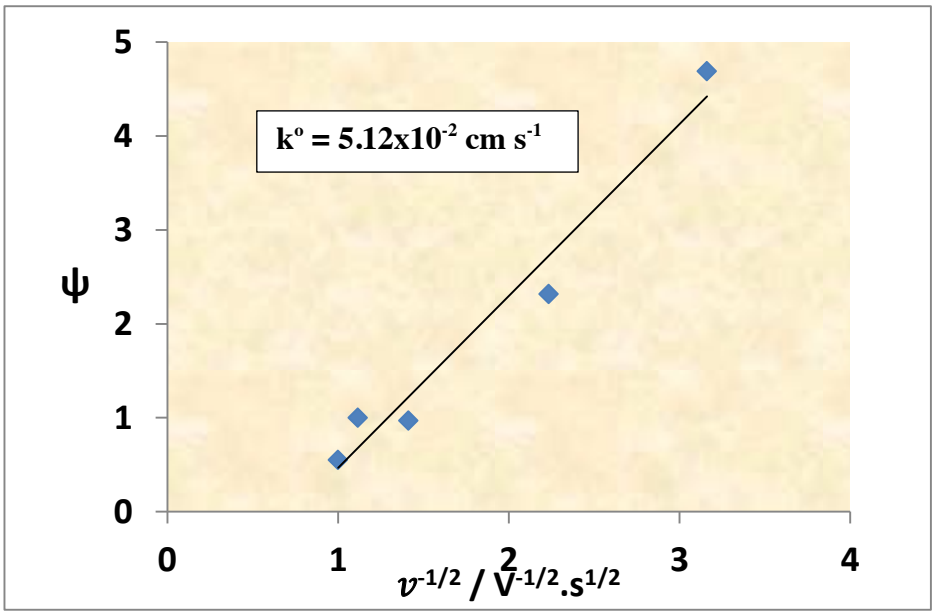

Figure S1B. Variation of ψ with the scan rate using for k° determination from the slope of the $\psi = f(v^{-\frac{1}{2}})$ dependence for a-C:N (10%) film.

References

1. Nicholson, R. S. Theory and Application of Cyclic Voltammetry for Measurement of Electrode Reaction Kinetics. *Anal. Chem.* 1965, 37, 1351-1355.

2. Lavagnini, I.; Antiochia, R.; Magno, F. An Extended Method for the Practical Evaluation of the Standard Rate Constant from Cyclic Voltammetric Data. *Electroanal.* 2004, 16, 505-506.